A hydrodynamic study of nickel suspension in stirred tanks

A thesis submitted to the University of Cape Town

in fulfilment of the requirements for the degree of

Doctor of Philosophy

by

Ochieng Aoyi DipEd (Sc), BEng (Chem. Eng.), MSc (Eng.)

Department of Chemical Engineering

University of Cape Town

August 2005

Acknowledgement

First of all I would like to thank my supervisor, A/Prof Alison Emslie Lewis for her insightful ideas that enabled the completion of this work. The dedication with which she read the thesis draft and the feed back period for this was nothing but excellent. I wish to thank my wife, Achieng, for her support and patience. Dr Howard Pearce gave an important push during take off. Discussions with Prof Jim Petrie and Dr Paul Musonge were very inspiring. I wish to thank all those who made a contribution in one way or another to make this work come to a successful completion: Thanks to Dr. Phil Schwarz, Mr. Graeme Lane (CSIRO, Australia), Dr Harro von Blottnitz, Dr Silke Sauerbeck, Dr Rob van Hille, Auntie Fran Pocock, Mr Alex Mwale, Mr. Jeteen Nathoo, Ms Mandy Roberts, Mr Ryan Bass, Dr. Christian Taty Costodes, Dr. Yifei Zhang, Mr. Freeman Ntuli, Mr. Mfandaidza Hove and other members of the group.

I wish to give special thanks to Prof. Eric van Steen and to my parents for their encouragement when things appeared very difficult.

Finally, I wish to thank Moi University, Impala Platinum and the National Research Foundation for the financial support and the Departmental team for ensuring that the support systems worked.

Ochieng Aoyi

August 2005

Certification by supervisor

In terms of paragraph 8 of "General rules for the degree of PhD", I A/Prof. Alison E. Lewis, as supervisor of the candidate, Ochieng Aoyi, certify that I approve of the incorporation in this thesis of material that has been published.

List of publications

- Ochieng Aoyi, Alison E. Lewis, CFD simulation of nickel solids off-bottom suspension and cloud height, *Hydrometallurgy* journal (accepted).
- Ochieng Aoyi, Alison E. Lewis, CFD simulation of nickel solids concentration distribution in a stirred tank *Minerals Engineering* journal (in press).
- Ochieng Aoyi, Alison E. Lewis (2004). CFD simulation of mixing and power consumption in a tank with a low impeller clearance, *4th South African Conference on Applied Mechanics,* Johannesburg, South Africa, 18th-21st January 2004, (81), 1-9.
- Ochieng Aoyi, Alison E. Lewis, Howard Pearce, (2003). CFD simulation of the hydrodynamics of a reactor with draft tube, In, *Proceedings of the XXII International Mineral Processing Congress,* Cape Town, South Africa, 28th September-3rd October 2003, 1682-1691.

A/Prof. Alison E. Lewis
Department of Chemical Engineering, University of Cape Town,
Private Bag, Rondebosch, 7701, Cape Town

Abstract

Many studies on solid-liquid mixing have been dedicated to low density particles at low solids concentrations. In the present work, computational fluid dynamics (CFD) simulation and experimental methods were employed to study suspension of high density particles (nickel) at high solids concentration in water. The work first focused on establishing the velocity field in a liquid-only system and then progressed to a solid-liquid system. In the liquid-only system, the influence of tank geometry and simulation strategies, including turbulence models, on fluid flow pattern and mixing was investigated in a tank stirred by a Rushton turbine. The standard k-ε model gave better overall predictions of mean velocity fields than the k-ω and RNG k-ε models. The CFD simulation and experimental results obtained with the laser Doppler velocimetry (LDV) method showed that mixing time and homogenization energy decreased with a decrease in the impeller bottom clearance. It was further shown that there is a bottom clearance range in which a draft tube can aid mixing in a tank stirred by the Rushton turbine.

In the solid-liquid system, a hydrofoil impeller was used to investigate the influence of simulation strategies, particle properties and hydrodynamic operating conditions on mixing features such as the off-bottom solids suspension, cloud height, solids concentration distribution and local particle size distribution. The simulation results were compared with experimental ones, in which the off-bottom solids suspension was determined visually and an optical attenuation technique was employed to determine the cloud height and solids concentration distribution. The local particle size distribution (PSD) in the tank was measured by a laser diffraction method. A better agreement between the simulation and experimental results was obtained with drag models that account for the solids loading or free stream turbulence than those that do not. It was shown that the Stokes law applies up to a diameter of 150 μm for the nickel particles. A CFD simulation strategy for studying mixing of high density solids is proposed and it is shown that a CFD simulation method can be used to develop empirical models that predict mixing features. A CFD simulation approach that takes particle size into account gives predictions that are more representative of practical applications than the mono-size particle simulation approach. Reactor configurations and hydrodynamic parameters that improve mixing were identified. These can also aid optimal design of mixing systems.

Table of contents

List of figures

List of tables

Nomenclature

a_o	constant in equation (4.1)
A	geometry dependent coefficient in equations (3.10) and (3.11).
A_o	constant in equation (3.20)
Ar	Archimedes number $Ar = \frac{d_p^3}{\nu^2}\left(\frac{g\Delta\rho}{\rho_L}\right)$
C	impeller bottom clearance, m
c	concentration, kg m^{-3}
c_m	compaction modulus
CFD	computational fluid dynamics
$C_{\varepsilon 1}$, $C_{\varepsilon 2}$, C_μ	turbulence model constants
c_1,c_2	constants in equation (3.63)
C_Δ,$C_{\Delta,p}$	constants in equation (3.53)
C_D	drag coefficient
C_{Do}	drag coefficient for quiescent liquid
C_L	non-dimensional lift coefficient
C_{MT}	momentum transfer coefficient, kg ms^{-1}
C_N	emperical constant, equation (3.10)
C_o	dimensionless constant in equation (3.31)
c_o	mean concentration, kg m^{-3}
C_{TD}	non-dimensional drag coefficient
C_{VM}	non-dimensional virtual mass coefficient
D	impeller diameter, m
D_{LS}	turbulent diffusivity, $m^{-2}s^{-1}$
DT	draft tube
d	draft tube diameter, m
d_p	particle diameter, m
d_{50}	mean particle diameter, m
F_B	body forces, kg $m^{-2}s^{-2}$
F_C	Coriolis and centrifugal forces, kg $m^{-2}s^{-2}$
F_D	drag forces, kg $m^{-2}s^{-2}$
F_I	interfacial forces, kg $m^{-2}s^{-2}$
F_L	lift force, kg $m^{-2}s^{-2}$
F_{ND}	non-drag forces, kg $m^{-2}s^{-2}$

Fr	Froude number, $Fr = N^2D/g$
F_{TD}	turbulent dispersion force, kg $m^{-2}s^{-2}$
F_{VM}	virtual mass force, kg $m^{-2}s^{-2}$
F_{WL}	wall lubrication force, kg $m^{-2}s^{-2}$
F_Φ, F_ϕ	source terms for body forces, kg $m^{-2}s^{-2}$
g	acceleration due to gravity, ms^{-2}
G	turbulence production term, kg $m^{-1}s^{-3}$
G_o	reference elasticity modulus, Pa
h	cloud height, m
H	liquid height, m
H15T	configuration with hydrofoil propeller at C=0.15T
k	turbulent kinetic energy, m^2s^{-2}
i, j, k	directional coordinates
I	signals passing through a slurry, V
I_o	signals passing through liquid without slurry, V
IBC	impeller boundary condition
k_o	constant in equation (2.1)
l	length scale of the largest eddy, m
l_1	transition distance traveled by a particle in a settling tank, m
l_2	total distance traveled by a particle in a settling tank, m
LDV	laser Doppler velocimetry
t_1	time taken by particle in the transition distance in a settling tank, s
t_2	total taken by particle in a settling tank, s
l_m	mixing length scale, m
M	impeller torque, Nm
MFR	multiple frames of reference
N	impeller speed, s^{-1}
n_b	number of impeller blades
n_c	critical impeller speed, s^{-1}
N_{js}	impeller speed for just off-bottom solids suspension, s^{-1}
n_o	total number of phases
n_w	unit normal pointing away from the wall
N_P	impeller power number ($N_p = P/\rho N^3D^5$)

N_Q	pumping number ($N_Q = 0.8(P/\rho)^{-0.7}(w/T)n_b^{0.6}$)
P	power, W
p	pressure, $kgm^{-1}s^{-2}$
p''	modified pressure, $kgm^{-1}s^{-2}$
Pe	Peclet number ($Pe = \rho u/(\Gamma/\Delta x)$)
r	tank radial dimension, m
rps	revolutions per second
rpm	revolutions per minute
R	tank radius, m
R15T	configuration with Rushtone turbine at C=0.15T
Re	impeller Reynolds number ($Re=ND^2/\nu$)
Re_p	particle Reynolds number ($Re=d_pU_r/\nu$)
Re_p'	modified particle Reynolds number, ($Re_p' = \varphi_L Re_p$)
S	geometry dependent coefficient in equations (3.9) and (3.10)
SG	sliding grid
St	Stokes number ($St = Nd_p^2/18\nu$)
t_i	particles settling time, s
t	time, s
t_Θ	mixing time, s
T	tank diameter, m
u	instanteneous velocity vector, ms^{-1}
U	axial velocity component, ms^{-1}
U	mean velocity vector, ms^{-1}
U_{core}	overall maximum velocity in the wall jet, ms^{-1}
U_m	local maximum velocity in the wall jet, ms^{-1}
U_r	slip velocity, ms^{-1}
U_t	terminal velocity, ms^{-1}
u'	fluctuating velocity, ms^{-1}
V_T	volume of fluid domain, m^3
V_{tip}	impeller tip speed ($V_{tip}= \pi ND$), ms^{-1}
W	tangential velocity component, ms^{-1}
w	width of impeller blade, m
V	radial velocity component, ms^{-1}

v	local volume fraction
v_o	mean volume fraction
w_s	percentage mass ratio of solids, %
$\boldsymbol{Y}$	location vector
x	axial distance, m

Greek symbols

α_1, α_2	constants in equation (3.13) and (3.14)
β	constants in equation (3.13) and (3.14
δ_{ij}	Kronecker delta function
ε	local turbulent kinetic energy dissipation rate, m^2s^{-3}
ε_{CFD}	simulated local turbulent kinetic energy dissipation rate, m^2s^{-3}
ε_{LDV}	experimental local turbulent kinetic energy dissipation rate, m^2s^{-3}
$\bar{\varepsilon}_{CFD}$	simulated specific kinetic energy dissipation rate, m^2s^{-3}
$\bar{\varepsilon}_P$	experimental mean specific kinetic energy dissipation rate, m^2s^{-3}
ϕ	instantaneous transport property
η	homogenization energy, m^2s^{-2}
φ	phase hold up
φ_{sm}	maximum packing parameter
κ	constants in equation (3.14)
λ	Kolmogoroff length scale ($\lambda=(\nu^3/\varepsilon)^{1/4}$), m
μ	molecular viscosity, $kgm^{-1}s^{-1}$
μ_t	turbulent viscosity, $kgm^{-1}s^{-1}$
ν	kinematic viscosity, m^2s^{-1}
θ	tangential dimension, degrees
ρ	density, kgm^{-3}
σ_k, σ_ε	Prandtl numbers that connect the diffusivity of k and ε
σ_t,	turbulent Schmidt numbers
τ	stress tensor
σ_t	turbulent Schmidt number
ϖ	rotation of the fluid flow field, radians s^{-1}
ω	turbulent frequency, s^{-1}

Φ	mean transport property
Θ	level of homogeneity
ϑ	velocity scale, m
Γ	molecular diffusivity, $kgm^{-1}s^{-1}$
Γ_e	turbulent eddy diffusivity, $kgm^{-1}s^{-1}$
Ω	rotational speed of the reference frame, radians s^{-1}
Λ	turbulent length scale, m
Δx	cell width, m

Subscripts and superscripts

b	blade
D	drag
L	liquid
P	power
p	particle
S	solid
t	turbulence
T	tank
P	particle
CFD	computational fluid dynamics
LDV	laser Doppler velocimetry
js	just suspended
′	fluctuating property

1. Introduction

Hydrodynamics and mixing efficiency in stirred tanks are important for the design of many industrial processes such as precipitation, flotation and biochemical processes. Smith (1990) reported that the lack of a fundamental understanding of the processes in stirred vessels leads to losses of the order of US$10 billion per year due non-optimal energy utilization. The economics of a process depends on the performance of a stirred tank with respect to mixing, power consumption, and rate of reactions as well as the product quality. Mixing in stirred tanks is driven by the impeller generated convective motion at larger scales, by turbulent transfer at smaller scales and down to diffusion at molecular scales (Nagata, 1975).

In a multiphase system, hydrodynamic characteristics influence phase mixing and mass transfer, and these affect conversion in a reactor. Detailed information on the effects of the hydrodynamics on the performance of an agitated system with high density particles like nickel is still required for the design and operation of hydrometallurgical systems. There is a need to identify and quantify the operating hydrodynamic parameters that influence the quality of mixing, and this can be done by both experimental and simulation methods. The relative influence of the hydrodynamic parameters on the mixing performance of a stirred tank may vary with the detailed system specifications, which keep changing with time.

1.1. General introduction

Experimental methods have typically been used to study the hydrodynamics in mixing tanks. Interpretation of the experimental data can be enhanced if there is an understanding of the physics of the flow. In this regard, mathematical models based on experimental data or on the fundamental principles of fluid flow have been employed to obtain detailed information on the flow field, and this enhances the understanding of the mixing mechanisms involved. The level of sophistication of these models ranges from a single linear equation to a complex non-linear set of partial differential equations. Computational fluid dynamics (CFD) method, which is based on partial differential equations describing fluid flow, has proved to be a useful tool for studies of system hydrodynamics, especially, in the last ten years.

1.1.1. Experimental methods

Measurement of mixing time and circulation time can be used to investigate the macro scale mixing performance of a stirred tank resulting from the bulk fluid flow. These mixing parameters do not account for spatial variations, which are the characteristic features of stirred tanks. Information on these spatial variations can be obtained by high precision measurement methods such as the laser Doppler velocimetry (LDV). However, this technique is only applicable to a translucent tank and fluid, and not suitable for most chemical engineering applications. These technical limitations can therefore preclude the use of such a method to study the influence of hydrodynamics on reactor performance in many practical applications.

In solid-liquid systems, it is important to determine the distribution of the solids in the tank in accordance with the process requirements. Some processes require that the particles are just suspended off the bottom, whilst, in some processes, complete off-bottom solids suspension is necessary. The analysis of these two conditions requires different experimental approaches, of which visual method is the simplest. The visual method is subjective but more adequate for determining off-bottom solids suspension than for complete suspension. To determine solids concentration distribution, a sampling method can be employed. However, the implementation of this method involves an interference with the fluid flow, and there are many other sources of error. Non-intrusive techniques such as the optical attenuation technique (OAT) and particle image velocimetry (PIV) can give more accurate data. The non-intrusive techniques are generally costly and their operation may require specialized training. Other equipment such the scanning electron-microscopy (SEM), which are used to measure particle morphology are equally costly. Due to the high cost of the equipment and the technical limitations, simulation techniques such as CFD can be employed for the same purpose.

1.1.2. Simulation methods

Successful implementation of simulation techniques depends on the computational power al well as the robustness of the solution algorithms. In recent years, there has been a growing demand for fluid dynamic simulation software due to the rapid development in computational technology, which has made CFD an important tool for research and design. It has been employed to study hydrodynamics and mixing, much of which has focused on the performance of axial and radial pumping impellers. The currently available computational

resources cannot simultaneously resolve the turbulence structures at the length scales of both industrial reactor and particle. Thus, the models applied in the CFD simulation need to be validated with experimental results. The information obtained with a validated model can provide some insights into flow homogeneity, and in particular, the existence of dead zones in the tank.

1.2. Motivation and aim

In a nickel reduction process, hydrogen gas must first dissolve into the bulk liquid and then adsorb onto the surface of the seed nickel particles before it can react with the ammoniacal nickel sulphate solution. The rate of the reaction, therefore, depends on the available nickel surface area (Willis and Essen, 2000). The mass transfer of hydrogen between nickel particles and the solution depends on the motion of the solids surface relative to the surrounding liquid. There are two ways of introducing hydrogen into the reactor; either below the impeller or above the liquid free surface. In both cases, hydrofoil impellers are typically employed for the mixing of the phases. In a case where hydrogen is introduced above the liquid surface (not directly into the liquid), the influence of the hydrogen on the impeller performance is reduced, and in that way, the system operates like a solid-liquid phase. This makes the solid-liquid mixing, and specifically, the solids concentration distribution, an important aspect of this process. However, there is no information in the open literature on the concentration distribution of high density solids in a stirred tank.

1.2.1. Problem statement

Compared to the Rushton turbine and pitched blade impellers, hydrofoil impellers have complex blade geometry and the flow generated by these impellers in a solid-liquid system is not well understood. Thus, there is a need to obtain information on the flow patterns and the level of homogeneity generated by the interaction of the impeller blade and the tank geometry as well as the fluid properties. In a solid-liquid system, these flow structures influence mixing both at reactor scale and at the particle scale. CFD predictions can provide information on the axial and radial solids concentration distributions as well as the particle size distribution in the tank.

1.2.2. General objective

The main objective of the work is to apply a CFD technique to obtain detailed information on hydrodynamics of liquid-only and solid-liquids system and to validate the CFD simualtions with experimetal measurements.

1.3. Outline

This thesis is divided into eight chapters:

- Chapter 2 deals with the literature review, in which flows generated by different impeller assemblies in single and multiphase systems are discussed. Experimental and simulation work on mixing and solids suspension that has been reported in literature is discussed.
- Chapter 3 covers the details of the models outlined in Chapter 2. The governing CFD simulation equations for single and multiphase turbulent flows, and closure for the additional terms in these equations, are defined.
- Experimental and simulation methods are described in Chapter 4. Methods were developed that correlate the typical experimental and simulation approaches to solids suspension studies. The LDV and OAT measurement techniques are described.
- In Chapter 5, results and discussion for the liquid-only system are presented. The influence of the discretization schemes, impeller modelling and k-ε turbulence model parameters on the flow field are investigated. Model parameters that influence fluid flow patterns and mixing in a tank stirred by a pitched blade impeller and the Rushton turbine are determined.
- In Chapter 6, the results and discussion on solids suspension with a hydrofoil propeller only are presented. The conventional methods of determining the impeller speed required to achieve just off-bottom solids suspension and solids cloud height are discussed and correlated to the CFD simulation methods. Factors that affect solids suspension are investigated.
- The overall conclusions are drawn in Chapter 7.
- Chapter 8 is the list of references, after which, the appendices are given.

CHAPTER 2

2. Literature review

Hydrodynamic characteristics in a reactor depend on factors such as physical properties of the fluid, the operating parameters and the reactor geometry. Often, one of the main design objectives is to maximize homogeneity at the minimum possible cost. In crystallization and precipitation processes, both solids hold-up and particle size increase with time, and these require an increasing amount of energy dissipation if the level of the homogeneity is to be maintained. On the one hand, keeping the impeller tip speed constant during the process results in an inefficient power utilization and on the other hand, increasing the impeller tip speed to keep up with the increasing load requires more complex design specifications and operation procedures. All these factors contribute to the process operating costs. The initial capital cost depends on the reactor configuration, which influences the fluid flow pattern and, consequently the quality of mixing. Therefore, the reactor configuration influences not only the initial capital cost but also the operating cost. In this regard, the optimal design and operation of a solid-liquid system is a field in which more work is still required. Both experimental and simulation approaches can be used determine the optimal design and operating condition for a particular application.

Experimental hydrodynamic methods have traditionally been used to study such systems with the focus being either on the influence of reactor configuration and fluid properties on flow patterns or on mixing. An investigation into the influence of the reactor geometry and impeller type on flow patterns can give an insight into the quality of mixing and power draw. The main limitation of experimental methods is the cost involved, especially for measurement of turbulent fields.

In the last two decades, developments in computer technology have resulted in increasing use of simulation and modelling methods. There are two major categories of process modelling: functional block or empirical and first principle modelling approaches. The functional block approach may be referred to as black box modelling. This approach treats the system as a black box such that there is no physical or chemical analysis of the process. In developing the black box models, an empirical hydrodynamic model is fitted to experimental data, from which the model parameters are determined. The fitted parameters may represent chemical

or hydrodynamic properties. These empirical models, typically defined by dimensionless numbers, do not resolve spatial and temporal variations in the entire domain of a stirred tank. In solid-liquid systems, such models can be employed to investigate the off-bottom solids suspension by relating the impeller speed to the vessel geometry and, properties of the particles and liquid.

In the first principle approach, models are derived from the fundamental physical and chemical laws like mass, heat and energy balances. These can be represented by models based on the fundamental principles of fluid flow (such as the Navier-Stokes equation) and the models can have a more general application. The solution to these equations can be obtained by computational fluid dynamics (CFD) techniques. CFD is a first principle simulation model, in which the partial differential equations that describe the fluid flow are formulated and discretized in a control volume (for a finite volume method) and solved by introducing boundary conditions. The simulation domains are typically multiphase and turbulent flow systems. Flows in a solid-liquid system are affected by turbulent structures both at the reactor scale and at the particle scale. At a reactor scale, solids distribution in a stirred tank depends on the bulk fluid flow resulting from the interaction between the reactor geometry and the impeller generated flow. At the particle scale, the intensity of the free stream turbulence generated by the impeller affects the flow field around the particle, and this influences the drag force. Further, there is an interaction between particles and eddies at the Kolmogoroff length scale. Such small scale mechanisms require microscopic hydrodynamic modelling (Torbacke and Ake, 2001), which is highly computationally demanding.

2.1. Experimental methods

Flows generated in stirred tanks can be either laminar or turbulent depending on the relative ratio of the inertial forces to viscous forces, which is represented by the impeller Reynolds number (Re). Many flows encountered in industrial processes are turbulent and the value of Re at which a system can be regarded as turbulent varies in the literature. A value of $Re > 10^4$ is generally considered to represent turbulent flow (Tatterson, 1991). The Reynolds number does not account for the size or aspect ratio of the tank, which influences the distribution of the intensity of the turbulence in the tank. The fluid flow in tank regions closer to the wall and liquid surface may be laminar, depending on the ratio of the impeller diameter to the diameter of the tank and the tank aspect ratio.

2.1.1. Reactor geometry

Mixing tanks can have a flat or profile-based bottom, and the degree of the bottom curvature depends on the intended operation. Flat-bottomed stirred tanks are commonly used for liquid systems, while dished or elliptically bottomed tanks are used in solid-liquid or solid-liquid-gas systems to aid particle suspension. Many studies have been conducted in flat-bottomed tanks and with conventional impellers such as the Rushton turbine, pitched blade impeller and flat blade paddles (Fajner et al., 1985; Magelli et al., 1990; Armenante and Nagamine, 1998; Murugesan, 2001; Kee and Tan 2002; Derksen, 2003). Relatively few studies have been carried out with round or dished-bottomed tanks (Barresi and Baldi, 1987; Cate et al., 2001; Sharma and Shaikh, 2003). It is known that round bottomed tanks enhance particle suspension by eliminating dead zones at the wall junctions (Sharma and Shaikh, 2003). Dead zones or regions of segregation can be found at the wall junctions, especially for the high aspect ratio tanks with flat bottoms. The main advantages of the high aspect ratio tanks include high volumetric loading and economy of space, and the disadvantages are the increased regions of segregation and hydrostatic head. In order to reduce the dead zones in high aspect ratio tanks, tank internals such as baffles and draft tubes are used to improve mixing. Configurations of the high aspect ratio tanks deviate from the standard ones, in which the liquid height (H) is typically the same as the tank diameter (T), for a tank stirred by a single impeller. The standard impeller diameter (D) and its clearance from the bottom is 1/3T (Oldshue, 1983). Differences in the definition of the bottom impeller clearance with respect to the tank bottom profile and edge finishing accuracy may cause disparities in experimental results. Thus, many results reported in literature are not easily reproducible.

Baffles

Turbulent mixing is typically carried out in baffled tanks. These tanks are usually equipped with four equally spaced baffles with the width of the baffle usually being 1/12 to 1/10 of the tank diameter (Oldshue, 1983). Power consumption increases with the number of baffles, but a decrease in the number of baffles results in a poor mixing. Without baffles, swirl and central vortex formation may be experienced, which result in low shear rate, even if a high shear impeller like the Rushton turbine is used. Baffles change the flow patterns by converting part of the circumferential and radial velocity components into the axial velocity component. This enhances the axial circulation of the fluid, and at the same time introduces loops in the vicinity of the baffles. These loops can be suppressed by an increased upward current induced by a draft tube. In solid-liquid systems, wall off-set baffles have been

employed to avoid solids deposition at the junction of the baffles and the tank walls. In baffled tanks, the radial solids concentration gradient is lower than the axial one (Barresi and Baldi, 1987).

Draft tubes

The design parameters for a draft tube include the liquid level above the draft tube, bottom clearance and the ratio of draft tube diameter to that of the tank. Oldshue (1983) recommends that the draft tube bottom clearance should be at least one draft tube diameter. Draft tubes enhance the axial mixing and reduce inter-particle collision, (Cate et al., 2001) which leads to a decrease in particle attrition. The highest flow per power can be obtained by this device (Oldshue, 1983), especially if used in a fully baffled tank. A small draft tube cross-sectional area results in a high velocity in the draft tube. This leads to an increased head loss, which is a function of the square of the fluid velocity in the draft tube (Oldshue, 1983).

2.1.2. Impellers

Impellers are classified either as axial or radial pumping, and the ones that do not fall into these two categories are referred to as mixed flow impellers. The axial ones are high flow while the radial ones are high shear impellers. The choice of an impeller influences both capital and operation cost in mixing processes. One major component of the capital cost is the gear drive, which is specified according to the required torque. The subsequent cost of operation depends on the power dissipated, and this is determined by the required level of homogenization.

Impeller types

The Rushton turbine is the most widely used radial pumping impeller, for which the principal direction of discharge is normal to the axis of rotation. The impeller is typically made of six vertical blades bolted to a support disc and is used in applications that require high shear (Oldshue, 1983). It has been extensively studied in both single phase (Oldshue, 1983; Lee and Yianneskis, 1998) and multiphase (Murugesan, 2001; Guillard and Tragardh, 2003) systems. It has widely been used for precipitation reactions in which micro-mixing is required (Rielly and Marquis, 2001). Most impeller blades and baffles influence mixing at the meso scale. This scale of mixing can be affected by the formation of the vortex behind

the impeller blade, as a result of a reduction in pressure. The vortex that forms behind impeller blade may be referred to as a meso vortex, which is analogous to the description of the mixing at the impeller blade scale (meso mixing), as has been suggested by Ranade and van den Akker (1994).

Axial impellers have traditionally been employed to provide solids suspension (McKee et al., 1995; Armenante and Nagamine, 1998; Pattersson and Ake, 1998; Kuzmanic and Ljubicic, 2001). The axial impellers, which include the pitched blade impeller and marine propeller, generate a high circulation flow. This enhances suspension of solid particles in the bulk liquid, and therefore increases the surface area of the particles available for mass transfer. The marine propeller has been employed for solids suspension by Cate et al. (2001) and Biswas et al. (1999). Zauner and Jones (2000) reported that a marine propeller in a draft tube can provide a smooth and even flow field throughout the reactor.

Mixed flow impellers are a later generation impellers, and they include the Lightnin A315 propeller (Bouaifi and Roustan, 2001), Chemineer, Maxflot-T and Erato Intermig (Szalai et al., 2004), which have all been used for solids suspension (Bujalski et al., 1999; Kee and Tan, 2002; Pinelli and Magelli, 2000; Bittorf and Kresta, 2003). The Lightnin A315 propeller is used in systems where high circulation and high dispersive mixing are important, such as in gas-liquid systems (Baker, 1992; Smith et al., 2001; Lane et al., 2005) and solid-liquid systems (Bujalski et al., 1999).

Multiple impellers are used in a tank with a high aspect ratio, where a single impeller may not generate momentum high enough to overcome the hydrostatic head. The multiple impellers could all be Rushton turbines (Fajner et al., 1985; Pinelli and Magelli, 2001; Montante et al., 2003), pitched blade impellers (Ljungqvist and Rasmuson, 2001; Montante et al., 2001b; Sha et al., 2001a and 2001b; Sharma and Shaikh, 2003) or mixed type (Bouaifi and Roustan, 2001). In systems where the Rushton turbine is one of the impellers used, it is a common practice for the lowest impeller to be a Rushton turbine (Gunkel and Weber, 1975; Bujalski et al., 2002). In this type of impeller assembly, the clearance between the respective impellers and the clearance from the tank bottom affect their performance.

Impeller clearance

Impeller bottom clearance (C) may be defined as the distance from the bottom of the vessel to the centre of the hub, on which a blade (or disc, for the Rushton turbine) is attached. A clearance that is less than a third of the diameter of the tank is regarded as low. Most studies have been carried out at the standard impeller clearance (one third of the tank diameter). It has been shown (Nienow, 1968; Montante et al., 2001a; Wei et al., 2001) that the impeller clearance does affect the fluid flow pattern. It has been reported that the flow pattern generated by the Rushton turbine changes from the typical two loops at a standard clearance to a single loop pattern at a low clearance (Montante et al., 1999; Wei et al., 2001). At the same time, the discharge angle changes from the radial to axial direction (Montante et al. 1999). For a multiple impeller system, the optimal clearance at which there is minimal interference between the flow generated by the upper and lower impellers is equivalent to the tank diameter (Pinelli and Magelli, 2001; Bouaifi and Roustan, 2001).

Impeller performance indicators

Power number and pumping number are indicative of the circulation velocity and power draw, respectively. A retrofitting operation with constant power and impeller speed can be carried out to evaluate the relative influence of impeller geometry and pumping characteristics on the quality of mixing. It has been found that large impeller diameters are better for bulk mixing than large power number, small diameter ones (Nienow, 1996).

2.1.3. Mean and turbulent fields

Mixing in stirred tanks is influenced by both mean velocity and turbulent fields. Detailed information on the impeller generated flows can be obtained by measuring the spatial variation of the mean velocity and turbulent fields. The variation in pressure levels arising from the periodic movement of the blade relative to the baffles leads to the formation of turbulent structures such as trailing vortices behind the rotating blades. The upward stream of the flow interacts with the free surface, causing a vortex along the shaft. The downward stream impinges onto the bottom wall and gets deflected and consequently a vortex is formed. These turbulence structures and the bulk fluid pattern in general, have been studied for decades using parameters like flow number, mixing time and power number. In particular, it has been reported that trailing vortices behind the impeller blades influence the pumping capacity of the impellers (Ranade, 1999; Ranade and Despande, 1999; Ranade and Tayalia, 2001). Mean flow parameters like the impeller power number, pumping number and

mixing time do not give detailed information on the level of turbulent field distribution and local pressure or concentration gradients, which affect mass transfer, and consequently product quality.

The mean flow field has been measured by methods like hot wire anemometry (HWA) (Ewing et al., 1995); hot film anemometry (HFA) (Burmann and Pleschles, 1986; Bruun, 1996) electrochemical probes (EP) (Deglon, 1998), laser Doppler velocimetry (LDV) (Wu and Patterson, 1989; Ng et al., 1998; Andersson and Rasmuson, 2000) and digital particle image velocimetry (DPIV) (Fan et al., 2004). The most accurate results, at a very high cost, are obtained with both LDV and DPIV. The Doppler technique works on the principle that the Doppler effect is used to determine the velocity by examining the change in light signals reflected by the particles in the fluid. The LDV studies have shown that the interaction between the upward flow stream and the free surface results in the formation of one vortex at the corner where the free surface and the vertical wall meet (Montante et al., 2001a) and the other one forms just below the region where the shaft and the free surface meet (Yianneskis et al., 1987; Lee and Yianneskis, 1998). Such structures affect mixing quality.

2.1.4. Mixing and power

Mixing influences conversion for fast reactions and the efficiency of a mixing process can be determined by the power draw and mixing time. A high mixing intensity results in species possessing interpenetrating energies that promote macro- and micro transport processes. Mixing is caused by a complex interaction of these structures, the fluid bulk flow and turbulent and molecular diffusions. The interaction can be represented by two mixing models that have been reported by Nienow (1996): bulk flow and turbulent models. The bulk flow models have been found to give shorter mixing times than the turbulent flow ones due to the fact that the turbulent flow models account for mixing at smaller scales, which the bulk flow ones do not. Some previous studies have focused on bulk flow models, using power number and mixing time (Nienow, 1997; Jaworski et al., 2000) to study the system homogenization. Mixing time can be defined as the time required to achieve a given level of homogenization in a tank. The mixing time at different homogenization levels can be determined by empirical models (Nienow, 1968; Fasano and Penny, 1991; Jaworski et al., 1996 and 2000).

Experimentally, mixing time can be determined by a conductivity meter (Nienow, 1968; Jaworski and Pianko-Oprych, 2002; Bujalski et al., 1999), pH meter (Guillard and Tragardh, 2003) and decolourization method (Kuzmanic and Ljubicic, 2001). The mixing time required to achieve 90% homogenization (t_{90}), for example, is the time it takes for the fluctuation of the response signal to be below 10% of the concentration achieved at the perfect mixing, which is adequate for most systems. For the decolourization method, the visual determination of the point at which the colour changes can be very subjective, and this compromises the reproducibility of such results. This is compounded by the fact that there is no unanimous agreement on the level of homogeneity that the decolourization method gives. Kraume and Zehner (2001) took the decolourization point to be equivalent to the 95% homogenization level, whilst Bujalski et al. (2002) reported that decolourization occurs at the 90% homogenization level obtained by conductivity meter. Many authors do not report the level of homogenization that decolourization represents.

It was earlier reported (Rao and Joshi, 1988) that location of the probe has no influence on mixing time. However, more recent studies show that the mixing time depends on the probe and injection locations (Otomo et al., 2003; Guillard and Tragardh, 2003), probe size (Bouaifi and Roustan, 2001; Jaworski and Dudczak, 1998) and tracer concentration (Bujalski et al., 1999). Guillard and Tragardh (2003) found that a shorter mixing time could be obtained with the top injection as compared to bottom injection. However, even with top injection, Otomo et al. (2003) obtained results which varied with radial location with as much as 100%. It is important to consider the power required to achieve a given level of homogenization. Homogenization energy, which is a product of mixing time and the corresponding power dissipated, has been used to evaluate the efficiency of the mixing (Bouaifi and Roustan, 2001). In a solid-liquid system, the presence of particles may dampen the turbulence intensity and this leads to a decrease in mixing, which is characterised by longer mixing time than in a particle-free liquid. Further, the resistance to the blade motion increases with an increase in solids loading. Very little has been reported on mixing time in solid-liquid systems (Bujalski et al., 1999; Kraume and Zehner, 2001).

2.1.5. Off bottom solids suspension and cloud height

Solids suspension studies focus on three aspects: off-bottom solids suspension (Zwietering, 1958), solids cloud height (Bittorf and Kresta, 2003) and solids concentration distribution

(Barresi and Baldi, 1987). The off-bottom solids suspension has been investigated in tanks stirred with single impellers (Zwietering, 1958; Barresi and Baldi, 1987; Armenante and Nagamine, 1998; Bujalski, 1999) and with multiple impellers (Montante et al., 2003; Pilelli and Magelli, 2001; Wu and Pullum, 2001). Different levels of homogeneity may be required in a mixing tank, depending on the process, and it is on this basis that the three aspects may be studied independently, or in relation to one another.

Determination of the off-bottom solids suspension

One criterion that is typically used to investigate off-bottom solids suspension is the critical impeller speed (N_{js}) at which particles do not remain stationary at the bottom of the vessel for more than 1 to 2 seconds (Zwietering, 1958). It has been reported (Armenante and Nagamine, 1998) that N_{js} depends on both impeller clearance and the ratio of the impeller diameter to that of the vessel (D/T). Sharma and Shaikh (2003) have shown that the response of the N_{js} to a change in the impeller clearance depends on the clearance range, and identified three different ranges. At a low clearance, there is a higher efficiency in energy transfer from the impeller to the solids, and the ratio of the local energy to the overall energy dissipation per unit volume is constant. The original form of the N_{js} correlation as developed by Zwietering (1958) has limited application. The modification of this correlation by Sharma and Shaikh (2003) enables its wider application to different tank configurations. More importantly, empirical constants in the correlations should represent meaningful aspects of the reactor configuration and the physics of the flow.

Cloud height

More recently, Bittorf and Kresta (2003) developed a model that predicts the solids cloud height, which the authors defined as a well-defined interface that appears at the location where the downward velocity of the particles is exactly balanced by the upward velocity of the fluid at the wall. Bittorf and Kresta (2003) assumed that, once the particles have been lifted and prevented from settling, a force must move them away from the bottom and that this force depends on the wall jet. Therefore, their model was based on a relation between the solids cloud height and the maximum velocity in the wall jet, which is a flow created when fluid is blown tangentially along a wall. The determination of the cloud height does not

give any indication of the uniformity on the system and more information would still be required to determine the solids concentration distribution in the entire volume of the tank.

2.1.6. Solids axial concentration profile

Studies on the solids concentration distribution have been constrained by the cost of equipment required to obtain such data. Experimental methods have been developed to acquire data that is required to develop empirical or semi empirical models (Barresi and Baldi, 1987; Magelli et al., 1990). The quality of prediction obtained with these models depends on the accuracy of the experimental data.

Measurement of solids concentration distribution

Local solids concentration can be measured by a sampling method (Barresi and Baldi, 1987). However, this is an intrusive method and the sampling probe may significantly interfere with the liquid flow, causing measurement errors. A less intrusive method that is gaining a wide application is electrical resistance tomography (ERT) and positron emission tomography (McKee et al., 1995; Ma et al., 2001). The ERT method is an imaging technique that can be used to map the electrical conductivity distribution that occurs in the system. Typically, the ERT method is employed in multiphase systems and the conductivity distribution is as a result of the phase distribution. The conductivity distribution is obtained by imaging the system by passing current through electrodes, which are equally spaced around the internal circumference of the tank containing the mixture to be imaged. The major limitation of the ERT method is that the interference with the bulk fluid flow increases as the number of measurement nodes increases. The size of the electrodes limits the number (typically 8-16) of planes along which measurements can be taken.

Fajner et al. (1985) developed a very simple non-intrusive optical attenuation technique. This method and other methods based on the same principle have been employed to investigate solids concentration distribution (Brucato et al., 1998a; Pinelli and Magelli, 2001). In the optical method, light is transmitted across the tank by a light emitting diode and received on the opposite side of the tank by a silicon photo diode. The amount of light passing through the tank depends on the quantity of particles suspended.

Empirical models

The models that account for the concentration distribution are more informative than those that model the just off-bottom solids suspension or cloud height. Models based on the Peclet number (which is the ratio between convective flow and diffusion) and dimensionless standard deviation (σ) of the actual solids concentration profile relative to vertical homogeneity have been used (Magelli et al., 1990; Barresi and Baldi, 1987; Pinelli and Magelli, 2001) to predict the axial solids concentration profile. The Pinelli and Magelli (2001) model is one dimensional, which is a reasonable approximation for flows in tall baffled tanks stirred by multiple impellers. This method lacks universality of application due to the three dimensional flow in stirred tanks. Montante et al. (2003) pointed out that σ varies with tank configurations, operating conditions and fluid properties, and lacks physical significance.

2.1.7. Solids suspension theories

Solid-liquid mixing studies in the literature are based on a number of theories that have been put forward to describe particle suspension in stirred tanks. These theories relate the forces due to gravity, pressure, viscosity, inertia and turbulent structures. Solids suspension theories have been described by Rieger and Ditl (1994):

- Barresi and Baldi's (1987) work is based on the theory that the energy needed to suspend the particles from the bottom is proportional to the turbulent vortices;
- Mersmann et al. (1998) and Pinelli et al. (2004) assumed that there is a balance between the energy dissipated by the settling particles and the energy dissipated in the fluid by the agitator;
- Molerus and Latzel's (1987a and 1987b) work is based on the assumptions that (a) the agitator must overcome the pressure differences caused by the differences in particle concentrations in upward and downward flow and (b) there is a balance between the force of fluid affecting the particles and the gravitational force reduced in the buoyancy;
- The work by Mersmann et al. (1998) is based on the theories that (a) there is a balance between the potential energy necessary to achieve suspension and the kinetic energy of the fluid flow being discharged from the agitator and (b) there is a balance between the upward fluid velocity and particle settling velocity.

It is possible that more than one of these theories may describe solids suspension mechanisms in a given system. This is due to the fact that the relative magnitude of the forces responsible for solids suspension may change with a flow regime as well as with variations in particle properties and loading.

Mersmann et al. (1998) presented a theoretical description of solids suspension using the Archimedes number and the local fluid fluctuating velocity as the parameters. A relation between the fluctuating velocity and the kinetic energy was established and a model was developed on the basis of a balance between particle settling energy and kinetic energy dissipated by the impeller. This model accounted for both off-bottom lifting and avoidance of settling. However, this did not go far enough to account for what happens in the regions away from the bottom.

The just off-bottom suspended solids condition provides sufficient to expose the solid surface to the liquid, which is adequate for some industrial processes. Further suspension of the solids in such processes may not be cost effective, in terms of power consumption, as it results only in small increase in mass transfer from particle to liquid (Zwietering, 1958). However, for reactions that are influenced by the solids surface available for mass transfer, complete solids suspension is required.

2.1.8. Scale-up

Scale-up criteria depend on the impeller performance, flow regime, reactor geometry, phase hold-up and physical properties of the phases involved. Also, the scale-up criteria depend on whether the flow generated by the impeller is convective mixing or turbulent dispersion. A scale-up can be done on the basis of a constant impeller tip speed, which is related to the convective flow or specific power, which is in turn related to turbulent dispersion (Montante et al., 2001b). Scale-up criteria can be given in the form of an equation (Montante et al., 2003):

$$ND^n = k_o \tag{2.1}$$

where k_o is a constant, N is the impeller speed, D is the diameter of the impeller and the exponent '*n*' depends on the process investigated. Rieger and Ditl (1994) reported that scale-up with constant impeller tip speed is applicable to particles of 0.7 mm diameter and that, for bigger particles, scale-up criteria should be based on the power dissipation per unit mass.

Wernersson and Tragardh (1999) employed multiple Rushton turbines in tanks of different sizes and concluded that scale-up with constant power was valid for the system. Flat-bottomed tanks, for example, scale-up with higher value of n compared to round bottomed tanks (Chudacek et al., 1985).

In an earlier work, Montante et al. (2001b) recommended the impeller tip speed criterion. However, in their later work (Montante et al., 2003), they concluded that the solids concentration profile can be scaled with a criterion in between the impeller tip speed and constant power per unit mass. It is apparent that all aspects of the hydrodynamics need to be considered in order to arrive at an optimal design of a mixing system. This requires a significant amount of data both on mean velocity field and turbulent field. Given the difficulties with experimental, techniques, the CFD technique is an important tool that can be used to obtain such data, once the model has been validated.

2.2. CFD simulation methods

The CFD simulation technique comprises grid generating, equation solving and results processing modules. It works in such a way that the partial differential Navier-Stokes equations are discretized and solved in control volumes (for finite volume method) defining the domain. These equations represent the mathematics, physics and, in some cases, the chemistry of the system. The main aspects of the simulation strategies involve specifying boundary condition, grid size, discretization scheme, equation solvers, turbulence and impeller models.

2.2.1. Grid generation and boundary conditions

The primary objective of a simulation and modelling work is to accurately predict the performance of the real system and to show a trend in given process. Grid refinement can improve the accuracy of the simulation results, and it is desirable to obtain grid independent solutions. For engineering design purposes, it is important to refine the grid to the extent that the simulation results are quantitatively and qualitatively comparable with experimental ones. Any further improvement in accuracy obtained with a finer grid may not deserve the additional computational cost required. The main factors to be considered in determining the grid size of a stirred vessel include the following: (a) boundary conditions, (b) impeller modelling approach, (c) model volume, (d) flow regime (turbulent or laminar), (e) the number of phases involved, (f) accuracy of results required and (g) computational resources.

All these factors influence the computation time and must be taken into account in order to obtain simulation results that agree reasonably with experimental ones. A summary of a sample of grid sizes that have been reported in the literature is given in Table 2.1.

Table 2.1. Grid size and system specifications reported in literature for a whole tank.

References	Grid size	Tank vol., L	Re/rpm	Impeller models	Phase(s)
Javed et al., 2006	112,480	10/82	600	SM	L
Hartmann et al., 2004	228,096/240[3]	10	2672	SG	L
Bartels et al., 2002	3,984,640*	2.8	Re=0.1-106	MFR	L
Alexopaulos et al., 2002	166,656	4.7	400	SG/MFR	L
Murthy and Jayati, 2002	1,376,000	0.79	Re=10-480	SG	L
Lane et al., 2002	175,680	785	180	MFR	G,L
Nere et al., 2001	N/S	21	105-270	IBC	L
Ranade and Tayalia, 2001	N/S	21	160	Snap Shot	L
Mavros et al., 2001	120,000-260,000	86	600	MFR	L
Rielly and Marquis 2001	162,590	13	2165	In-house	S,L
Wei et al., 2001	201,625	42	150-600	SG	S,L
Ljungqvist and Rasmuson, 2001	208,000	21	360	IBC	L,S
Montante et al., 2001a	160,272	19	250	SG,IO	L
Montante et al., 2001b	190,000	39	1020	SG	S,L
Yoon et al., 2001	311,040	N/S	50-150	MFR	L
Rousseaux et al., 2001	216,000	2.5	1200-3000	MFR	S,L
Koh et al., 2000	N/S	38	1200	IBC	L,G,S
Sahu et al., 1998 and 1999	88,800	98	N/S	IBC	L
Ng et al., 1998	46,016-240,000	0.79	2165	SG	L
Schafer et al., 1998	N/S	98	1200	N/S	L
Harris et al., 1996	73,600	N/S	N/S	SG	L
Ranade and van den Akker, 1994	N/S	21	N/S	Snap shot	L
Luo et al., 1994	151,200	19	300	SG	L
Luo et al., 1993	151,200	19	300	MFR	L

Key
L - Liquid, S - Solid, G-gas, MFR - Multiple Frame of Reference, SG - Sliding Grid, and IO - Inner Outer, IBC – Impeller Boundary Condition, N/S Not specified,*-Parallel computers equivalent to 120 Pentium 4PCs, each with a memory of 1GB.

Boundary conditions

The way boundary conditions like the impeller disc, blades, baffles and vessel walls are defined determine the required grid size. The blades, disc and baffles may be defined as thin surfaces (2D) (Ochieng and Lewis, 2004; Murthy and Jayati, 2002; Montante et al., 2001a) or (3D) surfaces with thickness (Ng et al., 1998; Luo et al., 1994). In the case of a blade with

thickness, some CFD solvers put a limitation on the number of cells that must separate the opposite walls defining the blade, and this requires much higher grid resolutions than other regions. Similarly, the implementation of the k-ε turbulence model with the standard wall function puts a restriction on the minimum wall distance of the first interior grid point required in order to obtain accurate predictions of the surface shear stress. A very fine grid close to the wall surface may violate this requirement, resulting in poor predictions. In more recent versions of the CFD codes, there are wall functions that allow resolution of the boundary layer down to the wall. The presence of a draft tube requires special attention with regards to grid distribution to account for an additional wall in the domain.

Model volume

The model volume is important in determining the grid size due to the fact that the central focus of any simulation work, which is the control volume in a given domain, is determined by the grid size and the model volume. By decreasing the cell size, the control volume decreases, and this results in an increase in the value of the diffusion conductance at the cell face. This causes a decrease in the Peclet number, and enhances better resolution of the turbulent field. Murthy and Jayati (2002) employed 1,376,000 cells in a 0.79 litre tank to simulate the velocity field for a single phase system. Lane et al. (2002) modelled a more complex multiphase system using 175,680 cells in a 785 litre tank. Despite the relatively coarse grid used by Lane et al. (2002), possibly due to resource limitations, some important insights into multiphase mixing were provided.

2.2.2. Discretization schemes and equation solvers

The discretization schemes that are widely used are upwind, power law, higher upwind, central differencing, hybrid and quadratic upstream interpolation for convective kinetics (QUICK). The upwind scheme is first order accurate, and may be used to initiate a simulation. The hybrid effectively becomes upwind if the cell Peclet number is less than 2; otherwise, the second order central scheme is applied. The hybrid discretization scheme is formulated on the basis of the cell Peclet number (Pe), which gives the ratio of the convective flow to diffusion. The cell Peclet number depends on the flow and fluid properties (Versteeg and Malalasekera, 1995):

$$Pe = \frac{\rho u}{\Gamma / \Delta x} \tag{2.2}$$

where Δx is the cell size, ρ is the fluid density Γ is the diffusion coefficient, u is the velocity. The third order accurate scheme, QUICK, is obviously more computationally demanding than the others. Sahu and Joshi (1995) assessed the competitiveness of upwind, hybrid and power law schemes, and concluded that power law was the most robust of the three schemes. More recently, Aubin et al. (2004) compared upwind, higher order upwind and QUICK, and concluded that the best prediction of the circulation number was obtained with QUICK, followed, interestingly, by the upwind and not the second order upwind scheme as would be expected.

Solution algorithms

The pressure and velocity terms in the equation require special attention (coupling) before the equations are solved. The coupling algorithm depends on whether the system is in steady or unsteady state. For a steady state flow, velocity-pressure coupling is done by algorithms such as the semi implicit pressure linked equations (SIMPLE), SIMPLE-revised (SIMPLER), SIMPLE-consistent (SIMPLEC) and pressure implicit with splitting operators (PISO). Unlike the other schemes, SIMPLEC and PISO can be used in both steady and unsteady state systems. Sahu et al. (1998) employed both SIMPLE and SIMPLER and reported that simulation with higher grid sizes (finer grids) could not converge easily with SIMPLE. For a transient simulation approach, which is the most appropriate for stirred tanks, SIMPLEC has been more widely used (Ljungqvist and Rasmuson, 2001; Brucato et al. 2000; Brucato et al., 1998b).

2.2.3. Impeller modelling

The hydrodynamic modelling of a stirred vessel centers on the way the impeller is modelled. Some of the most recent approaches to modelling an impeller are impeller boundary condition (IBC) (Brucato et al., 1994), snap shot (Ranade and van den Akker, 1994), sliding grid (SG) (Luo et al., 1993), multiple frames of reference (MFR) (Luo et al., 1994) and inner outer (IO) (Brucato et al., 1998b). The accuracy with which these models predict experimental results and the corresponding computational demands forms the basis upon which the choice of an approach is made. Most of these approaches (IO, SG and MFR)

address the key problem of stirred tank modelling, which is the simultaneous meshing of the rotating impeller and the stationary baffles.

The IBC, being a black box approach, requires input of experimentally determined velocity and turbulence quantities at the surface swept by the impeller, and it is the least computationally demanding approach. Firstly, its major limitation is its dependency on experimental data. Therefore, the accuracy of the simulation is influenced by the accuracy of the experimental data used at the boundary. Secondly, boundary conditions are tank geometry specific. Therefore, data obtained in a given geometry may only be applicable to closely similar geometries (Brucato et al., 1998b).

With the IO approach, the vessel is subdivided into two partially overlapping zones, and an unmatched boundary is specified between the impeller tip and the baffles. It has been reported that the IO approach gives a poor prediction of experimental results (Harris et al., 1996; Brucato et al., 1998b; Montante et al., 2001a), and therefore, it is less commonly applied in recent years.

The MFR and SG approaches are similar in the sense that in both cases, the vessel is divided into two sub-domains; the inner sub-domain moves with the impeller, while the outer sub-domain is stationary with the baffles. For the MFR approach, the domain is defined in two frames of reference separated by an interface located between the impeller tip and the baffles. The interface is located at a distance where the flow is assumed to be cylindrically symmetric. The inner sub-domain rotates with the impeller, and in this sub-domain the flow is time-independent with respect to the impeller. The outer sub-domain is attached to the baffles and the flow in this sub-domain is time-independent with respect to the tank. A steady state calculation can be done on the respective sub-domains and a coupling of the two separate flows is done at the interface. There is no relative movement of the cells in the opposite sides of the interface. The MFR approach is best employed in unbaffled tanks, in which there is no interaction between the stationary and the rotating domain. The main limitations of the MFR include failure to account for the transient interaction between the impeller and the baffles, failure to predict the rate of decay of the local maximum velocity in the wall jet (Bhattacharya and Kresta, 2002) and it cannot predict mixing time. In some applications, unbaffled tanks have been employed to simplify the numerical complexity

involved in modelling the interaction between the baffles and the rotating impeller blades (Lamberto et al., 2001; Alexopaulos et al., 2002).

The SG method is defined in a similar way except that the interface is treated implicitly and the meshes in the rotating and stationary frames move relative to each other. The domain must include an integer number of baffles and blades to allow periodic boundary conditions to be defined in the azimuthal direction. The position of the impeller is updated at every time step. A time dependent calculation is applied simultaneously in the two sub-domains and a coupling, that allows the grid to slide, is done at the interface. The transient flow fields due to the periodic movement of the impeller blades relative to the baffles in a stirred tank can be captured by this method. The SG approach enhances computational stability and accuracy by resolving the non-linearity at every time step. However, it is more computationally demanding than MFR. Due to the higher computation demand for SG compared to MFR, the SG approach has widely been applied to single phase systems (Ng et al., 1998; Brucato et al., 1998b; Jaworski et al., 2000; Montante et al., 2001a), whilst the MFR approach has been employed in multiphase systems and single phase systems in which high density grids were defined (Mavros et al., 2001; Bartels, 2002; Bujalski et al., 2002; Lane et al., 2002). Montante et al. (2001a) reported that the SG approach produced better results with finer grids than the IO one, such that beyond 160,272 cells, the IO approach did not produce an observable improvement in the accuracy. With advancement in computer technology, the SG has in recent years been employed in multiphase systems (Montante et al., 2001b; Wei et al., 2001), as seen in Table 2.1.

2.2.4. Turbulence modelling

The turbulence models based on the Reynolds averaged Navier-Stokes (RANS) equations fall into two categories, namely, eddy-viscosity model and Reynolds-Stress models (RSM). The two-equation eddy-viscosity models include the renormalization group (RNG) k-ε, standard k-ε (Launder and Spalding, 1974), and k-ω (Wilcox, 2000) models.

The eddy-viscosity models are based on the assumption that there is an analogy between the viscous stress and Reynolds stress, and that the turbulent flow is isotropic (Versteeg and Malalasekera, 1995). The major weakness of the models based on the assumption of the isotropy of turbulence is that the predictions are less accurate in regions of anisotropic

turbulence. Aubin et al. (2004) reported that there was no significant difference between the predictions of the velocity field obtained with the k-ε and RNG k-ε turbulence models. A comparison between the RSM and eddy-viscosity models showed that RSM do not give better predictions of the turbulent and mean velocity field than the eddy-viscosity ones. Recent studies (Hartmann et al., 2004; Yeoh et al., 2005) have shown that better prediction of mean velocity and turbulent fields can be obtained with the large eddy simulation (LES) approach.

2.2.5. Mixing

The one major problem with mixing time simulation is the CPU time it requires to reach a homogeneous condition. Simulation studies of mixing time have been conducted in a liquid phase only (Jaworski et al., 2000; Guillard and Tragardh, 2003) solid-liquid system (Bujalski et al., 1999). The mixing time obtained by the RANS-based models does not give good predictions of the turbulent field, and this is a major limitation of these models, which depend on both mean velocity and turbulent field.

2.2.6. Solids suspension

In addition to the information that can be obtained by empirical models, the CFD method can provide more insights into the mixing features such as the axial and radial solids concentration distribution. In the CFD simulation method, the governing equations for a multiphase system can be described by the Langrangian or Eulerian method. The Eulerian method is sometimes referred to as a two-fluid model, with the fluids being treated as two interpenetrating media. The resulting turbulence momentum equations can be closed by the k-ε or other turbulence models. The Lagrangian method, on the other hand, treats one phase as continuous (described by the Eulerian equation) and the other as dispersed in a moving Lagrangian frame with Newton's second law of motion.

A summary of the literature review in Table 2.2 shows a general lack of detailed LDV/CFD studies on solids concentration distribution. In particular, there is a lack of information on the solids concentration distribution for high density particles and on local distribution of particle sizes. Similarly, CFD studies on round bottomed tanks and the hydrofoil impeller are lacking due to the grid generation difficulties in many commercial software packages.

Lagrangian method

Derksen (2003) employed the large eddy simulation (LES) method and the Lagrangian approach for a 3D flow in a dilute system. This approach reveals more details of the flow field than the Eulerian approach. In the Lagrangian approach, only the velocity field is solved for, which is a valid approximation for low solid hold-up systems. However, as the solids loading increases, the resulting flow field depends on the interaction between the two phases. This interfacial interaction was not accounted for by the method employed by Derksen (2003), and the forces acting on the particles were based on correlations for single particles in unbounded flow.

Eulerian method

In CFX, the k-ε model is employed within the two fluid formulation context (Lopez de Bertodano, 1998). In this approach, the flow field is solved for both phases and the interaction between the phases is accounted for through the source terms. This approach has been employed in many studies reported in the literature (Gosman et al., 1992; Koh et al., 2000; Ljungqvist and Rasmuson, 2001; Lane et al., 2002). Many researchers employ this method to simulate mono-size particles, and therefore, the influence of particle size on the solids suspension is not taken into account. Shah et al. (2001a and 2001b) employed an Eulerian based poly-disperse multiphase simulation approach with six solid phases. However, very little quantitative information was given on the solids concentration distribution. Barrue et al. (2001) employed the black box impeller modelling approach (IBC) to study solids suspension in a high solids volume fraction (20%) system. It has been reported that results obtained with the black box approach have limited application to other systems (Brucato et al., 1998b).

The typical CFD simulation method for investigating solids suspension is that the simulation is initiated with particles uniformly distributed in the domain. Such a simulation approach is likely to account only for the "avoidance of settling" mechanism and neglect the "bottom lifting" one. Both these two mechanisms have been shown by Mersmann et al. (1998) to be important for solids suspension. The simulation results obtained this way may not be easy to correlate to the classical methods for investigating solids suspension, such as the N_{js} approach. Kee and Tan (2002) proposed a CFD simulation method to determine N_{js} in a flat-

bottomed tank. In their method, the simulation was initiated with the particles at the bottom of the tank. However, the flow was only 2-D and the simulation results were not validated experimentally. The flow in a stirred tank is typically turbulent and three-dimensional and, therefore, a 2-D approach is a non-representative description of the complex flow in the stirred tank.

2.2.7. Drag and non-drag forces

Drag is the dominant force in a system where one phase is continuous and the other one is dispersed. Non-drag forces, which include the turbulent dispersion, virtual mass, lift force the wall lubrication, may be accounted for depending on the fluid flow properties as well as particle and fluid physical properties (Lopez de Bertodano, 1998; Lahey and Drew, 2001).

Drag coefficients and models

There are different drag models available in CFD commercial packages, and these include the Schiller-Naumann, Ihme (cited in AEAT, 2003); Ishii-Zuber (Ishii and Zuber, 1979); Gidaspow (Gidaspow, 1994) models. Ljungqvist and Rasmuson (2001) compared the performance of the Ishii-Zuber, Ihme and Schiller-Naumann models against experimental results and reported that the predictions obtained with the three models were very similar. The authors made a further comparison between these built-in models and the Brucato model (Brucato et al., 1998a), and again reported that there was no difference in the results. The main difference between the Brucato model and the other models is that the Brucato model accounts for free stream turbulence. It is can be noted that, except for the Gidaspow and Brucato models, the other models were developed for a single particle immersed in a unidirectional flow. The fact that Ljungqvist and Rasmuson (2001) did not observe any difference in the prediction with those models can be attributet to the dilute systems that these authors used, and therefore it may not be an indication that the models give the same performance.

The Brucato model has been employed in both gas-liquid (Lane et al., 2002) and solid-liquid (Ljungqvist and Rasmuson, 2001; Montante et al., 2001b) systems. The solid-liquid systems in which these authors employed the model were dilute: with solids volume loadings of 5%

for the Montante et al. (2001b) system and 0.001-0.02% for the Ljungqvist and Rasmuson (2001) system. In both systems, the model was reported to give a reasonable prediction of the solids concentration distribution. The free stream turbulence is accounted for by the Brucato model through the Kolmogoroff length scale. At high Reynolds number, there exists a separation of the length scales of the energy-containing eddies and inertial sub-range. Kolmogoroff hypothesised that there exists a range of eddy sizes between the largest and the smallest scale, for which the cascade process is independent of the statistics of the energy containing eddies (Wilcox, 2000). The Kolmogoroff length scale (λ) is a function of the kinetic energy dissipation rate. Assuming uniformity of the kinetic energy dissipation rate, Brucato et al. (1998a) used the value of power dissipation per unit mass of fluid to compute ε. This assumption did not account for the spatial variation of the turbulence intensity in a stirred tank. Montante et al. (2001b) employed the Brucato model with λ calculated by the same method described by Brucato and co-workers and further computed λ from the CFD domain determined local turbulent kinetic energy dissipation rate. They reported that there was no difference in the predictions by the two approaches. In principle, the CFD method is more representative of the spatial distribution of the turbulence intensity in the tank. However, this is only true if ε can be calculated accurately, which is not the case for RANS-based models (Sahu et al., 1998; Nere et al., 2001).

The main distinguishing feature of the Gidaspow model is the fact that it is more suitable for higher solids loading than the other drag models available in most CFD packages due to the fact that solids volume fraction is accounted for. The performance of this model is yet to be assessed against the traditional drag models and the relatively new Brucato model.

Non-drag forces

For most of the studies involving dilute systems, the influence of non-drag and solid pressure on solids suspension has generally been ignored. However, Ljungqvist and Rasmuson (2001) and Sha et al. (2001a) investigated the influence of lift, virtual mass, and turbulent dispersion on slip velocity and observed that there was very little effect of these forces on the slip velocity. Ljungqvist and Rasmuson (2001) studied solids suspension using very small nickel particles (75 μm diameter) in a dilute system for which the influence of the particles on the bulk fluid may not be significant.

Table 2.2. Experimental and simulation studies on solids distribution

Author(s)/Year	Tank Bottom	Impeller	Concept	Response Variable	$\rho_p x10^3$ kgm^{-3}	Method
Derksen, 2003	Flat	RT	Conc. distrib.	Vol. frac.	1.1	CFD
Montante et al., 2003	Flat	6 RTs	Conc. distrib	Vol. frac	2.4	OAT
Bittorf and Kresta, 2003	Flat	PBI, A310	Cloud height	Jet Vel.	1.0-2.5	LDV, CFD
Sharma and Shaikh, 2003	Round	PBI4	Off-Bot. Susp.	N_{js},P	1.3-1.6	Visual
van Wachem and Almstedt, 2003	Flat	-	Conc. distrib	Vol. frac	-	CFD
Kee and Tan., 2002	Flat	Lightnin A310, R100	Off-Bot. Susp.	N_{js},P	2.6	CFD
Kuzmanic and Ljubicic, 2002	Flat	PBI-U	Mixing	N_{js}, Nt_m	0.84	CM,Visual
Barrue et al., 2001	Flat	3 Propellers	Conc. distrib	Vol. frac	2.6	CFD, LDV
Sha et al., 2001a	Flat	PBI6	Conc. distrib	Vol. frac	0.8-1.0	CFD
Sha et al., 2001b	Flat	Prop4	Conc. distrib	Vol. frac	2.6	CFD
Ljungqvist and Rasmuson, 2001	Flat	PBI4	Flow field	U_{slip}	8.9	CFD, PDV
Murugesan, 2001	Flat	RT	Off-Bot. Susp.	N_{js}, P	1-2.6	Visual
Montante et al., 2001b	Flat	4PBI	Conc. distrib	Vol. frac	2.5	CFD, OAT
Pinelli and Magelli, 2000	Flat	Hydrofoil, A315	Mixing (3-phase)	Mixing time	-	CM,
Biswas et al.,1999	Flat	Marine	Piping	Mass fraction	2.65	Sampling
Bujalski et al., 1999	Flat	A310, A315	Mixing	Nt_m	2.5	CFD, CM
Armenante and Nagamine, 1998	Flat	RT,PBI, FBT,HE3	Off-Bot. Susp.	N_{js}, P	2.5	Visual
McKee et al., 1995	Flat	PBI	Conc. distrib	N_{js}	2.4	ERT
Magelli et al.,1990	Flat	6 RTs	Conc. distrib	Vol. frac	0.8-2.4	OAT
Barresi and Baldi, 1987	Dish	PBI	Conc. distrib	Vol. frac	2.6	Sampling
Fajner et al., 1985	Flat	4 RTs	Conc. distrib.	Vol. frac	2.4	OAT

Key

CFD - Computational fluid dynamics CM - Conductivity meter

ERT – Electrical resistance tomography LDV – Laser Doppler velocimetry

Nt_m – Dimensionless mixing time PDV – Phase Doppler velocimetry

OAT – Optical attenuation technique RT - Rushton turbine

CHAPTER 3

3. Hydrodynamic modelling and simulation

Hydrodynamic models can be defined by empirical or semi-empirical correlations developed on the basis of experimental results. Most of the empirical correlations that are based on bulk fluid flow are system specific, and therefore lack universality in their application. However, the cost of computation involved is low and the experimental techniques required to validate the empirical models are simple.

CFD simulation models are based on the law governing the conservation of mass and energy of fluid flow. The Navier-Stokes (NS) equations, on which the CFD simulation models are based, are the fundamental partial differential equations that describe fluid flow according to Newton's law of motion. The governing equations involved are scalar transport, continuity and momentum equations. These equations are solved simultaneously in a given domain with appropriate boundary conditions, source and sink terms. Therefore, the CFD models, which are capable of describing any geometry, are correlated to the simple semi-empirical models.

3.1. Empirical hydrodynamic models

The dimensionless numbers that define empirical hydrodynamic models correlate the forces induced by the impellers with the reactor geometry and fluid properties. These models can be used to predict the impeller speed required for off-bottom solids suspension, solids cloud height and mixing time. Further, these models can represent terms required for closure in the governing equations.

3.1.1. Dimensionless numbers

Dimensionless numbers typically give a representation of the relative magnitude of the forces acting in a system or relate flow features to system geometry. There are many dimensionless numbers but in this work, only the most frequently used ones are discussed. The impeller performance characteristics can be represented by dimensionless numbers such as the pumping number (N_Q), impeller Reynolds number (Re), power number (N_P), Froude number (Fr), Archimedes number (Ar) and Stokes number (St).

Solids suspension depends on the forces associated with the liquid and particle properties, of which, drag, buoyancy and gravitational forces are important. The relative magnitude of these forces is given by the impeller performance indicators such Fr, N_P and N_Q. The pumping number depends on the impeller and reactor geometries, and for the Rushton turbine at the standard bottom clearance, N_Q can be calculated as (Tatterson, 1991):

$$N_Q = 0.8\left(\frac{D}{T}\right)^{-0.7}\left(\frac{w}{T}\right)n_b^{0.6} \tag{3.1}$$

where n_b is the number of impeller blades, w is the width of the blades and D and T are diameters of impeller and tank, respectively.

The impeller Reynolds number (Re) gives the ratio between inertial and viscous forces and is given by:

$$\mathrm{Re} = \frac{ND^2}{\nu_L} \tag{3.2}$$

where ν_L is the fluid kinematic viscosity, N is the impeller rotational speed.

The power number, which depends on the width and speed of the impeller as well as the fluid density, gives an indication of the power dissipated in the system as a result of the impeller rotation, and is given by:

$$N_p = \frac{P}{\rho_L N^3 D^5} \tag{3.3}$$

where P is the power dissipated, ρ_L is the liquid density. The action of the impeller causes a liquid surface deformation characterized by the Froude number (Fr), which is the ratio of the inertial force to the gravitational force.

$$Fr = \frac{N^2 D}{g} \tag{3.4}$$

where g is the acceleration due to gravity.

In a solid-liquid system, the forces acting on the surface of the particle and the gravitational force influence the distribution of the particles. This can be represented by the Archimedes

number (Ar), which gives an indication of the relative magnitude of the drag with respect to the gravitational force and is expressed as (Mersmann et al., 1998):

$$Ar = \frac{d_p^3}{v_L^2}\left(\frac{g\Delta\rho}{\rho_L}\right) \tag{3.5}$$

where d_p is the particle size, $\Delta\rho$ is the difference between particle and liquid densities. The difference between the solid and liquid densities is one of the parameters that determine the particle terminal settling velocity (U_t). The suspension of the particles is influenced by the particle terminal settling velocity, which can be obtained by equating the gravitational force to the drag forces, and, after rearrangement, U_t is given by:

$$U_t = \left(\frac{4g\Delta\rho d_p}{3C_D\rho_L}\right)^{0.5} \tag{3.6}$$

where C_D is the drag coefficient. For a particle with a low Reynolds number ($Re_p < 1$), the terminal settling velocity can be expressed as:

$$U_t = \left(\frac{4g\Delta\rho_L d_p^2}{18\mu}\right) \tag{3.7}$$

where μ is the liquid molecular viscosity. Equations (3.6) and (3.7) are derived from a balance between the force of gravity and drag, without considering the influence of eddies. The Stokes number (St), which shows how quickly a particle adjusts its speed to an interacting eddy, is given by (Derksen, 2003):

$$St = \frac{Nd_p^2}{18\nu_L} \tag{3.8}$$

Particles will settle at the bottom of the tank if the gravitational force is greater than the sum of the upward forces. One of the indicators of the quality of the solids suspension is the presence of particles settled at the bottom of the tank.

3.1.2. Off-bottom solids suspension

The impeller speed (N_{js}) at which the just off-bottom solids suspension can be achieved is of interest. This critical impeller speed depends on the geometry of the tank and the properties

of the solid-liquid mixture. Most of the recent works on the N_{js} are based on the pioneering correlation developed by Zwietering (1958):

$$N_{js} = SD^{-0.85}A \tag{3.9}$$

where A is a coefficient that depends on the particle and liquid properties, and S, which is a function of the impeller width and the tank bottom clearance, is given by (Sharma and Saikh, 2003):

$$S = C_N\left(\frac{D}{T}\right)^{-1.15}\left(\frac{C}{T}\right)^{0.453} = \frac{N_{js}}{A}D^{0.85} \tag{3.10}$$

where C_N is a coefficient that depends on the impeller clearance and type, C is the impeller bottom clearance, A is given by (Sharma and Saikh, 2003):

$$A = v_L^{0.1}d_p^{0.2}\left(\frac{g(\rho_s - \rho_L)}{\rho_L}\right)^{0.45}w_s^{0.13} \tag{3.11}$$

where w_s is the percentage mass ratio of the solid to liquid, and is given by:

$$w_s = \frac{\rho_s\varphi_s}{\rho_L(1-\varphi_s) + \rho_s\varphi_s} \tag{3.12}$$

where φ_s is the solids hold-up.

3.1.3. Wall-jet and cloud height

The off-bottom solids suspension is enhanced by the mean bulk fluid flow, which can be characterized by the wall jet (Bittorf and Kresta, 2003) which is a fluid current resulting from the interaction beteen the impeller discharge and the wall baffles. Once the solids have been lifted from the bottom, further suspension is enhanced by the upward bulk fluid flow. This flow depends on the wall jet decay and the magnitude of the maximum velocity in the jet. Bittorf and Kresta (2003) have shown that the wall jet is important for the prediction of the solids suspension, and they gave a correlation for the local maximum velocity in the wall jet (U_m) as:

$$\frac{U_m}{U_{core}} = \alpha_1\left(\frac{1}{x/T}\right)^{\beta} \tag{3.13}$$

where α and β are constants that are system dependent, x is the axial distance and U_{core} is the overall maximum velocity in the wall jet. As the liquid height increases, U_m decreases, with the maximum value being at the impeller tip level. Thus, the maximum value of U_m is the U_{core}. The cloud height, h, is calculated as (Bittorf and Kresta, 2003):

$$h = \left(\alpha_2 \frac{U_{core}}{V_{tip,js}} \right)^{\kappa} \tag{3.14}$$

where $V_{tip,js}$ is the tip speed of the impeller blade running at N_{js}, α_2 and κ are constants that may be system dependent. These empirical models and the classical experimental methods used to study the off-bottom solids suspension (Zwietering, 1958) and cloud height (Bitorff and Kresta, 2003) can be correlated to the CFD simulation techniques, and this is described in Chapter 4.

3.1.4. Mixing time

The time taken to achieve homogeneity in a system, for a given power draw, determines the efficiency of a stirred tank. A classical mixing decay model for the macro mixing time (t_Θ) has been suggested by Fasano and Penny (1991) as:

$$t_\Theta = \frac{-\ln(1-\Theta)}{1.06\, N (D/T)^{2.17} (T/H)^{0.5}} \tag{3.15}$$

where Θ is the level of homogeneity ($0< \Theta <1$) and H is the liquid height. For the time required to achieve 95% homogeneity (t_{95}), $\Theta = 0.95$. This mixing model, unlike Nienow's model (Nienow, 1997), gives various levels of homogeneity and accounts for the liquid height.

The power (P) corresponding to the impeller speed required to achieve a given level of homogeneity can be calculated from the respective power numbers as:

$$P = N_p \rho_L N^3 D^5 \tag{3.16}$$

The power numbers and flows numbers for the Rushton turbine (RT), pitched blade impeller (PBI) and the hydrofoil impeller (HI) are given in Table 3.1.

Table 3.1. Power numbers for various tank configurations

Impeller	C	n_b	N_p	Bottom	N_Q	Author
RT	0.33T	6	5.10	Flat	0.76	Bakker (1992)
RT	0.15T	6	3.10	Flat	-	Montante et al. (2001a)
PBI	0.33T	4	1.55	Flat	0.81	Bakker (1992)
HI	0.33T	4	1.10	Elliptical	0.98	Present

The power is obtained from the torque computed from the forces acting on the blades or baffles as (Nienow, 1997):

$$P = 2\pi NM \tag{3.17}$$

where M is either a measured or simulated torque. The mean specific kinetic energy dissipation rate, $\bar{\varepsilon}_P$, is calculated from the power draw as:

$$\bar{\varepsilon}_P = \frac{P}{V_T \rho_L} \tag{3.18}$$

where V_T is the volume of the tank. The mixing efficiency parameter (homogenization energy) can be obtained as (Pinelli and Magelli, 2001):

$$\eta = \bar{\varepsilon}_P t_\Theta \tag{3.19}$$

An optimal operating condition is obtained with the minimum value of this parameter (η). In equation (3.18), it is assumed that the flow field of the kinetic energy dissipation rate in the tank is uniform, and thus the local variations in the tank are not accounted for. The local turbulent kinetic energy dissipation rate can be estimated from the laser Doppler velocimetry (LDV) measurements of the fluctuating velocities as (Wu and Patterson, 1989):

$$\varepsilon_{LDV} = A_o \frac{k^3}{\Lambda} \tag{3.20}$$

where the constant $A_o = 0.85$, and the turbulent length scale, Λ, is estimated as Λ=0.1D, and k is the turbulent kinetic energy given by:

$$k = \frac{1}{2}\left(\overline{u'^2_i} + \overline{u'^2_j} + \overline{u'^2_k}\right) \tag{3.21}$$

where $\overline{u}'_i$, $\overline{u}'_j$, and $\overline{u}'_k$ are the mean fluctuating velocity components. At this stage, it is clear that expensive experimental techniques are required to obtain the turbulent parameters. The most economical way to obtain such information is by using an appropriately validated CFD simulation technique.

3.2. CFD simulation

Formulation of the governing equations depends on the number of real (thermodynamic) or assumed phases defined in the domain. Solid, liquid and gas are the typical thermodynamic phases. However, in a liquid-solid system, for example, a specific particle size range can be considered as a phase. This method, referred to as poly-disperse multiphase simulation, is based on the Eulerian scheme. In this way, a thermodynamically two phase system can be represented by three or more phases in a CFD simulation domain. All these assumed phases are dispersed and their influence on the continuous phase is through the interface interaction. The accuracy of the resolution of a multiphase system depends on how well the flow in the bulk continuous (liquid) phase is predicted, due to the fact that the interfacial forces largely depend on the bulk phase.

3.2.1. Governing equation for single phase

The general form of the Navier-Stokes or transport equation is given by:

$$\frac{\partial \rho \phi}{\partial t} + \nabla \cdot (\phi \rho \boldsymbol{u}) = \nabla \cdot (\Gamma \nabla \cdot \phi) + F_{\phi} \tag{3.22}$$

where u is the instantaneous velocity vector; ϕ is a general transport property that may represent quantities such as the velocity, temperature, turbulent kinetic energy and turbulent kinetic energy dissipation rate; Γ is the diffusivity for the quantity ϕ; ρ is density of the bulk fluid and F_{ϕ} represents the body forces. For $\phi = 1$, $\Gamma = 0$, and equation (3.22) simplifies to the continuity equation:

$$\frac{\partial \rho}{\partial t} + \nabla \cdot (\rho \boldsymbol{u}) = 0 \tag{3.23}$$

The momentum transport equation, which relates the fluid particle acceleration to the surface and body forces, is obtained from equation (3.22) as:

$$\frac{\partial \rho \boldsymbol{u}}{\partial t} + \nabla \cdot (\rho \boldsymbol{u} \otimes \boldsymbol{u}) = -\nabla \cdot p + \nabla \cdot \mu[\nabla \cdot \boldsymbol{u} + (\nabla \cdot \boldsymbol{u})^T] + F_B \tag{3.24}$$

where ϕ is replaced by the velocity components ($\phi = u_i$), p is the pressure, Γ is replaced by the dynamic molecular viscosity (μ), F_B represents body forces including Coriolis, centrifugal and gravity. The Coriolis and centrifugal forces are given by (AEAT, 2003):

$$F_c = -2\rho\Omega \times \boldsymbol{U} - \rho\, \Omega \times (\Omega \times \boldsymbol{Y}) \tag{3.25}$$

where Ω is the rotational speed of the reference frame, $\boldsymbol{Y}$ is the location vector. For incompressible flows, the last term in equation (3.25), representing the centrifugal force, may be neglected.

Equation (3.24) represents three momentum equations for the axial (u_i), radial (u_j) and tangential (u_k) velocities. The three momentum equations plus one continuity equation need to be solved for u_i, u_j, u_k and real pressure, p. The four equations and four unknowns form a closed set of equations for which a unique solution can be obtained. Turbulent flows vary with time and space; therefore, the fluctuating velocity must be accounted for by introducing the mean and fluctuating components of the velocities in the governing equations.

Reynolds (or time) averaging and Favre averaging methods are typically used to obtain averaged forms of the NS equations. The Reynolds Averaged Navier-Stokes (RANS) equations are expressed in terms of the mean quantities and the terms arising from the averaging procedure. Only the time averaging procedure is described in the present work since it is the most commonly used method. The mean scalar quantity is given as:

$$\Phi = \frac{1}{\Delta t}\int_0^{\Delta t} \phi(t)dt \tag{3.26}$$

This results in the mean velocity being:

$$U_i = \frac{1}{\Delta t}\int_0^{\Delta t} u_i(t)dt \tag{3.27}$$

The variable ϕ is now written in form of the time averaged quantity (Φ) and the fluctuating component (ϕ'); $\phi = \Phi + \phi'$ and the instantaneous velocity (u_i) is written in terms of the

fluctuating velocity (u_i'.) and the time averaged velocity (U_i); $u_i = U_i + u_i'$. After the time averaging, the continuity equation remains unchanged except that u is replaced by U:

$$\frac{\partial \rho}{\partial t} + \nabla \cdot (\rho \boldsymbol{U}) = 0 \tag{3.28}$$

The momentum transport equation (3.24) becomes:

$$\frac{\partial}{\partial t}(\rho \boldsymbol{U}) + \nabla \cdot (\rho \boldsymbol{U} \otimes \boldsymbol{U}) = -\nabla \cdot p + \nabla \cdot \left(\rho \overline{\boldsymbol{u}' \otimes \boldsymbol{u}'}\right) + \nabla \cdot \mu[\nabla \cdot \boldsymbol{U} + (\nabla \cdot \boldsymbol{U})^T] + F_B \tag{3.29}$$

Taking ϕ to represent a scalar quantity, such as the volume fraction of a mixing tracer, the general transport equation (3.22) becomes:

$$\frac{\partial}{\partial t}(\rho \Phi) + \nabla \cdot (\rho \Phi \boldsymbol{U}) = \nabla \cdot (\Gamma_\Phi \nabla \cdot \Phi) + \nabla \cdot \left(\rho \overline{\varphi' \boldsymbol{u}'}\right) + F_\Phi \tag{3.30}$$

3.2.2. Closure for single phase turbulent flow

After the time averaging, the additional terms in the scalar transport equation (scalar flux) and those in the momentum equation (Reynolds stress) require closure. The method of obtaining the closure forms the basis of turbulence modelling. The classical turbulence models include the zero-equation, two equation and Reynolds stress models. The Prandtl mixing length model is the most commonly used zero-equation model, and the k-ε is the most commonly used two-equation model. The Reynolds stress models are not as widely used as the two-equation models. Among those that are available, the versions developed by Launder et al. (1975) are the most widely applied RSM.

Zero-equation model

There is no transport equation solved for the turbulent kinetic energy (k) and its dissipation rate (ε) in the zero-equation model, since μ_t is expressed in terms of mean velocity and geometrical length scales by an empirical correlation (Warsi, 1999):

$$\mu_t = C_0 \rho \vartheta l \tag{3.31}$$

where C_0 is the dimensionless constant, ϑ is the velocity scale which can be taken as the maximum velocity in the domain and l is the length scale of the largest eddies containing the kinetic energy of turbulence. The length scale can be approximated by (AEAT, 2003):

$$l = \frac{V_T^{1/3}}{7} \tag{3.32}$$

where V_T is the volume of the fluid domain.

For the Prandtl mixing length model, μ_t, is expressed as (Warsi, 1999):

$$\mu_t = l_m^2 \rho \left| \frac{\partial \boldsymbol{U}}{\partial y} \right| \tag{3.33}$$

where l_m is the mixing length scale and $\partial \boldsymbol{U}/\partial y$ is the mean velocity gradient. These simple models can be used to obtain initial values for relatively more complex models such as the two equation and Reynolds stress models.

Two-equation models

The k-ε (Launder and Spalding, 1974) and k-ω (Wilcox, 2000) turbulence models are based on the eddy-viscosity hypothesis. This hypothesis, which is sometimes referred to as the Boussinesq eddy-viscosity approximation, assumes that the principal axes of the Reynolds stress tensor are coincident with those of the mean strain rate and that there is an analogue between the Reynolds stress and the viscous stress. For incompressible flows, the viscous stress is taken to be proportional to the rate of deformation, and is modelled as (Versteeg and Malalasekera, 1995; Lapin and Lubbert, 1994):

$$\tau = \mu[\nabla \cdot \boldsymbol{U} + (\nabla \cdot \boldsymbol{U})^T] \tag{3.34}$$

Using the same analogue, the Reynolds stress can be expressed as:

$$\rho \overline{\boldsymbol{u}' \otimes \boldsymbol{u}'} = \mu_t[\nabla \cdot \boldsymbol{U} + (\nabla \cdot \boldsymbol{U})^T] - \frac{2}{3}\delta_{ij}\rho k \tag{3.35}$$

where μ_t is the turbulent or eddy viscosity, δ_{ij} is the Kronecker delta function defined as $\delta_{ij} = 0$ for $i \neq j$ and $\delta_{ij} = 1$ for $i = j$. The last term on the right hand side accounts for the normal stresses

for isotropic flows. Scalar fluxes of the transported quantity are linearly related to the mean scalar gradient:

$$-\rho\overline{\phi' \boldsymbol{u}'} = \Gamma_e \nabla \cdot \Phi \tag{3.36}$$

where Γ_e is the turbulent or eddy diffusivity ($\Gamma_e = \mu_t/\sigma$) and σ is the turbulent Prandtl number that can take values in the range of 0.5-0.9, with the default value being 0.9 (Versteeg and Malalasekera, 1995). The form that equation (3.35) takes depends on the definition of the length and the velocity scales through μ_t, which is defined differently by different eddy-viscosity based models.

The two commonly used two-equation turbulence models are k-ε and k-ω, in which both velocity and length scales are solved using two separate transport equations for k and ε or the turbulence frequency (ω). The turbulent velocity scale is obtained from the k transport equation and the turbulent length scale is obtained from both k and ε transport equations. There has been a wide application of the k-ε model due to its low computational cost and the capability to give reasonable predictions of experimental results in a wide variety of geometries. The velocity and length scales are given by (Versteeg and Malalasekera, 1995; Wu and Patterson, 1989):

$$\vartheta = k^{1/2} \tag{3.37}$$

and

$$l_m = \frac{k^2}{\varepsilon} \tag{3.38}$$

From equation (3.31):

$$\mu_t = \rho_L C_\mu \frac{k^2}{\varepsilon} \tag{3.39}$$

where C_μ is a turbulence model constant and ε is the local turbulent kinetic energy dissipation rate. The k-ε model is defined by replacing ϕ in the general transport equation (3.22) by k and ε and introducing the relevant generation and sink terms.

$$\frac{\partial \rho k}{\partial t} + \nabla \cdot \boldsymbol{U} k = \nabla \cdot \left(\left(\mu + \frac{\mu_t}{\sigma_k} \right) \nabla k \right) + G - \rho \varepsilon \tag{3.40}$$

and

$$\frac{\partial \rho \varepsilon}{\partial t} + \nabla \cdot \boldsymbol{U} \varepsilon = \nabla \cdot \left(\left(\mu + \frac{\mu_t}{\sigma_\varepsilon} \right) \nabla \varepsilon \right) + \frac{\varepsilon}{k} G C_{1\varepsilon} - \rho \frac{\varepsilon^2}{k} C_{2\varepsilon} \tag{3.41}$$

where σ_ε and σ_k are Prandtl numbers that connect the diffusivity of k and ε and G is the turbulence production term given by:

$$G = \nabla \cdot \boldsymbol{U} \left(\mu_t [\nabla \cdot \boldsymbol{U} + (\nabla \cdot \boldsymbol{U})^T] - \tfrac{2}{3} \delta_{ij} \rho k \right) \tag{3.42}$$

The empirical parameters used in the standard k-ε model are given in Table 3.2 (Launder and Spalding, 1974):

Table 3.2. Values for the standard k-ε model parameters

Parameter	C_μ	$C_{\varepsilon 1}$	σ_ε	σ_k	$C_{\varepsilon 2}$
Value	0.09	1.44	1.3	1.0	1.92

For incompressible turbulent flows, the molecular viscosity and the transient density terms in equation (3.28) can be neglected. After substituting equation (3.35) into equation (3.29), the set of equations solved for in the k-ε model can be summarised and simplified as:

$$\nabla \cdot \boldsymbol{U} = 0 \tag{3.43}$$

$$\frac{\partial \boldsymbol{U}}{\partial t} + \nabla \cdot (\boldsymbol{U} \otimes \boldsymbol{U}) = -\frac{\nabla \cdot p''}{\rho} + \nabla \cdot \nu_t [\nabla \cdot \boldsymbol{U} + (\nabla \cdot \boldsymbol{U})^T] + F_B \tag{3.44}$$

$$\frac{\partial k}{\partial t} + \nabla \cdot \boldsymbol{U} k = \nabla \cdot \left(\frac{\nu_t}{\sigma_k} \nabla k \right) + \frac{G}{\rho} - \varepsilon \tag{3.45}$$

$$\frac{\partial \varepsilon}{\partial t} + \nabla \cdot \boldsymbol{U} \varepsilon = \nabla \cdot \left(\frac{\nu_t}{\sigma_\varepsilon} \nabla \varepsilon \right) + \frac{\varepsilon G}{k \rho} C_{1\varepsilon} - \frac{\varepsilon^2}{k} C_{2\varepsilon} \text{ where } \nu_t = \mu_t / \rho. \tag{3.46}$$

where p'' is the modified pressure, which is given by:

$$p'' = p + \frac{2}{3} k \tag{3.47}$$

Reynolds stress models

In the Reynolds stress models, separate transport equations are solved for the six Reynolds components of $\rho\overline{\boldsymbol{u}'\otimes\boldsymbol{u}'}$ in addition to the transport equation for ε. Compared to the *k*-ε model, five additional transport equations are solved (the transport equation for *k* is not solved). The full Reynolds stress models includes the Baseline (BSL) zonal *k*-ω based model, the shear stress transport (SST) zonal *k*-ω based model (Menter, 1994) and Launder-Reece-Rodi (LRR) Reynold stress models based on the Isotropisation of Production (IP) and Quasi Isotropic (QI) assumptions, respectively (Launder et al., 1975). In general, the Reynolds stress models are expected to give better predictions than the *k*-ε models in systems where there is swirl. However, this is not always the case, despite the fact that they require more computational power than the two-equation models (Versteeg and Malalasekera, 1995). The governing equations for the Reynolds stress models are very long (Wilcox, 2000), and therefore are not described in this work.

3.2.3. Governing equations for solid-liquid flow

For multiphase systems, the RANS equations are modified with the introduction of phase hold-up and interfacial related forces. The continuity and transport equations for momentum, *k* and ε must be modified to account for the influence of the additional phase(s) on the bulk fluid flow. The resulting set of equations can be solved by the Lagrangian particle tracking model (Derksen, 2003) or the Eulerian two-fluid model. The Lagrangian method is applicable to low phase hold-ups, as the equation of motion is solved for the individual particles. The Eulerian method is typically applied to high phase hold-up systems, in which the influence of volume fraction on the mixing is important and the two phases are treated as two interpenetrating continua. Multiphase flows can be homogeneous or inhomogeneous, both of which can be modelled by the Eulerian method, and this is the method described in this chapter. For homogeneous flows, the interface transfer rate is very high and therefore only one flow field is solved for the two phases. However, for inhomogeneous flow, there is a separate solution field for each phase, and the transported quantities interact through the interface transfer terms. This interaction between the phases could be one-way or two-way coupling. Two-way must be used if the phase hold-up of the dispersed phase is close to that of the continuous phase. The nature of the interaction is, therefore, system specific.

The main assumption on which the Eulerian method is based is that any small volume in the domain contains both phases such that the sum of the volume fractions is unity. The interaction between the liquid and the solid phases is accounted for through the interfacial forces, of which the drag force has the most important influence. Neglecting the terms arising from the fluctuations of the hold-up, the general formulation of the continuity equation is given by:

$$\frac{\partial}{\partial t}(\rho_n \varphi_n) + \nabla \cdot (\rho_n \varphi_n \boldsymbol{U}_n - \nabla D_{LS} \varphi_n) = 0 \tag{3.48}$$

where φ_n is the phase hold-up for phase '*n*', ρ and U are the density and the mean velocity vector, respectively; D_{LS} is the turbulent diffusivity, which is specified if the Reynolds averaging approach is used, otherwise it is set to zero for the Favre averaged equations. The momentum conservation equation for the liquid phase is given by:

$$\frac{\partial}{\partial t}(\rho_L \varphi_L \boldsymbol{U}_L) + \nabla \cdot (\rho_L \varphi_L \boldsymbol{U}_L \otimes \boldsymbol{U}_L) = -\varphi_L \nabla \cdot p'' + \varphi_L \nabla \cdot \tau_L + F_I + F_B \tag{3.49}$$

where F_B represents body forces including gravity, Coriolis, and centrifugal force, p is the pressure; F_I represents the interfacial forces, which include drag (F_D), non-drag forces (F_{ND}) and turbulent dispersion force (F_{TD}). The turbulent dispersion force appears in the momentum equation for the Favre averaged equations. Since mass transfer is not accounted for, the momentum transfer induced by mass transfer is ignored. The momentum balance for the solid phase has an additional term that accounts for the interaction between the particles and is given by:

$$\frac{\partial}{\partial t}(\rho_s \varphi_s \boldsymbol{U}_s) + \nabla \cdot (\rho_s \varphi_s \boldsymbol{U}_s \otimes \boldsymbol{U}_s) = -\varphi_s \nabla \cdot p'' - \nabla \cdot p_s + \varphi_s \nabla \cdot \tau_s + \varphi_s \nabla \cdot \tau_L + F_I + F_B \tag{3.50}$$

where τ_s is the solids stress, which has been neglected in some commercial CFD codes such as CFX5; p_s is the solid pressure that accounts for interaction between the particles, and is given by (Gidaspow, 1994):

$$\nabla \cdot p_s = G_o \exp(-c_m(\varphi_s - \varphi_{sm}))\nabla \cdot \varphi_s \tag{3.51}$$

where G_o is the reference elasticity modulus, c_m is the compaction modulus and φ_{sm} is the maximum packing parameter. The sum of the volume fraction in each control volume should add up to one:

$$\sum_{n=1}^{n_\varphi} \varphi_n = 1 \tag{3.52}$$

3.2.4. Closure for solid-liquid turbulent flow

The forces representing the interaction between the phases need to be modelled in order to obtain closure for the resulting transport equations. The interfacial forces include the drag, non-drag and turbulent dispersion forces, of which the drag force is the most dominant. The coupling between the two phases is achieved by interphase coupling algorithms such as Partial Elimination Algorithm (PEA) and SImultaneous solution of Non-linear Coupled Equations (SINCE). Interface coupling is incorporated into the mass balance pressure shared correlation step by the interface slip algorithm-coupled (IPSA-C) method. A detailed description of these algorithms is given by Karema and Lo (1999). Turbulence induced in the liquid phase by the particle can be accounted for through the turbulent viscosity by the model proposed by Sato and Sekoguchi (1975):

$$\mu_{t,L} = \rho_L C_\mu \frac{k^2}{\varepsilon} + \rho_L C_{\Delta,p} \varphi_s d_p |U_s - U_L| \tag{3.53}$$

where the constants C_Δ and $C_{\Delta,p}$ can be taken as 0.09 and 1.0, respectively (Lane et al., 2005).

Drag force

For spherical particles, the total drag per unit volume on the liquid phase is given by:

$$F_D = -\frac{3\varphi_L \rho_L C_D |U_r| U_r}{4 d_p} \tag{3.54}$$

where U_r is the relative velocity vector between solid and liquid phases.

The drag coefficient (C_D) can be expressed by different correlations, depending on the system (AEAT, 2003) as shown in Table 3.3.

Table 3.3. Drag models

Model	Expression	
Schiller-Naumannn	$= \max\left(\frac{24}{\mathrm{Re}_p}\left(1 + 0.15\ \mathrm{Re}_p^{0.687}\right), 0.44\right)$	(3.55)
Brucato	$C_D = C_{Do}\left[1 + 8.76\ x10^{-4}\left(\frac{d_p}{\lambda}\right)^3\right]$	(3.56)
WenYu	$C_D = \varphi_L^{-1.65} \max\left(\frac{24}{\mathrm{Re}_p'}\left(1 + 0.15\ \mathrm{Re}_p^{0.687}\right), 0.44\right)$	(3.57)
Ergun	$C_D = 150\frac{\varphi_s^2 \mu_L}{(1-\varphi_s)d_P^2} + 7/4\frac{\varphi_s \rho_L \lvert \boldsymbol{U}_r \rvert}{d_P}$	(3.58)
Gidaspow	Equation (3.57) for $\varphi_s < 0.2$, otherwise Equation (3.58)	

where $\mathrm{Re}_p = \frac{d_p \boldsymbol{U}_r}{\nu}$ and $\mathrm{Re}_p' = \varphi_L \mathrm{Re}_p$

The Gidaspow model (Gidaspow, 1994) effectively becomes Wen-Yu and Ergun models for low ($\varphi_s < 0.2$) and high ($\varphi_s > 0.2$) solid hold-ups, respectively. The discontinuity at the crossover solids hold-up is taken care of by interpolating between Wen Yu and Ergun over the range $0.7<\varphi_L<0.8$ (AEAT, 2003). The fluid drag coefficient for a quiescent liquid, C_{Do}, can be taken as C_D in equation (3.55) and λ is the Kolmogoroff length scale ($\lambda = (\nu^3/\varepsilon)^{1/4}$). The energy dissipation rate, ε, can be the local turbulent kinetic energy dissipation rate, obtained from the CFD simulation, or the mean specific kinetic energy dissipation rate given by equation (3.18).

Non-drag forces (F_{ND})

Non-drag forces include the turbulent dispersion (F_{TD}), virtual mass (F_{VM}), lift (F_L) and wall lubrication (F_{WL}) forces. The turbulent dispersion force represents the effect of turbulent fluctuations on the effective momentum transfer. The virtual mass force is an inertial force, which is caused by the relative acceleration of the phases due to the movement of the particle (AEAT, 2003). The lift force denotes the traverse force caused by rotational strain, and the wall lubrication force tends to push the dispersed phase away from the wall. There are various versions of the non-drag forces and the turbulent dispersion force, and detailed descriptions of these forces are given by Lopez de Bertodano, (1998) and Lahey and Drew,

(2001). The way the turbulent dispersion force is accounted for depends on the averaging approach. For the time averaging approach, the turbulent dispersion force appears in the continuity equation as a function of the Schmidt number (Montante et al., 2001b), and for Favre averaging, it appears as a force in the momentum equation (Lopez de Bertodano, 1998; Lahey and Drew, 2001; Lane et al., 2005). Correlations to calculate these forces are given by (Antal et al., 1991; Burns et al., 2004; ANSYS, 2004; Lopez de Bertodano, 1998):

$$F_{TD} = C_{TD} C_{MT} \frac{\nu_{tL}}{\sigma_{tL}} \left(\frac{1}{\varphi_s} \frac{\partial \varphi_s}{\partial x_i} - \frac{1}{\varphi_L} \frac{\partial \varphi_L}{\partial x_j} \right) \tag{3.59}$$

$$F_{TD} = C_{TD} \rho_L k_L \frac{\partial \varphi_L}{\partial x_j} \tag{3.60}$$

$$F_{VM} = \varphi_s \rho_L C_{VM} \left(U_{pi} \frac{\partial U_p}{\partial x_i} - U_{pj} \frac{\partial U_p}{\partial x_j} + 2\Omega \times U_r \right) \tag{3.61}$$

$$F_L = \varphi_s \rho_L C_L U_r (\varpi_L + 2\Omega), \tag{3.62}$$

$$F_{WL} = -\rho_L \varphi_s \frac{((U_r - (U_r n_w) n_w))^2}{d_p} \max\left(c_1 + c_2 \frac{d_p}{y_m}, 0 \right) n_w \tag{3.63}$$

where equations (3.59) and (3.60) are Burns and Lopez de Bertodano F_{TD} models, respectively, C_{TD} is the turbulent dispersion coefficient, C_{MT} is momentum transfer coefficient for the interface drag force, ν_{tL} is the liquid turbulent viscosity, σ_{tL} is the turbulent Schmidt number for volume fraction, C_{VM} is the non-dimensional virtual mass coefficient, Ω is the speed of the rotating frame of reference, C_L is the non-dimensional lift coefficient, ϖ_L is the rotation of the fluid flow field ($\varpi = \nabla x U_L$), c_1 and c_2 are non-dimensional constants, y_m is the distance to the nearest wall and n_w is the unit normal pointing away from the wall.

Table 3.4. Default values for non-drag model coefficients

Force	Symbol	Coefficient
Lift	C_L	0.5
Virtual mass	C_{VM}	0.5
Turbulent dispersion	C_{TD}	0.1
Wall lubrication	c_1, c_2	c_1= -0.01, c_2 = 0.05

All the governing equations are solved in CFD codes by defining the domain and the necessary boundary conditions, discretization schemes and operating conditions. The empirical correlations required for the closure are introduced through user defined routines. A detailed description of the simulation procedures is given in Chapter 4.

CHAPTER 4

4. Experimental and simulation methods

Hydrodynamics studies with different impeller types were carried out using CFD simulation and LDV experimental techniques. The simulations were run using CFX codes (AEAT, 2003) for both liquid-only and solid-liquid systems. Preliminary simulation studies were carried out with the liquid-only system in a flat-bottomed tank stirred by a pitched blade impeller (P33T). This was to investigate the influence of the simulation strategies on the prediction of the flow field. For these preliminary simulations, experimental results from the literature were used for validation. Subsequently, simulations were carried out in tanks stirred by the Rushton turbine and a hydrofoil impeller (Mixtec HA735), and for these, LDV experiments were conducted to obtain the data for validation. The Rushton turbine and the hydrofoil impeller were employed in the liquid-only system to investigate the influence of impeller clearance and tank geometry on the flow pattern, mixing time and power. For both simulation and experimental methods, the liquid was water.

In the solid-liquid system, a fully baffled Perspex tank with an elliptical bottom and stirred by the hydrofoil impeller was employed to investigate the solids mixing features such as the off-bottom solids suspension, cloud height, solids concentration distribution and local particle size distribution in the tank. Methods were developed to correlate the experimental and CFD simulation techniques of determining these features. A visual method was used to determine the off-bottom solids suspension and an optical attenuation technique (OAT) was used to determine the cloud height and solids concentration distribution. Corresponding CFD simulation methods were developed to determine the same features. The experiments were conducted with nickel solids only while the simulations were carried out with sand, flint glass and nickel particles. Table 4.1 shows the impeller tip speed ($V_{tip}=\pi ND$) and other operating parameters such as the impeller bottom clearance (C) and the grid sizes used in different configurations. The pitched blade impeller (PBI) was not used with a draft tube (DT) as opposed to the Rushton turbine (RT) and the hydrofoil impeller (HI), which were employed with and without DT. All impellers used in the present work were of diameter (D) 0.33T.

Table 4.1 System specifications

Configuration	Impeller	C	V_{tip}, ms^{-1}	Cells for full tank	Code	Phase(s)
P33T	PBI, no DT	0.33T	1.77	160,000	CFX4	L
R15T	RT, no DT	0.15T	1.96	345,600	CFX4	L
R15T-DT	RT + DT	0.15T	1.30-3.30	345,600	CFX4	L
R33T	RT, no DT	0.33T	1.96	345,600	CFX4	L
H15T-DT	HI + DT	0.15T	1.30	1,052,000	CFX5	L
H15T	HI, no DT	0.15T	1.96	1,052,000	CFX5	L/S-L

4.1. Experimental methods and material properties

The mean velocity and turbulent fields in a liquid-only system were determined by the LDV method. For the solid-liquid system, both particle settling velocity and solids concentration distribution were determined by the optical attenuation technique. Sieves were used to divide the samples into different sizes, within which the particle size distribution was measured using a laser diffraction technique (LDT) (Malvern mastersizer S long bed). The detailed morphology of the particles was analysed by the scanning electron-microscopy (SEM). A sampling method was employed to determine the solids concentration distribution as well as the local particle size distribution in the mixing tank.

4.1.1. Reactor geometry

Figure 4.1 shows the fully baffled Perspex tank with a diameter (T) of 0.378 m employed in the present work. The four baffles were each 0.1T wide, the diameter (D) for all impellers was 0.33T and the impeller bottom clearance was in the range of 0.10T to 0.40T. The impeller clearance was taken as the distance from the bottom of the tank to the middle of the impeller blade. The direction of the rotation of the impeller was clockwise, as viewed from the top. The liquid height was equal to the diameter of the tank, except when the draft tube was used, the height was 1.4T. The diameter of the draft tube (d) was in the range of 0.47T-0.80T. The Rushton turbine blade width and length were 0.2T and 0.25T, respectively. Both the Rushton turbine and hydrofoil impeller were used with or without a draft tube.

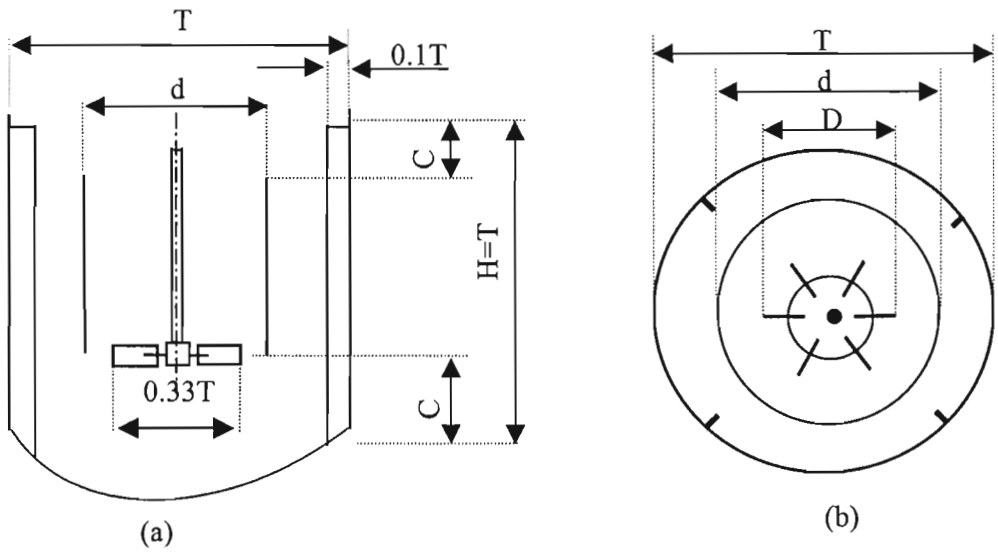

Figure 4.1. Schematic representation of the Rushton turbine stirred tank:

(a) side view (b) top view.

The hydrofoil impeller shown in Figure 4.2, which was employed for mixing in liquid-only and solid-liquid systems, is a mixed flow type of impeller that resembles the Lightnin A315 propeller.

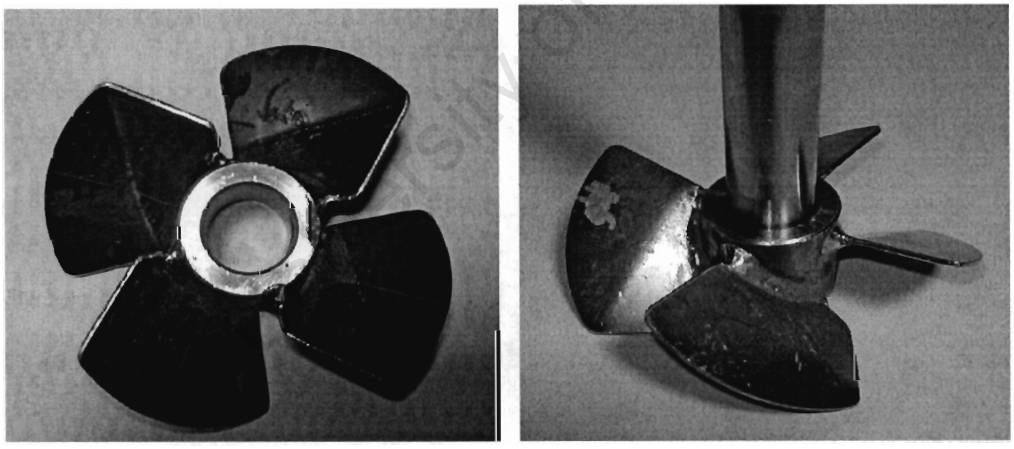

(a) (b)

Figure 4.2. Mixtec HA735 hydrofoil impeller (a) bottom view, (b) side view.

4.1.2. LDV measurements

The LDV measurements were carried out with an impeller speed of 300 rpm for all configurations except for the configuration with the draft tube, where it was 200 rpm. The speeds correspond to the impeller Reynolds numbers ($Re = ND^2/\nu_L$) of $7.81x10^4$ and $5.21x10^4$, respectively. The lower speed of 200 rpm for R15T-DT was necessary to avoid entrainment of air that was experienced with a speed of 300 rpm, which interfered with LDV measurements. The measurements were taken for the three-dimensional mean velocity and turbulent fields in a Perspex vessel, which provided a good refractive matching between the tank and water for the measurement. The LDV probe was mounted on a robotic arm as shown in Figure 4.3 and the measurements of the three velocity components were taken in the middle of two baffles ($\theta = 0^o$). The working vessel was encased in an outer transparent trough with a square cross-section, and both filled with tap water to a required depth. No seeding was required for the tap water as the naturally existing particles in tap water could adequately reflect the Doppler signals.

Time averaged velocity data was obtained using a time weighted bias correction method. The laser source was a spectra Physics 2017 argon-ion laser; the optical transmitter was an aerometrics fibre drive and the optical system-focussing unit was an aerometrics optical fibre probe. Sampling time was either one minute or timing out if a certain number of data points were obtained (either 500, 1000 or 2000). The LDV measurement volume, which is at the point of intersection of the two laser beams out of the optical unit, was of 46.7 μm in diameter and 370 μm in length. The refractive index of water was taken into account in determining the position of the measuring volume. The Doppler signals were processed by the discrete Fourier transform to obtain the Doppler frequency. The optical axis of the velocimeter was consistently perpendicular to the trough walls. The mean and root mean square (rms) velocity bias were corrected with the transit time weighting approach and the LDV measurements were taken in backscatter mode.

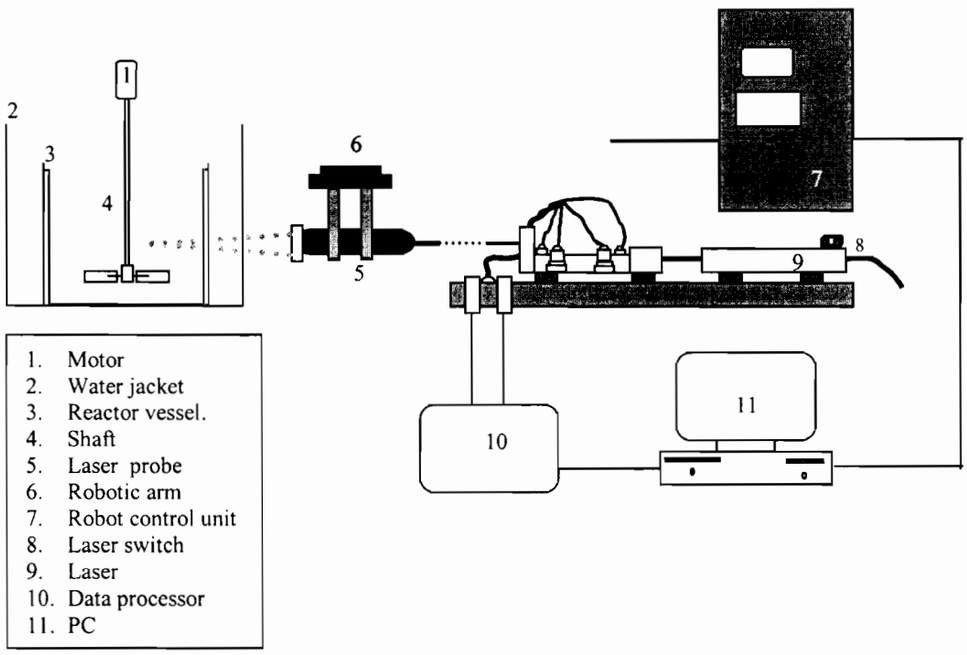

Figure 4.3. LDV experimental set-up

4.1.3. Particle properties

The properties of these materials and solids loading are given in Table 4.2. It should be noted that of the three particles listed in Table 4.2, only nickel was employed for experimental studies. The nickel solid loadings by mass were in the range of 0.3-20%, and subsequent references to solid loadings are percentages by mass, unless stated otherwise. The nickel particle size range was 75-1000 μm, within which some specific investigations into the effects of particle size on the solids suspension were conducted with three sub-ranges: 150-300, 300-500 and 500-1000 μm. The LDT method was used to measure the mean particle diameters (d_{50}) for the entire particle size range as well as the sub-ranges. For the sub-ranges, the mean respective particle diameters, were 230, 400 and 750 μm. These sub-ranges are, therefore, denoted by Ni230, Ni400 and Ni750, respectively.

Table 4.2 Material properties

Material	dp, μm	density kgm^{-3}	Loading, %	Re_p
Nickel	75-1000	8903	0.3-20	2.36-271
Flint glass	750	4200	10	223
Sand	750	2500	10	153

4.1.4. Off-bottom solids suspension

Different mases of solid samples in the size range of 75-1000 μm were employed to determine the respective N_{js} using the visual method. From these experimental values of N_{js}, the geometry dependent parameters such as C_N, in the Zwietering (1958) correlation (equations (3.9) and (3.10)), were determined. For the particle size range investigated, C_N was found to be 2.75. This value is comparable to that reported for axial impellers by Armenante and Nagamine (1998) as 2.7, and the value was subsequently used to calculate N_{js}, from the Zwietering (1958) correlation for different particle sizes and loadings.

A special visual method was proposed for the determination of N_{js} in the elliptically bottomed tank using a "maximum bottom radius coverage" concept. This method is similar to that proposed by Rieger and Ditl (1994), in which the accumulation of solids at the centre of the tank below the impeller and the accumulation at the tank edges were investigated. The difference between their method and the present one is that, in the present case, the bottom of the tank was elliptical, therefore, only the solids coverage below the impeller could be considered. The maximum bottom radius (r_m) covered by the solids, when the impeller was running at N_{js}, was determined experimentally.

A given mass was introduced into the tank and then the impeller speed was increased gradually until no particle remained static on the bottom for more than 1-2 s. For this condition to be achieved, there was a maximum radius (r_m) covered by the particles at the bottom, and beyond this radius, the particles on the bottom could not move. The radius decreased with an increase in the impeller speed leading to completed off bottom suspension as the covered redius diminished. The radius referred to is a maximum (and not a minimum), with reference to the possibility of particles movement. Subsequently, r_m was used to determine the CFD simulated N_{js} as explained later in section 4.2.5.

4.1.5. OAT measurements

The optical attenuation technique works on the principle that the attenuation of light passing through slurry depends on the solids concentration on the light path. Light was transmitted from an infrared light emitting diode (LED) through the tank to a photodiode (PD) on the opposite side of the tank as shown in Figure 4.4. The light beam was about 1 cm from the surface of a centrally located shaft. Light from the infrared spectrum was chosen to minimize the interference of ambient light. The LED had a viewing angle of 15 degrees and a lens was used to focus the light through the tank onto the PD. The receiving sensor (PD) operated at the same light frequency. The output signal from the receiver was processed by an integrated circuit (IC) unit.

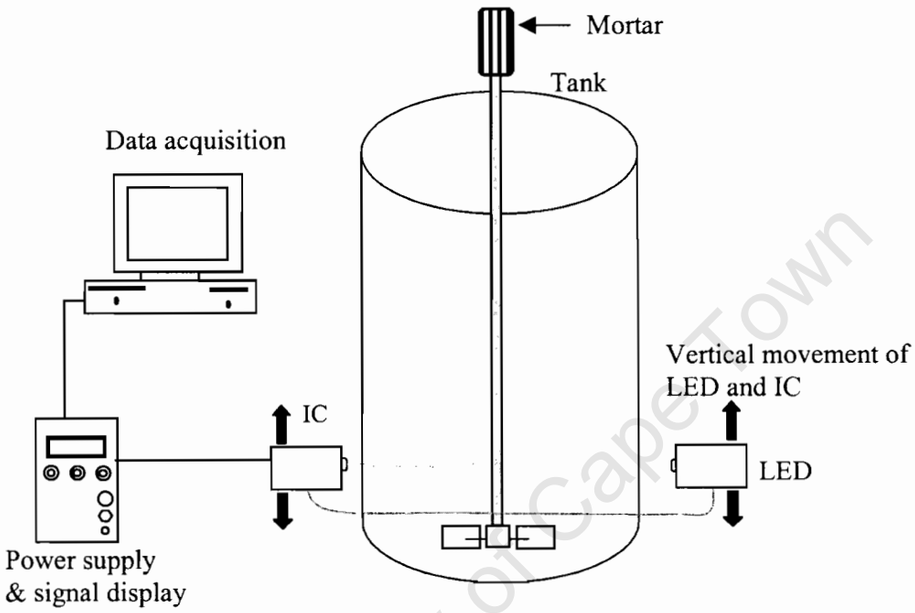

Figure 4.4. Schematic diagram of the optical attenuation experimental set-up.

There is a linear relationship between the light intensity received and the output voltage, and therefore, the output voltage was taken as a measure of the light intensity. The output of the PD was then passed through a combination of amplification and filtering in the IC. There was also a synchronous detection system incorporated, which only sampled the signal at the precise time of transmission. Sampling was done at a rate of 100 per second. During the inactive transmission period, the output of the receiving device was inverted.

What followed was a direct current (DC) component of the signal. A low pass filter cleaned up the DC component, which was then fed into an operational amplifier set up in voltage following mode. This drives the signal with high impedance. This analogue signal was digitally converted at a chosen frequency using a data acquisition board and stored in a PC. The light intensity indicated by the signals from the IC was a measure of the quantity of particles suspended on the light path. Three samples were taken at a given point and the average of these represented the solids concentration on the horizontal plane at the point of measurement. Measurements were taken above the curved bottom region of the tank up to a point 2 cm from the surface of the liquid at rest. There were a total of 28 axial data sampling points corresponding to an interval length of two cells in the CFD model of the structured grid. The system was calibrated with different particle sizes, and the relation between the output voltage from the IC and the solids concentration followed a logarithmic function, as shown in Figure 4.5. The output signal (I) was normalized with respect to the signal obtained in the particle free liquid (Io). The intensity of signals passing through the tank for a given solids mass increased with particle size. This is due to the fact that the smaller particles have a larger surface area to mass ratio; therefore, for a given solid mass, the small particles obstruct more light than the bigger ones.

Solids concentration distribution

Solids concentrations up to 500 g (1.33%) loading of Ni230 could be measured within a standard deviation error acceptable in this study (about 8%). A higher loading resulted in a rapid increase in the measurement error up to 70% for a 1 kg loading. The increase in the error was as a result of a rapid increase in attenuation (signals close to zero), for which data reproducibility was low. Therefore, the maximum loading for Ni230 was taken as 1.33%. The correlation for the solids concentration is a Lambert-Beer-type of equation (Brucato et al., 1998a), which holds for intensity attenuation of a narrow beam of light traversing dilute particle dispersions. The solids concentration (c) is calculated as:

$$c = a_o \ln\left(\frac{I}{I_o}\right) \tag{4.1}$$

where a_o is the constant that depends on the path length and particle size. In this application, the path length was constant.

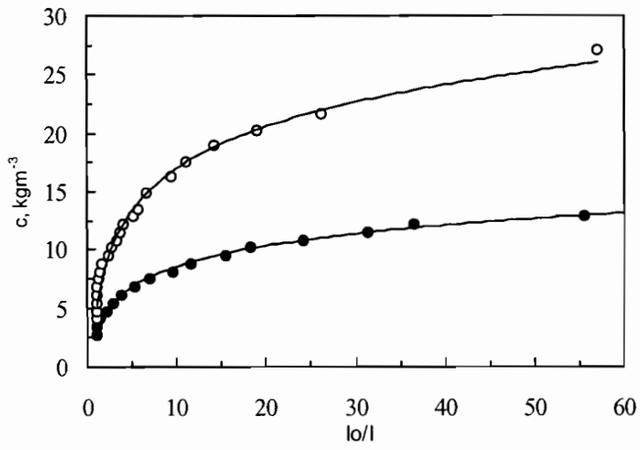

Figure 4.5. Solids concentration calibration curve: (o) Ni230, • Ni400, — Logarithmic fit.

Settling velocity

The typical visual method of determining a particle settling velocity by observing and timing the movement of the particle in a settling column could not be applied in the case of small particles (less than 200 μm). A non-visual method was proposed, by which the particles were released at the same time and across the entire diameter of the tank. This was done by spreading a one particle diameter layer of solids on the surface of a particle releasing device. The device was made of a polystyrene slab with a length of T and width of 0.1T and covered with a porous fibre material to allow particle attachment. The particles were introduced into the liquid by tilting the device to allow the particles to be released into the water uniformly along the diameter coinciding with the beam from the LED. The settling velocity (U_t) was determined by equations (4.2) and (4.3). The particle releasing device provided an initial uniform distribution of the particles in the radial direction, resulting in a modified Dirac delta-like curve response given by the OAT in Figure 4.6. The settling velocity was determined with five different loadings for a given particle size range. The five different masses (5, 10, 15, 20, 25 g) of particles were introduced into the system in turn and the mean settling time was calculated. The low loading (5 g) represented a light packing and the loading of 25 g represented a dense packing on the device. The signals were converted to concentration by equation (4.1) and the settling time was calculated as;

$$t_i = \frac{\int_0^\infty tc(t)dt}{\int_0^\infty c(t)dt} \tag{4.2}$$

where c(t) is the solids concentration at time t. Assuming a constant dispersion coefficient, along the tank (Brucato et al., 1998a), the settling velocity is calculated as:

$$U_t = \frac{l_2 - l_1}{t_2 - t_1} \tag{4.3}$$

where t_1 and l_1 are the time and distance for the transition period, respectively; t_2 and l_2 are the total time and distance, respectively. It is worth noting that the values of a_o in equation (4.1) cancel out in equation (4.2). The transition distance (l_1) was 30 cm while the maximum distance (l_2) was 75 cm. This is comparable to the range used by Brucato et al. (1998a), in which l_1-l_2 was 27 - 43 cm).

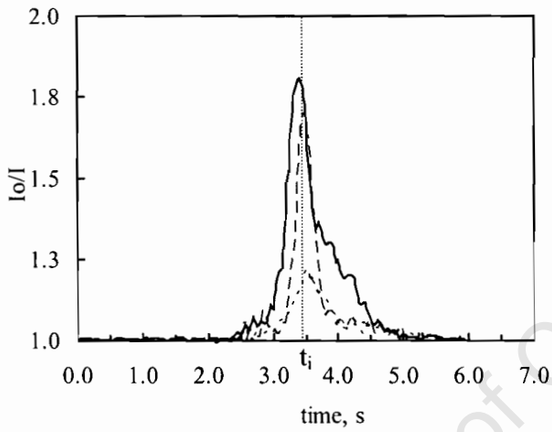

Figure 4.6. Determination of particle settling time: ——25 g; - - - 15 g; ----5 g.

Further tests were conducted by the same method but in a settling column of 1.6 m height and 0.14 m diameter. There was a good agreement between the two methods. The mean particle settling velocity was therefore used to estimate the sampling velocity.

4.1.6. Determination of drag coefficient in quiescent liquid

The optical attenuation technique was employed to measure the particle terminal settling velocities in a quiescent fluid as shown in Figure 4.6. The volume fraction for the particle

samples injected into the liquid was kept very low (less than 0.1%), at which the influence of the particle-particle interaction on the particle settling velocity was negligible. Further, for the range of sample masses used in the present work, there was a negligible influence of the mass of solids on U_t. There was a 5% error in determining U_t, and a similar level of error was obtained in a different set-up of a taller (1.6 m) settling column. For the numerical simulation approach, a FORTRAN routine was written on the basis of the fundamental equation of particle settling velocity and the Schiller-Naumann model. The routine was applied to compute both U_t and Re_p, and subsequently the drag coefficient for quiescent liquid (C_{Do}).

4.1.7. Sampling method

Isokinetic sampling is known to improve the accuracy of the sampling method. However, to avoid the settling of the particle in the sampling tube, the sampling velocity was set to 3 times the mean particle settling velocity. Sampling was done using a peristaltic pump connected to a vertical sampling tube. The sampling tube diameter was 15 times the diameter of the largest particles. On the one hand, a small sampling tube diameter would result in an increase in the wall effect, and on the other hand, a large diameter would result in a low sampling velocity or a high sampling volume. Since the ratio of the tank diameter to that of the particles (d_{50}) was 1500, the wall effect was neglected in computing the particle settling velocity. Samples were taken from 7 radial and 16 axial points. Each radial location represented a set of axial points, one of which was 20 mm from the tank wall (Barresi and Baldi, 1987). Three samples were taken from each point, out of which the mean value was obtained.

4.1.8. LDT and SEM measurement of particle size distribution and morphology

The samples taken from the mixing tank were analysed using LDT to determine the particle size distribution and the mean particle size at each sampling point, and the morphology of the particles was analysed using SEM. Detailed information on the flow field, including the influence of particle size on the solids concentration distribution, which could not be obtained by the OAT, was provided by the CFD simulations.

4.2. CFD Simulations

The simulations were run on two P4, 2 GB memory, 3 GHz PCs using CFX codes (AEAT, 2003). Thereafter, all simulations were carried out with geometries described in subsection 4.1.1, in which the experiments were conducted. For the preliminary studies, only structured grid version of the CFX code (CFX4) was used. The unstructured grid version of the CFX code (CFX5) was used for the elliptically bottomed tank stirred by the hydrofoil impeller. For all the simulation work, the impeller shaft and the gravitational force were defined along the x-axis. Although different turbulence models were tested at the preliminary stage, the k-ε model was employed with both the MFR and SG approaches for all subsequent studies. Boundary conditions were the same for both the solid-liquid and liquid-only systems. Simulation methods were developed to link the typical experimental and theoretical approaches for investigating solids suspension to the CFD simulation methods.

4.2.1. Boundary conditions

A free surface boundary condition was defined at the liquid surface, where the shear stresses were set to zero. The blades, disc (for the Rushton turbine) and baffles were defined as thin surfaces, and grids were refined in the wall and impeller regions. On the walls, a no-slip condition was specified for the liquid, while free slip was specified for the particles. In the SG approach, the inner block rotates while the outer one is stationary, and for both MFR and SG, the radial location of the interface was at 0.585T. The bottom part of the rotating block was set to rotate in the opposite direction, making it stationary with respect to the stationary frame. The interconnectivity between the rotating and stationary domain was achieved by the general grid interface (GGI) algorithm (AEAT, 2003).

4.2.2. Solution strategies

Initial flow fields were obtained with the MFR approach whilst the final results were obtained with the SG approach for both single and multiphase simulations. For the CFX4 simulations, the hybrid discretization and quadratic upstream interpolation for convective kinetics (QUICK) schemes were used for the convective terms. The semi-implicit pressure linked equation-consistent (SIMPLEC) algorithm was used to couple the pressure and momentum

equations. Equation solvers such as the block Stone and algebraic multi-grid (AEAT, 2003) were employed with the quadratic time differencing scheme. In CFX5, the blend factor and high resolution discretization schemes were used. The Eulerian multifluid model was employed to obtain the solids concentration field. The Partial Elimination Algorithm (PEA) and the SImultaneous solution of Non-linearly-Coupled Equations (SINCE) with the Interface Slip Algorithm-Coupled (IPSA-C) were employed for the interface coupling. Most of the results, for both the single and two phase systems, were obtained with the standard k-ε turbulence model and the SG approach. The Gidaspow (1994) drag model was used with the default values for the non-drag forces.

4.2.3. Grid resolution and times steps

The simulation work was started with CFX4, for which structured grids were used. A half section of the tank was modelled with three grid sizes: 53x42x36, 60x48x60 and 64x56x60; in the axial, radial and azimuthal directions, respectively. For the later work with CFX5, three grid sizes were used to model a quarter of the tank with one impeller blade: 109,000, 263,000 and 350,000. These grids are hereafter referred to as coarse, base and fine, respectively. Unstructured grids were employed for the solid-liquid system. As expected, the mesh employed for the unstructured grid was finer than that for the structured grid. This was due to the fact that it was possible to refine grids in the wall region without encountering the problem associated with wall treatment. In CFX4, there is a limitation that not more than 10% of the total number of the cells in the domain could be allowed in the region closer to the wall, where the dimensionless distance from the wall (y^+) is less than 11.2. There is no such restriction in CFX5.7, in which either the standard k-ε model with a scalable wall function or the shear stress transport model with automatic wall function (Menter, 1994) was employed.

4.2.4. Mixing time and homogenization energy

Mixing time was studied with a passive tracer in the liquid-only system using the CFX4 code. The time-dependent local concentration of the tracer was calculated by solving the scalar transport equation given in Chapter 3 with the turbulent Prandtl number of 0.9. The tracer was injected below the impeller shaft and its concentration was monitored at five points distributed radially, tangentially and axially on the stationary frame. The flow field for the

mixing time was initiated from a fully developed field obtained with the MFR method and then the mixing simulations were run using SG method. The mixing times required for different degrees of homogeneity were calculated using the Fasano and Penny (1991) correlations given in Chapter 3. Homogenization energy was calculated from the mixing time and the mean specific kinetic energy dissipation rate. For the experimental studies, the power input (P) was calculated from the Nienow (1997) correlation given in Chapter 3. As opposed to the mixing in the single phase system, mixing time was not determined in the solid-liquid system due to high computational cost involved.

4.2.5. Just off-bottom solids suspension

Solids suspension simulations were initiated with particles settled at the bottom of the tank as shown in Figure 4.7. The solution, which was obtained using double precision for all variables, was considered converged when all the root mean square residuals fell below $1.1x10^{-4}$. This was at least three orders of magnitude smaller than that at the beginning of time step. Upon the attainment of the level of the set residuals, further checks were carried out to ensure that the domain mass imbalances were all below 1.0%, that there was no change in impeller blade torque and that the value of the volume fraction of nickel at a specified point remained pseudo-constant for more than 10 seconds within the total simulation time. The axial solids concentration profiles with solids loading up to 1.3% were compared with OAT measurements.

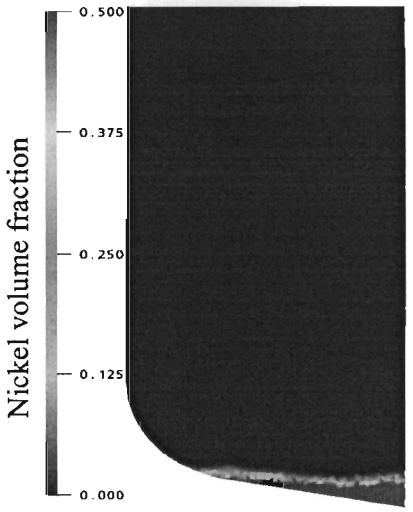

Figure 4.7. Initial position of the solid particles.

Detemination of Njs

The value of the maximum bottom radius covered (r_m), determined experimentally as decribed in section 4.1.4 (Figure 4.8), and was an indication of the degree of the solids suspension. At r_m, less than 2% of the total solids in the tank remained stationary at the bottom of the tank for 1-2 s.

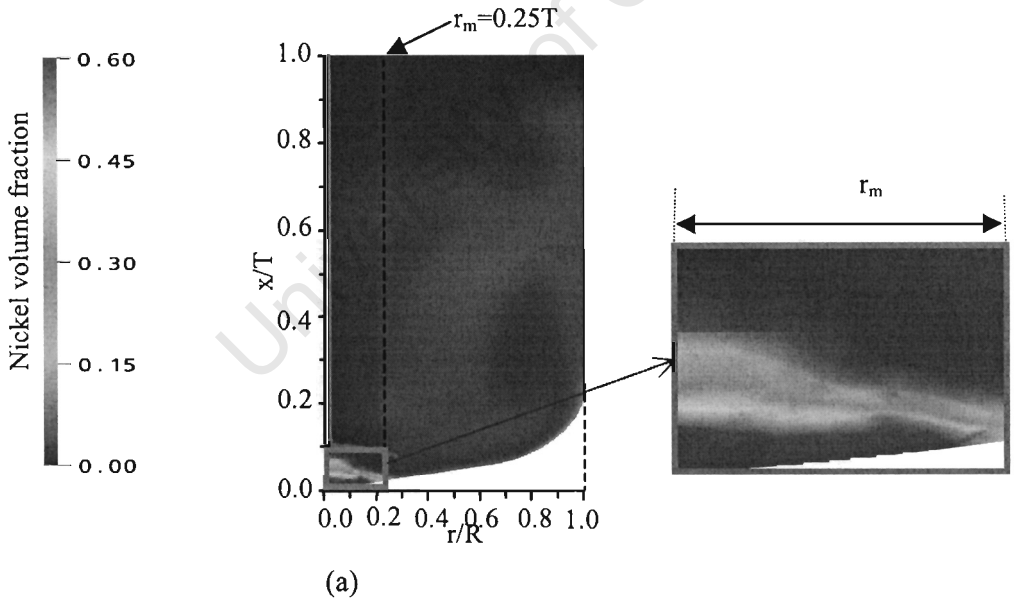

Figure 4.8. Determination of the maximum bottom radius covered at N_{js} with 14% Ni750.

An arc was defined on the simulation domain at r_m. The solids concentration (c_{js}) at r_m

when the impeller was running at the experimentally measured N_{js}, was determined from the CFD simulation. This was done by defining monitoring points along the arc at r_m. A mean value of c_{js} was obtained with different particle sizes and loadings. The mean value of c_{js} was subsequently used as a response variable for the determination of N_{js}. Thus, the subsequent predictions of N_{js} were based on the attainment of c_{js} along the arc.

4.2.6. Cloud height

Cloud heights were taken to represent the level of homogeneity in the tank. A cloud height of 0.9T, therefore, represented a 90% level of homogeneity, and the impeller speed required to achieve this was denoted by N_{90}. The curves representing the axial solids concentration profile, obtained by the CFD and OAT, showed a point of highest curvature close to the axis along the shaft. Above this point, the solids concentration (represented by volume fraction, v/v_o) was low and the variation in the concentration with the radial distance was less than in the region below this point. This point of highest curvature was therefore taken to represent the cloud height, as illustrated in Figure 4.9. The determination of the cloud height by this method involved a single data point, for which the accuracy may be influenced by the intensity of turbulence. Data obtained for the axial solids concentration distribution with OAT is more statistically representative than the single data point method for the cloud height. However, even the OAT does not give any information on the radial concentration gradient. A sampling technique is the simplest method to obtain such information, and this requires a knowledge of the particle settling velocity, which was obtained as described in section 4.1.5.

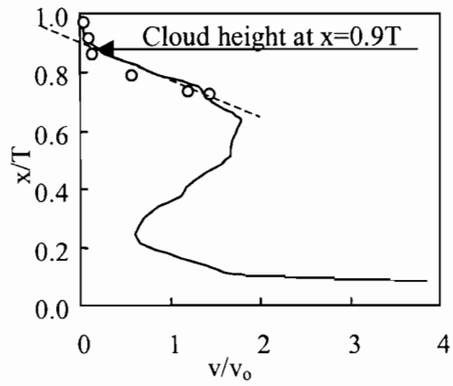

Figure 4.9. Cloud height determination by point of highest curvature method with 14% Ni750:(o) OAT, —CFD.

4.2.7. Solids concentration profile

The poly-line CFX post-process method was used to obtain the local nickel volume fraction from the radial and axial points in the simulation domain. The axial points provided the data for the determination of the axial solids concentration distribution and the cloud height. The radial solids concentration distribution was predicted but no comparison was made with experimental data, since such information cannot be obtained using the OAT. The general information on the solids concentration profile was obtained with mono-disperse particles. More analyses were done with a system in which three particle sizes were defined in one domain, and this approach is referred to as the poly-disperse multi phase simulation.

4.2.8. Local particle size distribution in the tank

The poly-disperse multiphase simulation method was employed since the approach adequately accounts for the influence of the particle size on the solids concentration distribution. Equal masses (1.3 kg) of Ni230, Ni400 and Ni750 were introduced into the domain with the quantity of each particle size representing a dispersed phase in the Eulerian scheme. One of the three phases was taken as a reference phase and the influence of the other phases on the solids distribution of the reference phase was investigated and compared with the results of the mono-disperse systems.

4.2.9. Interfacial forces

The built-in CFX drag models were compared with the Brucato drag model (Brucato et al., 1998a), which is a function of the Kolmogoroff length scale and drag coefficient for a quiescent fluid (C_{Do}). The particle settling velocity required as input data for calculating C_{Do} was determined by the OAT. A FORTRAN routine, based on the fundamental equation for settling velocity and the Schiller-Naumann drag coefficient correlation, was written to compute C_{Do}. The interparticle collisions that take place at high solid loadings were accounted for by the solid pressure, for which the Gidaspow (1994) solid pressure model was used. In the solid pressure model (equation (3.51)) is defined by parameters such as the reference elasticity modulus (G_o) and compaction modulus (c_m). The influence of these parameters on solids suspension was investigated at a constant maximum packing (φ_{sm}) of 0.6.

The non-drag forces accounted for were turbulent dispersion, virtual mass, lift and wall lubrication. For all these forces, the CFX5.7 default coefficient values in Table 3.4 were adopted (ANSYS, 2004). The turbulence induced in the liquid phase by the particle was accounted for by the Sato enhanced eddy-viscosity model (Sato and Sekoguchi, 1975).

CHAPTER 5

5. Results and discussion I: Hydrodynamics of liquid-only system

In this section, the performance of all the three impellers employed in the present work (Rushton turbine, pitched blade impeller, and hydrofoil propeller) was investigated in the liquid-only system. It was only for the purpose of investigating the simulation procedures that the pitched blade impeller was used. The initial simulation studies focused on evaluating the modelling procedures in the CFX code. This was done by first comparing the results obtained in the present work with those in the literature. Further investigation into the influence of the simulation procedures on the three dimensional flow fields, mixing and power consumption was carried out with the Rushton turbine, and a comparison was made with the flow generated by the hydorofoil propeller.

Flow profiles were obtained for the axial (U), radial (V) and the tangential (W) mean velocities. A positive value of U, V and W represented a flow in the upward, outward and clockwise directions, repectively. Radial profiles for these profiles were obtained for half of the tank and a radial distance where r=0 represented the centre of the tanks and r=R was at the wall.

5.1. Preliminary investigation with a pitched blade impeller

The multiple frames of reference (MFR) method has been employed in this section to investigate the influence of turbulence models, discretization schemes and the model k-ε constants on velocities and turbulent fields. The simulations were carried out in a single phase system with only one grid size (80,000 cells) for a domain that represented half of a fully baffled tank (P33T). The simulation results were compared with both simulation and experimental results reported by Nere et al. (2001). Nere et al. (2001) used the impeller boundary condition (IBC) with different k-ε models parameters and the sliding grid (SG) method with the standard k-ε. Their simulation results, for which the default model constants (C_μ=0.09, $C_{\varepsilon 1}$=1.44, $C_{\varepsilon 2}$=1.92) were used, have been compared with the present work. The simulation strategies employed in the present work were the same as those specified by Nere et al. (2001). However, additional turbulence models and discretization

schemes were studied in the present approach. Also, the influence of impeller models and the *k*-ε model constants on both mean velocity and turbulent fields was investigated. All experimental results and references to the IBC method are for the work done by Nere et al. (2001), whilst the MFR method refers to the present work.

5.1.1. Eddy-viscosity turbulence models

The k–ω, standard k–ε and RNG-k–ε models, which are some of the most commonly used turbulence models that are based on the isotropic eddy-viscosity approximation were studied. Figure 5.1 shows that all these models gave a better prediction of the axial velocity component (U) in the region closer to the wall, with less variation in accuracy compared to the results obtained in the impeller discharge region. The k– ω model gave a better prediction than the k– ε model only in the region away from the impller (r > 0.7R). Despite the k–ω model giving the best level of convergence of the residuals, it gave the most severe over-predictions. In the impeller tip region (0.2R-0.4R) the predictions by the k–ω model in Figure 5.1 were worse than those obtained with the k–ε model. The prediction in the impeller region is of utmost interest, and is where the best prediction is sought, due to the fact that 57% of the total energy input is dissipated below the impeller (Sahu et al., 1999). Even though the k–ω model gave a better prediction than the k–ε model in the wall regions, its failure to give reasonable predictions in the region of interest makes its application less desirable in comparison to the k– ε model.

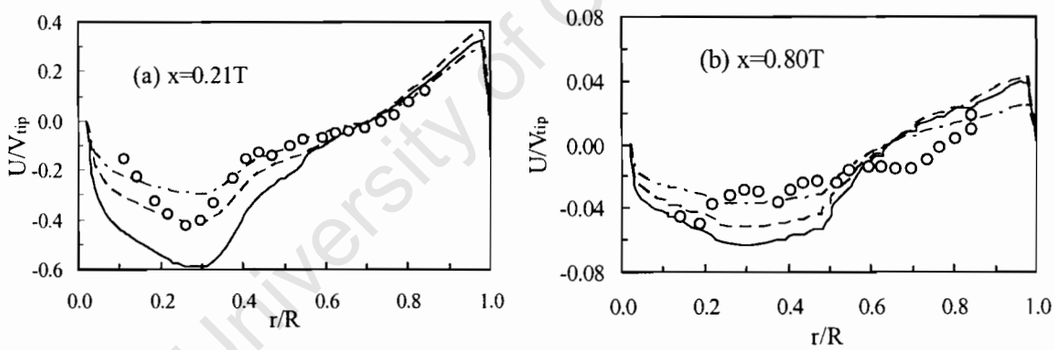

Figure 5.1. Effect of turbulence models on the axial velocity profile: (o) Nere-Experiments, ——*k*-ω, – – Standard *k*-ε, – ·– ·– RNG *k*-ε

Comparing the standard k-ε and RNG-k-ε models, there are two issues to consider: the turbulence intensity and the presence of swirl and flows with curvatures. There was a better prediction of U with the RNG-k-ε model in the regions closer to the surface and wall. Firstly, these are regions of considerable circulation flows arising from the influence of the baffles on the flows impinging onto the wall as well as from the interaction between the primary circulation loop and the free surface. Secondly, there is low turbulence intensity in the upper region of the tank. The axial velocity component in the upper region of the tank (Figure 5.1(b)) was about ten times less that that in the lower region in Figure 5.1(a), indicating significantly less turbulence intensity. In these regions, the RNG-k-ε model prediction was the best. This is expected, given the fact that swirls and circulation flows are known to be better modelled by the RNG-k-ε model than by the standard k-ε model. The standard k-ε model is known to give better prediction in regions of (or systems with) high Reynolds number flows, such as in the impeller region as shown in Figure 5.1(a). Apparently, the general mismatch between experimental and simulation results obtained with all these models could be as a result of the limitations imposed by the eddy-viscosity assumption.

5.1.2. Discretization schemes

A very good convergence of the mass residuals (10^{-5}) was obtained with the first order scheme (upwind differencing scheme). However, the results were a gross over-prediction of the velocity field by as much as 120%. These results were only used to initialize the simulations for further runs with higher order discretization schemes shown in Figure 5.2.

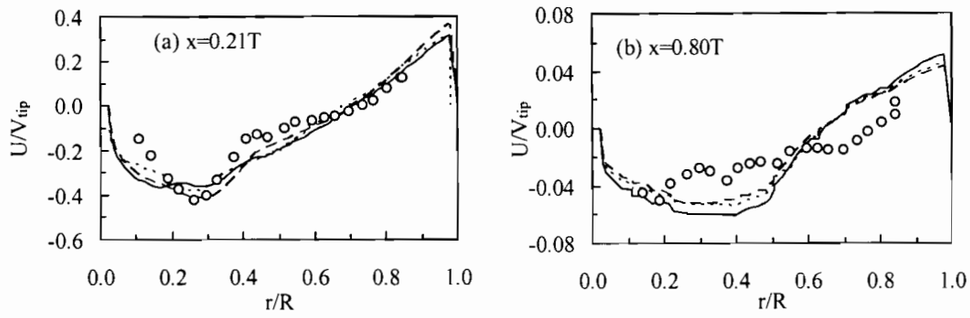

Figure 5.2. Effect of discretization scheme on the axial velocity profile:

(o) Nere-Experiments, —Higher upwind, – – Hybrid, ----- QUICK.

The higher order discretization schemes employed were the hybrid, higher upwind and QUICK. The influence of these schemes on the flow field was investigated in the upper and lower regions of the tank. It is shown in Figure 5.2 that there was a marginal influence of the discretization schemes on the axial velocity profile. It can be seen in Figure 5.2 that the hybrid scheme gave a reasonable prediction in the lower region (Figure 5.2(a)) of the tank. In the upper region (Figure 5.2(b)), predictions by all the schemes were poor. However, the prediction with the hybrid scheme was in general better than the other two schemes.

It is shown in Figure 5.2 that the predictions in the impeller discharge region, in which the Peclet number is higher, are better than in the top region. Due to the high Peclet number in the lower region, it is expected that the hybrid scheme effectively becomes the upwind scheme. However, it is known that this first-order scheme (upwind) is prone to numerical diffusion, especially in high Reynolds flow regions like the impeller discharge region. The fact that better predictions were obtained with this scheme in this region suggests that the discretization schemes were not the major factors influencing the accuracy of the results. The predictions by the higher upwind scheme were better in the impeller region than in the upper tank region. The QUICK scheme, which is third order accurate, is the most computationally demanding and the simulations in which it was used could not converge easily. Even when the residuals finally settled, the level of convergence could not go below 4.5×10^{-4}, which was the worst convergence in comparison to the other two schemes. This could be attributed to the lower diagonal dominance (Aubin et al., 2004), which leads to unboundedness of the solution. A solution is unbound if it is outside the prescribed

boundary conditions. For the maximum downward velocity, the higher upwind scheme gave the highest over-estimation. The maximum upward and downward velocity values give an indication of the magnitude of the circulation flow. An over-prediction of these parameters is indicative of an over-prediction of the circulation flow. The over-prediction of these parameters with the QUICK scheme in Figure 5.2 is in agreement with the work of Brucato et al. (1998b), in which it was reported that the QUICK scheme over-predicts the circulation rate. The maximum upward velocity was over-predicted by all schemes. In general, Figure 5.1 and Figure 5.2 show that the best predictions were obtained by the standard k-ε model and the hybrid scheme. Therefore, the standard k-ε model and the hybrid discretization scheme were subsequently employed to investigate the influence of the impeller models on the flow field.

5.1.3. Impeller modelling and flow field

The predictions of the flow fields generated by the impellers are influenced by the performance characteristics of the impellers and the methods of modelling the impellers. The two impeller modelling methods investigated in this section were MFR and IBC.

Axial velocity (U)

The predictions of U by the MFR and IBC method were compared throughout the entire domain, with profiles at some representative levels in the tank given in Figure 5.3. There was a reasonable agreement between the simulation results obtained with both the MFR and IBC methods and the experimental ones, for the entire radial length. The MFR method gave a better prediction than the IBC method in the upper and lower regions of the tank. The IBC method gave an over-prediction, especially in the regions of maximum axial velocity.

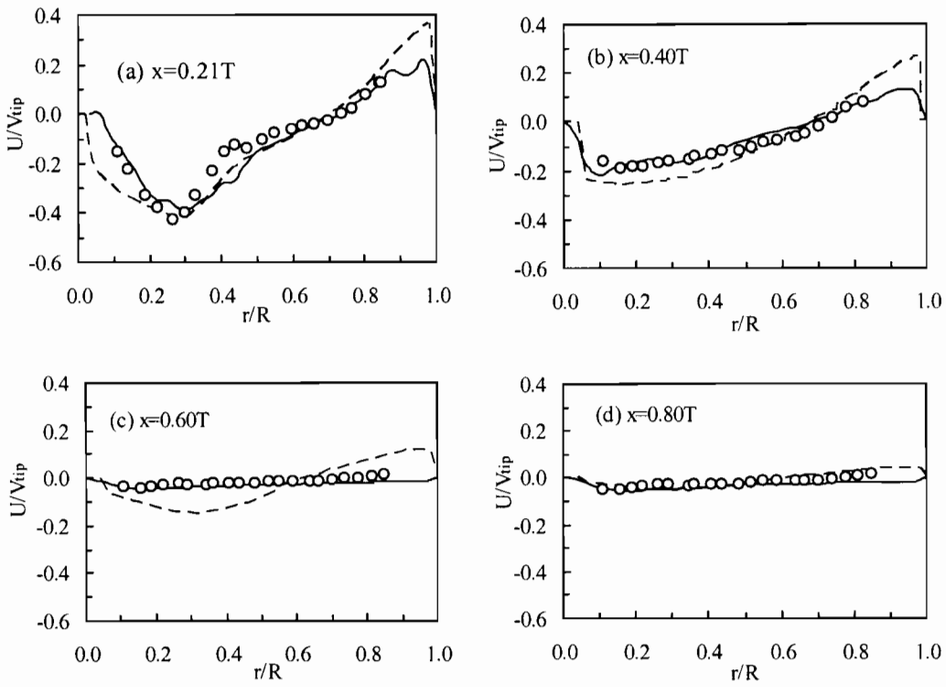

Figure 5.3. Effect of impeller models on the axial velocity profile: —MFR, – – IBC, (o) Nere-Experiments.

Radial velocity (V)

Below the impeller (x = 0.21T), both MFR and IBC methods under-predicted the radial velocity (Figure 5.4) by 80% and 50%, respectively. At this same level, the predictions were reasonable in the outer region (r > 0.35R), where there was less than 10% over-prediction by both methods. It is interesting to note that both methods predicted the experimental trend only in the impeller discharge region (for example, x = 0.21T), and elsewhere, the trend was not well predicted. Considering the entire tank, good predictions were only obtained in the inner region (r < 0.3R), both in the upper and lower regions of the tank. There was an over-prediction of V by the IBC method in the region away from the shaft (r > 0.40R), with an opposite prediction of the experimental trend at x = 0.8T. The MFR method gave a better prediction of the trend at this level in particular and generally in the whole tank. At this level, x = 0.8T, there was a significant scatter of the experimental data. This can be attributed to the free surface deformation, which may result in transient flow structures or small scale secondary circulation loops.

Tangential velocity (W)

The MFR method consistently under-predicted the tangential velocity, in the entire tank as shown in Figure 5.5, and both methods generally gave very poor predictions, except in the inner region (r < 0.3R). There was an under-prediction of W by both methods in the inner region (r < 0.4R): by 23% and 33% by the IBC and MFR methods, respectively, as shown in Figure 5.5(a). At this level (x = 0.21T) there was an over-prediction by 32% with the MFR method and an under-prediction by 46% with the IBC method in the outer region (r > 0.5R).

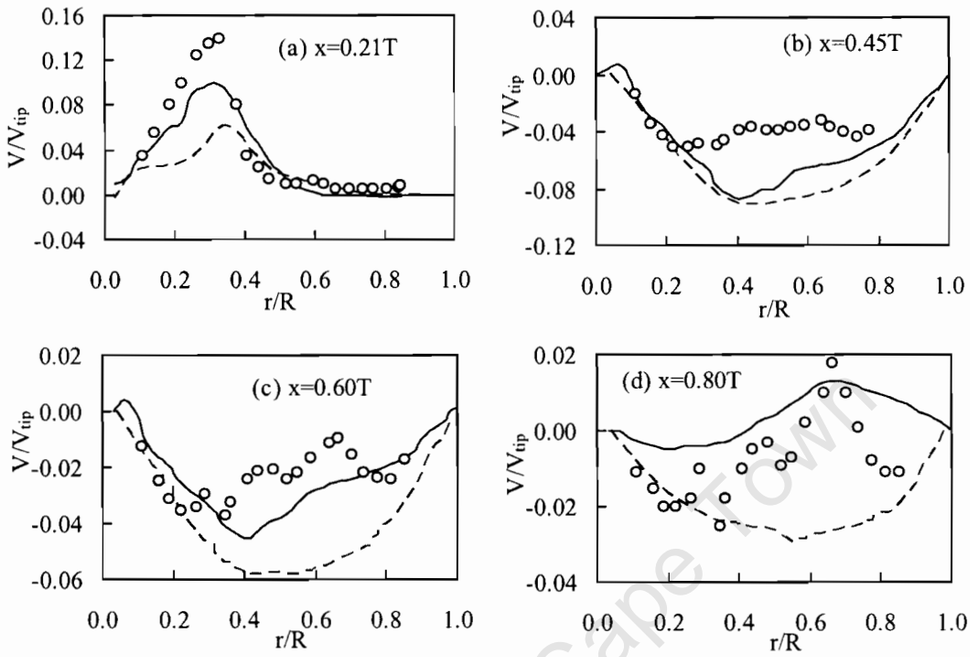

Figure 5.4. Effect of impeller models on the radial velocity profile:
— MFR, – – IBC, (o) Nere-Experiments.

Similar to the V predictions, Figure 5.5(b) shows that the simulation results were the reverse of the experimental ones. This can be attributed to the fact that both methods did not capture the back circulation in the region closer to the liquid surface. A similar observation was reported by Sahu et al. (1999). Nere et al. (2001) attempted many different simulation strategies with k-ε but all gave poor qualitative and quantitative predictions of W. As opposed to the prediction of U, the predictions of V and W by both methods were not good. This could be due to the influence of the interaction between the baffle and impeller on the flow profile. On impacting with the wall, V and W are deflected by both the wall and

baffles, leading to the formation of circulating flows and swirl, which result in anisotropic turbulence.

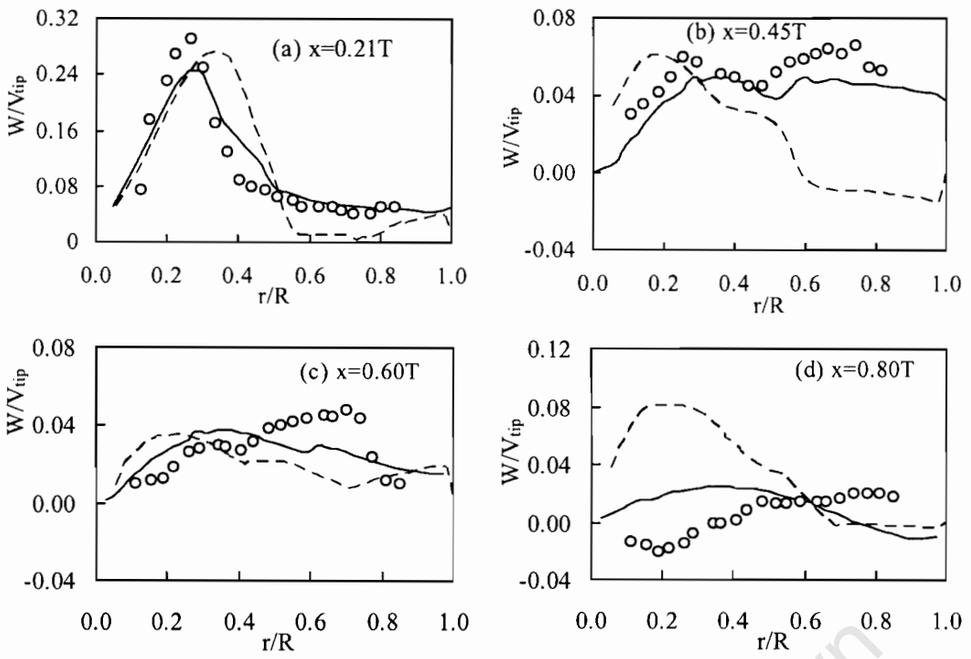

Figure 5.5. Effect of impeller models on the tangential velocity profile: — MFR; - - IBC; (o) Nere-Experiments.

The baffles have a greater influence on W and V compared to U, and this explains the relatively better prediction of U than both W and V. Firstly, the poor prediction of V and W by both methods can be attributed to the circulating flows, which are not accounted for by the k-ε turbulent model. Secondly, baffles act as sinks to the azimuthal flow, and this is shown by the low values of W in the wall region in Figure 5.5. The influence of the baffles varies with both radial and azimuthal distances from the junction of baffle and tank wall. With the IBC method, azimuthally uniform values of the velocity and turbulent parameters are imposed on the cylindrical cell layer bounding the impeller swept volume. Therefore, the variation of these parameters from the junction of baffle and tank wall is not accounted for. Consequently, steep velocity gradients like the one shown in Figure 5.5(c) may not be well predicted. Similarly, the MFR method does not account for the interaction between the impeller and the baffles. It is of interest therefore to note that, in the region closer to the surface, both methods predict an opposite flow direction.

Turbulent kinetic energy (k)

A reasonable qualitative prediction of the turbulent kinetic energy was only obtained by both models in the region below the impeller (x < 0.21T) (Figure 5.6). The quantitative prediction was poor in the entire tank, with the MFR method giving an under-prediction in most parts of the tank. The general trend was that the velocity predictions by the IBC method were higher than those by the MFR method as shown in Figure 5.6.

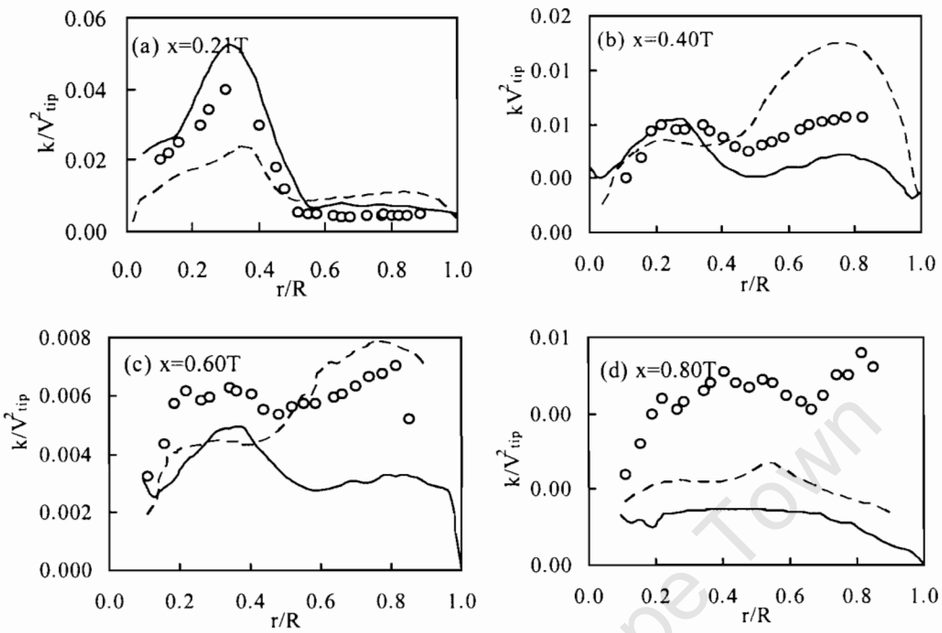

Figure 5.6. Effect of impeller models on the turbulent kinetic energy profile:
— MFR; – – IBC; (o) Nere-Experiments.

There was a severe mismatch between experimental and simulation results, with the MFR and IBC results deviating from the experimental ones by 54% and 72%, respectively. Globally, there were under-predictions by 361% and 170% with the MRF and IBC methods, respectively. In the region closer to the surface, the flow pattern can be influenced by the free surface deformation, which is not well accounted for by these methods. Also, the flow in this region is less turbulent (possibly laminar), therefore, the standard values of the constants ($C_{\varepsilon 1}$ and $C_{\varepsilon 2}$) in the *k*-ε model cannot correctly represent the hydrodynamics in this region. The situation is further compounded by the fact that, in this region, the Peclet number is low; consequently the hybrid discretization scheme effectively becomes the central discretization scheme. One of the downsides of the central scheme is its inadequacy

in accounting for flow directionality and thus it would not adequately represent the stochastic changes of the flow direction in the upper region due to the interaction between the free stream and the primary circulation loop.

The results generally show that the MFR model gave better predictions than the IBC model and that a given set of the k-ε model constant could not give the same lever of accuracy in prediction of the mean velocities in all regions in the tank.

5.1.4. The *k*-ε model constants

The simulation results in section 5.1.1 showed that, in general, the standard *k*-ε model gave a better prediction in comparison to the RNG *k*-ε and *k*-ω models. A further investigation with the MFR method (Figure 5.7) was therefore focused on the *k*- model constants (C_μ , $C_{\varepsilon 1}$ and $C_{\varepsilon 2}$) in the upper region of the tank (x = 0.8T). Different sets of the *k*-ε model constants were investigated. There was no clear trend (applicable to the entire tank) in the response of the flow field to the constants. Therefore, only three sets are reported in Figure 5.7 for the upper region of the tank where C_μ was always kept constant at its default value of 0.09. Only one of the two constants was changed at a time, leaving the other at its default value. The sets of the *k*-ε model parameters, for which the results are shown in Figure 5.7, are given in Table 5.1. These are the sets of the model constants reported by Sahu et al. (1998) to give better predictions than the default settings. The profile obtained with the higher value of $C_{\varepsilon 2}$ in Figure 5.7 shows an improved prediction for all parameters at x = 0.80T. However, for the lower region (x < 0.4T), which is not presented here, worse predictions of U were obtained in the impeller and wall regions.

Table 5.1. Set of model constants for the *k*-ε model.

Set	C_μ	$C_{\varepsilon 1}$	$C_{\varepsilon 2}$)
1	0.09	1.44	1.92
2	0.09	1.44	2.12
3	0.09	1.34	192

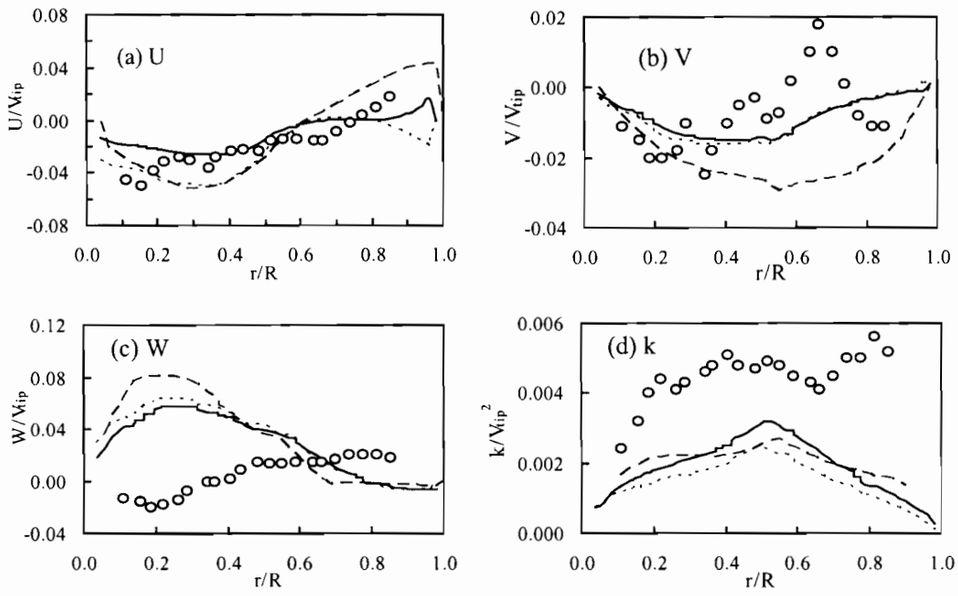

Figure 5.7. Effect of the *k*-ε model constants on the velocity and turbulent field at, x = 0.8T: (o) Nere-Experiments; — *k*-ε model, $C\varepsilon_2 = 2.12$; – – Standard *k*-ε model; ----- *k*-ε model, $C_{\varepsilon 1} = 1.34$

The regions in which the poorest predictions were obtained with the higher value of $C_{\varepsilon 2}$ were the same regions in which U was highest. This confirms that higher values of $C_{\varepsilon 2}$ result in poorer prediction in regions of higher turbulence intensity. Further, a given value of $C_{\varepsilon 2}$ could not give the same quality of prediction in the entire radial or axial distance in a stirred vessel. A higher value of $C_{\varepsilon 1}$ worsened the prediction of U and k. However, the influence of a higher value of $C_{\varepsilon 1}$ on W and V was not consistent.

In the *k*-ε model, $C_{\varepsilon 1}$ accounts for the generation of the turbulent kinetic energy dissipation rate due to the vortex stretching by turbulence. Conversely, $C_{\varepsilon 2}$ accounts for the destruction of the turbulent kinetic energy dissipation rate due to the tendency of viscosity to smear out velocity fluctuations in the modelled form of Reynolds stresses (Sahu et al., 1999). A very comprehensive study was done by Sahu et al. (1998) and Sahu et al. (1999), which showed that no single set of these constants could apply in all regions of a stirred tank. Predictions of the turbulent kinetic energy dissipation rate (ε) have been shown to be very poor by many researchers (Sahu et al., 1999; Nere et al., 2001; NG et al., 1998). Therefore, no attempt was made in the present work to show the predictions of ε in this section.

5.2. Flow field and mixing with the Rushton turbine

In this section, the standard k-ε model the MFR and SG approaches, and hybrid scheme were employed to simulate the flow generated by the Rushton turbine in different reactor configurations (R15T, R15T-DT and R33T). The MFR approach was essentially used to initiate the flow field for the SG approach. A half section of the tank was modelled with three grid sizes: 53x42x36, 60x48x60 and 64x56x60; in the axial, radial and azimuthal directions, respectively. The flow field was determined at different impeller clearances by the LDV and CFD simulation techniques, in a tank with and without a draft tube. A comparison was made with an earlier work on flow field evolution reported in the literature (Montante et al., 2001a). The central focus was on mixing in the region above the impeller with the response variable taken as the axial velocity component (U). Some results of the other velocity components and turbulent kinetic energy are also reported. The influence of fluid flow patterns on mixing and homogenization energy were analysed and quantified. From this section onwards, all LDV results were obtained according to the procedure described in Chapter 4.1.2.

5.2.1. Flow field evolution and flow pattern

The flow field was initiated and developed by the method described by Montante et al. (2001a). The initial flow field obtained was compared in Figure 5.8 with the simulation and experimental work reported by Montante et al. (2001a), in which a similar system was investigated using the SG approach. Tank configuration and model parameters such as tank diameter (0.29 m), impeller tip speed (1.3 ms^{-1}), impeller clearance (C = 0.15T), grid size (53x42x36) and discretization scheme (hybrid) were set to be identical to the aforementioned work.

Transient flow field evolution

At a clearance of 0.15T, there was a change in the flow pattern from double to single loop with the development of the flow field. It was observed that, after the transition from the double loop to the single loop pattern, the flow field continued to evolve. The loop stretched further upwards with an increase in the number of impeller revolutions resulting in an increase in the axial velocity in the upper region of the vessel. This phenomenon, indicating

an increase in the large scale convective flow in this region, can be compared to the work of Campolo et al. (2003), in which it was reported that, for the SG simulation started from a still fluid, the turbulent kinetic energy kept changing until 20 impeller revolutions. However, in the present work, the stretching of the single loop continued until 54 impeller revolutions. The advantage of the vertical stretching loop is that the energy generated by the impeller is dissipated not only in the impeller region but also in the bulk fluid. In a baffled tank, the influence of the impeller on the flow field in the region closer to the liquid surface depends on the magnitude of the axial velocity component.

The type of flow field evolution referred to in this case is caused by an interaction between the macro-scale circulation loops as opposed to the transient (periodic) changes that occur as a result of the interaction between the baffles and impeller blades. The axial velocity component (U) is one of the most important parameters that can give an indication of the flow field evolution resulting from the formation and destruction of the macro scale loops in such flows. Figure 5.8 shows radial profiles of U obtained in a fully developed flow field. There was a good agreement between the present simulation results and both experimental and simulation results of Montante et al. (2001a) at a level just above the impeller (x = 0.3T). The predictions by Montante et al. (2001a) were better than those for the present work in the region closer to the impeller. However, in the wall region, the present simulation was better. In general, the present work over-predicted U. The cause for the slight difference between these two simulation results is not easily apparent. It could be due to the possible differences in the solution strategies and problem definition, which are not evident from the published work. It is not clear, for example, which equation solvers and time differencing scheme were employed. In the present study, block Stone and algebraic multi-grid equation solvers and the quadratic time differencing scheme were employed. Grid distribution and the level of convergence achieved could also cause the difference. Despite the total number of grid points employed in both studies being the same, it is possible that the grid distribution in the impeller and wall regions was not the same.

For a fully developed flow field, the flow pattern would only change if there was a change in one or more of the operating parameters. This type of change is not time dependent and is simply referred to as flow pattern change. It is apparent that the observation made by

Montante et al. (2001a) falls into the "flow pattern change" category, whereas that described by Campolo et al. (2003) could be described as flow field evolution. The flow field evolution is a transient flow pattern change, which has little or no practical relevance to most systems since, in practical applications, the flow field is fully developed after several impeller revolutions. However, it is relevant to simulation studies, especially in determining the end of a simulation run. Given the computational limitations in simulation methods, mixing may be studied with just a few impeller revolutions, therefore, it is important that the maximum number of time steps or impeller revolutions give a fully developed flow field. Subsequent work focuses on the change in flow pattern as opposed to the flow field evolution.

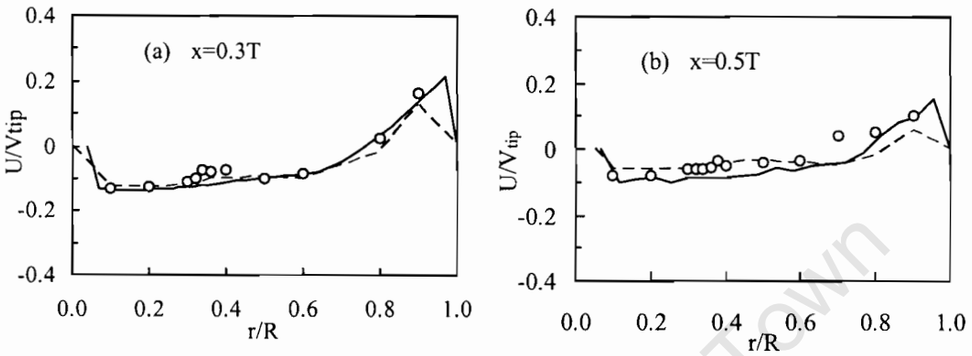

Figure 5.8. Comparison of experimental and simulation results for the axial velocity profiles: ——Present work; – – – Montante et al., 2001a; (o) Experiments.

Changes in flow patterns

Changes in flow patterns resulting from an interaction between the impeller pumping characteristics and the tank geometry were investigated with impeller clearances between 0.10T and 0.40T. Within the clearance range of 0.33T and 0.40T, there was a poorly defined flow pattern. The typical double loop flow pattern was obtained at a clearance of 0.33T, as shown in Figure 5.9. These circulation loops create undesirable regions of segregation in a mixing tank, which retard the mixing process. It is therefore necessary to reduce the number of these loops. Thus, the lower loop was suppressed by systematically decreasing the clearance from 0.33T to 0.15T (Figure 5.15), at which the bottom loop was severely suppressed and subsequently eliminated at a clearance less than 0.13T. Within the clearance range of 0.33T to 0.15T, there was also an increase in U in the region above the impeller. However, below the 0.15T clearance, there was a decrease in U in the region

above the impeller with a decrease in the clearance. The increase in the axial velocity component at a low clearance (C=0.15T) was not at the expense of the radial and/or tangential velocity components. This is due to the fact that there are different mechanisms that cause flow in the three dimensions. The driving force for the axial velocity component is the pressure field associated with blade shape, whilst the other two components are driven by the flow of the fluid along the rotating blade due to viscosity and drag (Ibrahim and Nienow, 1999).

For small clearances, the resistance due to the wall effect would result in a decrease in all velocity components. It was observed that, at the standard impeller clearance, the angle of the impeller discharge stream was slightly more than 90° with respect to the vertical axis. The angle increased with an increase in impeller clearance above 0.33T, but decreased with a decrease in the clearance. The decrease in the impeller discharge angle resulted in an axial impeller generated type of flow pattern, in which the lower loop was either suppressed or eliminated altogether. There was no observable change in the discharge angle for clearances less than 0.15T. An impeller discharge at a closer range to the tank bottom results in more destruction of the momentum of the reflected current by the incident one compared to that at the standard clearance. The results therefore indicate that a further decrease in the clearance (below 0.15T) to eliminate the lower loop would be counter-productive.

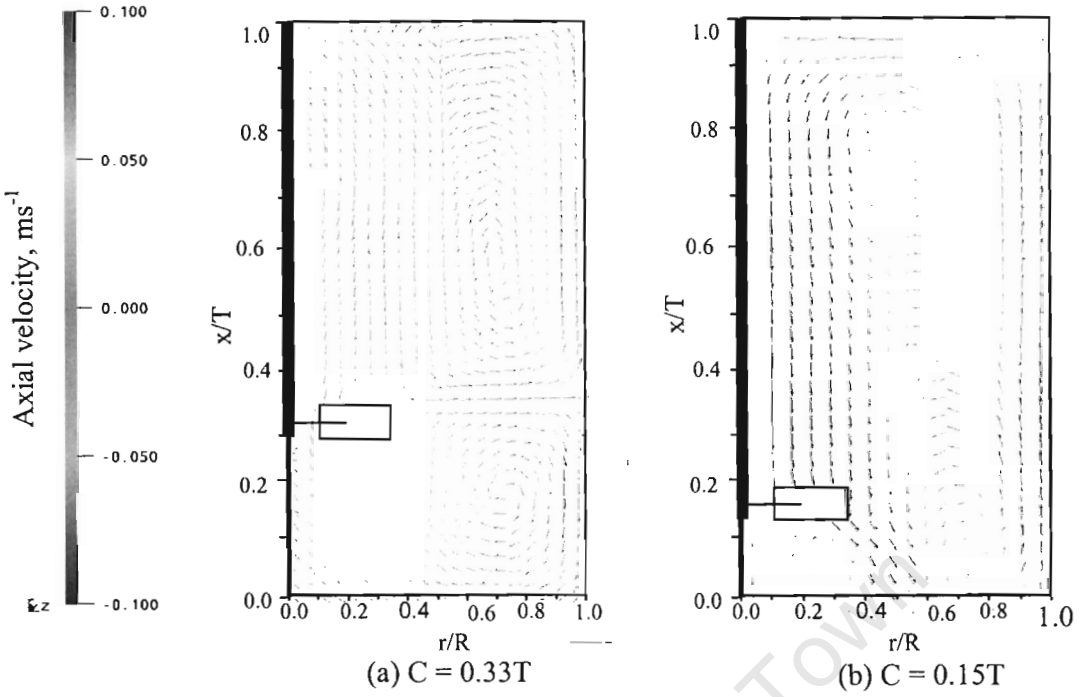

Figure 5.9. Vector plots of the axial velocity profile in the R33T and R15T configurations.

The mean axial velocity field was determined in the impeller region and in the region near the free surface. There was a better agreement between the simulation results of the axial velocity and the LDV measurements in the regions closer to the impeller ($x < 0.5T$), as shown in Figure 5.10. The k-ε model is known to give better predictions in highly turbulent flows, as typical of the impeller region. A general under-prediction in the regions away from the impeller, especially closer to the wall region, is shown in Figure 5.10. A similar observation has been reported for both the axial (Sahu et al., 1998; Nere et al., 2001) and the radial (Montante et al., 2001a) pumping impellers. In the wall region, the damping of the wall jet by the bulk fluid results in velocity decay.

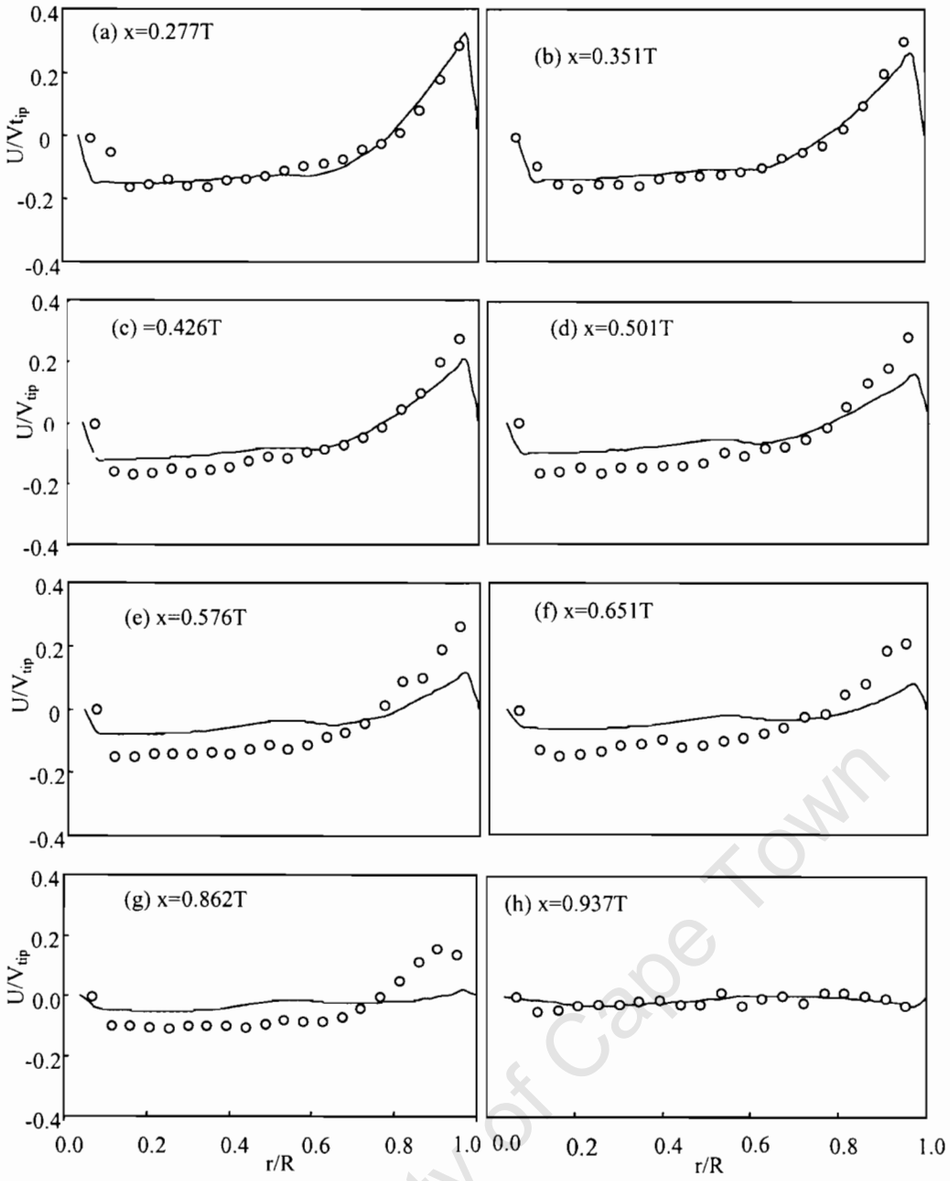

Figure 5.10. Axial velocity profile in the R15T configuration:
——Present work; (o) Experiment

An over-prediction of the velocity decay could be responsible for the under-prediction of U. It has been reported that the wall friction leads to rapid velocity decay due to the influence of the inner layer and the shear stress at the wall (Bittorf and Kresta, 2003). The influence of the wall friction may be minimal for a relatively small boundary layer, and in that case, the effect of wall baffles on the tangential velocity component (W) could be considered.

Additionally, the mismatch between the experimental and simulation results in the wall region could be attributed to the formation of small circulation loops at the junction of the baffles and the wall. The small circulation flows formed at the junction of the baffles and the tank wall are not well predicted by the *k*-ε model. It is therefore likely that the mismatch in the wall region could be as a result of the errors involved in the implementation of wall treatment algorithms (wall functions) and the anisotropic flows caused by the baffles.

5.2.2. Draft tube induced flow field

Draft tube diameter and clearance are the key design parameters for a draft tube mixing tank and were investigated using simulation and experimental methods. Different draft tube diameters were considered, of which the most well defined single circulation pattern was obtained in Figure 5.11 with d = 0.7T. The typical design of a draft tube reactor is that the draft tube cross-sectional area is equal to that of the annulus. For these two cross-sectional areas to be equal, the diameter of the draft tube must be equal to 0.701T. The CFD vector plot result in Figure 5.11 is in agreement with this. A draft tube of this diameter that is centrally positioned in the tank can be very conveniently defined on the stationary frame of the MFR or SG. For a draft tube diameter smaller than this, the superficial velocity was higher in the draft tube than in the annulus, and this resulted in a poor flow pattern, forming a double loop in the annulus when the draft tube diameter was less than 0.4T. The small diameter caused a double loop flow pattern similar to that generated by the Rushton turbine located at the standard clearance. The other problem associated with a small draft tube diameter is that the resulting pressure difference between the annulus and draft tube causes more air to be drawn from the surface, especially for an open-top tank. This reduces the efficiency of the impeller, which has to overcome the pressure build up in the annulus. However, for processes that require surface aeration like nickel reduction by hydrogen (Willis and Essen, 2000), a draft tube with a smaller cross sectional area than that of the annulus may be used. In that case, the draft tube diameter is expected to depend on a number of factors, such as the number of impellers used (if more than one), the performance characteristics of the impellers and the required impeller tip speed.

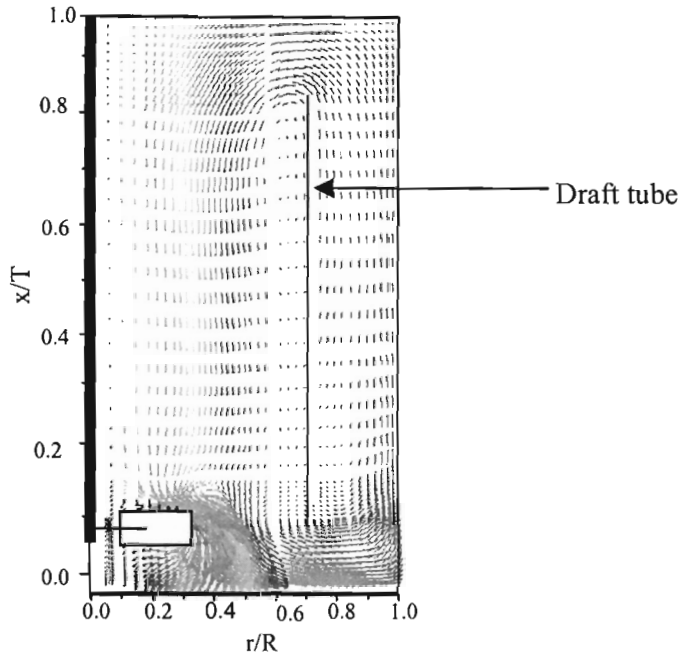

Figure 5.11. Vector plots of the axial velocity profile in the R15T-DT configuration.

From a simulation point of view, the radial location of the draft tube walls must be carefully considered for a model in which the MFR or SG approach is employed. The draft tube wall should neither coincide with the interface, between the rotating and stationary frames, nor be too close (less than three cells away from the interface) to it. In the SG method, the mesh connectivity method is used across the interface between the rotating and stationary blocks, and this could be a source of local numerical errors, if the interface is in a region of high velocity gradient. For a smaller diameter draft tube, the interface must be located very close to the impeller tip in order to define the draft tube on the stationary frame. The impeller tip is in a region of high velocity gradient, and locating the interface in a region like that may lead to numerical errors due to the resulting turbulent anisotropy, which the k-ε turbulence model does not take into account. The problem has been minimized in the MFR approach by prescribing the optimal radial location of the interface as 0.585T (Luo et al., 1994).

Draft tube clearance was investigated only for $C < 0.33T$. A draft tube clearance less than 0.15T resulted in a high flow resistance due to the narrow gap created between the bottom wall and the edge of the draft tube. The advantage of a small clearance (0.15T) was the suppression of the lower loop, hence a reduction in the tendency for dead zones to form directly below the shaft. The best flow pattern was obtained with the draft tube clearance at

the level of the impeller disc. The effect of a small draft tube clearance from the liquid surface on the flow pattern was found to be similar to that of a small draft tube diameter, for which a high entrainment of air from the surface occurred. The top clearance was specified according to the impeller speed. Gas entrainment from the surface increased with an increase in the impeller speed. A large top clearance resulted in short circuiting of the flow. The top impeller clearance was therefore maintained in the range of range of 0.14T-0.4T, corresponding to impeller speeds of 200-500 rpm. In a baffled tank, the influence of the impeller on the flow field in the region closer to the liquid surface depends on the magnitude of the axial velocity component.

In Figure 5.12, the experimental data points are shown as lines for clarity of presentation. However, in the subsequent figures, data points are clearly shown. The purpose of the dotted line across (at $U/V_{tip} = 0$) is to aid visualization of the region in which there is an upward or a downward flow. Experimental results in Figure 5.12 show that the system with a draft tube (R15T-DT) gave the highest axial velocity for the corresponding points in the other configurations without a draft tube. The axial variation of the radial profile of U for the three configurations (R15T, R33T and R15T-DT) in Figure 5.12 shows a zero value of U at r=0.7R, which represents the position of the draft tube wall. In all the three configurations, the axial velocities were of comparable magnitude in the region closer to the impeller (Figure 5.12(a)-(d). However, the use of the draft tube resulted in more than 100% increase in the axial velocity in the regions further from the impeller (Figure 5.12(c) and (d)) in the axial direction. The results show that the axial velocities in R15T were either higher or of comparative magnitude to those in R33T. It can be seen in Figure 5.12(d) that, for R15T and R33T, there was a negative velocity in the region closer to the wall. This was an indication of a small secondary circulation loop in the top region closer to the surface. This was not the case with R15T-DT, in which the draft tube destroyed the loop.

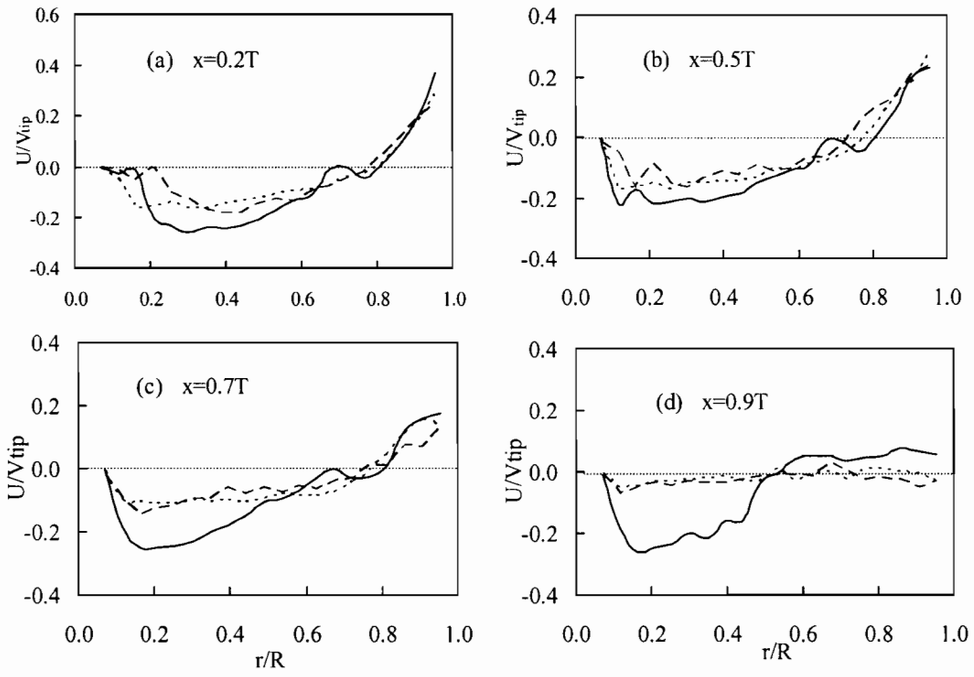

Figure 5.12. LDV measurements of the axial velocity profile at 300 rpm:
– – – R33T; ------R15T; —— R15T-DT.

Figure 5.13 shows a reasonable agreement between experimental and simulation results for the R15T-DT configuration. The prediction trend was similar to that for a system without a draft tube, where better predictions were obtained in the impeller region. There was a consistent mismatch between the experimental and simulation results in the annulus. Wall influence on the flow is expected to be highest in the annulus, and this is likely to result in a worse prediction by the k-ε model in R15T-DT than R15T. The small circulation loops at the tank wall and baffle junctions were suppressed or completely eliminated in R15T-DT compared to R15T. In contrast to the wall effect, the elimination of the circulation loops should result in a better prediction in the wall region for R15T-DT than R15T. An attempt to improve the prediction in the annulus by using the shear stress transport (SST) turbulence model did not improve the results. Both simulation and experimental results of the axial velocity in the annulus were positive up to the last data point closest to the wall. This shows that the draft tube reduced or eliminated the loops resulting from the instabilities due to the interaction between the single loop (obtained with a low clearance) and the free surface. A clearance in the range of 0.13T to 0.165T gave a single loop flow pattern in R15T-DT. Within the clearance range of 0.165T to 0.22T, the flow pattern could be either a single or a

double loop. However, with the use of the draft tube, a single loop was always obtained up to a clearance of 0.22T for the tank used in the present work.

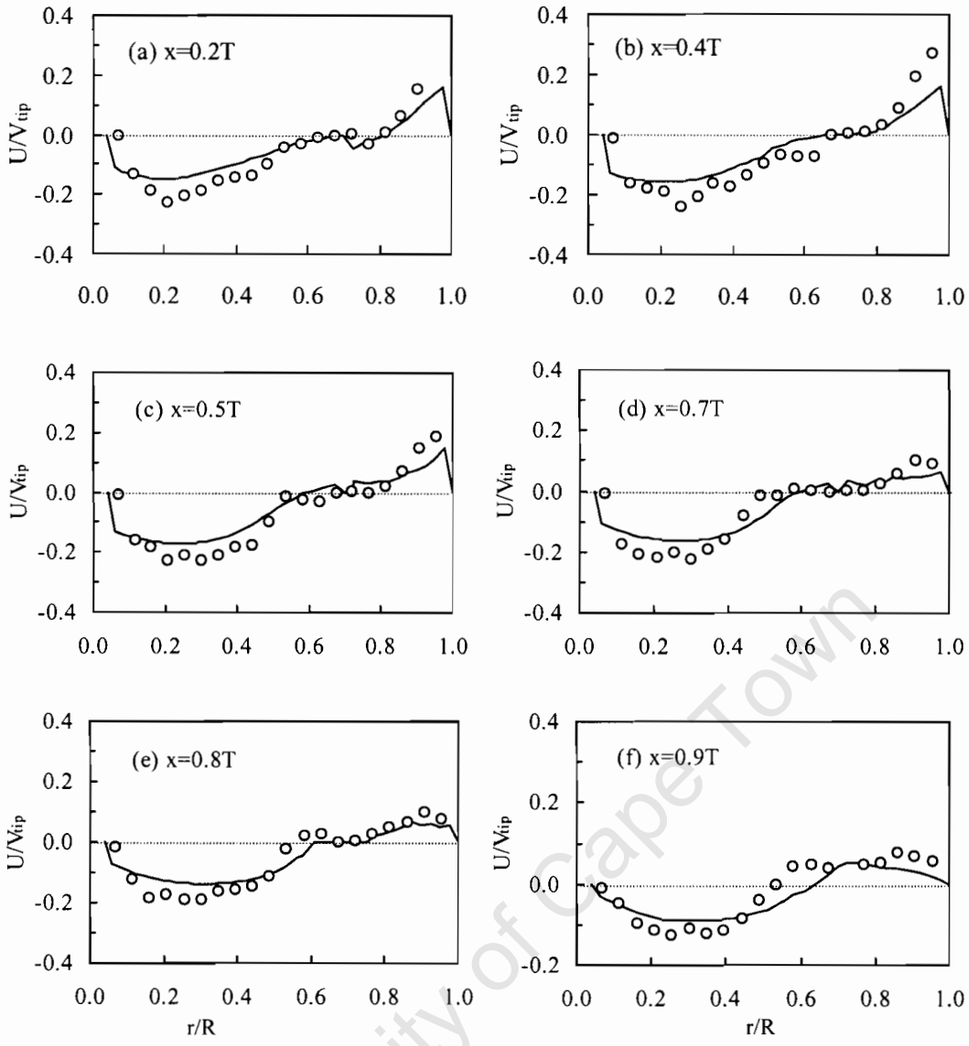

Figure 5.13. Radial profiles of the axial velocity for the R15T-DT configuration: — CFD; (o) Experiments.

The mismatch shown in the annulus for all axial locations in R15T-DT suggests that the errors arising from the wall effects dominated over the advantage of eliminating the circulation flows. It is evident from the flow pattern shown in Figure 5.9(a) that a draft tube will not improve mixing with the Rushton turbine at the standard clearance. The flow profile (vector plot) for R15T in Figure 5.9(b) shows an axial impeller type of flow pattern

reported by Montante et al. (2001a). This flow pattern in Figure 5.9(b) gives an indication of the radial point of minimum flow (loop centre) at which a draft tube can be located without interfering with the flow. It can be seen that the radial position of the draft tube could be in the range of 0.65R-0.80R. In a fully baffled tank fitted with a draft tube, the tangential and radial velocity components are constrained in the rest of the tank regions apart from the top and bottom regions of the draft tube. The prediction of these velocity components is given, and for the sake of brevity, only a few results are shown in Figure 5.14 for V, W and k.

There was a reasonable prediction of V, with a better prediction being in the impeller region than in the middle region as shown in Figure 5.14(a) and (b)). For W, the disagreement between the simulation and experimental results (Figure 5.14(c) and (d)) was higher than that for V. The turbulent kinetic energy was grossly under-predicted by up to 120% as shown in Figure 5.14(e) and (f). The causes of the poor prediction of W and k by the k-ε model have widely been discussed in literature (Lee and Yianneskis, 1998; Sahu et al., 1999; Ng et al., 1998). The experimental values of ε can be computed from the measured fluctuating velocities (u_i') and the approximated turbulent integral length scale (Λ). However, the calculation of Λ from the autocorrelation of the fluctuating velocity is only accurate when the value of u_i' is small in comparison to the mean velocity U ($U>>u_i'$) (Lee & Yianneskis, 1998). This condition is applicable for low Reynolds number flows, which is not the case in the present work. The alternative approximation of Λ from u_i' and impeller blade width (or $\Lambda = 0.1D$, Wu and Patterson, 1989) results in large under-prediction between experiments and simulation results as shown by Sahu et al. (1999) and Nere et al. (2001). It is unlikely that an accurate assessment of the simulated turbulent quantities against experimental ones can be obtained with this method.

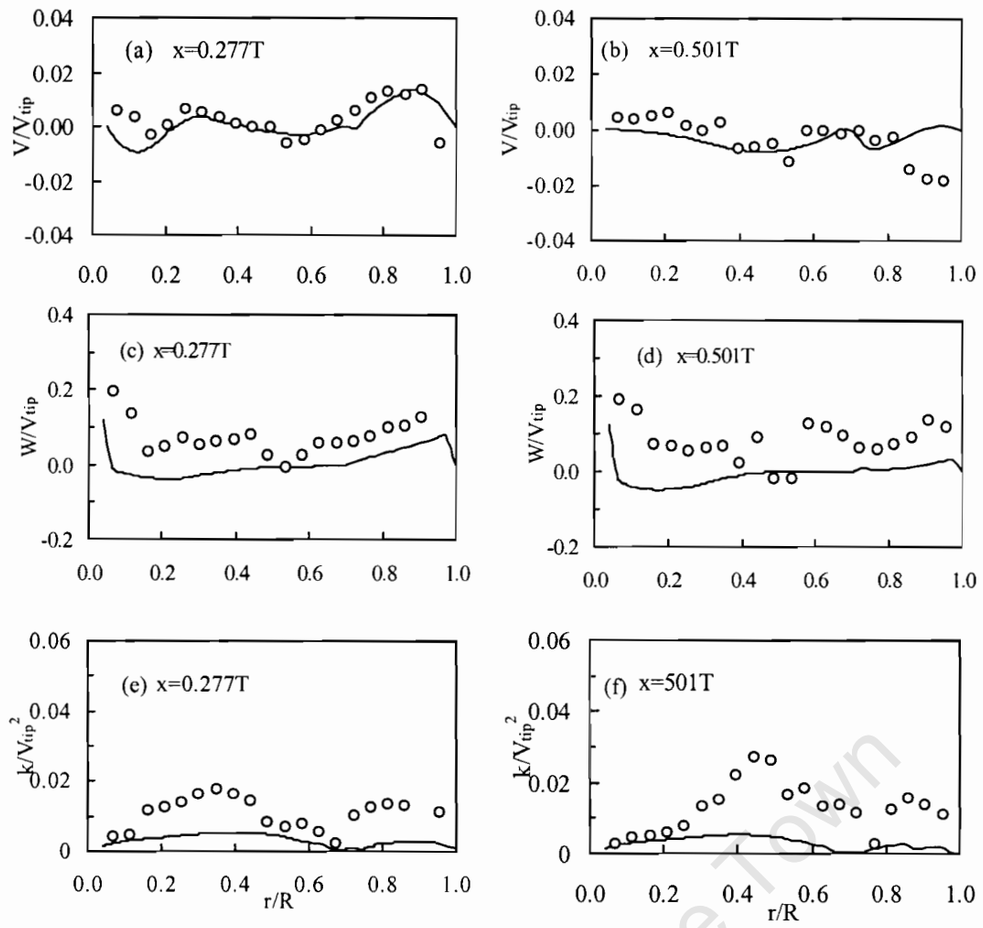

Figure 5.14. Mean velocities and turbulent profiles in the R15T-DT configuration: (a)-(b) Radial velocity; (c)-(d) Tangential velocity and (e)-(f) Turbulent kinetic energy;
——CFD; (o) Experiments.

On the one hand, there is an error involved in approximating Λ and on the other hand, the prediction of ε by the k-ε turbulence model is not accurate, especially in a stirred tank where the flow is anisotropic in certain regions. Figure 5.14 (e) and (f) show an under-estimation of the turbulent kinetic energy, which is as a result of the isotropic approximation of the turbulence by the k-ε model. This limitation of the k-ε model and the error associated with the approximation of Λ makes it difficult to obtain reasonable comparison of ε obtained by the two methods.

However, the simulation results by the *k*-ε model are acceptable for industrial applications. Also, for a given computational cost, there is no other turbulence model in the open literature that has been shown to provide results with the same level of accuracy as can be obtained with the *k*-ε model. This is the reason *k*-ε model has been used for many years and may only be replaced as computational cost reduces with further developments of computer technology.

5.2.3. Mixing time

A CFD simulation of mixing time was done by solving the scalar transport equation for a passive tracer, and for clarity, the response at only four points at different locations is shown in Figure 5.15. The legends represent the cell number in the respective coordinates. Thus, P-50-10-4 respresents a point that is 50, 10 and 4 cells in the axial, radial and tangential coordinates, respectively. The results in this figure indicate a damped semi-sinusoidal response of the tracer concentration at four separate detection points with a varying degree that depends on the distance from the impeller, below which the tracer was injected. It is shown in Figure 5.15 that the final mixing time (t_{90}) was independent of the point of detection.

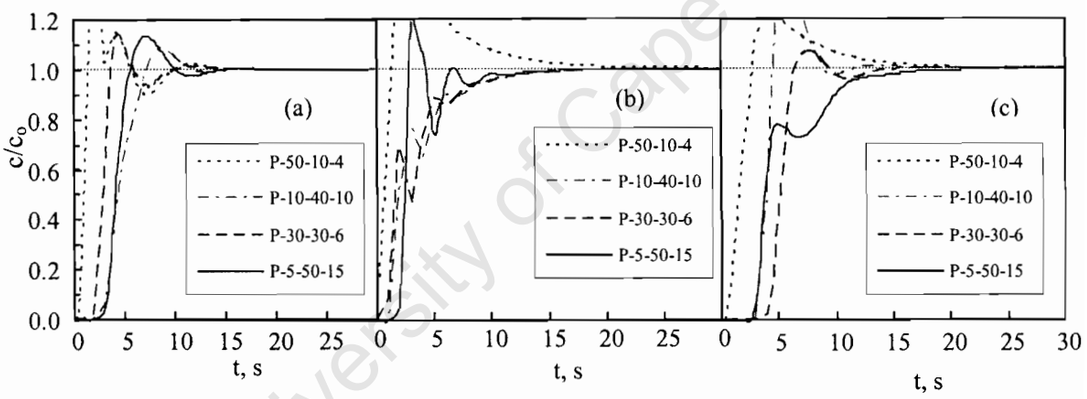

Figure 5.15. Mixing time (a) R33T (b) R15T (c) R15T-DT: Point P-50-10-4 is closest to the bottom; P-5-50-15 is closest to the surface and the other two are in the middle of the tank.

The trend of the tracer concentration variation was different to that expected from the idealized mixing decay model, upon which the Fassano and Penny (1991) mixing time

correlation is based. From the simulation results, the shortest mixing time was obtained with R15T-DT followed by R15T, with R33T giving the longest time. Mixing times were not affected by the time steps used (2.5 $x10^{-3}$ and 1.5 $x10^{-2}$ s). Figure 5.16 shows the snapshots of the tracer concentration taken at a plane mid-way between the baffles at different time intervals, in the R15T configuration. Initially, the tracer concentration was set to zero in all cells (Figure 5.16(a)), and Figure 5.16(b) shows the concentration after an injection time of 1 s, with complete homogenization (Figure 5.16(f)) being achieved after 30 s. The blue colour represents very low (<0.0001) tracer concentration and purple is the final tracer concentration.

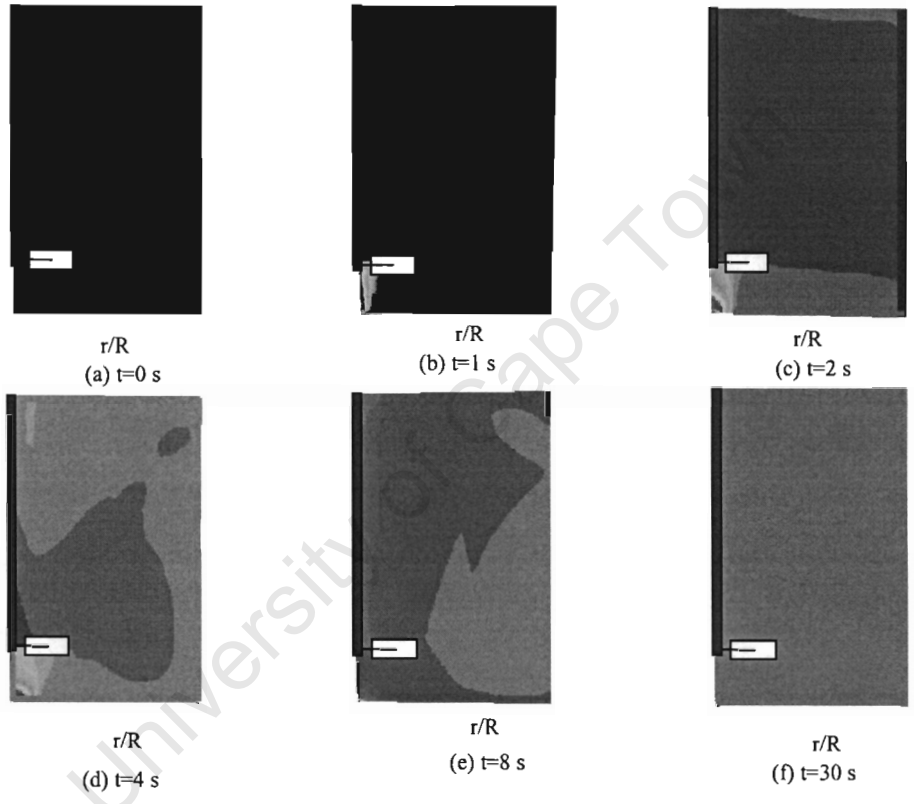

Figure 5.16. Snap-shots of the tracer concentration variation with mixing time.

The results in Figure 5.16 indicate that mixing intensity increased from the wall towards the centre of the tank and followed the same trend shown by the axial velocity component vector plots in Figure 5.11. This shows that U profile is an important indicator of the quality of mixing. The high axial velocity in the wall region represents a high fluid circulation,

which is more important than the pumping capacity, as has been suggested by Jaworski et al., (1996). This indicates that a deviation from the typical double loop, generated by the Rushton turbine, to single a loop flow pattern results in an increase in macro mixing.
There are three regions of interest in Figure 5.16(d); two of them are regions of low concentration (a larger one at the centre and a smaller one at the top right corner) and the third small region in the upper left corner next to the shaft. The larger and smaller regions of low concentration represent the centres of the larger and smaller loops, respectively. The other small region of high concentration next to the shaft could represent the backward flow relative to the impeller motion.

The accurate prediction of the mixing time in a draft tube stirred tank requires careful attention due to some model limitations. The top and bottom regions of the draft tube are invariably zones of high velocity gradient and consequently high tracer concentration excursions. A fine grid is therefore necessary in these regions for a more accurate computation of the flow field. Finer grids result in a higher percentage of cells with nodes closest to the wall lying in the wall boundary layer restricted by the k-ε model. The isotropic approximation of turbulence, on which the k-ε model is based, precludes calculation in the near-wall region where anisotropy is known to be highest. The standard wall function is valid if the first nodal point adjacent to the wall is within the log-law region of the turbulent boundary layer. This ensures that the dimensionless boundary layer length scale (y^+) is in the range of 30-500. Failure to meet this condition resulted in either a very long simulation time or non-convergence of the solution. A possible way out of this would be to use coarser grids in the regions on the opposite sides of the draft tube walls. This, too, may result in numerical diffusion. An accurate prediction of the mixing time in a system like this is still limited by the computational cost.

In some more recent CFD codes such as CFX5.6, the restrictions on calculations in the wall region are more relaxed. However, the work in this section was completed before the CFX5.6 code was available. Given the long simulation time required for mixing time studies, even with the k-ε model, the application of models like Reynolds Stress Model (RSM) and large eddy simulation (LES) with fine grids to calculate mixing time were precluded in this work. With the improved computer technology in the recent past, RSM

and LES are already being successfully implemented in single phase systems. Employing LES or RSM with fine grids improves the resolution of the local velocity gradients, which influence the effective diffusivity in turbulent flow. LES methods have been shown to improve prediction of the flow field and mixing time predictions (Derksen, 1999; Yeoh et al., 2005) compared to the RANS based models.

A comparison of both experimental and simulation mixing time results for the present work with experimental data reported by Kraume and Zehner (2001) (Table 5.2) shows that there is a fair agreement between the present CFD simulation results and the experimental ones reported by Kraume and Zehner (2001), as well as with those given by the Fasano and Penny (1991) model. Experimental values of mixing times vary greatly in the literature. The possible causes for such discrepancies are the probe size (Bouaifi and Roustan, 2001), response time of the meter and the injection and detection points. Guillard and Tragardh (2003) found that a shorter mixing time could be obtained with the top injection as compared with the bottom injection. However, even with the top injection, Otomo et al. (2003) obtained results which varied with radial location by as much as 100%. One of the possible reasons for the longer mixing time for the present work compared to that of Kraume and Zehner (2001) is that, in the present work, the tracer was added at the bottom whilst Kraume and Zehner (2001) added the tracer at the top. The bottom injection point was chosen due to the fact that it is typical to introduce a feed below the impeller; therefore, the introduction of the tracer at this location is more representative of the practical application. The position of the probe and the injection pipe with respect to the loop orientation has a significant influence on the contact probability between the tracer and the probe. From the simulation point of view, the over-prediction of the mixing time can be attributed to the fact that the k-ε model under-estimates the energy dissipation in the system.

Table 5.2. Experimental and simulation mixing times for R33T.

Method	V_{tip}, ms^{-1}	T, m	t_{95} (s)
Kraume and Zehner (2001) experiments	2.1	0.40	7
Present work, CFD	1.9	0.378	10
Fasano and Penny model (1991)	1.9	0.378	6

The fact that the R15T configuration gave a shorter mixing time than R33T is indicative of less axial mixing in R33T compared to the other two. This could be as a result of some of the tracer getting trapped in the lower loop as has been observed by Campolo et al. (2003) who used a Lagrangian scheme to study the flow characteristics above and below the impeller. The existence of toroidal segregation regions identified by Lamberto et al. (2001) can further explain this phenomenon. For a standard Rushton turbine configuration, Campolo et al. (2003) found that particles injected below the impeller could remain indefinitely trapped in the lower loop. It has been shown in section 5.2.1 that the lower loop was suppressed, almost to non-existence, in the R15T and R15T-DT configurations, and this was responsible for the improved mixing. Campolo et al. (2003) reported that mixing of the particles injected into the upper region was enhanced by the interaction of the free surface and the whirlpool-type vortex near the shaft (previously observed by Yianneskis et al. (1987)) rotating in the opposite direction with reference to the impeller blade.

The flow field evolution has an influence on the procedure for determining mixing time. In the CFD simulation, the tracer is typically introduced into a fully developed flow field obtained after several impeller revolutions. It is important therefore, that, for a consistent comparison of experimental and simulation results, the procedure should be the same for both the experimental and simulation methods.

5.2.4. Homogenization energy

Mixing performance of the Rushton turbine was further evaluated by investigating the influence of the mean specific kinetic energy dissipation rate and mean velocity field on mixing time and homogenization energy. The mean specific kinetic energy, $\bar{\varepsilon}$, was calculated from the power dissipated in the system for which the power numbers obtained from the CFD simulation were lower than the experimental values as shown in Table 5.3. The equation used to calculate these parameters are given in section 3.1. The highest power number, and consequently $\bar{\varepsilon}$, was obtained in the R33T configuration. Some of the energy in the 0.33T configuration is lost in the impeller region due to the flow interference between the upper and lower circulation loops. This explains the low value of $\bar{\varepsilon}$ in comparison to that of R15T and R15T-DT.

Energy dissipation

General information as to how much energy is dissipated per unit mass of liquid is given by $\bar{\varepsilon}$, but this does not give any indication as to how well distributed the kinetic energy is in the vessel. The local values of k and ε can be obtained by CFD simulation. However, the gross under-prediction of these parameters does not allow for reasonable quantitative computation of the homogenization energy to be obtained. For the evaluation of the performance of the different configurations, power was calculated from the torque on the baffles, from which $\bar{\varepsilon}_{CFD}$ was obtained. The homogenization energy (η) was therefore calculated from $\bar{\varepsilon}_{CFD}$, as opposed to local values of the same parameter. These parameters are given in Table 5.3. Configurations R15T and R15T-DT provide a better distribution of the energy compared to R33T, and this explains the shorter mixing time obtained with these two configurations. An improved distribution of the dissipated energy increases the intensity of the mixing.

Power dissipation in the R33T configuration was used as the basis upon which comparison of the power draw was made. Table 5.3 shows that reduced power consumption (ΔP) of 19.3% was obtained with R15T. The corresponding homogenization energy ($\Delta\eta$) were higher (25.9%). Similarly, the power savings obtained in R15T-DT was 33.3%, and this corresponds to an improvement of the homogenization energy by 44.4%. There was a higher percentage increase in the mixing efficiency compared to that of the power. This is due to the simultaneous shorter mixing time and lower power consumption for the lower impeller clearance configuration.

Table 5.3. CFD simulation of mixing time and homogenization energy (η) at N = 300 rpm

Configuration	t_{95}, s	N_p	P, W	$\bar{\varepsilon}$, m^2/s^3	η, m^2/s^2	ΔP, %	$\Delta\eta$, %
R33T	10.0	3.0	11.4	0.27	2.7	--	--
R15T	9.0	2.4	9.2	0.22	2.0	19.3	25.9
R15T-DT	8.5	2.0	7.6	0.18	1.5	33.3	44.4

Effect of the mean velocity field

The change in the flow pattern from single to double loop, which is due to the interaction between the impeller discharge stream and the bottom wall, is bound to affect the system hydrodynamics and mixing. The cause of the change in flow pattern is still not clear. However, it is thought that it could be due to a decrease in pressure difference between the front and back of the blades resulting from a reduction in the rate of rotation of the trailing vortex system (Ibrahim and Nienow, 1999). The one loop pattern, generated at a lower clearance, provides better mixing due to the reduced number of circulation loops, which cause long circulation times.

It has been shown in the previous sections (5.2.1 and 5.2.2) that U, V, W and k are generally under-predicted, resulting in under-prediction of the forces that govern the flow. Consequently, the intensity of macro-scale turbulence in the tank is under-predicted. This is responsible for the over-prediction of the mixing time and the under-prediction of the torques on the wall, and thus power numbers. A practical implication of this is that the under-prediction of the turbulence intensity in the tank may lead to over-design of stirred tanks. From a design point of view, it is important to consider the feed point in relation to the impeller clearance. A higher clearance is important for a feed point in the middle or upper part of the vessel, whilst feed introduced below the impeller can be better transported by the flow generated by the low clearance impeller. The application of this concept to a gas-liquid system, for example, is that, for systems in which surface aeration is important, a high impeller clearance would give better mixing. However, a low clearance impeller would be best suited for solid suspension. The other possible application is in a dual-impeller and draft-tube system in which the lower impeller is a Rushton turbine. There would be a loss in energy if the clearance of the lower impeller were 0.33T due to the fact that the upper impeller would first have to overcome the upward stream generated by the lower impeller before the downward fluid motion could be achieved in the draft tube.

5.2.5. Comparison of velocity profile in flat and elliptically bottomed tanks

A further comparison was made between the flow generated in the flat and elliptically bottomed tanks by the Rushton turbine at a clearance of 0.15T. The result of a simulation in a tank with the elliptical-bottom in Figure 5.17 shows a slight increase in the axial velocity

compared to the flat-bottomed tanks. This could be attributed to the elimination of the minor circulation loop at the bottom edge of the tank. These minor loops act as sinks for the momentum convective transport. In an elliptically bottomed tank, the downward impeller jet is smoothly deflected upwards rather than being partially damped as is the case in the flat-bottomed tank.

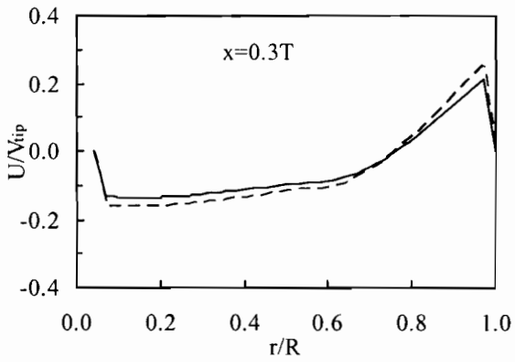

Figure 5.17. Comparison of the axial velocity profiles in flat and elliptically bottomed tanks: – – Elliptical; ——Flat

5.3. Flow field generated by the hydrofoil impeller (H15T)

The hydrofoil impeller has been employed in this section to investigate mixing and power in the elliptically bottomed tank. The flow generated by the Rushton turbine is the bench-mark for many hydrodynamic studies. The hydrofoil impeller, which can be viewed as a hybrid of the pitched blade impeller and the Rushton turbine is employed in the pilot scale nickel precipitation process, on which this work is based. The hydrodynamic features influencing the flow field, mixing time and homogenization energy were investigated. The hydrofoil impeller was used at a low clearance (C = 0.15T), and the flow generated at 300 rpm was compared with that of the Rushton turbine at the same conditions. The standard k-ε turbulence model was employed with three unstructured grid sizes; 108,000, 263,000 and 350,000 cells, in the modelled quarter tank. These grid sizes, hereafter referred to as coarse, base and fine respectively, were generated using the CFX5 code. Both the MFR and SG approaches and a blended advection scheme (ANSYS, 2005) were employed. An initial blend factor of 0.75 was used, and this was increased gradually as the simulation progressed to a quasi steady state. In order to improve the accuracy and ensure boundedness, the final results were obtained with a high-resolution scheme, as opposed to the blend factor of 1.

5.3.1. Mean velocity flow field

It has been shown in section 5.1.3 that the predictions of W and V were not as good as those of U. Further, there was a wider scatter of the experimental data obtained with the LDV for W and V than U. Similar trends have been reported by Nere et al. (2001) and Sahu et al. (1999). Therefore, U was chosen for further investigations (Figure 5.18) into the influence of the grid size and impeller model on the flow field. The results for V, W and k are given in Appendix II. The LDV measurements of the velocities in the bottom region of the tank showed broadly dispersed data, therefore only the data obtained as from the axial level of 0.2T are reported in Figure 5.18, in which the results obtained with different impeller models and grid sizes are compared. In general, a good agreement between simulation and experimental results for the axial velocity profile was obtained in a fully developed single-phase flow field. A comparison between the results obtained with the MFR and SG methods showed a better prediction with the SG method, especially in the impeller region where the intensity of turbulence was higher. This indicates that, in this region, the high level of turbulence resulting in temporal variations can better be accounted for by the fully predictive SG approach than the MFR one.

The predictions in Figure 5.18 are better than those in the previous sections (5.1 and 5.2), especially in the wall region. The improved prediction in the wall region could be attributed to the scalable wall function employed in CFX5, as opposed to the standard wall function that was used in the case of CFX4, in the previous sections. The prediction obtained by different grid sizes and different impeller modelling methods showed a marginal difference in most regions of the tank. The major difference can be seen in Figure 5.18(g) and (h), which shows that the direction of the upward current changed from the axial to radial and circumferential flow at approximately x = 0.8T. The turning point of this current was not well predicted by all methods shown in Figure 5.18. The flow in this region is influenced by the interaction between the free surface and the wall. Therefore, the prediction of the flow in this region depends on the treatment of the wall, free surface and the circulation flows. There was no apparent sensitivity of the simulation results in this region to the grid resolution in the range of the grid resolutions tested. The coarse grids gave an over-prediction of U with the MFR and SG methods. On the basis of the physics of the flow, in a given cell, a coarse grid captures fewer macro scale turbulent structures than a fine grid.

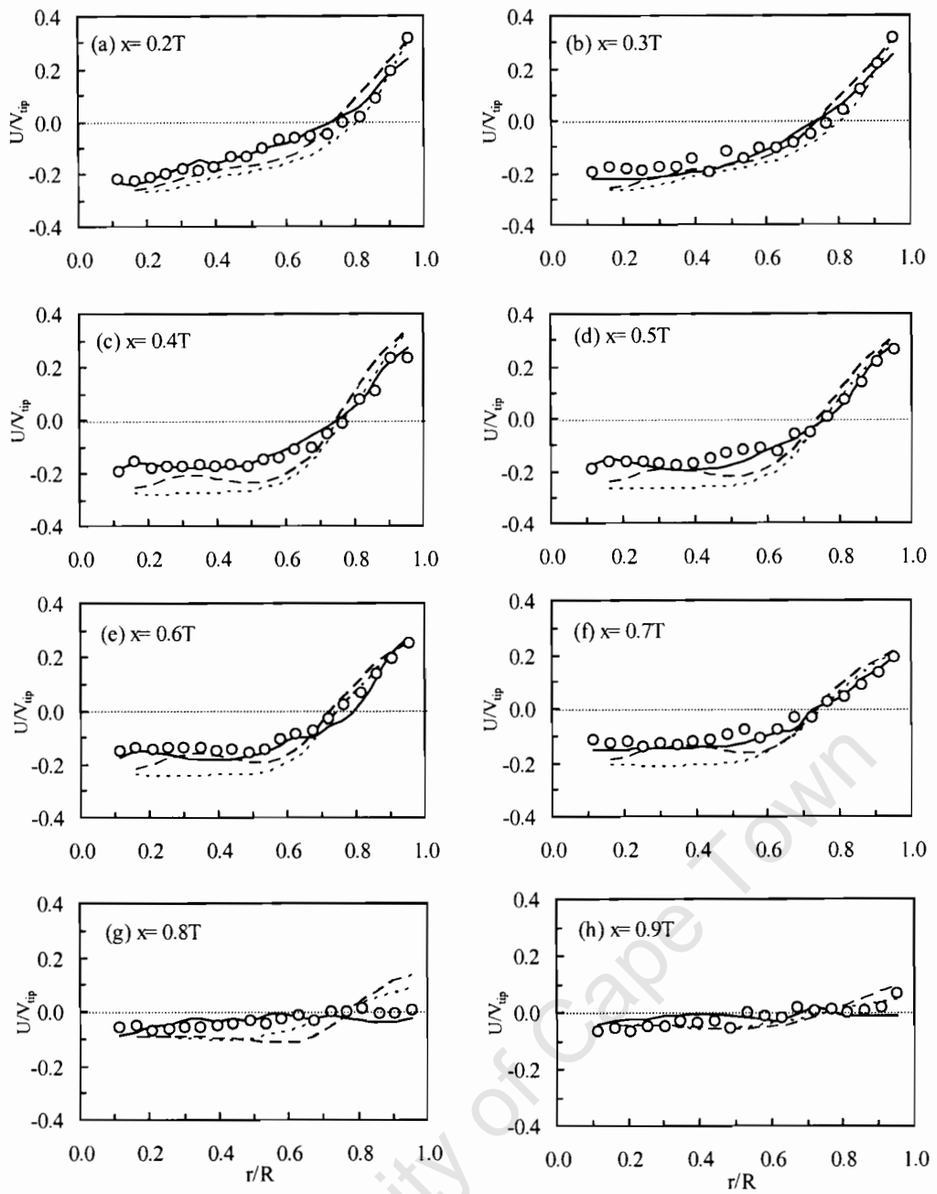

Figure 5.18. Axial velocity profile with different grid sizes and impeller models: – – – – Coarse-SG; -----Coarse-MFR; —— Base-SG; (o) Experiment.

These structures act as momentum sinks, and the fact that a coarse grid captures less of these could explain the over-prediction obtained with the coarse grid. From the numerical point of view, an increase in the cell size results in an increase in the cell Peclet number (Pe), which is the ratio of the convective flow to diffusion. An increase in the cell size has the same effect as an increase in velocity, which results in an increase in Pe. This may result in an

over-prediction of the mean flow obtained with the coarse grid in Figure 5.18. Also, by decreasing the cell size, the control volume decreases, and this results in an increase in the value of the diffusion conductance at the cell face, leading to a decrease in the cell Peclet number. This favours most discretizatization schemes, especially those, in which transportiveness (flow directionality) is not well accounted for.

There was a mismatch between experimental and simulation results at a radial distance of about 0.6T with the coarse grid but not the fine one. It should be noted that the interface between the stationary and the rotating frames was located at 0.585T. Therefore, the prediction results are indicative of the sensitivity of the interface to the grid resolution. The interface was at the cylindrical plane on which the interaction between the impeller and the baffle is minimum (Luo et al., 1994). However, a finer grid is expected to improve the accuracy of the results interpolated across the interface.

Grid resolution

In this work, the grid resolution was constrained by the available computational power to the three grid sizes tested. The sensitivity to the grid resolution was higher in the impeller region than in the wall region, with the results obtained with the base and fine grids being almost indistinguishable in the wall region ($r > 0.8R$). Despite the difference between the prediction with the base grid and with the fine grid in the impeller region, it has been seen in Figure 5.18 that the prediction with the base grid was good in this region. A grid resolution study shown in Figure 5.19 gave a difference of about 8% between the coarse and base grid. However, the difference between the base and fine grid at $x = 0.3T$, as shown in Figure 5.19, was marginal (less than 2%). Considering that the CPU time difference between the base grid and the fine grid was more than 18% (for a difference in simulation results of 2%), it was found to be more economical to adopt the base grid for further investigations. The subsequent simulations were therefore carried out with the base grid (corresponding to 1,052,000 cells in the full tank), with a maximum cell size of 0.5 cm.

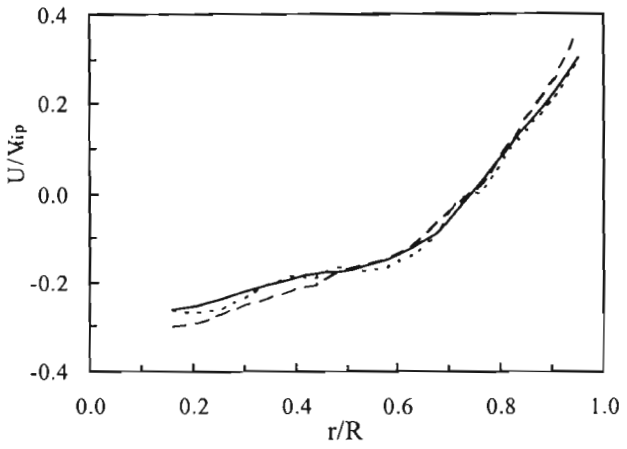

Figure 5.19. Grid independence evaluation with SG at x = 0.3T: —— Fine; ----- Base; – – – Coarse.

Axial velocity profile

In section 5.2, it was shown that a low impeller clearance enhances mixing in a Rushton turbine stirred tank. Figure 5.20 shows that, for the fully developed flow field at the low clearance, there was only one primary circulation loop.

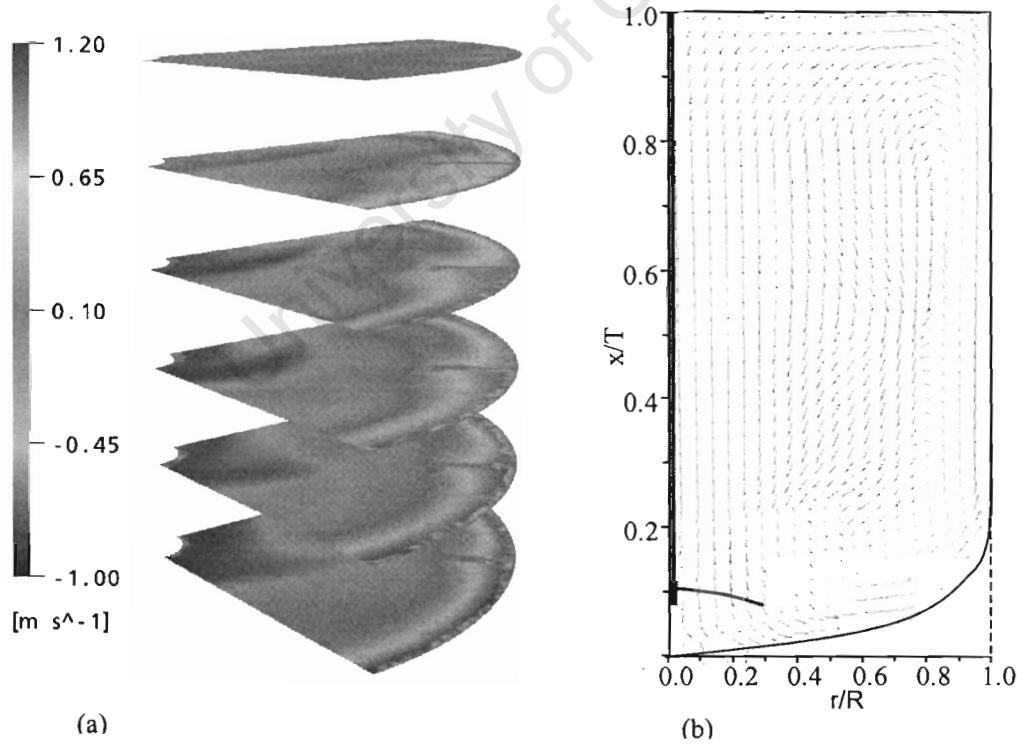

Figure 5.20. Fringe and vector plots of the axial velocity profile in the R15T configuration.

The secondary circulation loop that is typically found below the impellers at the standard clearance was completely suppressed due to the low impeller clearance and the tank bottom curvature used. The upward stream covered more than 90% of the liquid height, and this was indicative of a well mixed system with high circulation flow. Figure 5.20(a) shows the radial and azimuthal distributions of U, which appear to be confined to the wall as shown in Figure 5.20(b). This distribution could not be visualized in Figure 5.20(b) due to the fact that the plane on which the vector plots were obtained was located in the middle of two baffles. The top most and bottom most planes of the fringe plots in Figure 5.20(a) are at an axial distance of x = 0.95T and x = 0.2T, respectively. Closer to the baffles (near the junction of the baffles and the tank wall), there was a wider spread of U, which was as a result of the partial conversion of W into U by the baffles. In Figure 5.21, the profiles for U (right side plane) and *k* (left side plane) show a high axial velocity and turbulent kinetic energy in the impeller discharge region and along the wall.

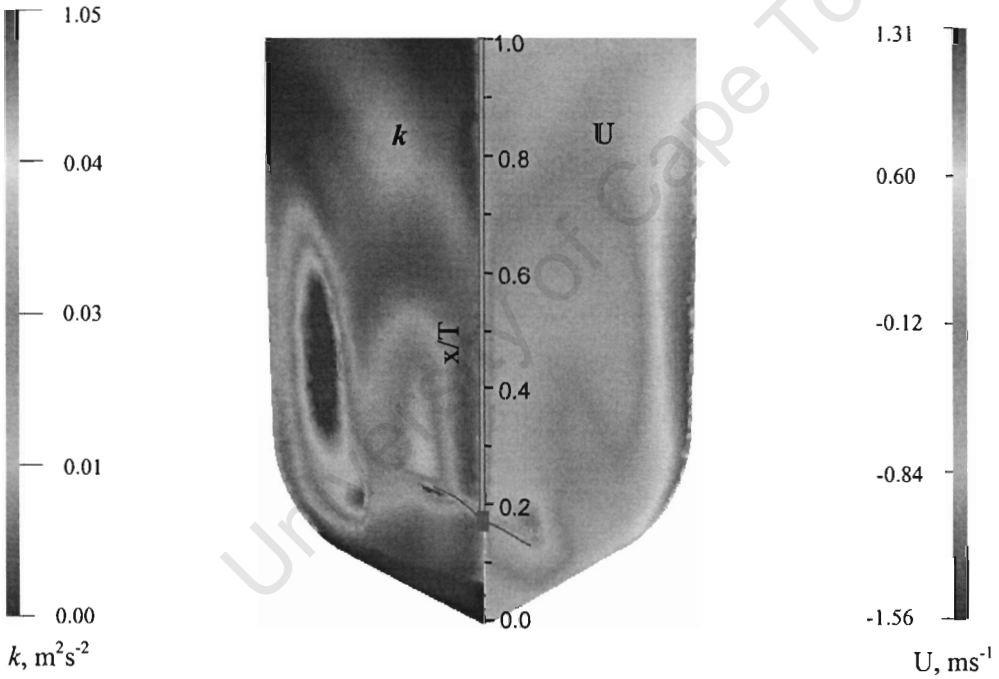

Figure 5.21. Flow field for the turbulent kinetic energy (left) and the axial velocity component (right).

The high axial velocity along the wall represents the wall jet, which decayed only minimally up to a height of x = 0.85T. Beyond this point, there was a rapid decay marked by the inner edge of the primary loop being at x = 0.9T, above which the flow was dominated by the

radial and tangential velocity components. The fringe plot for the turbulent kinetic energy in Figure 5.21 shows one region of high *k,* which was between x = 0.3T and x = 0.6T and another one around the impeller tip. The latter is a region of maximum for all the components of the fluctuating velocity, as shown later.

5.3.2. Turbulent field

The mismatch between the experimental and simulation results of the turbulence field can be attributed to the isotropic assumption in the *k*-ε model. It can be seen from the LDV measurements at three axial positions in Figure 5.22 that the three fluctuating velocity components are not the same in the entire tank volume. Further, all the fluctuating velocity components were highest in the impeller tip region, which is in agreement with the fringe plot for *k* in Figure 5.21. The turbulent kinetic energy dissipation rate was calculated from the experimentally determined velocity fluctuations by equation (3.20). A comparison between these results with the CFD ones obtained with the *k*-e model showed a severe disagreement in the entire tank as shown in Figure 5.23. This disagreement has been explained in section 5.2.2 and in the literature (Nere et al., 2001; Sahu et al., 1999 and 1998).

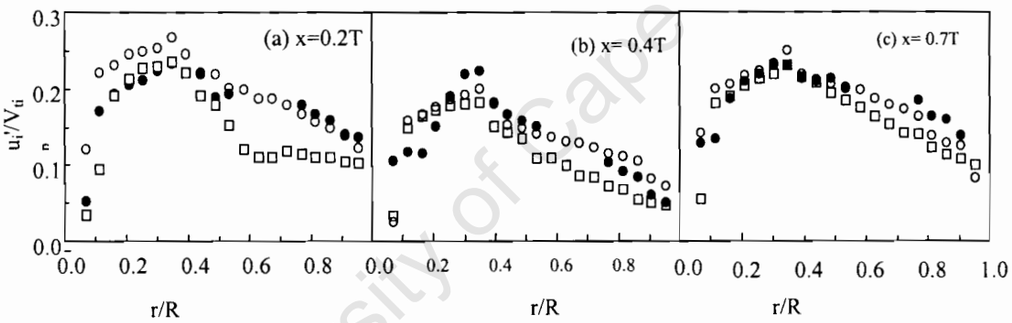

Figure 5.22. LDV radial profile of the fluctuating velocities: (o) u'; (•) v' and (□) w'.

5.4. Comparison of the mixing with H15T and R15T.

A comparison between the experimental results of the flows generated by H15T and R15T show that the most significant differences in the magnitude of the flows generated by the two impellers were in the wall and impeller regions. A line has been drawn at U = 0 in

Figure 5.24(g) and (h) to aid visualization of the direction of U in this region. It is shown that U tends to zero in the wall region, which is as a result of a change in the flow direction in the upper wall region. The axial point at which this change takes place depends on how far the wall jet penetrates into the bulk fluid, which is in turn influenced by the rate of the jet decay. It can be seen in Figure 5.24(g) and (h) that, for H15T, the axial velocity was positive in this region, which is an indication of a higher performance of H15T in generating axial flow in comparison to R15T.

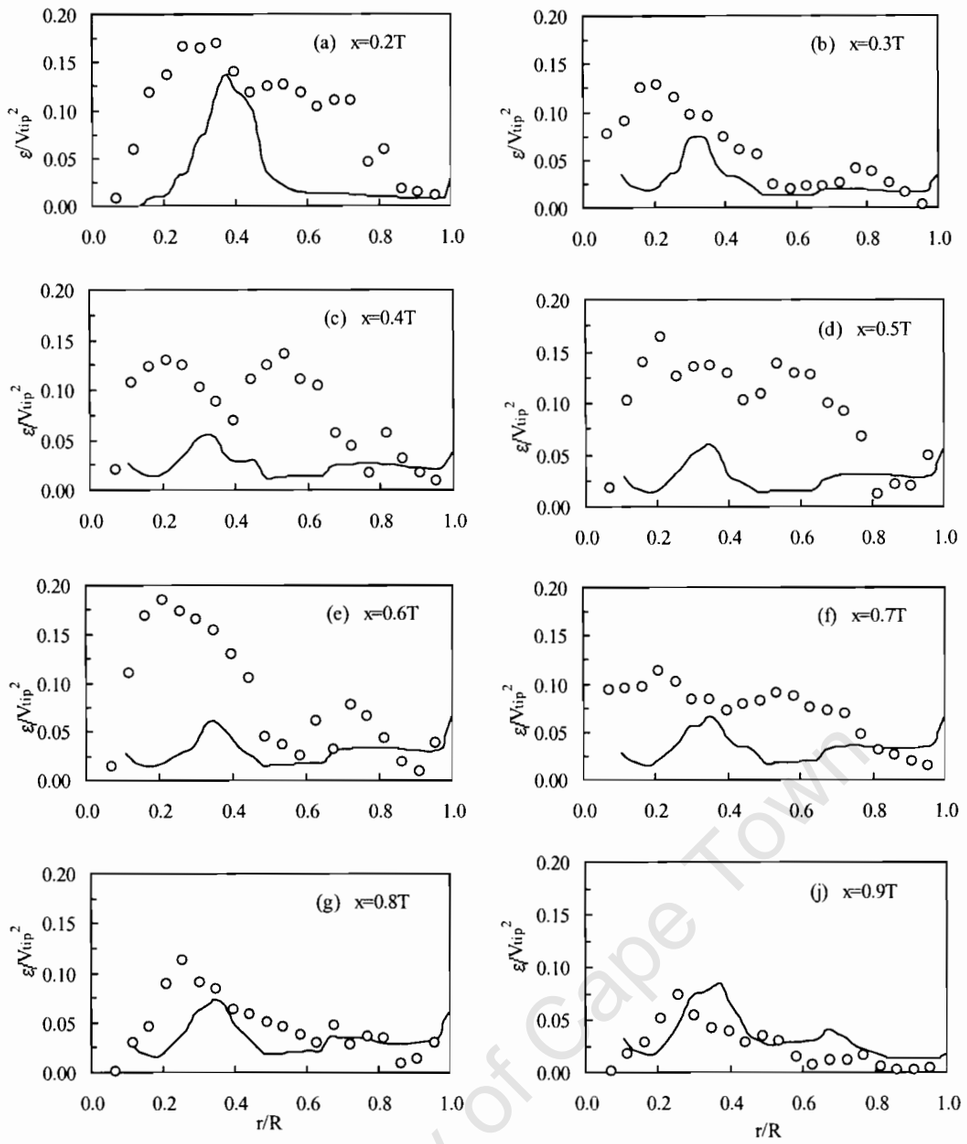

Figure 5.23. Radial profile of the turbulent kinetic energy dissipation rate:
(o) Experiments, —— CFD.

5.4.1. Flow field

Figure 5.24 shows that H15T generated a higher axial velocity than R15T, and the differences were more significant both in the impeller and wall regions. The maximum impeller and wall jet velocities were calculated for both R15T and H15T. The impeller jet was taken as the maximum downward velocity in the impeller discharge region ($r < 0.45R$), and for the wall jet, this was taken as the maximum velocity in the wall region ($r > 0.60R$).

The impeller jet velocity obtained with H15T was 21% higher than that obtained with R15T, and for the wall jet velocity, the same parameter was 51% higher with H15T. This indicates that, compared to H15T, a greater amount of the momentum generated by R15T was lost (or more energy was dissipated) in the lower region.

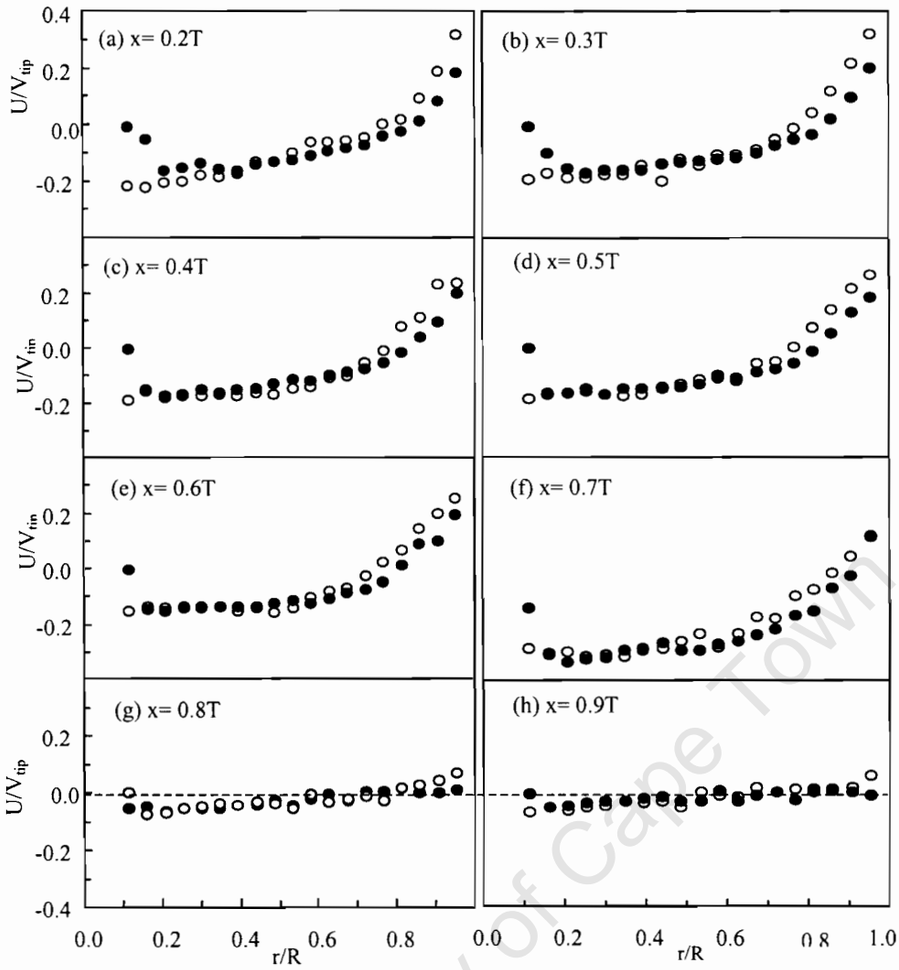

Figure 5.24. LDV measurement of the axial velocity profiles for R15T and H15T: (•) R15T; (o) H15T.

This shows that R15T may provide a better intensive mixing in the bottom region whilst H15T would provide a better overall macro mixing. Rielly and Marquies (2001) reported that the Rushton turbine provides better mixing in precipitation processes, in which micro-mixing is required. The velocities generated by both impellers were comparable in the middle of the tank radial distance. For systems in which reactions take place, a high circulation flow generated by H15T causes a distribution of the concentration gradient of the

reacting species, which is one of the driving forces for the rate of many chemical reactions. Even at a low clearance, R15T may not perform as well as H15T in systems that require high circulation, which leads to high macro mixing.

5.4.2. Mixing time

Mixing time required to achieve 90% homogenization was determined for both R15T and H15T, with the vertical dotted lines in Figure 5.25 showing the corresponding times at which this level of homogenization was achieved. The mixing simulation was initialized from a fully developed flow field obtained with the SG method, and all other mixing simulation strategies are as described in section 5.2. It is shown in Figure 5.25 that the hydrofoil impeller provided a shorter macro mixing time than the Rushton turbine (R15T): both being at an impeller clearance of 0.15T. Without the draft tube (DT), the mixing simulation results showed that it took 6.5 s and 6.0 s to achieve 90% homogenization in R15T and H15T configurations, respectively, whereas with the draft tube, the time was shorter: 5.0 s for R15T-DT and 4.3 s for H15T-DT. This indicates that a faster macro mixing can be achieved with H15T. This is consistent with the flow profiles in Figure 5.24, in which it was shown that the hydrofoil impeller generated a higher circulation flow than the Rushton turbine. Also, the flow numbers for these impellers were calculated as 0.78 for the R15T and 0.8 for H15T, which shows a comparative pumping capacity of these impellers at this clearance.

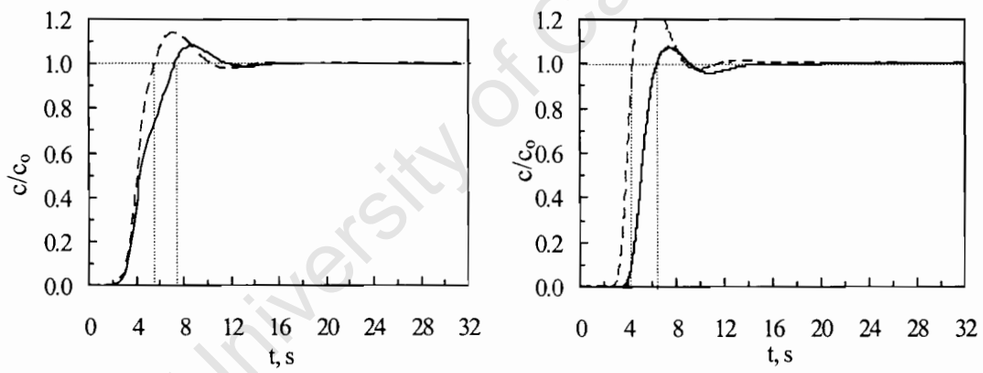

Figure 5.25. Comparison of mixing time with the Rushton turbine and hydrofoil impeller without and with DT: —— without DT;– – – with DT.

5.4.3. Homogenization energy simulation

Mixing efficiency was further evaluated by calculating the homogenization energy from the dimensionless mean kinetic energy dissipation rate, $\bar{\varepsilon}_{CFD}$. The torque on the wall baffles was used to calculate power, and this was in turn used to compute $\bar{\varepsilon}_{CFD}$ and the power numbers (N_p) in Table 5.4. The power number predictions obtained with this method were much closer to the experimental results than those obtained from the local simulation values of the turbulent kinetic energy dissipation rate. The power number for R15T was found to be 2.4 in the previous section but was 3.4, by the method employed in this section, against the experimental value of 3.8 (Montante et al., 1999). This represents a marked improvement (42%) in the simulation results, which can be attributed to a more refined grid and improved wall treatment in this case. However, the power numbers for R15T were still under-predicted by 14%. The under-prediction of the power number was due to the under-prediction of the torque, which is calculated from the azimuthal momentum component. An accurate computation of this momentum depends on W, which has been shown to be poorly predicted by the k-ε model.

It is apparent that $\bar{\varepsilon}_{CFD}$ for R15T was higher than that for H15T, which is due to the higher power number obtained with R15T. However, most of this energy was dissipated in the lower region of the tank as suggested by the results in Figure 5.24. The power numbers for the system with the draft tube were lower than those without. This is due to the fact that the draft tube enhances circulation, leading to a reduction in the azimuthal momentum, which is responsible for the torque on the baffles. The use of the draft tube resulted in a reduction in the homogenization energy by 19.2% and 17.7% for R15T and H15T, respectively. In a flow generated by H15T, there are relatively less circulation loops to be suppressed by a draft tube as compared to a flow generated by H15T. This could explain the slightly higher reduction of the homogenization energy in the flow generated by R15T compared to that for H15T.

Table 5.4 Mixing time and homogenization energy at 300 rpm.

Configuration	Nt_{90}	N_p	$\bar{\varepsilon}_{CFD}$, m^2s^{-3}	$\Delta\ \bar{\varepsilon}_{CFD}$, %
R15T	32.5	3.40	0.09	
R15T-DT	25.0	2.75	0.07	19.2
H15T	30.0	1.11	0.03	
H15T-DT	21.5	0.92	0.05	17.7

CHAPTER 6

6. Results and discussion II: Hydrodynamics of a solid-liquid system

It has been shown in section 5.4 that better mixing efficiency can be obtained at a clearance lower than the standard and that a more homogeneous mixing can be obtained with the hydrofoil impeller as compared to Rushton turbine. In this section, only the hydrofoil impeller (H15T) has been employed in a tank without a draft tube to investigate the off-bottom solids suspension and concentration distribution using both experimental and simulation methods.

The CFX5 code has been employed with the Eulerian approach, initially with the coarse, base and fine grids. The MFR approach was used to initialize the flow field and the final solution was obtained with the SG approach. The Gidaspow drag model was employed with the default values of the non-drag forces. The turbulence induced in the liquid phase by the particles was accounted for by the Sato model (Sato and Sekoguchi, 1975). The difference between the simulation results obtained with the base and fine grids was in the same order of magnitude as the single phase. The marginal difference in the results for these grids relative to the significant increase in the CPU time did not warrant the use of the fine grid. The subsequent simulations were therefore carried out with the base grid (corresponding to 263,000 in a quarter tank or 1,052,000 cells in the full tank), with maximum cell size of 0.5 cm. A good convergence ($<10^{-4}$) of the RMS residuals for the solids liquid system could generally be achieved with time steps of 2×10^{-3} s, and with maximum coefficient loops of at least 12. Gamwo et al. (2003) used a 2-D simulation of a three-phase system for which the grid size was given as 1.8 x 20 cm and a time step of 10^{-5} s. The present 3-D case, with a maximum cell size of 0.5 cm and minimum time step of 8.0×10^{-4} s, may be regarded as a larger time step with finer grid simulation, in comparison to that of Gamwo et al. (2003). The time steps were increased gradually up to a maximum of 8×10^{-2} s, when it was evident that a fully developed flow field had been attained. At the end of a simulation, the total mass of the solids in the domain was computed and compared with the quantity that was originally introduced into the domain, and it was found that the total mass remained the same. Further, it was ensured that the torque on the wall baffle was constant and the mass imbalance in all sub-domains was less than 1%.

The LDV method was used to validate the velocity field simulation results for the liquid-only system, after which, particles were introduced into the simulated system. The poly-disperse multiphase simulation approach was used to investigate the influence of the particle size distribution on the solids concentration distribution.

6.1. Solid-liquid mixing characteristics

Solids suspension depends on particle and fluid properties as well as the operating conditions such as the impeller speed. Dimensionless numbers can be used to give an indication of the response of the particles to the fluid flow. The response is characterized by mixing features such as off-bottom solids suspension and cloud height. These features determined the quality of mixing, which is constrained by power dissipated in the system. Some of the dimensionless numbers have been computed in this section and the CFD simulation methods have been developed to determine N_{js} and cloud height.

6.1.1. Dimensionless numbers

The particle Reynolds numbers (Re_p) shown in Table 6.1 were calculated from the experimental values of the particle terminal settling velocities (U_t) in a quiescent fluid. For the particle size range investigated, the Reynolds number was outside the range covered by the Stokes law ($Re_p < 1$).

Table 6.1. Particle flow properties and energy consumption for 5.1% (2 kg) solids loading.

d_p μm	N_{js}, rpm	Ar	P, W	ε, m^2s^{-3}	Re_p
75	435	41	16	0.42	2.36
100	461	98	18	0.50	4.46
300	461	781	30	0.81	7.78
400	608	6236	40	1.09	22.7
500	636	12205	49	1.31	52.6
750	694	41193	62	1.69	97.7
1000	730	97642	74	1.99	272

The SEM pictures in Figure 6.1 show that, in general, the particles were spherical, with a few irregularities shapes. The Archimedes number (Ar) for most particles was more than 100, indicating that, for such particles ($d_p > 100$ μm), the gravitational force dominated over the drag force (Mersmann et al., 1998).

For a given density, smaller particles will have lower values of Ar, which means that the drag force will be more important, and the terminal velocity, which depends on the gravitational force, will have less influence on the flow field. It has been reported (Mersmann et al., 1998) that homogeneity cannot be obtained if the gravitational force dominates significantly over the drag force, a condition indicated by $Ar > 10^2$.

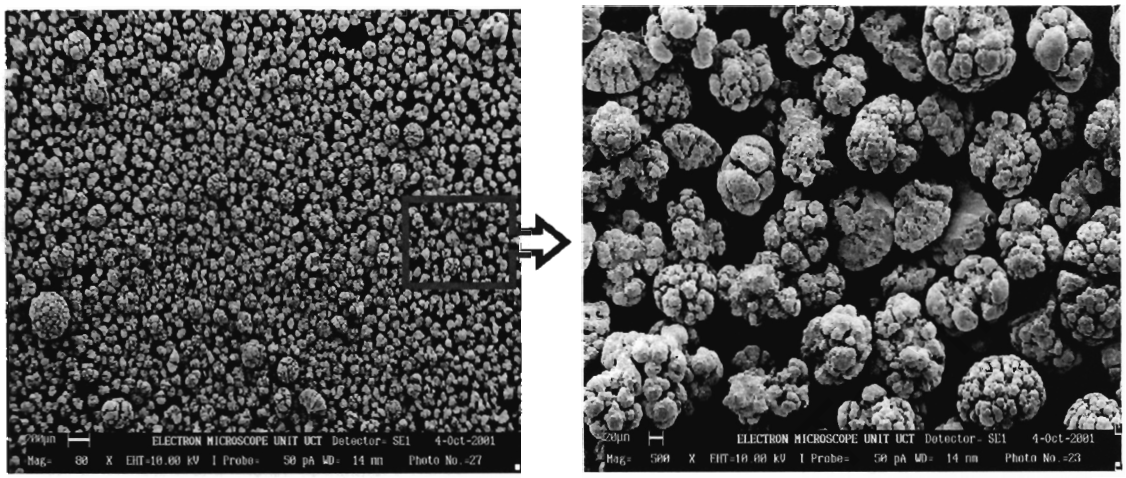

(a) (b)

Figure 6.1. Nickel particles SEM pictures: (a) Magnification=80x, (b) Magnification=200x.

6.1.2. Solid-velocity field

With the base grid, 40 days of CPU time was required to obtain a fully developed flow field. The discretization scheme with a blend factor of 1 showed some non-physical phenomena, where the highest solids concentration was in the liquid surface region. The variation of the solids concentration distribution with time is shown in Figure 6.2; from the initial condition (Figure 6.2(a)) up to the quasi steady state that was reached after 40 s (Figure 6.2(d)). There were voids behind the impeller blades, which represent the trailing vortices. In front of the blades there were small regions of high solids concentration.

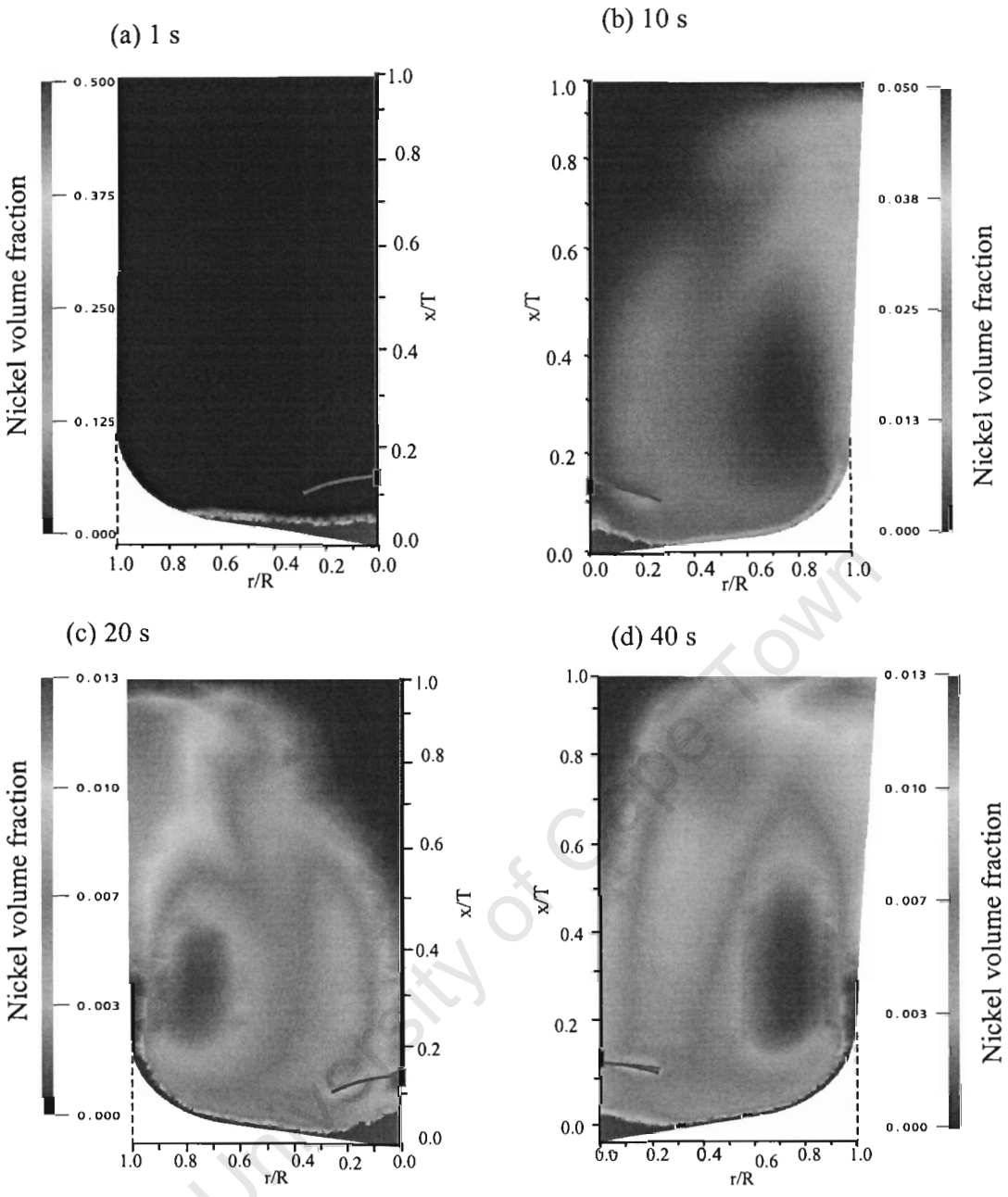

Figure 6.2. Fringe plots of the solids concentration profile for 1.3% Ni230.

6.1.3. Just off-bottom solids suspension

The simulation was initiated with particles settled at the bottom of the tank as shown in Figure 6.2(a) and the influence of the impeller clearance on the off-bottom solids suspension was investigated. The CFD simulation flow profiles showed that the angle of discharge (with reference to the vertical) increased with an increase in the clearance, and this explains the increased solids accumulation below the impeller with an increase in the impeller

clearance. As the clearance decreased, nickel particles moved from the bottom centre of the tank to the wall before being suspended by the wall jet. These results are not shown for the sake of brevity. A low clearance translates into a short path between the impeller blade tip and the tank bottom, and the turbulence decays along this path. A shorter path leads to the particles at the bottom experiencing both the effect of the turbulent dispersion and bulk flow mixing. This results in better mixing with a low clearance impeller. The 0.15T clearance was therefore adopted for further studies. This clearance is in the range ($C < 0.17T$) where the ratio of the local energy to the energy dissipated per unit mass of liquid is constant (Sharma and Shaikh, 2003). At this clearance, the quantity of the particles that settled below the shaft decreased with an increase in the impeller speed.

The maximum radius covered (r_m) was determined experimentally according to the method described in Chapter 4. For all the particle sizes studied, the r_m was found to be 0.25R for Ni230, Ni400 and Ni500 (Figure 6.3 (a)), and if the particles bottom coverage exceeded this radius, no particle motion was observable. The CFD simulations were run at the experimentally determined N_{js} with different particle sizes and loadings. The volume fraction at this radius, for different solid loadings at a constant particle size, and for different particle sizes at a constant loading, is given in Figure 6.3 (b). The data points shown in the figure represent snapshots of the concentration taken at r_m, and this concentration fluctuated with the passage of the impeller blades even after a pseudo steady state had been reached. The mean value for the volume fraction (v_{js}) for different particle sizes was found to be 0.4. This was the volume fraction at the maximum radius when the system was operating at N_{js}. The subsequent N_{js} values were obtained by starting with the solids settled at the bottom and increasing the impeller speed gradually until the volume fraction at the monitoring points defined at r_m stabilised at 0.4.

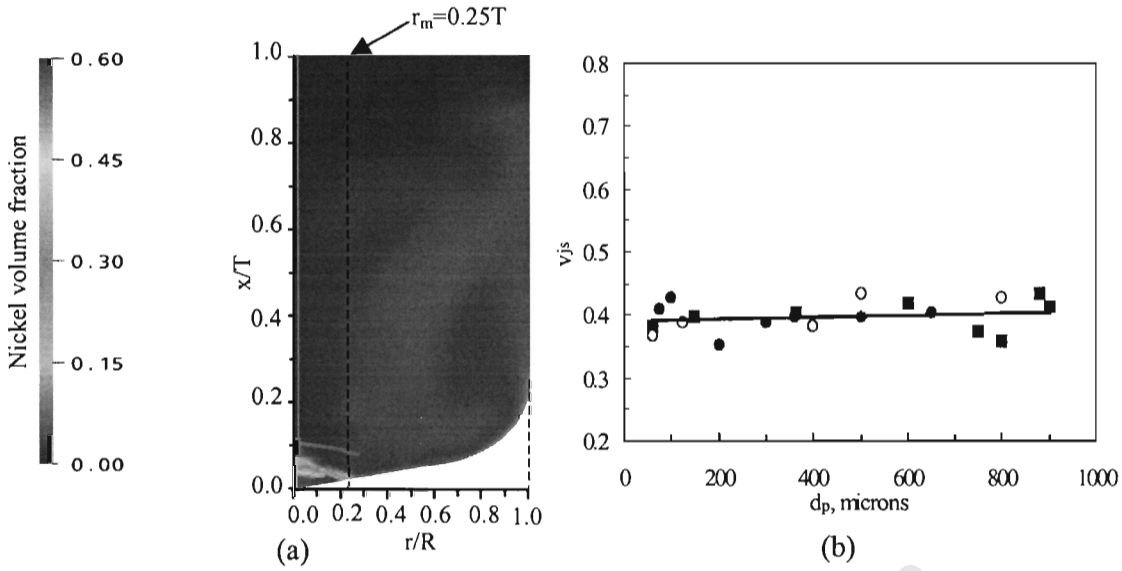

Figure 6.3. Determination of the maximum bottom radius covered at different loadings: (■) 6%, (o) 10%, (•) 20%.

The CFD simulation under-predicted N_{js} especially for the larger particles ($d_p > 150$ μm), as shown in Figure 6.4. This is in agreement with Kee and Tan (2002), who attributed this disparity to the assumption that the particles were spherical. The SEM analysis in Figure 6.1 shows that there were some particles with irregular shapes, resulting from either particle aggregation or breakage, and that the surface roughness increased with the particle size. The increase in the surface roughness could cause a decrease in the particle bulk density and a decrease in drag. An increase in surface roughness may result in an increase or a decrease in C_D, depending on the intensity of turbulence, which influences the relative magnitude of form and skin drags. Skin drag is caused by the flow resistance due to the boundary layer. Starting from a smooth surface, turbulence increases with an increase in surface roughness, and this leads to the boundary layer detachment point being pushed to the back of the particle in motion. This is a situation that is commonly encountered in free fall. In such a situation, a point is reached where a further increase in roughness results in an increase in C_D due to the resistance offered by the rough surface and an increase in the form drag. The form drag is caused by the pressure difference between the front and back side of the particle. This may result in an increase in C_D. However, Brucato et al. (1998a) reported that surface roughness did not influence C_D for the range of particles (2500 kgm^{-3} silica and glass) they investigated.

The r_m method provided a direct link between the experimental method, suggested by Rieger and Ditl (1994) for determining the N_{js} and a CFD simulation method. The error involved in the visual determination of the N_{js} increased with a decrease in particle size, and this agrees with Ibrahim and Nienow's (1999) experimental investigation. For the larger particles (d_p > 300 μm), both the Zwietering correlation and CFD simulations under-predicted N_{js}. The deviation from the experimental results for the Zwietering correlation and CFD simulation were 4% and 6%, respectively. It is evident that, in general, there was a better agreement between experimental results and those obtained with the Zwietering correlation. However, the CFD predictions were better than the latter for the smaller particles (d_p < 150 μm). Solids off-bottom lifting could be influenced by the velocity in the boundary layer. The fact that there was a reasonable prediction of N_{js} despite the boundary layer not being resolved shows that the influence of the boundary layer was not significant in this study. The determination of N_{js} by the CFD simulation method involves a tedious procedure that may only be employed in systems with small particles for which the Zwietering correlation does not give satisfactory results.

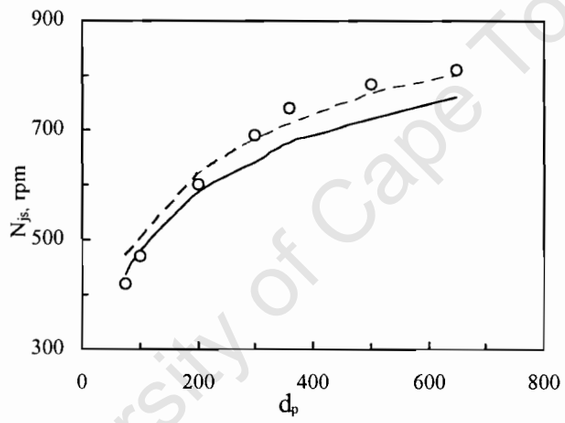

Figure 6.4. Variation of N_{js} with particle size at 20% Ni230 loading:
— CFD, (o) Experiments; – – – Zwietering.

6.1.4. Cloud height

The cloud height was identified by a point of highest curvature on the curve representing the variation of volume fraction with axial distance as described in Chapter 4. Both the OAT measurement and CFD simulation did not show the point of highest curvature for low solids

loadings (less than 2.0%), indicating complete solids suspension. The fact that no cloud height could be visualised with such a low loading is indicative of the relation between the point of highest curvature and the cloud height. Cloud heights determined by the visual method, despite being less precise, were consistent with those determined by both CFD and OAT. Rieger and Ditl (1994) evaluated different methods for determining the cloud height and concluded that the visual method is the best of all direct methods.

The cloud height of 0.9T was taken to represent 90% homogenization. The impeller speed (N_{js}) required to achieve just off-bottom solids suspension was more than that required for 90% homogenization (N_{90}), as shown in Figure 6.5. This is contrary to the expectation and can be attributed to factors such as the elliptical tank bottom and particle size difference. A significant quantity of the solids could well be suspended while some particles still remained stationary on the elliptical bottom for more than 1-2 s, leading to N_{js} being greater than N_{90}. Also, smaller particles are easily suspended to form a cloud at a speed insufficient to lift larger particles. The average difference between N_{js} and N_{90} was higher (about $N_{js}=1.5N_{90}$) at lower loadings (<6%). However, the gap narrowed with an increase in the solids loading, especially for Ni400, giving a minimum difference ($N_{js}=1.15N_{90}$) with 12% loading. The increase in the impeller speed with solids loading was as a result of an overall increase in the solids potential energy in the system, which had to be balanced by a higher liquid kinetic energy. Both N_{js} and N_{90} for Ni400 were higher than those for Ni230, which was due to the higher terminal velocity of Ni400. The fact that the gap between N_{js} and N_{90} was narrower for Ni400 than for Ni230 can be attributed to the higher inertial force of the larger particles. The solids suspension is achieved as a result of the kinetic energy possessed by the particles, and the loss in particle kinetic energy resulting from collisions of the larger particles is more than the corresponding value for the smaller particles. As the solids loading increases, the chances of collisions increase, resulting in more kinetic energy of the particles being transformed into potential energy. This requires an increase in liquid kinetic energy to maintain the balance, and this energy must be provided by an increased impeller speed, as shown in Figure 6.5b. Also, the decrease in the gradient of the N_{js} curves can be attributed to the increased loss in the kinetic energy due to an increase in the rate of collision.

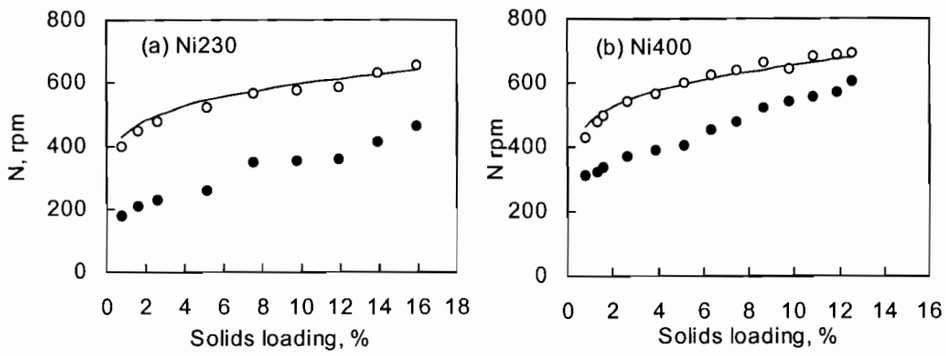

Figure 6.5. Effect of solids loading on N_{js} and N_{90}: (o) N_{js} experiments; — N_{js} model; (•) N_{90} experiments.

There was a rapid increase in the cloud height (h) with an increase in the impeller speed, as shown in Figure 6.6, and the increase was less steep above 500 rpm. More than 90% homogenization was obtained at 700 rpm with particle loading up to 14%. The empirical correlation for the cloud height (equation (3.14)) was fitted to the data obtained by LDV measurement and CFD simulation methods in order to obtain the empirical constants, and was then modified as:

$$h = \left(2.7 \frac{U_{core}}{V_{tip,js}} \right)^{0.6} \tag{6.1}$$

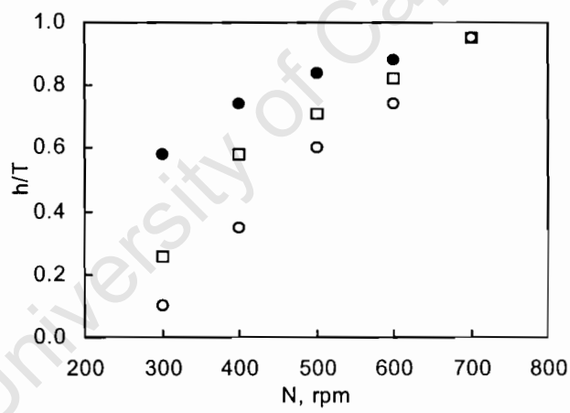

Figure 6.6. Variation of the experimentally determined cloud height with impeller speed for Ni230; (•) 5.1%; (□) 9.8%; (o) 14.0%.

The values of the two empirical constants in equation (6.1) are lower (2.7 and 0.6 for α_2 and κ, respectively) than those given by the Bittorf and Kresta (2003) correlation in equation (3.14) as 3.5 and 0.87 for α_2 and κ, respectively. This represents a scaling-down of the cloud height by equation (6.1). This can be attributed to the fact that the density of the particles employed in the Bittorf and Kresta's work was lower (2550 kg/m^3) than in this work (8903 kgm^{-3}). Once the particles have been lifted from the bottom, the suspension height decreases with an increase in the particle settling velocity. The scale-down of the cloud height by equation (6.1) as compared to equation (3.14) is therefore expected for the present system with high density particles. For a given U_{core}, there is an increase in wall decay with an increase in particle density. Consequently, the height at which the balance between the particle settling energy and the energy dissipated by the impeller (Mersmann et al., 1998) is reached is reduced. This view is supported by the fact that, for the liquid-only system, the empirical constants obtained in the present system were the same as those reported by Bittorf and Kresta (2003) in different systems. In Figure 6.7, the decrease in cloud height with an increase in the solids loading, at the corresponding N_{js}, was approximately linear.

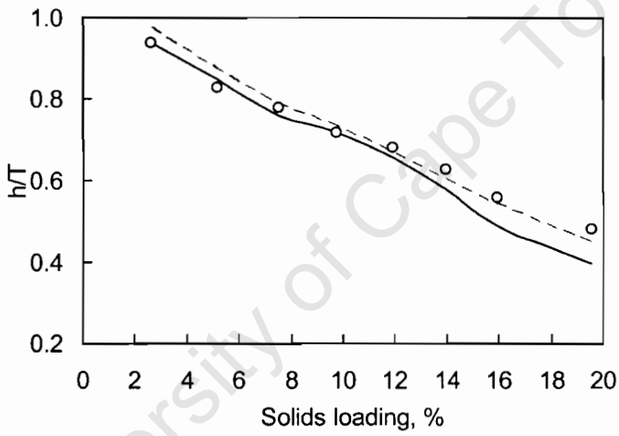

Figure 6.7. Variation of the cloud height with Ni230 loading at 500 rpm:

(o) Experiments; — CFD; – – – Equation (6.1).

The CFD prediction of the cloud height was in very good agreement with the experimental results up to 10% solids loading. There are many factors that could be responsible for the mismatch obtained at higher loadings, some of which can be attributed to the empirical

constants used in the formulation of the governing equations. Some of these constants, like those in the *k*-ε turbulence model, were determined in simple systems (Versteeg and Malalasekera, 1995) and may not be valid for systems with high solids loadings, for which the physics become more complex. Similarly, the drag models, non drag forces and solids pressure depend on a complex interaction of the reactor geometry and the scale of the turbulent eddies resulting from the effect of the solids loadings. In the RANS-based turbulence models, the influence of large eddies and macro-instabilities are not accounted for.

6.1.5. Power draw

Power consumption increased exponentially with the particle loading. All the three solids loadings considered in Figure 6.8 show the well known dependence of power on N^3. The power increased with N^{α} and the value of α varied with solids loading; $N^{2.97}$, $N^{2.98}$ and $N^{3.11}$ for 3%, 10% and 14%, respectively. The values of α generally agreed with the well known value (3.0). However, there was an increase in α by about 4.5% when the loading was increased from 3% to 14% loading. As a test case, the power prediction by the CFD simulation was computed, under the same conditions, from the torque on the baffles as 0.56 kW (for 10% loading), which is lower than the 0.66kW obtained experimentally. The under-prediction of the power is consistent with that of the N_{js}, which has been attributed to the particle shape. Even in the absence of solids, the CFD simulation has been shown (Ciofalo et al., 1996; Ochieng and Lewis, 2004) to under-predict power. The power consumed per unit mass and the levels of homogeneity achieved are both influenced by the hydrodynamic forces governing the flow. The relative influence of these forces on the solid suspension can be accounted for by the Archimedes number (Ar) (Barresi and Baldi, 1987).

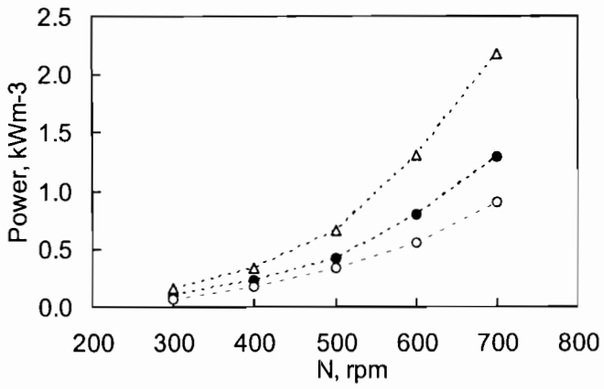

Figure 6.8. Variation of the CFD simulation power draw with impeller speed and particle loading for Ni230: (o) 3%; (•) 10%; (Δ) 14%.

The high value of Ar (> 100) was an indication that, in the present system, the gravitational force dominated over the drag force in accordance with the findings of Mersmann et al. (1998). These authors reported that, in such a system, it is not possible to achieve complete homogeneity, and both radial and axial concentration gradients exist. It is therefore important to obtain detailed information on the local solid solids concentration distribution, both in the radial and axial directions.

6.2. Solids concentration distribution

The influence of solids loading, particle size, simulation procedures and density on the mean velocity field, solids concentration distribution and slip velocity were investigated. The resulting mixing phenomena were explained using the solids suspension theories. Radial and axial solids concentration distributions were affected by the impeller speed, solids loading and particle size. Prediction of the solids suspension depends on the drag models, some of which have been investigated in this section.

6.2.1. Liquid axial velocity profile

The introduction of the solids into the system resulted in a decrease in the axial velocity component as shown in Figure 6.9. The greatest decrease for 0.54% and 1.33% loadings was in the wall region, where the decreases were 18%, and 50%, respectively. The decrease in the axial velocity in the wall region can be attributed to the interaction between the particles and the wall jet, which influences the axial solids distribution. Mersmann et al.

(1998) reported that a 0.1% solids volume fraction had a negligible influence on the liquid velocity flow field. However, in the present case, solids loading as low as 0.54% (equivalent to 0.06% volume fraction) had an influence on the liquid axial velocity, as shown in Figure 6.9. This can be attributed to the high density of the nickel particles used in the present study. The balance of forces of a particle and equal volume of liquid depends on both particle size and density. It is therefore apparent that the conclusion reported by Mersman and co-workers may be valid only for particles of the same density as the ones they used.

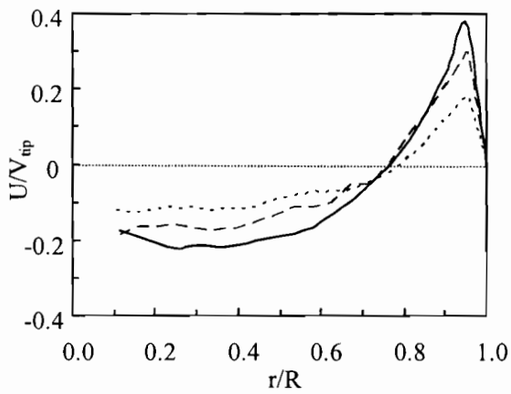

Figure 6.9. Effect of the solids loading on the axial velocity at x = 0.4T, N=300 rpm for Ni230: —— 0%; - - - 0.54%; ---1.33%.

6.2.2. Solids axial concentration with low solids loading (up to 1.33%)

Figure 6.10 shows that, for a dilute system of 0.1 kg loading (0.3%) of Ni230, complete homogeneity was achieved with an impeller speed at N_{js} (360 rpm), with a mean deviation of the simulation results from the OAT ones of 0.7%. This is a very good prediction. The concentration profile obtained in this dilute system showed a negligible axial solids concentration gradient, which is consistent with Montante et al. (2001b), who used similar experimental and simulation methods.

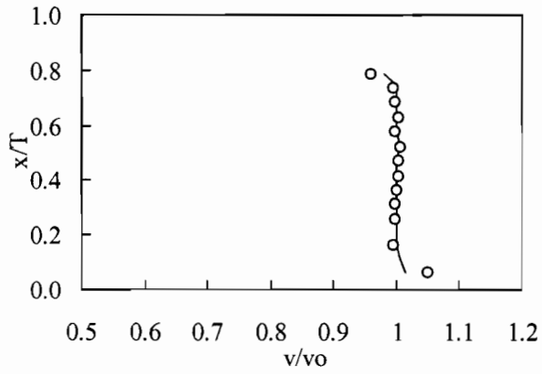

Figure 6.10. Axial concentration profile for 0.3% Ni230 at 360 rpm:

(o) Experiments; — CFD.

It is also important to note that, in the present work, the value of the drag coefficient (C_D) experimentally obtained in a still fluid, using the method described in section 4.1.6, was 2.4, which is of comparable magnitude to that (2.7) obtained by Montante et al. (2001b). It is expected that, in this work, the C_D would be smaller than the one obtained by Montante and co-workers given the higher density of the particles used in the present case. A more detailed investigation on C_D is presented in section 6.3.1.

At an increased solids loading of 1.33% Ni230, a steeper axial solids concentration gradient was obtained with the impeller speed at N_{js}. The mean deviation of the simulation results from the experimental ones were found to be 4.6% (Figure 6.11a) for Ni230 and 5.3% for Ni400 (Figure 6.11b). The most conspicuous feature in this figure is the occurrence of a maximum solids concentration, which was at x = 0.5T and x = 0.4T for Ni230 and Ni400, respectively.

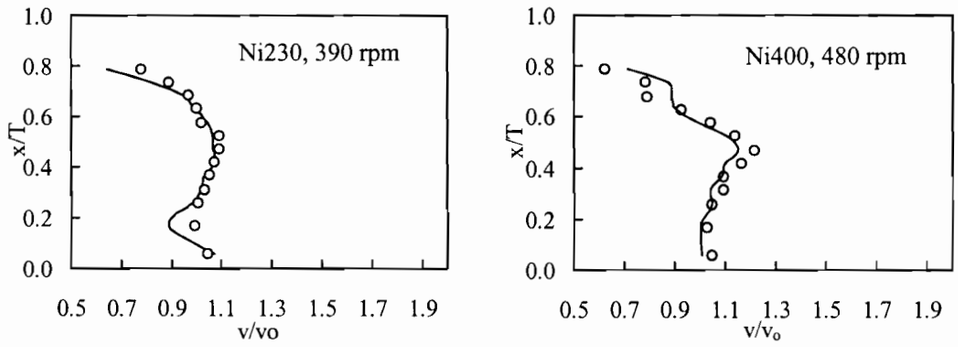

Figure 6.11. Axial concentration profile with 1.33% loading of Ni230 and Ni400: (o) Experiments; — CFD.

Figure 6.11 shows that an increase in the solids loading (mean concentration) and particle size results in an increase in the axial concentration gradient. For Ni230, the CFD simulation under-predicted the solids concentration in the entire tank volume. Similarly, for Ni400, under-prediction is observed in the lower 60% of the tank. This can be attributed to the influence of large eddies and macro-instabilities on the solids suspension. These turbulent structures do exist in reality and they affect mixing (Montes et al., 1997). However, they are not accounted for by the k-ε model employed in the present case. Furthermore, the turbulent kinetic energy (k) is known to be under-predicted by the k-ε model. Since the solids suspension increases with an increase in k (Caulet et al., 1996), the under-prediction of the volume fraction in Figure 6.11 is due to the under-prediction of k. This is compounded with other model limitations in accounting for factors such as particle-particle and particle-wall interactions.

The influence of the turbulent dispersion force on the solids concentration distribution was investigated with low solids loading. In all cases in Figure 6.10 and Figure 6.11, the accuracy of the final solids suspension simulations were not influenced by the value of the turbulent dispersion force, and this is in agreement with Montante et al. (2001b). However, when this force was set (in the solver), the CPU time required to achieve the pseudo steady state (homogeneous suspension) was shortened by 20%. For higher solids loadings (> 2%), the root mean square (RMS) residuals could not go below 10^{-4} if the turbulent dispersion force was not set.

A test case simulation with particles initially distributed uniformly in the domain and with different turbulent Schmidt numbers (implicitly changed through a user modifiable turbulent coefficient) showed neither a change in the CPU time nor the accuracy of the final results for low (1%) solids loading. This indicates that, in such a simulation set up, and with such a low solids loading, the influence of the turbulent dispersion force on the solids suspension is negligible. It is therefore apparent that, for low solids loadings, bulk fluid flow dominates over turbulent structures. A system like this can be scaled up on the basis of the impeller tip speed, which is in agreement with Montante et al. (2003).

However, the situation becomes more complex with increasing solids loading, as the suspension depends on whether the turbulent structures disperse the solids or the solids damp these structures. Whichever one of these two factors dominates depends on the intensity of the turbulence in relation to the damping effect of the solids on the fluctuating velocity, which defines the turbulent kinetic energy. In the range of operation in the present work, with a low impeller clearance (C = 0.15T), the results suggest that, for operations that require just off-bottom suspension, or for high solids loading, k is important. Mersmann et al. (1998) reported that the fluctuating velocity (u'), on which k depends, is necessary everywhere in the vessel for solids suspension, especially at the bottom of the tank, where particles tend to settle. In the region very close to the bottom, both mean and fluctuating velocities are zero, with the minimum value of u being just outside the boundary layer. According to Mersmann et al. (1998) the off-bottom lifting of particles is given by u'^4, and also depends on the minimum fluctuation velocity (u'_{min}). There is a decrease in u with an increase in distance away from the blade tip. Therefore, a decrease in the impeller clearance results in an increase in the value of u'_{min} available for solids lifting. Despite the fact that the boundary layer was not resolved in the present case, the influence of the dispersion force through u' could still influence off-bottom solids suspension in the region outside the boundary layer.

The impeller clearance used in the present work falls within the range (C < 0.17T), in which Sharma and Sheikh (2003) reported that the ratio of local energy to the energy dissipated per unit volume is constant. A possible application of this concept is that, for such systems, scale-up may be done on the basis of power per unit volume, which is proportional to the turbulent kinetic energy.

6.2.3. Effect of solids loading

The influence of the solids loading was investigated in Figure 6.12, with 5%, 10% and 18% solid loadings. The OAT data was not available for such high loadings due to the fact that the slurry could no longer allow light through. The impeller speed was constant throughout at N_{js} for the 10% solids loading. The deviation of v/v_o from unity increased with an increase in solids loading. One of the solids suspension theories is based on a balance between the potential energy of the particles and the liquid kinetic energy (Mersmann et al., 1998). On the basis of this theory, an increase in the solids loading results in an increase in the total potential energy in the tank. Therefore, the axial level at which the balance between the potential energy and the kinetic energy takes place decreases with an increase in the loading, as shown in Figure 6.12. This observation is expected if the particles in the simulation domain are mono-disperse. This theory is based on a global power balance in the system, which does not account for the spatial variations in solids concentration and particle size. It is a common practice to simulate mono-disperse particles. However, in reality, particle size distributions are more often encountered. It is therefore necessary to consider the influence of the particle size on the solids suspension.

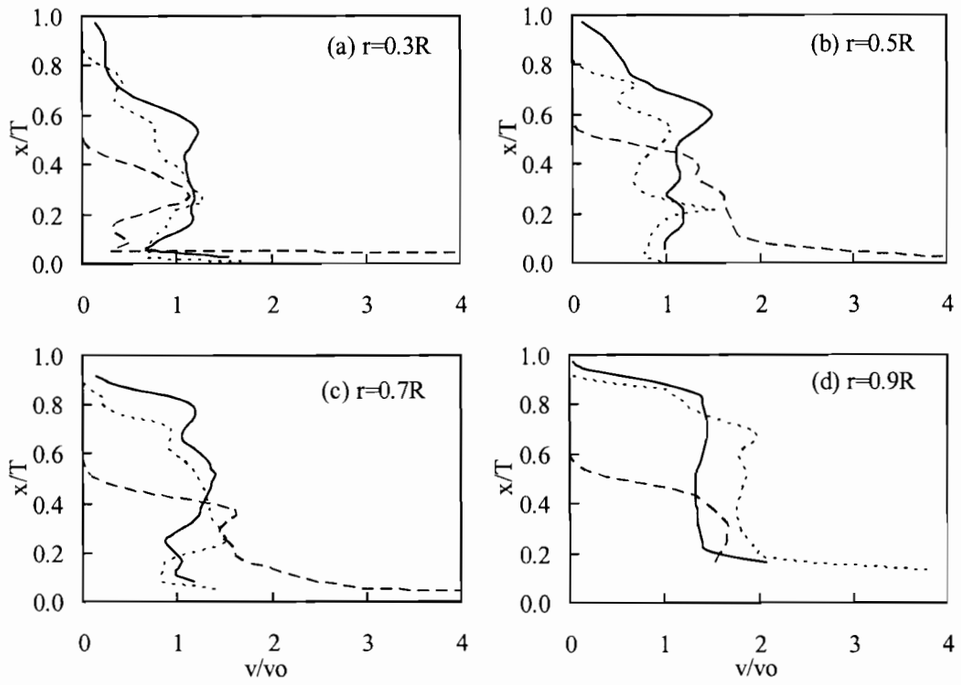

Figure 6.12. Effect of solids loading on the axial concentration profile of Ni230: — 5%; ------ 10%; - - - 18%.

6.2.4. Particle size effect

The mono- and poly-disperse multiphase simulation approaches were employed with three particle sizes to investigate the influence of the particle size on solids concentration distribution. The mono- and poly-disperse systems are denoted by S_I and S_{II}, respectively. The axial and radial solids concentration distributions were determined experimentally as described in Chapter 4.

Mono-disperse particles

The axial solids concentration profiles were determined at eight radial locations in the tank with three particle sizes. However, only results for the central location (r = 0.5R) are reported. A 10% loading of three mono-disperse particle sizes (Ni230, Ni400 and Ni750) were simulated separately at 250 rpm, 574 rpm and 700 rpm (Figure 6.13). The impeller speeds were chosen such that the 250 rpm was below N_{90} for all the particle sizes, 574 rpm was the N_{js} for the Ni230 and 700 rpm was above N_{js} for all the sizes at the loading

considered. At 250 rpm, the solids distribution was such that a very high proportion of the particles remained at the bottom of the tank, as this velocity was far below N_{js}. A reasonable suspension was achieved with an impeller speed of 574 rpm, reaching a cloud height of 0.92T, 0.66T and 0.50T for Ni230, Ni400 and Ni750, respectively. The normalized volume fraction (v/v_o) for all sizes deviated from unity for the greater part of the tank with an impeller speed of 574 rpm. An increase in the impeller speed from 574 rpm to 700 rpm, resulted in an increase in the axial level of the maximum solids concentration from 0.3T to 0.8T for the Ni400 case. At 700 rpm, there was a high homogeneity indicated by a very small (less than 8%) deviation of v/v_o from unity for all the three particle sizes. However, there was a well defined region of high concentration in the upper 20% of the tank.

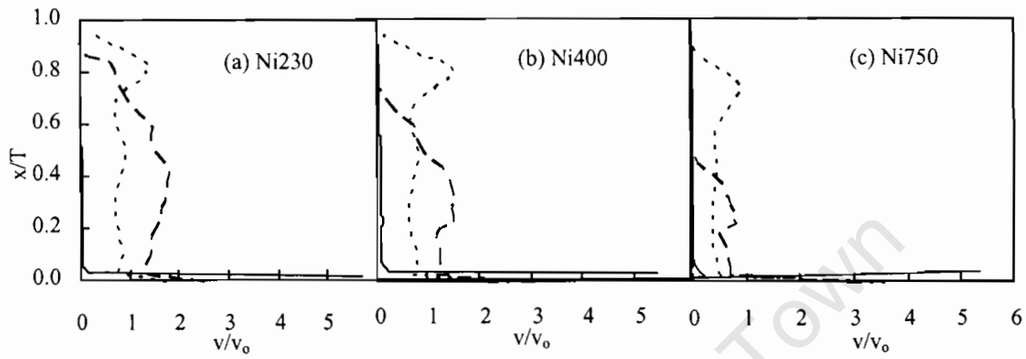

Figure 6.13. Variation of the axial solids volume fraction with impeller speed and particle size for 10% loading at r =0.5R; —— 250 rpm; – – – 574 rpm; ------ 700 rpm

The axial location of the point of maximum concentration decreased as the particle size increased; being at 0.88T, 0.8T and 0.74T for Ni230, Ni400 and Ni750, respectively. The disparity in the point of maximum concentration can be explained by the mechanisms that cause solids suspension. The potential energy of all the particle sizes in Figure 6.13 was the same (same mass), therefore, the theory that postulates that the solids suspension results from a balance between the suspension potential energy and kinetic energy cannot explain this disparity. Instead, the alternative theory by Mersmann et al. (1998) based on the assumption that the particles are suspended when there is a balance between the fluid upward velocity and particle settling velocity appears to be more applicable. Similarly, the disparity can be explained by the theory based on a balance between the energy dissipated by the settling particles and the energy dissipated in the fluid by the agitator (Mersmann et al., 1998, Pinelli et al., 2004). It is known that the axial velocity component decreases up with an increase in the axial distance from the impeller. For the bigger particles with a

higher settling velocity, this balance was achieved at a level lower than that for the smaller particles. This shifted the axial level of the maximum concentration downwards as shown in Figure 6.13.

Poly-disperse particles

In this section, masses of the solids loaded into the system are given for clarity of the presentation. The same mass of 4 kg (10%) of the three nickel particle size ranges shown in Figure 6.13 was simulated in a single domain in Figure 6.14 and Figure 6.15 to determine the influence of the particle size on the solids concentration distribution.

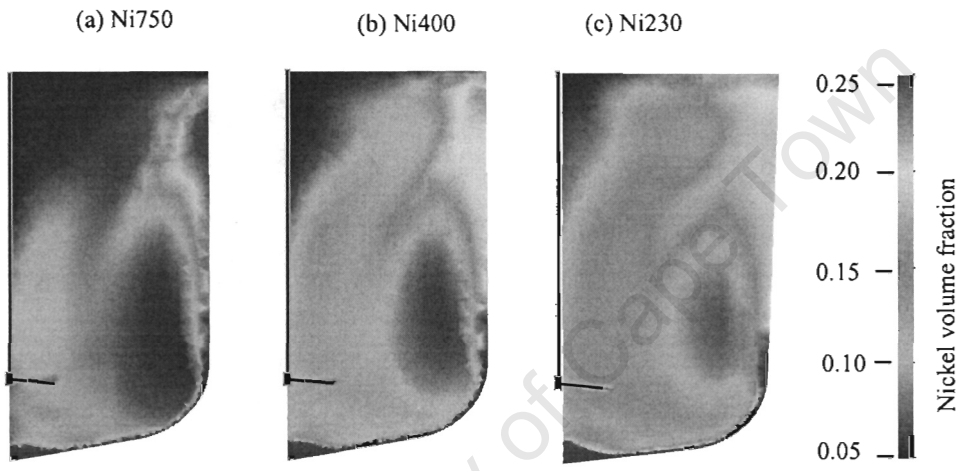

Figure 6.14. Fringe plots of the solids concentration profiles for Ni230, Ni400, Ni750, S_{II} 10% loading, 700 rpm.

Equal masses (1.33 kg) of Ni230, Ni400 and Ni750 were introduced into the domain; the quantity of each particle size representing a dispersed phase in the Eulerian scheme. The high concentration of Ni750 near the wall in the upper tank region in Figure 6.14(a) can be attributed to the circumferential flow and centrifugal force. A similar observation was made by Derksen (2003) with a Lagrangian simulation approach. In this region, the circumferential flow is constrained by the baffles and the liquid flow rate is relatively low. The solids collide with the baffles and, after losing their momentum, the liquid momentum cannot carry them through, especially the bigger ones with higher settling velocities. It is expected that the particles would lose momentum at this point and, instead of continuing with their initial trajectory, they tend to settle. However, some of the particles may be trapped in a small secondary circulation loop resulting from the wall separation, and thus

remain suspended at this point. This could explain the accumulation of Ni750 in the far right upper region of Figure 6.14(a). This region was just above the point at which the circulation loop separated from the vertical wall.

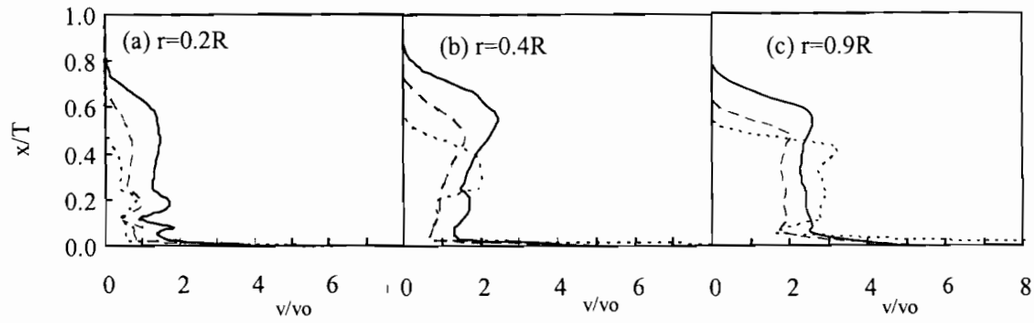

Figure 6.15. Effect of particle size on the axial solids suspension at 10% loading, 700 rpm: —— Ni230; – – – Ni400; ------ Ni750

The axial flow profiles at all radial locations in Figure 6.15 show that the largest particles were the least suspended, and the cloud heights shifted downwards with an increase in particle size. The cloud heights for Ni230, Ni400 and Ni750 were 0.78T, 0.68T and 0.52T, respectively. The concentration of Ni230 was higher than the mean concentration up to 70% of the liquid height. However, for Ni400 and Ni750, there was no specific pattern in this regard.

The radial solids concentration profiles in Figure 6.16 show a steeper gradient closer to the axis and tank wall. In the upper quarter of the tank, there was an increase in the solids concentration with an increase in distance from the tank centre. The typical accumulation of solids in the bottom edge of the tank was not observed since the elliptical-bottom enhanced the suspension of the particles by the impeller discharge stream. The region closer to the shaft is the impeller inlet stream, in which the turbulence intensity is low. Turbulence in a stirred tank decays with an increase in distance from the impeller and the high concentration in the middle region further confirmed that solids concentration gradient increases with a decrease in the turbulence intensity, especially in the absence of small secondary circulating loops. The region of high concentration in the middle or upper region can be easily eliminated by a multiple impeller system (Montante et al., 2001b).

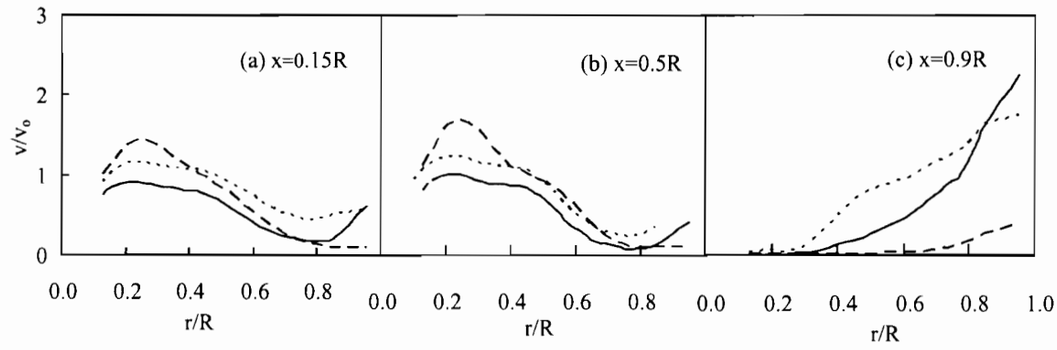

Figure 6.16. Variation of the radial solids concentration distribution with particle size with 10% total loading of 1.33 kg each at 700 rpm: —— Ni230; ------ Ni400; – – – Ni750.

For a well mixed tank, the radial concentration gradient should be negligible. The increased solids concentration in the wall region is responsible for the decrease in the axial velocity component shown in Figure 6.9.

Mono- and poly-disperse particles

The profiles of the mono-disperse particles (Figure 6.13) were superimposed onto those obtained with the poly-disperse particles in Figure 6.15 in order to determine the influence of particle size on the concentration distribution of a particular reference phase. For clarity, concentration profiles for Ni230 and Ni750 only are presented in Figure 6.18, and the systems represented in Figure 6.13 and Figure 6.15 are denoted by S_I and S_{II}, respectively. The link between the two systems can be obtained by assuming that for S_I, a 10% mono-disperse particle size loading of, for example, Ni230 is comprised of three phases of Ni230, with the mass of each phase being 1.33 kg. A reference phase can be taken for this case as 1.33 kg of Ni230, meaning that the other two secondary phases are identical to the reference phase. By taking the same 1.33 kg Ni230 in the system of poly-disperse particles, S_{II}, the secondary phases become Ni750 and Ni400 (1.33 kg each). The influence of the bigger particles on the suspension of the smaller particles can then be determined. The mean concentration of each phase was computed and used to normalize the concentration of the respective phase.

Taking the smaller particles as the reference phase in S_I, Figure 6.17 shows a higher axial solids suspension of Ni230 in the presence of the same size 'neighbours', S_I, than in the

presence of the bigger 'neighbours', S_{II}. This shows that the bigger particles inhibit the movement of the smaller particles. In the event of a smaller particle colliding with a bigger one, the smaller particle loses the most momentum, which increases its settling tendency. Considering a mass of 1.33 kg of the bigger particles (Ni750 in S_{II}) as the reference phase, Figure 6.17 shows a lower solids axial suspension of Ni750 mono-disperse particles than in the presence of Ni230 and Ni400. This can be attributed to the fact that, in the presence of the smaller particles, the net loss of momentum by the bigger particles is less compared to the case of larger interacting particles.

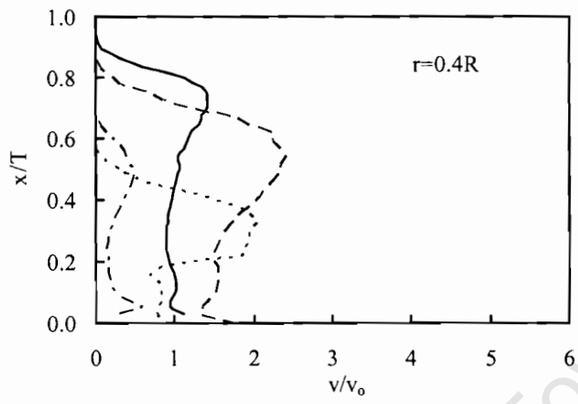

Figure 6.17. Variation of the axial solids suspension with mean particle size for mono-disperse (S_I) and poly-disperse (S_{II}) systems:—— Ni230 S_I; – – – Ni230 S_{II};----- Ni750 S_I; -·-·-Ni750 S_{II}

However, for systems with high solids loading or small particles, caution needs to be exercised since the suspension viscosity may change, resulting in a modified hydrodynamic field. The higher concentration of Ni750 at the bottom in S_I was due to the higher percentage of particles with higher settling velocities in the system of mono-disperse particles (S_I) than in that of the poly-disperse particles (S_{II}). In general, there was a lower axial solids suspension of Ni750 in the presence of the bigger secondary phases (1.33 kg+1.33 kg of Ni750, compared to 1.33 kg of Ni230 + 1.33 kg of Ni400). This observation is consistent with the observation made for Ni230 as a reference phase in S_{II}. This shows that the mono-disperse simulation approach alone cannot be relied upon to predict the solids concentration distribution in a system with a wide range of particle sizes. It is apparent that the suspension theory based on a balance between the potential energy and liquid kinetic energy cannot explain the profile. Both S_I and S_{II} had the same potential

energy (mass), therefore, if the theory based on the potential energy is to be applied in this case, then the same profile would be expected for both S_I and S_{II}. However, this was not the case. The suspension theory that is based on the assumption of a balance between the particle settling velocity and upward fluid velocity is therefore more applicable.

Local particle size distribution

A further investigation into the spatial variation of the local mean particle size was carried out by taking samples along the radial direction, and measuring the mean particle size using the laser diffraction method. The mean size (d_{50}) of the sample (which was in the range of 150-1000 μm) introduced into the tank was 430 μm, as obtained by the laser diffraction analysis. Figure 6.18 shows that, in the lower and upper regions of the tank, the mean particle size increased with an increase in the distance from the centre of the tank. At the centre of the tank (x=0.5T), the local mean particle size in Figure 6.19 deviated from the global mean by about 3% compared to the lower and the upper regions of the tank where the deviation was more than 10%.

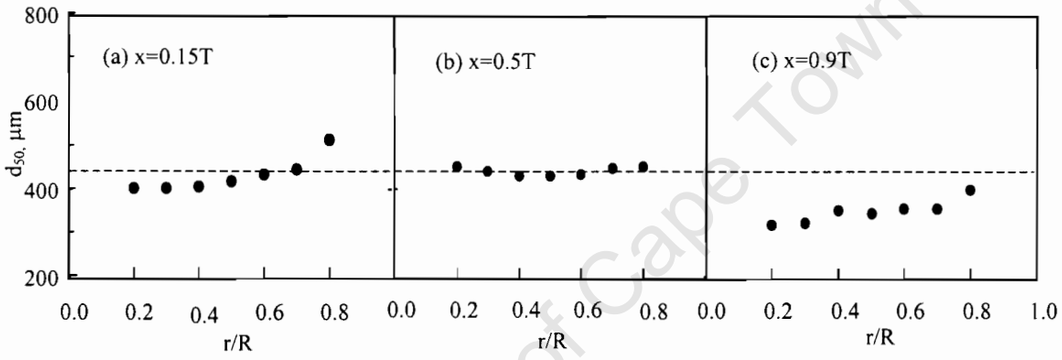

Figure 6.18. Variation of the mean particle size with radial and axial distances for 18% solids loading and particle size of 150-1000 μm.

The diameter of the particles in the middle of the tank was approximately equal to the global mean diameter, d_{50}. This indicates that, in comparing the mono-disperse simulation and experimental results, the size of the particles in the middle of the tank are the same as the simulated size.

6.2.5. Particle density effect

The density of nickel particles is very high compared to that of water, and the requirement that a complete suspension be achieved in order to maximize the surface area available for crystal growth poses a great challenge. Therefore, the nickel solids concentration distribution was compared with that of flint glass and sand. Table 6.2 shows the experimentally determined terminal settling velocity and other hydrodynamic parameters for the three different particles. The maximum Stokes number (St), which is the ratio of the Stokesian particle relaxation time to the time required for one impeller revolution (Derksen, 2003), was 0.76. The difference between the Ar for nickel and sand of the same size was more than one order of magnitude.

A comparison between the concentration profiles for the three particles is presented in Figure 6.19, where the nickel concentration profile is shown to deviate from the profile of the other particles. The difference in the concentration profiles of sand and glass was about 6% whereas that for the nickel deviated from the two others by up to 20% in most regions in the tank. Again, particles with higher densities accumulated more in the bottom region than the low density ones.

Table 6.2. Hydrodynamic properties for nickel, sand and flint glass.

Particle	d_p, μm	density, kgm^{-3}	U_t, m^{-1}	Re_p	Fr	St	Ar
Nickel	75-1000	8903	0.037-0.35	2.36-271.7	0.67-1.89	0.0025-0.76	41-97643
Flint glass	750	4200	0.182	136	0.746	0.268	16689
Sand	750	2500	0.111	83.5	0.378	0.191	7831

The region about the mid radial distance from the tank centre (Figure 6.19(b-d) is of special interest due to the fact that there was a higher concentration of nickel than sand and glass in this region, whilst it is expected that the nickel particles, being the most dense, would be the least suspended. It is important to note that this phenomenon is similar to what was observed with the larger particles in the last section.

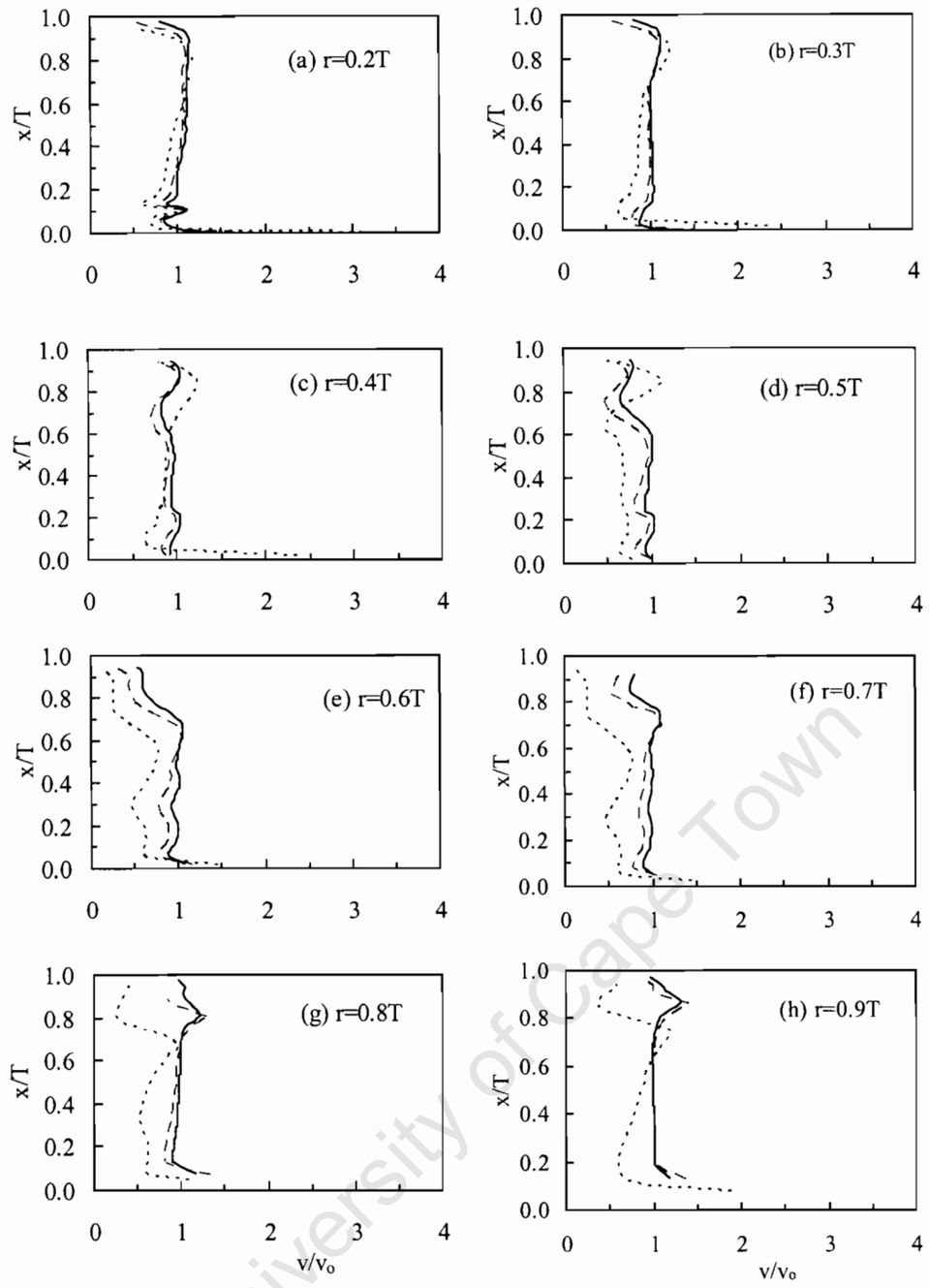

Figure 6.19. Variation of the axial solids concentration distribution with particle density for, 10% loading of 750 μm particles, at 700 rpm: ——Sand; – – – Glass; ------ Nickel.

This (as in the case of the larger particles) can again be attributed to the higher inertial force that the nickel particles have, in comparison to the sand and glass particles. In this region,

the liquid current caused by the wall jet suddenly changes direction, from upward flow to downward flow. The particles with a higher inertial force are expected to continue with the initial trajectory long after the liquid and smaller particles have changed course to downwards motion. The change of direction of the upward movement for the larger or heavier particles is eventually expected to take place in the region closer to the centre of the tank than in the case of the lighter or smaller particles. Therefore, this could lead to a higher concentration of the larger or heavier particles in this region.

It can be seen in Figure 6.19 that the difference between the concentration profile of nickel and that of the other two particles increased with an increase in the radial distance. This can be attributed to the fact that, closer to the wall, there is change in fluid flow direction and the response of the particles to this change depends on the particle density. Nickel particles, which have the highest density, are expected to have the slowest response.

6.2.6. Slip velocity simulation

The slip velocities were calculated from the CFD simulation of the particle and fluid local velocities. There was an increase in the slip velocity with an increase in particle size, and the trend remained the same throughout the tank as shown in Figure 6.20. The slip velocity (V_r) was lowest in the middle of the tank (x = 0.5T) and highest in the impeller region. The high V_r in the impeller region was due to the high fluid velocity relative to that of the solids in the impeller stream.

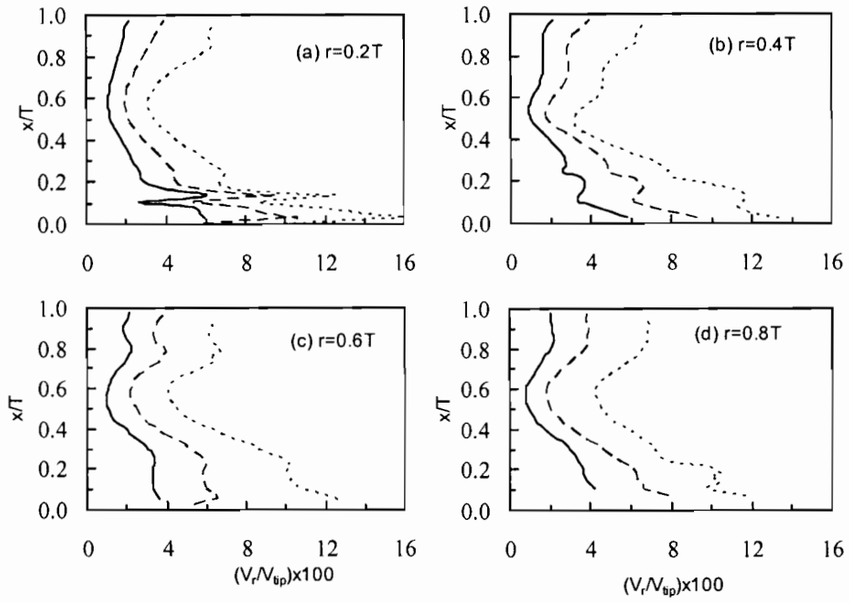

Figure 6.20. Variation of the slip velocity with the axial distance for 10% loading: —— Ni230, – – – Ni400, ------ Ni750.

As a result, the particles in the impeller region lag behind the liquid, similarly, those in the upward stream in the region closer to the surface also lag behind the liquid, whilst, for the downward stream, particles lead the fluid. This was shown by the local value of the difference between particle and liquid velocities (U_L-U_p). The high value of V_r in the regions closer to the surface and tank wall can be attributed to the particle inertial forces. This is consistent with the previous observations, in which it has been seen that larger particles with higher inertia accumulated more in these regions. Figure 6.20 shows, as expected, the highest slip velocity for Ni750 and the lowest slip velocity for Ni230. The difference between the slip velocities of the two sizes was greatest in the impeller region.

The CFD and LDV studies show that the greatest influence of the solids on the velocity field is in the wall region. The axial solids concentration distribution increases with both particle size and particle size distribution, and the influence of the turbulent dispersion force and solid pressure increases with an increase in the solids loading. The poly-disperse multiphase simulation strategy is more representative of the practical situations and can account for the influence of the particle size distribution on solids suspension. The application of the solid

suspension theories depends on the simulation strategy and the physical properties of the particles. For low solids loading, the solids suspension is governed by the bulk fluid flow and the influence of non-drag forces, whilst the turbulent dispersion force is negligible. Such a system may be scaled up on the basis of the impeller tip speed. However, for high solids loading, turbulence intensity influences the solids suspension and the scale-up may be based on power dissipated per unit volume. However, a further investigation with a high density solids suspension in different tank sizes is still required.

6.3. Drag models and solid pressure

Flow in most solid-liquid mixing tanks is dominated by the drag force, which is represented by the drag coefficient (C_D). Solids suspension in the previous sections was investigated using the Gidaspow (1994) drag model, which is one of the built-in CFX drag models. In this section, the Schiller-Naumann model, which is a built-in CFX drag coefficient, and an externally introduced model (Brucato et al., 1998a) have been compared with the Gidaspow (1994) model. These drag models are hereafter referred to as the Gidaspow model, Schiller-Naumann model and Brucato model. The models available in the CFX code do not account for the influence of free stream turbulence on solids suspension, which was investigated using the Brucato model. The implementation of the Brucato model requires the Kolmogoroff length scale and the drag coefficient for a quiescent liquid as input parameters. The terminal settling velocity (U_t) required to compute the particle Reynolds number (Re_p) and, consequently, the drag coefficient, was obtained by either experimental or numerical methods.

6.3.1. Drag coefficient in quiescent liquid

The particle terminal settling velocity and drag coefficient in a quiescent were determined fluid according to the method described in Chapter 4. A very good agreement was obtained between the simulation and experimental results, as shown in Figure 6.21.

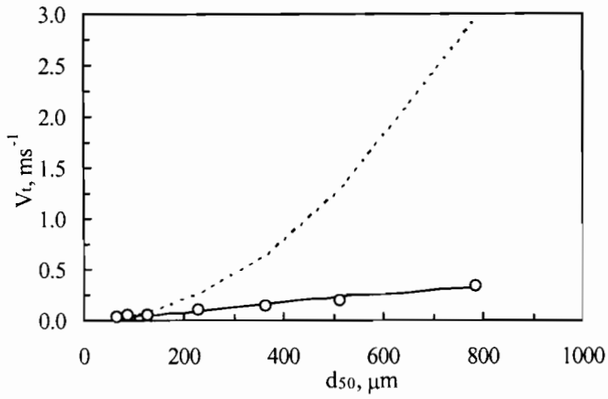

Figure 6.21. Variation of the particle settling velocity with particle size:
(o) Experiments, —— Schiller-Naumann model, ------ Stokes models.

Both experimental and simulation results showed a linear relation between U_t and the mean particle diameter, d_{50}. The predicted linear relationship shown in Figure 6.21 is in agreement with the findings of Brucato et al. (1998a). As expected, the settling velocity values obtained with the Stokes law agreed with the experimental result only for the smaller particles ($d_p < 100$ μm) with low Re_p. Stokes law under-estimated the drag coefficient for flows with high Re_p (>1), and this resulted in the over-estimation of U_t. Figure 6.21 shows clearly that the model based on the Stokes law could not be used to calculate the terminal velocity for the wide range of nickel particles used in the present work. The Stokes model results departed from the experimental ones at a point where the ratio of the particle diameter to the Kolmogoroff length scale (d_p/λ) was about 5. This corresponds to a particle diameter of 150 μm, with the value of the Stokes number (St), calculated from the N_{js}, of 0.012. For the particles outside the range covered by the Stokes law, St was about two orders of magnitude higher than within the range, and the St values for all particles were less than unity. Given that St shows how a particle adjusts its speed to an interacting eddy (Lane et al., 2005), a wide variation in St indicates a wide range of the particles' response to turbulence intensity.

The U_t obtained experimentally was used to calculate the Re_p required for the computation of C_{Do}, both of which are shown in Figure 6.22 and Figure 6.23. The typical qualitative response of the drag coefficient to particle size is shown in Figure 6.22, and it can be seen that there is a steeper gradient of C_{Do} for particle sizes within the Stokes law region (d_p<150

μm). An opposite trend is shown in the same figure for Re_p, in which there is a steeper gradient for the larger particles.

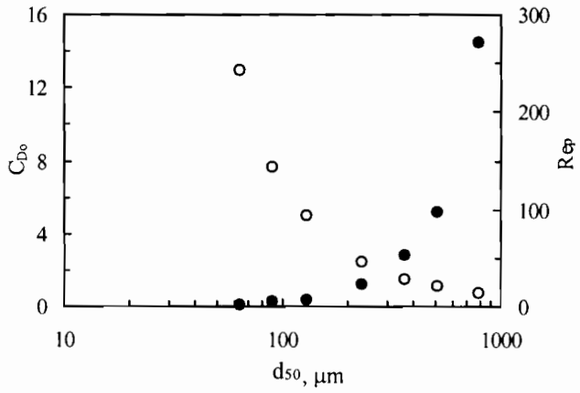

Figure 6.22. Variation of C_{Do} and Re_p with particle size; (•) Re_p, (o) C_{Do}.

Further information on the relation between the drag coefficient and Re_p was sought, and it is shown in Figure 6.23 that the value of the drag coefficient fell just below unity for Re_p of 140, corresponding to the particle size of 500 μm. The response variables (C_{Do} and R_{ep}) in Figure 6.21 to Figure 6.23, which were for a quiescent fluid, are solely dependent on the properties of the particles. However, in a stirred tank, the drag coefficient needs to be modified to account for the mean and turbulent flow structures as well as for inter-particle interaction.

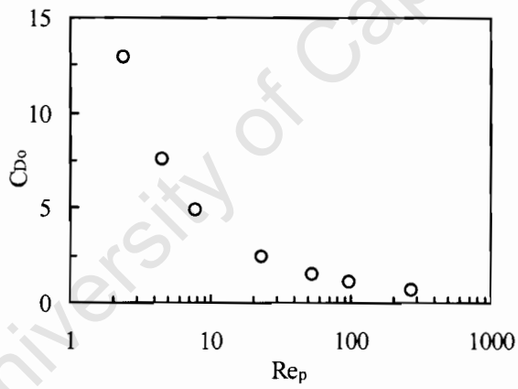

Figure 6.23. Variation of C_{Do} with Re_p

6.3.2. Comparison of drag models

In Table 6.3, the Kolmogoroff length scale (λ) was calculated from the mean kinetic energy dissipation rate per unit volume (ε_P). Power was calculated for the experimentally determined N_{js}. The Stokes number (St) was calculated by the correlation adopted by Derksen (2003) as defined in Chapter 3. It is shown in Table 6.3 that an increase in particle size by an order of magnitude resulted in a less than 40% increase in N_{js}. In contrast, the increase in the ratio d_p/λ was in the same order of magnitude as the increase in particle size, within the same particle size range. The ratio d_p/λ accounts for the particle-eddy interaction, and for the particle sizes for which the ratio d_p/λ is less than 5, there is a negligible interaction between the energy dissipating eddies and particles (Pinelli and Magelli, 2001). Consequently, the drag coefficient is not affected by turbulence and therefore, for such particle sizes, a constant drag coefficient may be used. Conversely, a value of the ratio d_p/λ greater than 10 indicates that the interaction between the energy dissipating eddies and the particles results in changes in settling velocity and drag coefficient (Brucato et al., 1998a).

Table 6.3. Variation of flow parameters with mean particle size for 1.3% solids loading.

d_{50}, μm	N_{js}, rpm	ε_p, m^2s^{-3}	$\lambda \times 10^{-6}$, m	d_p/λ	St x 10^3
75	363	0.245	41.2	1.82	2.12
100	385	0.292	39.5	2.53	4.00
200	442	0.442	35.6	5.62	18.4
300	479	0.564	33.5	8.96	44.8
400	508	0.670	32.1	12.5	84.4
500	531	0.766	31.0	16.1	138
750	576	0.977	29.2	25.7	336
1000	610	1.161	28.0	35.8	633

In Figure 6.24, the solids concentration distribution determined using this model was compared with those obtained with the Gidaspow and Schiller-Naumann models. The prediction by the Gidaspow and Schiller-Naumann models were similar in most parts of the tank, with deviations from the experimental results being 9.4%, 8.5%, and 7.0% for Gidaspow, Schiller-Naumann and Brucato models, respectively. At low solids hold up ($\varphi_s < 0.2$), the Gidaspow model effectively becomes the Wen-Yu model. The differences between the Wen-Yu and Schiller–Naumann models are the liquid hold up correction term ($\varphi_L^{-1.65}$) and the volume fraction modified particle Reynolds number ($Re_p' = \varphi_s Re_p$) in the latter, as shown in Chapter 3. In a system with low solids loading or in regions where the

solids hold up is low, φ_L tends to 1 and, consequently, the Wen-Yu and Schiller-Naumann models become identical. This is shown by the smaller difference (0.9%) between the predictions obtained with Gidaspow and the Schiller-Naumann models compared to that (1.5%) between the Schiller-Naumann and Brucato models.

There was almost an identical prediction of the solids concentration distribution in the upper region of the tank (x > 0.5%T), for all the three models. In the impeller discharge region, the best prediction was obtained with the Brucato model. With an increasing distance towards the liquid surface, there are two aspects to consider: firstly, there is an increasing dominance of the molecular viscosity over the turbulent viscosity; secondly, the particle volume fraction decreases. The turbulent viscosity is an important parameter for the formulation of turbulence theories and models, and it is a point of departure for many turbulence models. Particles in regions away from the impeller experience relatively less influence of the turbulent viscosity. In the upper region of the tank, both turbulent viscosity and volume fraction are low. The spatial variation of turbulence levels and solids concentration needs to be accounted for by the drag correlations, and this influences the quality of prediction.

Mixing due to turbulent eddies or turbulent dispersion, which is highest in the impeller discharge region, is not accounted for by both the Gidaspow and Schiller-Naumann models. The better prediction with the Brucato model in the impeller region can therefore be attributed to the fact that the latter accounts for the influence of the eddy dissipation on solids suspension through the Kolmogoroff length scale. This is consistent with the earlier results (section 6.2), which showed that there was an influence of the turbulent dispersion force in systems or regions of high concentration gradient. In the upper region, the fact that the results were almost identical can be attributed to the relatively low level of turbulence and concentration in the region. Therefore, mixing in this region was dominated by the bulk circulation and convective mixing over the turbulent mixing.

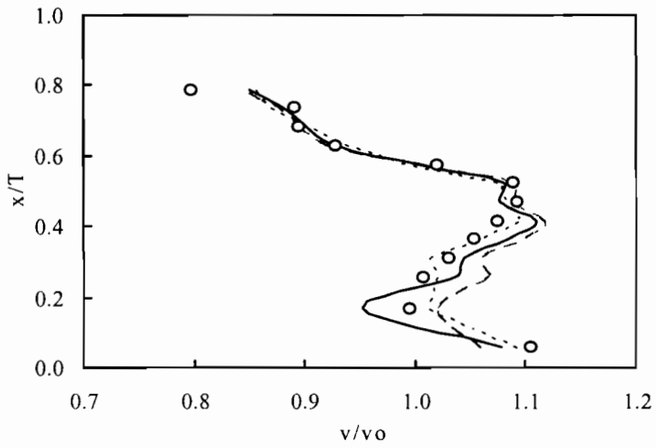

Figure 6.24. Effect of drag models on the solids concentration distribution of 1.3% loading of Ni750 at N_{js}: —— Schiller-Naumann; – – – Gidaspow; -----Brucato; (o) Experiments.

The fact that the Brucato model gave the best prediction is indicative of the influence of the free stream turbulence on the solids concentration distribution. It is worth noting that the ratio, d_p/λ, for the particles investigated in Figure 6.24 was found to be 26, and the Brucato model gave the best overall prediction. It has been mentioned earlier that for $d_p/\lambda > 10$, the interaction between energy dissipating eddies and particles become important for the solids concentration distribution.

For all these simulations, the effect of the free stream turbulence, macro-instabilities and larger eddies were not directly accounted for. Generally, with low solid loadings, the results obtained with the three models were of comparable magnitude, and agreed very well with experimental results. The fact that the prediction obtained with the Brucato model was only marginally better than the other two could suggest that mixing in the system investigated was dominated by the mean fluid flow. This is in agreement with the observations made by Montante et al. (2001b).

An attempt was made to compare the performance of the Brucato and Gidaspow models at a high solids loading. This was done using the method of off-bottom solids suspension described in section 6.1, due to the fact that the optical method could not be applied at the high solids loading. The prediction of the solids concentration distribution trend by the Brucato model in Figure 6.25 was different from that obtained with the Gidaspow model. For larger particles ($d_p/\lambda > 10$), the Brucato model gave a marginally better prediction than

the Gidaspow model. This is in agreement with the findings of Magelli et al. (1990) and Brucato et al. (1998a) that, for such particles, the free stream turbulence influences solids suspension. The trend obtained by both models did not reveal clearly which of the two was better since there was a higher mismatch between the experimental and simulation results obtained with the Brucato model for smaller particles. This may not be an indication that both models were equally good. Instead it may be indicative of the limitation of the current commercial codes in predicting solids suspension in high solids loading systems. At the tank bottom, there is a complex interaction of many factors in the boundary layer, which influence the solids off-bottom suspension. Firstly, the value of the energy dissipation rate in the boundary layer may deviate significantly from ε_P. Secondly, the flow near the wall is largely anisotropic, therefore it is expected that there would be errors in computing flow variables using a k-ε model-based approach. Thirdly, there is a considerable error in obtaining solid liquid data such as C_{Do}, a fact that has been acknowledged in the literature (Brucato et al., 1998a).

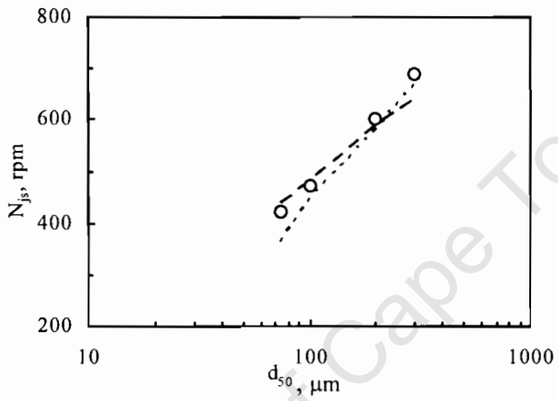

Figure 6.25. Variation of N_{js} with particle size and drag models:
– – – Gidaspow; ------ Brucato.

Particle off-bottom suspension depends on the velocity and the scale of turbulence in the boundary layer (Mersmann et al., 1998; Rieger and Ditl, 1994). In this regard, the grid size used in the present work was not fine enough for an effective evaluation of this kind. A better evaluation of the models could be made from experimental and simulation results of the solids concentration distribution for high solids loading. From the present work, a firm conclusion cannot be drawn on the basis of the present data as to the performance of the two models.

6.3.3. Determination of energy dissipation rate for the Brucato model

The results in Figure 6.24 show that the Brucato model gave the best prediction of the solids concentration distribution for the low solids loading system. Therefore, the methods of computing the Kolmogoroff length scale (λ) were further investigated. In the previous approach, the value of ε_P was independent of the simulation values of the energy dissipation rate, since ε_P was calculated from experimental data. The results obtained with this method were compared with those obtained by the simulated turbulent kinetic energy dissipation rate (ε_{CFD}). This parameter (λ) was firstly obtained from the CFD simulation of the local turbulent kinetic energy dissipation rate. The results of the solids concentration distribution obtained with ε_{CFD} were indistinguishable from those of Schiller-Naumann model. This is due to the fact that these values represent a gross under-prediction of the turbulent kinetic energy dissipation rate, as shown in section 5.3. This under-prediction of the turbulent kinetic energy dissipation rate resulted in an over-prediction of λ, leading to a small value of the free stream turbulence correction term in the Brucato model. Consequently, the Brucato model effectively becomes the Schiller-Naumann model. The simulated torque on the baffles was therefore used to calculate ε_{CFD}, for which the results are shown in Figure 6.26.

It can be seen that there was a small difference between the two predictions obtained with λ calculated from ε_P and that from ε_{CFD}. The two results obtained by the two methods were good, with an overall better prediction being obtained with ε_P. The higher deviation from the experimental results obtained with ε_{CFD} could be attributed to the under-prediction of the torque, as has been shown in section 6.3, which results in small values of ε_{CFD} in comparison to ε_P. Again, the model would effectively become the Schiller-Naumann model, which has earlier been shown in Figure 6.24 to give the highest deviation from the experimental results. There was an insignificant difference between the deviation obtained with ε_P in the upper and lower regions of the tank. As for the ε_{CFD} case, a smaller deviation was obtained in the lower half of the tank. In both methods in Figure 6.26, it was assumed that the turbulence level in the tank was homogeneous.

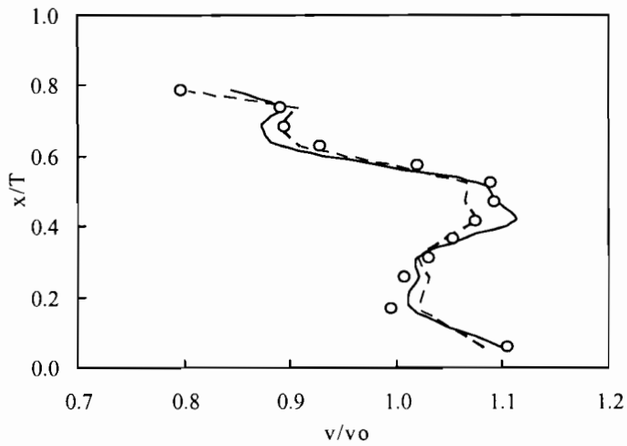

Figure 6.26. Effect of the kinetic energy dissipation rate on solids concentration distribution for 1.3% loading of Ni750 at N_{js}: —— ε_{CFD}; – – – ε_P; (o) Experiments.

This certainly is an over-simplification of the real situation as shown in sections 5.2 and 5.3 that the turbulent field varies in time and space. Given that ε_{CFD} was smaller than ε_P, it was expected that ε_{CFD} would be a greater under-estimation of the turbulence level than ε_P in the impeller region. This could explain the higher mismatch between experimental results and the simulation ones obtained with ε_{CFD} in the same region compared to those obtained with ε_P. The fact that both methods gave reasonable prediction of the experimental results despite the assumption that the turbulence is homogeneous is another indication that mixing in low solid loading systems was dominated by the mean velocity field.

6.3.4. Solid pressure

Particle-particle interaction was accounted for by the solid pressure, which is a function of elasticity modulus (G_o), maximum solids volume fraction (φ_{sm}) and compaction modulus (c_m). The influence of these parameters on the solids concentration distribution was investigated with 20% solids loading of Ni230. The default values for G_o and φ_{sm} are 1 Pa, and 0.6 respectively; and c_m can take values in the range of 20-600 (AEAT, 2003). A parameter sensitivity analysis was carried out on the solid pressure term by varying c_m between 10 and 700 while keeping the default values of G_o and φ_{sm}. The solids concentration distributions obtained with different values of c_m within this range were identical, suggesting that, within this range and in low solids loading systems investigated, the value of the compaction modulus did not influence the solids concentration distribution.

It is generally understood that the isotropic turbulence assumption, on which the k-ε model is based, does not accurately represent the physics of a turbulent flow in a stirred tank. However, it has been shown in the literature that, for many practical applications, the predictions obtained with this model agree reasonably with experimental results. The results obtained in the present work suggest that, for flows in single or dilute systems, the quality of the mixing is dominated by the mean fluid flow and for such flows, the k-ε model is still the most economical approach.

CHAPTER 7

7. Conclusions

Conclusions have been drawn from the investigations carried out in both the liquid-only system and the solid-liquid system. Preliminary and mixing studies were carried out in the liquid-only system. The preliminary studies focused on the influence of the simulation strategies on the flow field. For the mixing studies, the effect of reactor geometry and impeller type on the mean velocity and turbulent fields were investigated. It was shown that the CFD simulation approach can be used to obtain detailed information on the mean velocity and turbulence fields, which are important for multiphase mixing. In the solid-liquid system, mixing features such as the off-bottom solids suspension, cloud height and solids concentration distribution were determined by both experimental and simulation methods.

7.1. Preliminary investigation with a pitched blade impeller

The influence of simulation strategies such turbulence models, impeller models, discretization schemes and the k-ε model constants on the velocity and turbulent fields were investigated. The k-ε turbulence model gave the best overall prediction in comparison to the RNG-k-ε and k-ω turbulence models. In spite of the k-ε turbulence model giving better predictions than the other two, there was still a severe mismatch between the simulation and experimental results for the turbulence field. This can be attributed to the assumption that turbulence is isotropic, which is not the case as was shown by the LDV results. The prediction obtained by the k-ε model could be improved by changing the model constants in the transport equation for the turbulent energy dissipation rate. However, a given set of these constants did not give the same quality of prediction in the entire domain.

It is shown that the multiple frames of reference (MFR) method gives a better prediction of velocity and turbulent field than the impeller boundary condition (IBC) method, and there was a better prediction of the axial velocity component compared to the radial and tangential velocity components by both methods. Three discretization schemes investigated had a marginal influence on the flow field prediction, and the hybrid scheme gave predictions as good as or better than the third-order upwind scheme (QUICK). This shows that a higher-order scheme does not necessarily give better predictions for the systems investigated.

7.2. Flow field and mixing with the Rushton turbine

A hydrodynamic investigation into the interaction between reactor geometry and impeller pumping characteristics was carried out in a tank with and without a draft tube and stirred by the Rushton turbine. It was shown that the transient simulation method, sliding grid (SG), gives better predictions of the velocity field than the steady state method, MFR. CFD simulations revealed formation of circulation loops and dead zones resulting from the influence of the system geometry. It was shown that, at a low impeller clearance, the Rushton turbine generates a flow field that evolved from the typical two loops to a single loop flow pattern, which is similar to that of an axial impeller. The single loop widened with time, leading to an increase in the axial velocity component and this improved mixing. The resulting flow pattern enabled a draft tube to be used in a Rushton turbine stirred tank to enhance mixing in the regions away from the impeller.

The CFD simulations over-predicted mixing time but under-predicted power number. This can be attributed to the under-prediction of the turbulence intensity by the k-ε model, which is based on the Reynolds averaged Navier-Stokes equations. With the use of the draft tube, energy saving and improved mixing efficiency was achieved as a result of the suppression or elimination of the dead zones. CFD simulation results showed that the best radial location for the draft tube is in the range of 65% to 80% of the diameter of the tank.

7.3. Flow field and mixing with a hydrofoil impeller

Flow field and homogenization energy were studied in an elliptically bottomed tank stirred by a hydrofoil impeller. The SG method, which accounts for the temporal variations in the mixing tank, gave a better prediction of the velocity field than the MFR method. The simulation results of the flow field agreed reasonably well with the LDV measurements in most regions of the tank. However, the turbulent kinetic energy dissipation rate was not well predicted. Further, the flow resulting from the interaction between the free surface and the wall was not well predicted, and the prediction results were insensitive to the grid resolution over the range of grid sizes used.

A comparison was made between the flow fields generated by the Ruston turbine and the hydrofoil impeller. It was shown that at a low impeller clearance, the flow pattern obtained

with the hydrofoil impeller was comparable to that obtained with the Rushton turbine. However, the axial velocity obtained with the hydrofoil impeller was higher than that of the Rushton turbine in the impeller and wall regions. The use of a draft tube with the Rushton turbine and hydrofoil impeller resulted in a reduction in the homogenization energy by 19.2% and 17.7%, respectively. This shows that a reduction in the operating cost can be achieved with the use of a draft tube.

7.4. Just off-bottom solids suspension and cloud height

CFD simulations initiated with the particles at the bottom of the tank were a better representation of the practical applications, and the prediction of the off-bottom solids suspension obtained by this method agreed with experimental results. A CFD simulation method developed to predict the impeller speed (N_{js}) required to achieve the just off-bottom suspension gave results that agreed reasonably with experimental ones, especially with Stokesian particles, for which the typical N_{js} correlations fail to give consistent results

It was found that the impeller speed required for the cloud height to reach 90% of the liquid height was less than N_{js}. This can be attributed to the high density (8903 kg m^{-3}) of the nickel particles. The CFD simulation method and correlation developed to predict cloud height gave results that agreed with measurements obtained with an optical attenuation technique (OAT). This shows that CFD simulations can be used to develop empirical models that predict mixing features and this can enable improvements in the performance of solid-liquid systems to be made. In general, the CFD predictions of the off-bottom solids suspension and cloud height were better for smaller ($d_p < 150$ μm) particles than the bigger ones.

7.5. Solids concentration distribution

The CFD and LDV studies showed that the greatest influence of the solids on the velocity field was in the wall region. No radial solids concentration gradient was observed with mono-disperse solids loading up to 0.3%, and in comparison to other regions of the tank, a better prediction was obtained in the middle of the tank. This can be attributed to the fact that in the middle region, the experimental mean particle size is the same as the simulated size. This was confirmed by measuring the local mean particle size in the tank using the laser diffraction technique. Regions of inhomogeneity in the tank were identified and these

depended on the particle size. The axial concentration distribution decreased with an increase in both particle size and solids loading. The influence of the turbulent dispersion force and solid pressure on the solids suspension increased with an increase in the solids loading and solids concentration gradient. The poly-disperse multiphase simulation results show that, for a given solids loading, the larger particles inhibit the suspension of the smaller ones. A difference in the concentration distribution pattern was obtained with nickel, flint glass and sand particles.

Results suggest that solids suspension theories and scale-up rules are influenced by the operating conditions. The solids suspension theory based on a balance between the potential energy of the particle and the liquid kinetic energy is more applicable to mono-disperse particles than to the poly-disperse ones. For low solids loading (less than 1%), the solids suspension is governed by the bulk fluid flow, and the influence of drag forces, and the turbulent dispersion force are negligible. Further investigation using different tank sizes and high precision equipment for measuring solids concentration distribution is still required in this regard

7.6. Drag models

It was found that the Stokes law applied to the nickel particles up to a diameter of 150 μm. For the size range of the particles investigated, a high Archimedes number obtained was indicative of the importance of the free stream turbulence on solids suspension. Thus, a better agreement between the simulation and experimental results of the solids concentration distribution was obtained with the drag models that account for the free stream turbulence or solids loading. For the low solid loadings, the Brucato model, which accounts for the free stream turbulence, gave the best prediction. In a high (20%) solids loading system, the Gidaspow model, which accounts for solids loading, gave a better prediction than the Brucato model using the particles within the Stokes law region. The predictions of the Brucato model based on the Kolmogoroff length scale calculated using the mean kinetic energy dissipation rate were better than those obtained from the local turbulent kinetic energy dissipation rate. The solids suspension was not affected by the value of the compaction modulus (c_m) in the range of 10-700.

7.7. General concluding statement

It is shown that the k-ε model gives a better overall prediction of the mean velocity field than the k-ω and RNG k-ε models and the quality of the prediction is not improved in all cases if a higher order discretization scheme is used. Mixing efficiency in a Rushton turbine stirred tank can be improved with a draft tube. The use of a draft tube results in a higher reduction in energy demand in a Rushton turbine stirred tank than in the hydrofoil impeller stirred tank. CFD simulation methods can be used to develop correlations based on detailed information on the flow field. Solids concentration field and solids suspension theories depend on factors such as solids loading and particle size. A CFD simulation approach that takes particle size into account gives predictions that are more representative of practical applications than the mono-size particle simulation approach. The concentration profile for the nickel solids deviates significantly from those of sand and glass showing the importance of the effect of particle density on the concentration distribution. Drag models that account for the solid volume fraction and free stream turbulence give reasonable predictions of the solids suspension. The under-prediction of the turbulence intensity by the k-ε model can lead to an over-design of a stirred tank. This fact needs to be taken into account if simulation results obtained in the same way are to be used for the purpose of designing a stirred tank. The k-ε model constants need to be obtained for mixing systems.

CHAPTER 8

8. References

AEAT, (2003), CFX5 Flow solver user guide, *Computational Fluid Dynamics Services,* Harwell, Oxfordshire UK: AEA Industrial Technology.

ANSYS, (2004). CFX5 Flow solver user guide, www.ansys.com.

Armenante, P.M., Nagamine, E.U. (1998). Effect of low off-bottom impeller clearance on the minimum agitation speed for complete suspension of solids in stirred tanks, *Chemical Engineering Science,* 53(9), 1757-1775.

Alexopoulos, A.H., Maggioris, D., Kiparissides, C. (2002). CFD analysis of turbulence non-homogeneity in mixing vessels: A two-compartment model, *Chemical Engineering Science*, 57(10), 1735-1752.

Antal, S.P., Lahey, R.T., Jr., Flaherty, J.E. (1991). Analysis of phase distribution in fully developed laminar bubbly two-phase flow. *International Journal of Multiphase Flow,* 17(5), 635-652.

Andersson, S.R., Rasmuson, A. (2000). Flow measurements on a turbulent fibre suspension by laser Doppler anemometry, *Chemical Engineering Science,* 46(6), 1106-1119.

Aubin, J., Fletcher, D.F., Xuereb, C. (2004). Modeling turbulent flow in stirred tanks with CFD: the influence of the modelling approach, turbulence model and numerical scheme*Experimental Thermal, Fluid Science,* 28(5), 431-445.

Bakker, A. (1992). Hydrodynamics of stirred gas-liquid dispersion, PhD Thesis, *Technical University of Delft.*

Barresi, A., Baldi, G. (1987). Solids suspension in an agitated vessel, *Chemical Engineering Science,* 42(12), 2949-2956.

Bartels, C., Breuer, M., Wechsler, K., Durst, F. (2002) Computational fluid dynamics applications on parallel-vector computers: computations of stirred vessel flows, *Computers, Fluids,* 31(1), 69-97.

Barrué, H., Karoui, A., Le Sauze, N. Costes, J., Illy, F. (2001). Comparison of Aerodynamics and mixing mechanisms of three mixers: Oxynator™ gas–gas mixer, KMA, SMI static mixers, *Chemical Engineering Journal,* 84(3), 343-354.

Bhattacharya, S., Kresta, S.M. (2002). CFD simulations of three-dimensional wall jets in a stirred tank, *Canadian Journal of Chemical Engineering,* 80(4), 695-709.

Biswas, P.K., Dev, S.C., Godiwalla, K.M. and Sivaramakrishnan, C.S. (1999). Effect of some design parameters on the suspension characteristics of a mechanically agitated sand–water slurry, *Materials and Design,* 20(5), 253-265

Bittorf, K.J., Kresta, S.M. (2003). Prediction of cloud height for solid suspensions in stirred tanks, *Chemical Engineering Research and Design,* 81(A5), 568-577.

Bouaifi, M., Roustan, M. (2001). Power consumption, mixing time and homogenization energy in dual-impeller agitated gas-liquid reactors, *Chemical Engineering and Processing,* 40, 89-95.

Brucato, A., Ciofalo, M., Grisafi, F. Micale, G. (1994). Complete numerical simulation of flow field in baffled stirred vessel: inner–outer approach, *Institution of Chemical Engineering Symposium*, 136, 155-162.

Brucato, A., Grisafi, F., Montante, G. (1998a). Particle drag coefficients in turbulent fluids. *Chemical Engineering Science,* 53(18), 3295-3314.

Brucato, A. Ciofalo, M., Grisafi, F., Micale, G. (1998b). Numerical prediction of flow fields in baffled stirred vessels: A comparison of alternative modelling approaches, *Chemical Engineering Science,* 53(21) 3653-368.

Brucato, A., Ciofalo, M., Grisafi, F., Tocco, R. (2000). On the simulation of stirred tank reactors via computational fluid dynamics, *Chemical Engineering Science,* 55(2).

Bruun, (1996). Hot film anemometry in liquid flows, *Measurement Science Technology*, 7, 1301-1312.

Bujalski, W., Takenmaka, K. Paolini, S. Jahoda, M., Paghanti, A., Takahashi, K., Nienow, A., Etchells, A.W. (1999). Suspension, homogenization in high solids concentration stirred chemical reactors, *Transactions of the Institution of Chemical Engineers,* 77A, 241-247.

Bujalski, W., Jaworski, Z., Niewnow, W. (2002). CFD study of homogenization with dual Rushton turbine – Comparison with experimental results II: The Multiple frame of Reference, *Transactions of the Institution of Chemical Engineers,* 80A, 97-104.

Buurman, C., Resort, G., Pleschles, A. (1986). Scaling-up rules for solids suspension in stirred vessels, *Chemical Engineering Science,* 54, 2865-2871.

Burns, A.D.B., Frank, Th., Hamill, I., Shi, J-M. (2004). Drag model for turbulent dispersion in Eulerian multi-phase flows, *5th International Conference on Multiphase Flow, ICMF-2004,* Yokohama, Japan.

Campolo, M., Sbrizzai, F., Soldati, A. (2003). Time-dependent flow structures and

Lagrangian mixing in Rushton-impeller baffled-tank reactor, *Chemical Engineering Science,* 58(8), 1615-1629.

Cate, A. ten, Denksen, J.J., Kramer, H.J.M, van Rosemalen, G.M., van den Akker, H.E.A., (2001). Microscopic modelling of hydrodynamics in industrial crystallizers, *Chemical Engineering Science,* 56, 2495-2509.

Caulet, P.J.C., van der Lans, R.G.J.M., Luyben, K.Ch.A.M. (1996). Hydrodynamical interactions between particles and liquid flows in biochemical applications, *The Chemical Engineering Journal and the Biochemical Engineering Journal*, 62(3), 193-206

Ciofalo, M., Brucato, A., Grisafi, F., Torraca, N. (1996). Turbulent flow in closed and free-surface unbaffled tanks stirred by radial impellers *Chemical Engineering Science,* 51(14), 3557-3573.

Chudacek, M.W., Clift, R., Grace, J.R., Weber, M.E. (1985). Solids suspension behaviour in profiled bottom, flat bottom mixing tanks. *Chemical Engineering Science,* 40(3) 385-392.

Deglon, D.A. (1998). A hydrodynamic investigation of the particle floatation in a batch floatation cell. PhD Thesis, *University of Cape Town.*

Derksen, J.J., van den Akker, H.E.A. (1999). Large Eddy Simulations on the flow driven by a Rushton turbine, *American Institution of Chemical Engineering Journal,* 45(2), 209-221.

Derksen, J.J. (2003). Numerical simulation of solids suspension in a stirred tank. *America Institution of Chemical Engineers Journal*, 49(11), 2700-2714

Ewing, D.H., Hussein, W.J., George, K. (1995). Spatial resolution of parallel hot-wire probes for derivative measurements, *Experimental Thermal, Fluid Science,* 11(2), 155-173.

Fan, J., Rao, Qi., Wang, Y., Fei, .W. (2004). Spatio-temporal analysis of macro-instability in a stirred vessel via digital particle image velocimetry (DPIV), *Chemical Engineering Science*, 59, 1863 – 1873

Fajner, D., Magelli, F., Nocentini, M., Pasquali, G. (1985). Solids concentration profiles in a mechanically stirred, staged column slurry reactor, *Chemical Engineering Research and Design,* 63, 235-240.

Fasano, J.B., Penney, W.R. (1991). Avoid blending mix up, *Chemical Engineering Progress,* 10(89), 56-63.

Gamwo, I.K. Halow, J.S., Gidaspow, D., Mostofi, R. (2003). CFD models for methanol synthesis three-phase reactors: reactor optimisation, *Chemical Engineering Journal,* 93(2) 15, 103-112.

Gidaspow, D. (1994). Multiphase flow, fluidization: Continuum, kinematic theory description, *Academic Press*, New York.

Gosman, A.D., Lekakou, C., Politisis, S., Issa, R.I., Looney, M.K. (1992). Multidimensional modelling of turbulent 2-phase flow in stirred vessels, *American Institution of Chemical Engineering Journal,* 1946-1956.

Guillard, F., Tragardh, C. (2003). Mixing in industrial Rushton turbine agitated reactors under aerated conditions, *Chemical Engineering Process*, 421, 373-386.

Gunkel, A.A., Weber, M.E. (1975). Flow phenomena in stirred tanks I, II, *American Institution of Chemical Engineering Journal,* 21 931-949.

Harris, C.K. Roekae, D., Rosendal, F.J.J., Buitendijk, F.G.J. (1996). Computational fluid dynamics for chemical reaction engineering, *Chemical Engineering Science,* 51, 1569-1594.

Hartmann, H., Derksen, J.J., Montavon, C., Pearson, J., Hamill I.S., van den Akker, H.E. A. (2004). Assessment of large eddy and RANS stirred tank simulations by means of LDA, *Chemical Engineering Science,* 59(12), 2419-2432.

Ibrahim, S., Nienow, A.W. (1999). Comparing impeller performance for solid-suspension in the transitional flow regime with Newtonian fluids, *Transactions of the Institution of Chemical Engineers,* 77A, 721-727.

Ishii, M., Zuber, N. (1979). Drag coefficient, relative velocity in bubbly, droplet or particulate flows. *American Institution of Chemical Engineering Journal,* 25(5), 843-55.

Javed, K.H., Mahmud T., Zhu J.M. (2006). Numerical simulation of turbulent batch mixing in a vessel agitated by a Rushton turbine, *Chemical Engineering and Processing,* 45(2) 9-112.

Jaworski, Z., Nienow, A. W., Dyster, K. N. (1996). An LDA study of the turbulent field in a baffled vessel agitated by an axial, down-pumping hydrofoil impeller. *Canadian Journal of Chemical Engineerin*g, 74(1), 3-15.

Jaworski, Z., Dudczak, J. (1998). CFD modelling of turbulent macromixing in stirred tanks. Effect of the probe size, number on mixing indices, *Computers, Chemical Engineering,* 22(1), S293-S298.

Jaworski, Z., Bujalski, W., Otomo, N., Nienow, A.W. (2000). CFD study of homogenization of with dual Rushton turbine: Comparison with experimental results I Studies, *Transactions of the Institution of Chemical Engineers,* 78A, 327-333.

Jaworski, Z., Pianko-Oprych, P. (2002). Two-phase laminar flow simulations in a Kenics static mixer: Standard Eulerian, Lagrangian approaches, *Chemical Engineering Research* and *Design,* 80(A8), 910-916.

Karema, H. Lo, S. (1999). Efficiency of inter-phase coupling algorithms in fluidized bed conditions, *Computer and Fluids,* 28, 323-360.

Kraume, M., Zehner, P. (2001). Experience with experimental standards for measurements of various parameters in stirred tanks: A comparative test. *Transactions of the Institution of Chemical Engineers*, 79A, 811-818.

Kee, C.S., Tan B.H.R. (2002). CFD simulation of solids suspension in mixing vessels, *The Canadian Journal of Chemical Engineering,* 80, 1-6.

Koh, P.T.L., Manickam, M., Scharz, M.P. (2000). CFD simulation of bubble- particle collision in floatation cells, *Minerals Engineering,* 13(14-15), 1455-1463.

Kuzmanic, B. Ljubicic, N. (2001). Suspension of floating solids with up-pumping pitched blade impellers; mixing time, power characteristics, *Chemical Engineering. Journal,* 84(3), 325-333.

Lahey, T.R.Jr., Drew, D.A. (2001). The analysis of two phase flow and heat transfer using a multidimensional, four field, two-fluid model, *Nuclear Engineering and Design*, 204, 29-44.

Lane, G. L., Schwarz, M.P., Evans, G.M. (2002). Predicting gas–liquid flow in a mechanically stirred tank, *Applied Mathematical Modelling*, 26(2), 223-235.

Lane, G.L., Schwarz, M.P., Evans, G.M. (2005). Numerical modelling of gas–liquid flow in stirred tanks *Chemical Engineering Science,* 60(8-9), 2203-2214.

Lapin, A., Lubbert, A. (1994). Numerical simulation of dynamics of 2-phase gas-liquid flows in bubble columns, *Chemical Engineering Science,* 49(21), 3661-3674.

Lamberto, D.J., Alvarez, M.M., Muzzio, F.J. (2001). Computational analysis of regular and chaotic mixing in a stirred tank reactor, *Chemical Engineering Science,* 56(16), 4887-4899.

Launder, B.E., Spalding, D.B. (1974). The numerical computation of turbulent flows, *Computational Methods in Applied Mechanics and Engineering*, 3, 267-289.

Launder, B.E., Reece, G.J, Rodi, W. (1975). Progress in the developments of a Reynolds turbulence closure, *Journal of Fluid Mechanics,* 68, 537-566.

Lee, K.C., Yianneskis, M., (1998). Turbulence properties of the impeller stream of a Rushton turbine, *American Institution of Chemical Engineering Journal,* 44(1), 13-24.

Ljungqvist, M., Rasmuson, A. (2001). Numerical simulation of the two phase flow in an axial stirred vessel, *Transactions of the Institution of Chemical Engineers,* 789, A, 533-546.

Lopez de Bertodano, M.A. (1998). Two fluid model for two-phase turbulent jets, *Nuclear Engineering and Design*, 179, 65-74.

Luo, J.Y., Gosman, D.A., Issa, R.I., Middleton, J.C, Fitzgerald, M.K. (1993). Full flow field computation of mixing in baffled stirred vessels, *Transactions of the Institution of Chemical Engineers,* 71A, 342-344.

Luo, J.Y., Issa, R.I, Gosman, D.A. (1994). Prediction of impeller induced flow in mixing vessels using MFR, *ICHEME Symposium series,* 136, 549-556.

Ma, Y., Zhang, Z., Xu, L., Liu, X., Wu, Y. (2001). Application of electrical resistance tomography system to monitor gas-liquid two phase flow in a horizontal pipe, *Flow Measurement, Instrumentation*, 12, 259-265.

Magelli, F., Fajner, D., Nocentini, M., Pasquali, G. (1990). Solid distribution in vessels stirred with multiple impellers, *Chemical Engineering Science,* 45(3), 615-25.

Mavros, P., Mann, R., Vlaer, S.D., Bertr, J. (2001). Experimental visualisation and CFD simulation of flow patters induced by a novel energy-saving dual configuration impeller in stirred vessels, *Transactions of the Institution of Chemical Engineers,* 78A, 857-866.

McKee, S.L., Williams, R.A., Boxman, A. (1995). Development of solids mixing models using tomographic techniques, *Chemical Engineering Journal,* 56, 101-107.

Menter, F.R. (1994). Two equation eddy-viscosity turbulence models for engineering applications *American Institution of Aeronaumics and Astronautics Journal,* 32(18), 269-289.

Mersmann, A., Werner, F., Maurer, S., Bartosch, K. (1998). Theoretical prediction of the minimum stirrer speed in mechanically agitated suspensions, *Chemical Engineering and Processing,* 37(6), 503-510.

Molerus, O., Latzel, W. (1987a). Suspension of solid particles in agitated vessels—I. Archimedes numbers 40, *Chemical Engineering Science,* 42(6), 1423-1430.

Molerus, O., Latzel, W. (1987b). Suspension of solid particles in agitated vessels—II. Archimedes numbers > 40, reliable prediction of minimum stirrer angular velocities, *Chemical Engineering Science,* 42(6), 1431-1437.

Montante, G., Lee, K., Brucato, C.A., Yianneskis, M. (1999). Double to single loop flow pattern transition in stirred vessels, *Canadian Journal of Chemical Engineering*, 77, 649-659.

Montante, G., Lee, K., Brucato, C.A., Yianneskis, M. (2001a). Numerical simulations of the dependency of flow pattern on impeller clearance in stirred vessels, *Chemical Engineering Science,* 56, 3751-3770.

Montante, G., Micale, G., Magelli, F., Brucato, A. (2001b). Experimental and CFD prediction of solid particle distribution in vessel agitated with four pitched blade turbines, *Transactions of the Institution of Chemical Engineers*, 79A, 1005-1010.

Montante, G., Pinelli, D., Magelli, F. (2003). Scale up criteria for the solids distribution in a slurry reactor stirred with multiple impellers, *Chemical Engineering Science,* 58, 5363-5372.

Murugesan, T. (2001). Critical impeller speed for solids suspension in mechanically agitated contactors, *Journal of Chemical Engineering Japan*, 34(3), 423-429.

Murthy, S., Jayanti, S. (2002). CFD study of power, mixing time for paddle mixing in unbaffled vessels, *Transactions of the Institution of Chemical Engineers,* 76A, 482-498.

Nagata, S. (1975). Mixing principles, application, *John Wiley, Sons,* New York.

Needes, C.RS., Burkin, A.R. (1973). Kinetics of nickel reduction in ammoniacal sulphate solution by hydrogen, *Hydrometallurgy Meeting,* Imperial College, London, 18th December 1973, 91-96.

Nere, K.N., Patwardhan, A.W., Joshi, J.B. (2001). Prediction of flow in stirred tanks: New constitutive equations for eddy viscosity, *Industrial Engineering Chemistry Research.* 40, 1755-1772.

Ng, K., Fentiman, J.N., Lee, K.C., Yianesskis, M. (1998). Assessment of sliding mesh CFD prediction, LDV measurement of the flow in a tank stirred by Rushton impeller, *Transactions of the Institution of Chemical Engineers*, 76A, 737-747.

Nienow, A.W. (1968). Suspension of solid particles in turbine agitated baffled vessels,

Chemical Engineering Science, 23(12), 1453-1459.

Nienow, A.W. (1996). Mixing studies: A comparison of Rushton turbine with some modern Impellers, *Chemical Engineering Research and Design,* 74A1.

Nienow, A.W. (1997). On impeller circulation, mixing effectiveness in the turbulent flow regime, *Chemical Engineering Science,* 52, 2557-2565.

Oldshue, J.Y. (1983). Fluid mixing technology, *McGraw Hill*, New York, 15.

Ochieng, A., Pearce, H., Lewis, A.E. (2003). A CFD simulation of the hydrodynamics of a reactor with, without a draft tube, In, *Proceedings of XXII International Mineral Processing Congress,* 29th September - 3rd October 2003, Cape Town, 168-1691.

Ochieng, A., Lewis, A.E. (2004). CFD simulation of mixing, power consumption in a tank with a low impeller clearance, In, *Proceedings of South African Conference on Applied Mechanics,* 18th-21st January 2004, Johannesburg, (81), 1-9.

Otomo, N., Bujalski, W., Nienow, A.W. Koji, T., (2003). A novel measurement technique for mixing time in an aerated stirred vessel, *Journal of Chemical Engineering of Japan* (36(1), 66-74.

Pettersson, M., Åke C. R. (1998). Hydrodynamics of suspensions agitated by pitched-blade turbine, *American Institution of Chemical Engineering Journal,* 44(3), 513-527.

Pinelli, D., Magelli, F. (2000). Analysis of the fluid dynamic behaviour of the liquid and gas phases in reactors stirred with multiple hydrofoil impellers. *Industrial & Engineering Chemistry Research*, 39(9), 3202-3211.

Pinelli, D., Magelli, F. (2001). Solids distribution in slurry reactors with dilute pseudoplastic suspensions, *Industrial Engineering and Chemistry Research*, 40, 4456-4462.

Pinelli, D., Montante, G., Magelli, F. (2004). Dispersion coefficients and settling velocities of solids in slurry vessels stirred with different types of multiple impellers. *Chemical Engineering Science,* 59(15), 3081-3089.

Ranade, V.V., van den Akker, H.E.A. (1994). A computation snap shot of a gas liquid flow in a baffled stirred reactor, *Chemical Engineering Science*, 49(24B), 5175-5192.

Ranade, V.V., Despande, V.R. (1999). A gas liquid flow in stirred reactor: Trailing vortices, gas accumulation behind the impeller blades, *Chemical Engineering Science,* 54, 2305-2315.

Ranade, V.V. (1999). Towards better mixing protocols by designing spatially periodic flows: The case of a jet mixer, *Chemical Engineering Science,* 51(11), 2637-2642.

Ranade, V.V., Tayalia, Y. (2001). Modelling of fluid dynamics and mixing in shallow

bubble column reactors: influence of sparger design, *Chemical Engineering Science,* 1667-1675.

Rao, K.S.M.S.R., Joshi, J. B. (1988). Liquid-phase mixing, power consumption in mechanically agitated solid-liquid contactors, *The Chemical Engineering Journal*, 39(2), 111-124.

Rieger, F., Ditl, P. (1994). Suspension of solid paticles, *Chemical Engineering Science,* 49(14), 2219-2227.

Rielly, D.C., Marquis, A.J. (2001). A particle eye view of crystallizer fluid mechanics, *Chemical Engineering Science,* 56, 2475-2493.

Rousseaux, J.-M., Vial, C., Muhr, H., Plasari, E. (2001). CFD simulation of precipitation in the sliding-surface mixing device, *Chemical Engineering Science,* 56, 1677-1685.

Sahu, A.K., Joshi, J.B. (1995). Simulation of flow in stirred vessels with axial Flow impellers: Effects of various numerical schemes, turbulence model parameters, *Industrial and Engineering Chemistry Research,* 34(2), 626-639.

Sahu, A.K., Kumar, P., Joshi, J.B. (1998). Simulation of flow in stirred vessel with axial flow impeller: Zonal modelling, optimisation of parameters, *Industrial Engineering and Chemistry Research*, 37, 2116-2130.

Sahu, A.K., Kumar P., Patwardhan, A.W., Joshi, J.B. (1999). Modelling and mixing in stirred tanks, *Chemical Engineering Science,* 54(13-14), 2285-2293.

Sato, Y., Sekoguchi, K. (1975). Liquid velocity distribution in two-phase bubble flow *International Journal of Multiphase Flow,* 2(1), 79-95.

Schäfer, M., Yianneskis, M. Wächter P., Durst, F. (1998). Trailing Vortices around a 45° Pitched-Blade, *American Institution of Chemical Engineering Journal,* 44(6), 1233-1246.

Sha, Z., Oinas, P., Louhi-Kultanen, M., Yang G., Palosaari, S. (2001a). Application of CFD simulation to suspension crystallization-factors affecting size-dependent classification, *Powder Technology,* 121(1), 20-25.

Sha, Z., Palosaari, S., Oinas, P., Ogawa, K. (2001b) CFD simulation of solid suspension in a stirred tank, *Journal of Chemical Engineering Japan*, 34(5), 621-626.

Sharma, R.N., Shaikh, A.A. (2003). Solids suspension in stirred tanks with pitched blade turbines, *Chemical Engineering Science,* 58, 2123-2140.

Smith, J.M. (1990). Industrial needs for mixing research. *Transactions of the Institution of Chemical Engineers,* 68A, 3-6.

Smith, J.M., Gao, Z., Middleton, J.C. (2001). The unsparged power demand, of modern gas dispersing impeller in boiling liquids, *Chemical Engineering Journal*, 84, 15-21.

Szalai, E.S., Arratia, P., Johnson, K., Muzzio, F.J. (2004). Mixing analysis in a tank stirred with Ekato Intermig® impellers, *Chemical Engineering Science,* 59, 3793-3805.

Tatterson, G.B. (1991). Fluid mixing and gas dispersion in agitated tanks, *McGraw-Hill*, inc. New York.

Torbacke, M., Åke, C. R. (2001). The microscopic modelling of hydrodynamics in industrial crystallisers, *Chemical Engineering Science,* 56(7), 2495 – 2509.

Versteeg, V.K., Malalasekera, W. (1995). An introduction to computational fluid dynamics: The finite volume approach, Longman Scientific, Technical.

Warsi, Z.U.A. (1999). Fluid dynamics: Theoretical, computational approaches, *CRC Press*, London.

Wachem, B.G.M. van, Almstedt, A.E. (2003). Methods of multiphase computational fluid dynamics, *Chemical Engineering Journal*, 96, 81-98.

Wei, H., Zhou, W., Garside, J. (2001). CFD modelling of precipitation process in a semibatch crystallizer, *Industrial Engineering Chemistry Research*, 40, 5255-5261.

Wernersson, E.S., Tragardh, C. (1999). Scale up of Rushton turbine-agitated tanks, *Chemical Engineering Science,* 54, 4245-4256.

Wilcox, D.C. (2000). Turbulence Modelling for CFD, *DCW Industries*.

Willis, B., Essen, J.V. (2000). Precipitation of nickel metal by hydrogen reduction: A new perspective, *Nickel, Cobalt Conference Proceedings, Atlanta 2000 Nickel/Cobalt Conference,* Perth, 15th - 17th May 2000.

Wu, H., Patterson, G.K. (1989). Laser Doppler measurement of turbulent-flow parameters in stirred mixer, *Chemical Engineering Science*, 44(10), 2207-2221.

Wu, J., Pullum, L. (2001). Impeller geometry effects on velocity, solid suspension, *Transactions of the Institution of Chemical Engineers*, 79A, 989-997.

Yeoh, S.L, Papadakis, G., Yianneskis M. (2005). Determination of mixing time, degree of homogeneity in stirred vessels with large eddy simulation, *Chemical Engineering Science,* 60(8-9), 2293-2302.

Yianneskis, M., Popiolek, Z., Whitelaw, J.H. (1987). An experimental study of the steady, unsteady flow characteristics of stirred reactors, *Journal of Fluid Mechanics*, 175, 537-555.

Yoon, H.S., Sharp, K.V., Hill D.F., Adrian, R.J, Balachpartar, S., Ha, M.Y., Kar, K.

(2001). Integrated experimental, computational approach to simulation of flow in a stirred tank, *Chemical Engineering Science,* 56(23), 6635-6649.

Zauner, R., Jones, A.G. (2000). Scale-up of Continuous, Semibatch Precipitation Processes, *Industrial and Engineering Chemistry Research,* 39(7), 2392-2403.

Zwietering, T.N.H., (1958). Suspending of solids particle in liquid by agitators, *Chemical Engineering Science*, 8, 244-253.

Appendix I

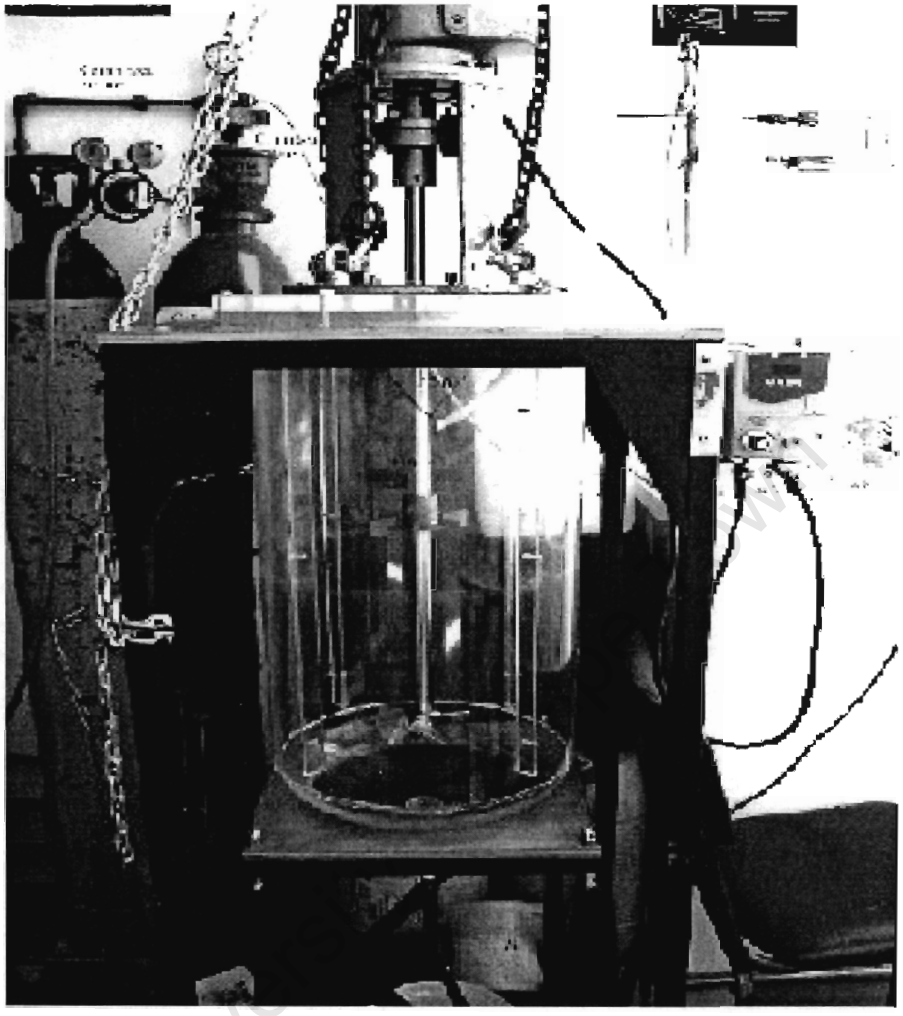

Figure A1 Experimental rig

LDV for tanks with and without a draft tube stirred by the Rushton turbine or the hydrofoil impeller

LDV data for the Rushton turbine (C=0.33T)

Table A 1. Axial velocity in the R33T configuration.

y/x---->	0.351	0.426	0.501	0.576	0.651	0.712	0.787	0.862	0.937
0.069	-0.01546	-0.01595	-0.01396	-0.00873	-0.01643	-0.02066	-0.01001	-0.01450	-0.01001
0.115	-0.01281	-0.02603	-0.04703	-0.08183	-0.02413	-0.09553	-0.01019	-0.09526	-0.07075
0.162	0.00000	0.00000	-0.16757	-0.21034	-0.11113	-0.14336	-0.06191	-0.07365	-0.05034
0.208	-0.11700	0.00000	-0.08774	-0.09164	-0.16460	-0.05094	-0.06836	-0.06753	-0.03495
0.255	-0.16000	0.00000	-0.15297	-0.17082	-0.16208	-0.11549	-0.07305	-0.06302	-0.04448
0.302	-0.18358	0.00000	-0.16423	-0.09528	-0.10527	-0.09629	-0.09444	-0.04208	-0.02849
0.348	-0.05928	0.00000	-0.13706	-0.13312	-0.10777	-0.09430	-0.06786	-0.06662	-0.03500
0.395	-0.17122	0.00000	-0.11364	-0.11894	-0.09061	-0.06022	-0.06686	-0.03558	-0.03510
0.441	-0.19430	-0.23490	-0.12590	-0.10466	-0.06340	-0.07813	-0.04777	-0.03667	-0.02775
0.488	-0.19546	-0.17348	-0.09593	-0.10848	-0.05948	-0.05868	-0.05737	-0.02515	-0.01678
0.534	-0.09066	-0.13556	-0.11640	-0.07713	-0.06372	-0.07264	-0.03863	-0.01582	-0.01056
0.581	-0.08544	-0.11224	-0.10254	-0.08644	-0.06779	-0.05631	-0.02820	-0.01758	-0.00934
0.627	-0.06587	-0.09004	-0.06853	-0.08583	-0.05352	-0.06404	-0.06564	0.00196	-0.01428
0.674	-0.06664	-0.06518	-0.06953	-0.05595	-0.07434	-0.03985	-0.03119	0.01559	0.02916
0.721	-0.04070	-0.04230	-0.02358	-0.04460	-0.01832	-0.02945	-0.01563	0.01219	-0.00067
0.767	-0.00348	0.01391	0.05018	0.00555	-0.01466	0.01030	-0.01110	0.00022	-0.02355
0.814	0.03983	0.03710	0.10296	0.05817	0.06872	0.01094	0.02884	-0.01854	-0.02268
0.860	0.12486	0.10843	0.12981	0.15346	0.09420	0.07729	0.00776	0.04774	-0.02721
0.907	0.19700	0.17430	0.20675	0.14861	0.14739	0.07059	0.09519	0.01401	-0.05112
0.954	0.24404	0.21929	0.23284	0.21351	0.15563	0.13722	0.07987	-0.07143	-0.03202

Table A 2. Radial velocity in the R33T configuration

y/x---->	**0.277**	**0.351**	**0.426**	**0.501**	**0.576**	**0.651**	**0.712**	**0.787**	**0.862**	**0.937**
0.069	0	-0.0155	-0.0159	-0.014	-0.0087	-0.0164	-0.0207	-0.01	-0.0145	-0.01
0.115	-0.0139	-0.0128	-0.026	-0.047	-0.0818	-0.0241	-0.0955	-0.0102	-0.0953	-0.0708
0.162	-0.05	0	0	-0.1676	-0.2103	-0.1111	-0.1434	-0.0619	-0.0736	-0.0503
0.208	0	0.117	0	-0.0877	-0.0916	-0.1646	-0.0509	-0.0684	-0.0675	-0.0349
0.255	-0.1006	0	0	-0.153	-0.1708	-0.1621	-0.1155	-0.073	-0.063	-0.0445
0.302	-0.1245	-0.1836	0	-0.1642	-0.0953	-0.1053	-0.0963	-0.0944	-0.0421	-0.0285
0.348	-0.173	-0.0593	0	-0.1371	-0.1331	-0.1078	-0.0943	-0.0679	-0.0666	-0.035
0.395	-0.1848	-0.1712	0	-0.1136	-0.1189	-0.0906	-0.0602	-0.0669	-0.0356	-0.0351
0.441	-0.1804	-0.1943	-0.2349	-0.1259	-0.1047	-0.0634	-0.0781	-0.0478	-0.0367	-0.0278
0.488	-0.1474	-0.1955	-0.1735	-0.0959	-0.1085	-0.0595	-0.0587	-0.0574	-0.0252	-0.0168
0.534	-0.1249	-0.0907	-0.1356	-0.1164	-0.0771	-0.0637	-0.0726	-0.0386	-0.0158	-0.0106
0.581	-0.138	-0.0854	-0.1122	-0.1025	-0.0864	-0.0678	-0.0563	-0.0282	-0.0176	-0.0093
0.627	-0.0974	-0.0659	-0.09	-0.0685	-0.0858	-0.0535	-0.064	-0.0656	0.00196	-0.0143
0.674	-0.0746	-0.0666	-0.0652	-0.0695	-0.056	-0.0743	-0.0398	-0.0312	0.01559	0.02916
0.721	-0.047	-0.0407	-0.0423	-0.0236	-0.0446	-0.0183	-0.0295	-0.0156	0.01219	-0.0007
0.767	-0.0217	-0.0035	0.01391	0.05018	0.00555	-0.0147	0.0103	-0.0111	0.00022	-0.0235
0.814	0.04062	0.03983	0.0371	0.10296	0.05817	0.06872	0.01094	0.02884	-0.0185	-0.0227
0.860	0.10814	0.12486	0.10843	0.12981	0.15346	0.0942	0.07729	0.00776	0.04774	-0.0272
0.907	0.19307	0.197	0.1743	0.20675	0.14861	0.14739	0.07059	0.09519	0.01401	-0.0511
0.954	0.24949	0.24404	0.21929	0.23284	0.21351	0.15563	0.13722	0.07987	-0.0714	-0.032

Table A 3. Tangential velocity in the R33T configuration

y/x---->	**0.277**	**0.351**	**0.426**	**0.501**	**0.576**	**0.651**	**0.712**	**0.787**	**0.862**	**0.937**
0.069	0.03516	0.04531	0.04384	0.02869	0.0451	0.04806	0.04015	0.04976	0.03011	0.03837
0.115	0.06876	0.05068	0.0832	0.04697	0.12194	0.14367	0.22223	0.05486	0.15188	0.19704
0.162	0.05967	0.21471	0.19067	0.12688	0.16148	0.1696	0.19572	0.09988	0.17582	0.16006
0.208	0.36769	0.35586	0.1486	0.12392	0.14204	0.15482	0.18654	0.1282	0.17337	0.14749
0.255	0.2943	0.33182	0.14596	0.18071	0.1408	0.17921	0.13277	0.13221	0.11581	0.17854
0.302	0.33672	0.21514	0.14545	0.14777	0.15551	0.16787	0.15936	0.12803	0.15099	0.10844
0.348	0.48727	0.18137	0.13752	0.15533	0.52832	0.26601	0.44705	0.16121	0.16721	0.11861
0.395	0.43982	0.13944	0.16425	0.15825	0.15738	0.167	0.38813	0.16568	0.14664	0.11927
0.441	0.46024	0.12658	0.14133	0.15142	0.45024	0.25711	0.17078	0.15337	0.13729	0.12439
0.488	0.59313	0.13466	0.14812	0.16996	0.17821	0.23255	0.15513	0.21839	0.14199	0.12661
0.534	0.51784	0.13335	0.17564	0.17401	0.21686	0.15805	0.17496	0.16129	0.15612	0.14712
0.581	0.43332	0.24381	0.15007	0.16941	0.16418	0.18712	0.16067	0.24815	0.16896	0.37668
0.627	0.33381	0.12789	0.18312	0.20105	0.17239	0.17599	0.17086	0.18184	0.15022	0.12189
0.674	0.27993	0.15019	0.16707	0.1693	0.18257	0.18304	0.18167	0.17006	0.15035	0.12459
0.721	0.22279	0.15477	0.17002	0.17371	0.178	0.21427	0.44257	0.16413	0.14373	0.12422
0.767	0.20081	0.16366	0.15564	0.17677	0.17014	0.24626	0.15244	0.15175	0.13786	0.13496
0.814	0.17409	0.16813	0.17477	0.15735	0.38728	0.16934	0.18343	0.38112	0.1271	0.11514
0.860	0.26923	0.18061	0.21669	0.1785	0.15745	0.17295	0.37892	0.14584	0.12072	0.10032
0.907	0.18979	0.16993	0.16514	0.1413	0.14685	0.14578	0.14892	0.14262	0.12324	0.12638
0.954	0.17323	0.15383	0.13322	0.15799	0.1538	0.14659	0.12893	0.12937	0.0696	0.04445

Table A 4. Turbulent kinetic energy in the R33T configuration

y/x---->	**0.277**	**0.351**	**0.426**	**0.501**	**0.576**	**0.651**	**0.712**	**0.787**	**0.862**	**0.937**
0.069	0.0042	0.00376	0.00656	0.00811	0.0061	0.02386	0.02729	0.01266	0.00645	0.00796
0.115	0.00725	0.0071	0.00603	0.02467	0.00993	0.01104	0.0254	0.31467	0.00967	0.02673
0.162	0.00801	0.00267	0.00277	0.00714	0.04805	0.10301	0.0571	0.1293	0.0166	0.02117
0.208	0.03602	0.01024	0.64948	0.16667	0.18916	0.03436	0.34612	0.03126	0.0295	0.04524
0.255	0.04353	0.02054	0.00826	0.14097	0.02602	0.05165	0.06743	0.02781	0.05786	0.01967
0.302	0.08331	0.22894	0.00876	0.07012	0.08831	0.06101	0.00996	0.04785	0.01088	0.03662
0.348	0.14484	0.04704	0.22812	0.09839	0.01434	0.04238	0.05657	0.0186	0.04196	0.03214
0.395	0.17153	0.03466	0.011	0.06786	0.0273	0.07506	0.04234	0.02729	0.02462	0.01453
0.441	0.16786	0.00945	0.06121	0.07447	0.08649	0.06638	0.05402	0.04754	0.04188	0.02657
0.488	0.1183	0.02638	0.06867	0.06215	0.02439	0.10035	0.07575	0.05178	0.01218	0.02428
0.534	0.06117	0.03214	0.14124	0.02718	0.08703	0.09866	0.01537	0.05069	0.00863	0.01143
0.581	0.29108	0.0404	0.00967	0.02547	0.03699	129496	0.00854	0.00931	0.02638	0.03042
0.627	0.03595	0.00535	0.00666	0.0289	0.03735	0.02919	0.03369	0.05672	129496	0.02358
0.674	0.02244	0.01507	0.00724	0.04879	0.03251	0.05107	0.03177	0.04352	0.02663	0.02254
0.721	0.01767	0.00555	0.00878	0.01025	0.04235	0.05162	0.01271	0.02614	0.02134	0.00428
0.767	0.02204	0.01905	0.00793	0.01987	0.03204	0.0286	0.03601	0.02279	0.02815	0.01492
0.814	0.03052	0.01214	0.01745	0.04401	0.022	0.02992	0.03654	0.01041	0.02413	0.01829
0.860	0.02086	0.01145	0.01673	0.01711	0.01414	0.022	0.04485	0.02487	0.01075	0.0115
0.907	0.01204	0.01758	0.0164	0.00983	0.04484	0.01189	0.02249	0.03247	0.02515	0.03055
0.954	0.00975	0.00806	0.02731	0.01462	0.07919	0.07003	0.0281	0.00923	0.0139	0.00566

LDV data for the Rushton turbine (C=0.15T)

Table A 5. Axial velocity in the R15T configuration

y/x---->	**0.351**	**0.426**	**0.501**	**0.576**	**0.651**	**0.712**	**0.787**	**0.862**	**0.937**
0.069	-0.00586	-0.00696	-0.00169	-0.00328	-0.00620	-0.00444	-0.00382	-0.00471	-0.00465
0.115	-0.09988	-0.16064	-0.17152	-0.15067	-0.13210	-0.10188	-0.11075	-0.07962	-0.05172
0.162	-0.15765	-0.17395	-0.16469	-0.15219	-0.14960	-0.10285	-0.10086	-0.07646	-0.04516
0.208	-0.17000	-0.16738	-0.14906	-0.14021	-0.14483	-0.10791	-0.09006	-0.06069	-0.03322
0.255	-0.15793	-0.15429	-0.17176	-0.14212	-0.13862	-0.11149	-0.08145	-0.05409	-0.02890
0.302	-0.15854	-0.16708	-0.14957	-0.13910	-0.11914	-0.10063	-0.08525	-0.04353	-0.02733
0.348	-0.16146	-0.15562	-0.14849	-0.13611	-0.11418	-0.10288	-0.06080	-0.05103	-0.01857
0.395	-0.13984	-0.14560	-0.14600	-0.13946	-0.09701	-0.10130	-0.09082	-0.03641	-0.01309
0.441	-0.13466	-0.12971	-0.14496	-0.12549	-0.12089	-0.10498	-0.07557	-0.04402	-0.02877
0.488	-0.12921	-0.11571	-0.13411	-0.11343	-0.11815	-0.09413	-0.07063	-0.05938	-0.02882
0.534	-0.12398	-0.11963	-0.10090	-0.12524	-0.10079	-0.08184	-0.06575	-0.01052	0.01009
0.581	-0.11583	-0.10135	-0.11153	-0.11099	-0.09529	-0.08516	-0.07338	-0.03630	-0.03220
0.627	-0.10257	-0.08894	-0.08823	-0.09011	-0.07979	-0.08444	-0.04920	-0.02923	-0.00657
0.674	-0.07287	-0.07637	-0.07927	-0.07592	-0.06100	-0.07394	-0.04648	-0.01515	0.00157
0.721	-0.05423	-0.05245	-0.05527	-0.04766	-0.02752	-0.04208	-0.01386	-0.03400	-0.02385
0.767	-0.03419	-0.01630	-0.01510	0.01028	-0.01449	-0.00571	-0.00710	0.00831	0.01111
0.814	0.02157	0.04057	0.05171	0.08744	0.04668	0.04648	0.04554	0.01894	0.01210
0.860	0.09379	0.09399	0.12762	0.10055	0.07776	0.11204	0.09197	0.03994	0.00195
0.907	0.19662	0.19684	0.18139	0.19045	0.18451	0.15571	0.12377	0.06317	-0.00743
0.954	0.30007	0.27202	0.28197	0.26130	0.20711	0.13706	0.10403	0.00503	-0.03063

Table A 6. Tangential velocity in the R15T configuration

y/x--->	0.277	0.351	0.426	0.501	0.576	0.651	0.712	0.787	0.862	0.937
0.069	0.19489	0.19625	0.19522	0.19485	0.19444	0.19582	0.19456	0.19156	0.19085	0.19134
0.115	0.14212	0.12557	0.16413	0.18068	0.07114	0.08590	0.09096	0.11543	0.07840	0.09960
0.162	0.05251	0.06180	0.06361	0.05197	0.05860	0.07326	0.06113	0.08643	0.07096	0.08897
0.208	0.07158	0.06682	0.06556	0.07728	0.07000	0.08206	0.08867	0.09608	0.09080	0.10014
0.255	0.06501	0.05951	0.06558	0.07011	0.08053	0.08609	0.08976	0.08513	0.09039	0.11133
0.302	0.07412	0.08147	0.06929	0.08800	0.09356	0.08587	0.09618	0.08895	0.08710	0.10447
0.348	0.08037	0.07659	0.09104	0.09878	0.10261	0.10511	0.10792	0.10066	0.08056	0.10400
0.395	0.08397	0.08850	0.08564	0.09952	0.11126	0.11022	0.09838	0.09614	0.09026	0.10460
0.441	0.08197	0.10031	0.11241	0.11178	0.12477	0.11287	0.09984	0.09088	0.08094	0.08944
0.488	0.09439	0.10710	0.10974	0.12848	0.13301	0.11745	0.11165	0.09656	0.07405	0.08960
0.534	0.10071	0.10057	0.11630	0.11300	0.12758	0.12424	0.10128	0.08067	0.07880	0.06080
0.581	0.09985	0.10050	0.12042	0.12322	0.12547	0.11350	0.10329	0.06867	0.06909	0.06612
0.628	0.09656	0.10622	0.11269	0.12247	0.11889	0.11012	0.09300	0.08008	0.05915	0.05693
0.674	0.10141	0.09174	0.11184	0.11181	0.10815	0.10002	0.09866	0.08133	0.06164	0.05400
0.721	0.09207	0.09200	0.09579	0.11402	0.10268	0.10654	0.09540	0.08342	0.05908	0.05073
0.767	0.09709	0.09312	0.07641	0.08779	0.08264	0.10054	0.08414	0.08181	0.05667	0.04676
0.814	0.09419	0.09875	0.11088	0.10586	0.08170	0.09175	0.09173	0.07954	0.05907	0.04665
0.860	0.10695	0.12368	0.12145	0.09684	0.09567	0.08990	0.09921	0.07583	0.05461	0.04515
0.907	0.12231	0.12440	0.12740	0.12212	0.12220	0.10292	0.10297	0.07295	0.06549	0.04234
0.953	0.14114	0.13619	0.13215	0.13092	0.11953	0.11376	0.09680	0.06015	0.03807	0.04909

Table A 7. Turbulent kinetic energy in the R15T configuration

y/x---->	0.277	0.351	0.426	0.501	0.576	0.651	0.712	0.787	0.862	0.937
0.069	0.03861	0.01766	0.03701	0.02632	0.02759	0.01483	0.01986	0.01037	0.01236	0.00295
0.115	0.04785	0.05969	0.05550	0.03649	0.04235	0.01474	0.02984	0.01603	0.03449	0.03124
0.162	0.03009	0.04078	0.04591	0.05837	0.02612	0.06297	0.02593	0.01984	0.02341	0.01881
0.208	0.01413	0.03445	0.04007	0.03343	0.04038	0.03475	0.03399	0.02217	0.02809	0.02141
0.255	0.04012	0.05194	0.03998	0.03578	0.05057	0.04326	0.03100	0.03233	0.03876	0.02211
0.302	0.04360	0.02242	0.03310	0.03404	0.03606	0.01970	0.02319	0.02293	0.01436	0.02508
0.348	0.01917	0.01884	0.02874	0.01703	0.02920	0.04098	0.05014	0.02592	0.03929	0.02010
0.395	0.02011	0.00795	0.02004	0.02713	0.02779	0.03894	0.02956	0.02700	0.01703	0.02063
0.441	0.02238	0.01586	0.03268	0.01552	0.02194	0.02853	0.02735	0.03205	0.03462	0.01640
0.488	0.02387	0.01188	0.02676	0.02436	0.03805	0.04367	0.03253	0.01398	0.02916	0.04409
0.534	0.01216	0.01279	0.02805	0.03779	0.03387	0.01581	0.04410	0.02164	0.01917	0.02004
0.581	0.01149	0.00962	0.01341	0.03301	0.01861	0.01867	0.01337	0.01708	0.02298	0.00939
0.627	0.01777	0.00953	0.01682	0.01911	0.01819	0.02364	0.01394	0.02329	0.02360	0.01000
0.674	0.01073	0.01493	0.01517	0.01457	0.02396	0.02186	0.01328	0.02811	0.02235	0.00986
0.721	0.00654	0.00726	0.01740	0.00968	0.05901	0.01248	0.01785	0.02001	0.03262	0.00622
0.767	0.01948	0.00833	0.01870	0.01913	0.02222	0.03771	0.02798	0.02974	0.03670	0.01653
0.814	0.01846	0.00978	0.04850	0.03661	0.04218	0.02957	0.07900	0.03747	0.02286	0.00869
0.860	0.02123	0.00799	0.01455	0.02801	0.01949	0.01613	0.00924	0.02180	0.00562	0.00466
0.907	0.02914	0.04630	0.03496	0.04153	0.04753	0.04723	0.01175	0.02139	0.01285	0.00477
0.954	0.06196	0.05356	0.03092	0.02526	0.01783	0.01635	0.02145	0.00980	0.00928	0.00236

LDV data for the Rushton turbine in a tank with draft tube (C=0.15T), H=1.4T, V_{tip}= 1.3ms^{-1}

Table A 8. Axial velocity in the R15T-DT configuration

y/x---->	0.277	0.351	0.426	0.501	0.576	0.651	0.712	0.787	0.862	0.937	1.012	1.087	1.162	1.282
0.069	0.0000	-0.0163	-0.0132	-0.0029	-0.0061	-0.0094	-0.0043	-0.0062	-0.0156	-0.0087	-0.0257	-0.0120	-0.0107	-0.0169
0.115	-0.0292	-0.0279	-0.1614	-0.2165	-0.2198	-0.1584	-0.1858	-0.2752	-0.2441	-0.2826	-0.1533	-0.2754	-0.2718	-0.1499
0.162	-0.0179	-0.2278	-0.1776	-0.1713	-0.1800	-0.1637	-0.2985	-0.2584	-0.1892	-0.2597	-0.1736	-0.2654	-0.2349	-0.1645
0.208	-0.2245	-0.2269	-0.1905	-0.2170	-0.2320	-0.2250	-0.2492	-0.2706	-0.2714	-0.2438	-0.2413	-0.2071	-0.2186	-0.1676
0.255	-0.2027	-0.1945	-0.2375	-0.2147	-0.2230	-0.2098	-0.2311	-0.1997	-0.2705	-0.2381	-0.2666	-0.2112	-0.2469	-0.1405
0.302	-0.0870	-0.2347	-0.2033	-0.2047	-0.2689	-0.2262	-0.2111	-0.2233	-0.1886	-0.1996	-0.2045	-0.1988	-0.2864	-0.1211
0.348	-0.1494	-0.2019	-0.1761	-0.2141	-0.1868	-0.2115	-0.1999	-0.1887	-0.1622	-0.2160	-0.1754	-0.2416	-0.2325	-0.1390
0.395	-0.2348	-0.2002	-0.1918	-0.1979	-0.2000	-0.1836	-0.1792	-0.1956	-0.1751	-0.1600	-0.1659	-0.1333	-0.1512	-0.1582
0.441	-0.3325	-0.1827	-0.1853	-0.1874	-0.2002	-0.1771	-0.2138	-0.1826	-0.1744	-0.1587	-0.1250	-0.0568	-0.0240	-0.1131
0.488	-0.0965	-0.1528	-0.0970	-0.0727	-0.0512	-0.0973	-0.1072	-0.0147	-0.1098	-0.0370	-0.0399	-0.0503	0.0200	-0.0869
0.534	-0.0447	-0.0700	-0.0644	-0.0098	-0.0296	-0.0153	-0.0426	-0.0140	-0.0232	-0.0034	0.0041	-0.0154	0.0548	0.0290
0.581	-0.1018	-0.1139	-0.1156	-0.0729	-0.0538	-0.0279	-0.0072	-0.0214	0.0202	0.0421	0.0116	0.0638	0.0787	0.0451
0.627	-0.1096	-0.0774	-0.0739	-0.0933	-0.0560	-0.0302	-0.0117	-0.0063	0.0265	0.0501	0.0560	0.0737	0.0763	0.0469
0.674	-0.0699	-0.0778	-0.0902	-0.0961	-0.0527	-0.0572	-0.0183	-0.0075	0.0240	0.0510	0.0523	0.0718	0.0861	0.0184
0.721	-0.0501	-0.0567	-0.1015	-0.0747	-0.0788	-0.0294	-0.0289	-0.0029	0.0225	0.0366	0.0688	0.0704	0.0714	0.0191
0.767	-0.0333	-0.0255	-0.0796	-0.0458	-0.0570	-0.0409	-0.0234	0.0009	0.0283	0.0479	0.0665	0.0708	0.0592	0.0266
0.814	0.0067	-0.0070	0.0034	0.0129	-0.0028	0.0200	0.0110	0.0245	0.0000	0.0509	0.0633	0.0619	0.0411	0.0147
0.860	0.0659	0.0905	0.0881	0.0871	0.1004	0.0700	0.1112	0.0585	0.0674	0.0763	0.0537	0.0577	0.0508	0.0006
0.907	0.1529	0.1646	0.1936	0.1999	0.1809	0.1477	0.1377	0.1016	0.0977	0.0683	0.0664	0.0534	0.0454	-0.0134
0.954	0.2870	0.2994	0.2730	0.2286	0.2020	0.1846	0.1642	0.0930	0.0793	0.0581	0.0343	0.0293	0.0420	-0.0374

Table A 9. Radial velocity in the R15T-DT configuration

y/x---->	0.2765	0.3514	0.4262	0.5010	0.5760	0.6508	0.7124	0.7873	0.8621	0.9370	1.0119	1.0868	1.1617	1.2817
0.0688	0.0188	0.0070	0.0050	0.0108	0.0069	0.0193	0.0155	0.0205	0.0152	0.0132	0.0245	0.0203	0.0119	-0.0167
0.1153	0.0246	0.0049	-0.0013	0.0083	0.0063	0.0130	0.0108	0.0181	0.0081	0.0208	0.0224	-0.0105	0.0017	-0.0251
0.1619	0.0074	-0.0075	0.0058	0.0108	0.0050	-0.0001	-0.0066	0.0118	0.0236	0.0203	0.0217	-0.0012	-0.0087	-0.0634
0.2084	0.0005	0.0112	0.0019	0.0062	-0.0009	0.0134	0.0159	0.0078	0.0310	0.0300	-0.0007	-0.0199	-0.0494	-0.0975
0.2551	0.0063	0.0069	-0.0082	0.0152	0.0087	0.0056	0.0222	0.0195	0.0089	0.0339	0.0091	0.0043	-0.0519	-0.1040
0.3015	-0.0056	0.0025	0.0026	0.0000	-0.0013	0.0070	0.0135	0.0000	0.0176	0.0313	0.0128	0.0190	0.0000	-0.1236
0.3481	-0.0113	0.0093	-0.0043	0.0025	0.0008	-0.0091	0.0025	0.0103	0.0136	0.0280	0.0200	0.0144	0.0000	-0.1201
0.3947	0.0011	-0.0026	-0.0112	-0.0066	-0.0120	0.0048	-0.0046	0.0057	0.0110	0.0116	0.0099	0.0215	0.0000	-0.1589
0.4412	-0.0091	-0.0095	-0.0093	0.0036	-0.0073	-0.0074	-0.0095	-0.0076	-0.0004	-0.0016	-0.0061	-0.0243	-0.0123	-0.1582
0.4878	0.0000	0.0000	0.0000	0.0000	0.0000	0.0000	0.0000	0.0000	0.0000	0.0000	0.0000	0.0000	0.0000	-0.0848
0.5344	-0.0057	-0.0066	-0.0115	-0.0114	-0.0048	0.0048	0.0030	-0.0061	-0.0033	-0.0057	-0.0082	-0.0075	-0.0171	-0.1030
0.5809	-0.0046	-0.0240	0.0000	0.0000	0.0000	0.0000	0.0000	0.0000	0.0000	0.0000	0.0000	0.0000	0.0000	0.0000
0.6275	-0.0010	0.0000	0.0000	0.0000	0.0000	0.0000	0.0000	0.0000	0.0000	0.0000	0.0000	0.0000	0.0000	0.0000
0.6741	0.0025	-0.0160	0.0000	-0.0145	-0.0140	-0.0032	-0.0121	-0.0019	-0.0008	-0.0092	0.0000	0.0000	0.0000	0.0000
0.7206	0.0061	0.0000	0.0000	0.0000	0.0000	0.0000	0.0000	0.0000	0.0000	0.0000	0.0000	0.0000	0.0000	0.0000
0.7672	0.0109	-0.0033	0.0000	-0.0139	-0.0150	-0.0356	-0.0217	-0.0248	0.0077	-0.0098	-0.0140	-0.0049	-0.0005	-0.0321
0.8138	-0.0031	-0.0085	-0.0176	-0.0129	-0.0282	-0.0254	-0.0216	-0.0318	-0.0047	-0.0014	-0.0060	-0.0051	-0.0158	-0.0050
0.8603	-0.0022	-0.0130	-0.0237	-0.0344	-0.0319	-0.0347	-0.0289	-0.0327	-0.0252	0.0064	-0.0069	-0.0075	-0.0090	-0.0284
0.9069	0.0137	-0.0180	-0.0226	-0.0178	-0.0267	-0.0292	-0.0267	-0.0140	-0.0240	-0.0082	-0.0125	-0.0084	-0.0089	-0.0165
0.9534	-0.0061	-0.0197	-0.0364	-0.0185	-0.0204	-0.0131	-0.0181	-0.0179	-0.0205	-0.0157	0.0030	-0.0252	-0.0117	-0.0240

Table A 10. Tangential velocity in the R15T-DT configuration

y/x---->	0.2765	0.3514	0.4262	0.5010	0.5760	0.6508	0.7124	0.7873	0.8621	0.9370	1.0119	1.0868	1.1617	1.2817
0.0688	0.1963	0.1931	0.1936	0.1916	0.1938	0.1927	0.1914	0.1909	0.1918	0.1909	0.1877	0.1856	0.1837	0.1813
0.1153	0.1378	0.1347	0.1868	0.1630	0.1466	0.1605	0.1565	0.1579	0.0851	0.0972	0.1047	0.1013	0.0905	0.0947
0.1620	0.0371	0.0563	0.0557	0.0709	0.0643	0.0724	0.0747	0.0805	0.0791	0.0834	0.0852	0.0898	0.0965	0.0896
0.2085	0.0494	0.0543	0.0555	0.0665	0.0580	0.0725	0.0728	0.0731	0.0789	0.0830	0.0811	0.0841	0.1197	0.0945
0.2551	0.0709	0.0356	0.0438	0.0535	0.0628	0.0671	0.0758	-0.0668	0.0765	0.0840	0.0807	0.0894	0.0989	0.0732
0.3017	0.0526	0.0579	0.0628	0.0629	0.0653	0.0673	0.0679	0.0895	0.0762	0.0765	0.0966	0.0902	0.0605	0.0517
0.3481	0.0637	0.0623	0.0665	0.0667	0.0690	0.0736	0.0639	0.0776	0.0667	0.0713	0.0441	0.0571	0.0737	0.0651
0.3946	0.0677	0.0754	0.0805	0.0227	0.0742	0.0693	0.0807	0.0821	0.0781	0.0657	0.0801	0.0560	0.0583	0.0428
0.4414	0.0837	0.0795	0.0806	0.0902	0.0779	0.0871	0.0690	0.0864	0.0910	0.0000	0.0896	0.0846	0.0741	0.0365
0.4877	0.0240	0.0480	-0.0152	-0.0160	0.0320	0.0870	0.0432	0.0037	-0.0120	0.0000	-0.0060	0.0560	0.0152	0.0460
0.5344	-0.0060	-0.0057	-0.0071	-0.0175	-0.0120	0.0000	-0.0069	-0.0053	-0.0167	-0.0144	0.0373	0.0000	0.0575	0.0839
0.5811	0.0284	0.0602	0.0938	0.1283	0.1290	0.1145	0.1224	0.0720	0.0960	0.0774	0.0960	0.0000	0.0808	0.0680
0.6274	0.0564	0.0595	0.0905	0.1202	0.1126	0.1133	0.1176	0.1147	0.0942	0.1063	0.0933	0.0360	0.0766	0.0526
0.6740	0.0602	0.0505	0.0807	0.0958	0.0880	0.0989	0.0880	0.0820	0.0938	0.0918	0.0797	0.0768	0.0662	0.0468
0.7206	0.0614	0.0656	0.0627	0.0646	0.0626	0.0753	0.0619	0.0603	0.0788	0.0793	0.0788	0.0703	0.0583	0.0337
0.7672	0.0781	0.0829	0.0653	0.0601	0.0549	0.0573	0.0580	0.0448	0.0595	0.0696	0.0540	0.0652	0.0505	0.0303
0.8138	0.0995	0.0930	0.0868	0.0729	0.0602	0.0497	0.0526	0.0337	0.0371	0.0468	0.0412	0.0377	0.0328	0.0339
0.8602	0.1036	0.1130	0.0962	0.0918	0.0769	0.0767	0.0602	0.0549	0.0460	0.0405	0.0450	0.0451	0.0417	0.0355
0.9069	0.1273	0.1333	0.1312	0.1382	0.1186	0.0808	0.0822	0.0625	0.0539	0.0482	0.0285	0.0197	0.0232	0.0229
0.9535	0.1464	0.1393	0.1412	0.1191	0.1121	0.0999	0.0519	0.0427	-0.0048	0.0960	0.0232	0.0147	0.0349	0.0254

Table A 11. Turbulent kinetic energy R15T-DT configuration

y/x---->	0.277	0.351	0.426	0.501	0.576	0.651	0.712	0.787	0.862	0.937
0.069	0.01197	0.04739	0.00497	0.00267	0.00553	0.00319	0.0028	0.00264	0.00595	0.00386
0.115	0.02446	0.12578	0.00882	0.04723	0.00912	0.13062	0.24905	0.05994	0.00453	0.05224
0.162	0.05602	0.08055	0.14957	0.13852	0.13633	0.25764	0.13958	0.09177	0.22462	0.39982
0.208	0.09234	0.0539	0.14734	0.09138	0.04203	0.12994	0.0512	0.13088	0.05296	0.15512
0.255	0.00406	0.15875	0.09249	0.13794	0.15664	0.10206	0.03344	0.59361	0.13427	0.12131
0.302	0.00866	0.06555	0.08124	0.13521	0.10354	0.16274	0.14105	0.03289	0.14813	0.11244
0.348	0.17591	0.09921	0.15668	0.05256	0.1205	0.129	0.07381	0.11969	0.23991	0.09633
0.395	0.06274	0.17483	0.08322	0.22339	0.20634	0.02553	0.01544	0.09197	0.13014	0.06302
0.441	0.24446	0.08243	0.02527	0.07088	0.12286	0.09393	0.11339	0.06452	0.04168	0.03712
0.488	0.00832	0.04032	0.00537	0.02632	0.02062	0.02083	0.01266	0.09393	0.02498	0.00408
0.534	0.00707	0.02612	0.00331	0.01652	0.05049	0.00366	0.00401	0.0101	0.00411	0.00376
0.581	0.0172	0.01924	0.02182	0.01868	0.02083	0.23575	0.10096	0.00937	0.00614	0.00538
0.627	0.05559	0.00663	0.09557	0.03437	0.04947	0.28141	0.01127	0.29206	0.00718	0.0061
0.674	0.02358	0.04684	0.06792	0.0385	0.00928	0.01919	0.0673	0.04689	0.00917	0.00581
0.721	0.01016	0.03019	0.03415	0.06144	0.06765	0.07316	0.03189	0.02741	0.02404	0.00993
0.767	0.01251	0.01317	0.04787	0.02734	0.0744	0.04193	0.02993	0.02761	0.05697	0.00959
0.814	0.01381	0.01318	0.01084	0.01527	0.02595	0.01709	0.01701	0.06252	0.04208	0.00897
0.860	0.01296	0.01123	0.0266	0.0568	0.02981	0.0243	0.01327	0.01491	0.02	0.0474
0.907	0.0853	0.01123	0.01188	0.04954	0.01221	0.02494	0.01306	0.01445	0.00896	0.01111
0.954	0.01147	0.01475	0.04752	0.10196	0.08638	0.11372	0.07941	0.06739	0.00687	0.01665

LDV data for the hydrofoil impeller

Table A 12. Axial velocity in the H15T configuration.

y/x---->	0.277	0.351	0.426	0.501	0.576	0.651	0.712	0.787	0.862	0.937
0.069	-0.0115	-0.073	-0.0897	-0.0191	-0.0455	-0.0319	-0.0729	-0.0234	-0.0145	-0.0447
0.115	-0.1945	-0.1947	-0.192	-0.1878	-0.1527	-0.1162	-0.133	-0.0875	-0.0601	-0.0672
0.162	-0.2257	-0.174	-0.1541	-0.1649	-0.1355	-0.1262	-0.1149	-0.0875	-0.0522	-0.0531
0.208	-0.2105	-0.1863	-0.1789	-0.1662	-0.1437	-0.1216	-0.117	-0.0868	-0.0695	-0.0641
0.255	0	-0.139	-0.1765	-0.1629	-0.1381	-0.1371	-0.1065	-0.0692	-0.0614	-0.0487
0.302	-0.1818	-0.1744	-0.1767	-0.1701	-0.1388	-0.1298	-0.1194	-0.0735	-0.059	-0.0466
0.348	-0.1881	-0.175	-0.1699	-0.1452	-0.1381	-0.1356	-0.0859	-0.065	-0.0569	-0.028
0.395	-0.1746	-0.1444	-0.1729	-0.1727	-0.1516	-0.1189	-0.0879	-0.0591	-0.0508	-0.0372
0.441	-0.1347	-0.1588	-0.1313	-0.1214	-0.1435	-0.116	-0.0955	-0.0603	-0.0474	-0.0294
0.488	-0.1319	-0.1173	-0.1258	-0.1416	-0.1588	-0.0936	-0.0892	-0.06	-0.0324	-0.0533
0.534	-0.1009	-0.1428	-0.146	-0.1167	-0.1434	-0.0757	-0.0777	-0.0611	-0.0464	0.00089
0.581	-0.0654	-0.1065	-0.1403	-0.1263	-0.1037	-0.1093	-0.0552	-0.0365	-0.0282	-0.0101
0.627	-0.0635	-0.1078	-0.1117	-0.1248	-0.0843	-0.0736	-0.0339	-0.0168	-0.0099	-0.0158
0.674	-0.0561	-0.0878	-0.1056	-0.0558	-0.0729	-0.0312	-0.0246	-0.0115	-0.0309	0.01996
0.721	-0.0504	-0.0527	-0.0521	-0.0537	-0.026	-0.0327	0.02596	0.024	0.00087	0.00321
0.767	-3E-05	-0.015	-0.0107	0.00363	0.02435	0.02628	0.04277	0.00738	0.00058	0.0128
0.814	0.01681	0.03914	0.07479	0.07482	0.06455	0.04456	0.06571	0.08223	0.01248	0.00103
0.860	0.0899	0.11772	0.11124	0.13841	0.14007	0.13668	0.1268	0.05223	-0.005	0.00853
0.907	0.18914	0.21724	0.23184	0.21471	0.19581	0.12006	0.13296	0.09843	-0.0034	0.0182
0.954	0.31269	0.31747	0.235	0.26373	0.25456	0.14223	0.08079	0.13901	0.00746	0.06389

Table A 13. Radial velocity in the H15T configuration.

y/x---->	0.277	0.351	0.426	0.501	0.576	0.651	0.712	0.787	0.862	0.937
0.069	0.0200	0.0120	0.0117	0.0084	0.0005	0.0058	0.0013	-0.0001	0.0000	-0.0100
0.115	0.0097	0.0043	0.0009	-0.0012	-0.0073	-0.0073	-0.0462	-0.0130	0.0000	-0.0081
0.162	0.0095	0.0087	-0.0014	-0.0045	-0.0117	-0.0198	-0.0152	0.0000	0.0000	-0.0200
0.208	-0.0043	-0.0068	-0.0079	-0.0030	-0.0244	-0.0193	-0.0134	-0.0174	0.0000	-0.0303
0.255	-0.0226	-0.0078	-0.0138	-0.0160	-0.0148	-0.0258	-0.0336	-0.0176	0.0000	-0.0329
0.302	-0.0257	-0.0029	-0.0142	0.0122	-0.0268	-0.0131	-0.0249	0.0000	-0.0206	-0.0321
0.348	-0.0242	0.0031	-0.0059	0.0000	-0.0157	-0.0229	-0.0180	-0.0171	-0.0202	-0.0355
0.395	-0.0125	-0.0130	-0.0023	0.0016	-0.0342	-0.0294	-0.0227	-0.0207	-0.0318	-0.0268
0.441	-0.0029	0.0098	-0.0116	-0.0029	-0.0294	-0.0202	-0.0425	-0.0332	-0.0290	-0.0257
0.488	0.0000	0.0042	-0.0017	0.0000	-0.0225	-0.0471	-0.0408	-0.0440	-0.0383	-0.0195
0.534	0.0000	0.0017	0.0091	0.0000	-0.0262	0.0000	-0.0485	-0.0444	-0.0282	-0.0398
0.581	0.0000	0.0000	0.0000	0.0000	0.0000	0.0000	0.0000	0.0000	0.0000	0.0000
0.627	0.0000	0.0000	0.0000	0.0000	0.0000	0.0000	0.0000	-0.0377	-0.0216	-0.0318
0.674	0.0110	0.0000	0.0000	0.0000	0.0000	0.0000	0.0000	0.0000	0.0000	0.0000
0.721	0.0101	0.0000	0.0000	0.0000	0.0000	0.0000	0.0000	0.0000	0.0000	0.0000
0.767	0.0144	-0.0047	0.0000	-0.0377	-0.0464	-0.0741	-0.0687	0.0000	-0.0444	-0.0292
0.814	-0.0012	-0.0143	-0.0238	-0.0436	-0.0575	-0.0655	-0.0486	0.0000	-0.0315	-0.0198
0.860	0.0036	-0.0340	-0.0228	-0.0471	-0.0584	-0.0520	-0.0483	0.0000	-0.0213	-0.0033
0.907	0.0000	-0.0304	-0.0348	-0.0465	-0.0406	-0.0404	-0.0291	0.0000	-0.0105	-0.0070
0.954	-0.0164	-0.0350	-0.0080	0.0000	0.0000	0.0000	0.0000	0.0000	0.0000	0.0000

Table A 14. Tangential velocity in the H15T configuration

y/x---->	**0.277**	**0.351**	**0.426**	**0.501**	**0.576**	**0.651**	**0.712**	**0.787**	**0.862**	**0.937**
0.069	0.184	0.18773	0.002	0.17938	0.17986	0.18292	0.18196	0.17951	0.16962	0.17403
0.115	0.09955	0.15367	0.02644	0.02833	0.01348	0.01132	0.02859	0.02974	0.01134	0.00029
0.162	0.00737	0.01236	-0.0094	0.01885	0.02677	0.00395	0.00814	0.00664	0.00786	0.02195
0.208	0.01684	0.00124	0.00128	4.8E-05	0.02072	-0.0055	-0.0073	0.01399	0.01354	0.03261
0.255	0.01609	0.00316	0.00103	0.01204	0.00458	0.00874	0.00173	-0.004	-0.0029	0.00277
0.302	0.02534	0.02264	0.01835	0.01888	-0.0088	0.01191	0.0125	0.00827	0.02087	0.01165
0.348	0.02963	0.0284	0.03688	0.01522	0.01252	0.01606	0.00668	0.00798	0.00428	0.01694
0.395	0.04849	0.03832	0.04833	0.07672	0.04091	0.03622	0.01559	0.02316	0.0179	0.00383
0.441	0.04556	0.04665	0.04691	0.0765	0.04104	0.01849	0.02165	0.01901	0.00631	0.00513
0.488	0.05978	0.06029	0.06652	0.06965	0.0451	0.05774	0.02756	0.03547	0.01527	0.03034
0.534	0.06442	0.0689	0.07556	0.06933	0.05285	0.03792	0.05696	0.03431	0.00277	0.00356
0.581	0.0721	0.07542	0.08696	0.0742	0.07237	0.06029	0.04515	0.06011	0.04186	0.02058
0.627	0.07116	0.07737	0.09265	0.07909	0.06198	0.07407	0.04358	0.04575	0.03024	0.02157
0.674	0.07412	0.0766	0.0797	0.07976	0.068	0.06057	0.06572	0.04218	0.0276	0.01888
0.721	0.05705	0.07074	0.08269	0.06638	0.08341	0.04641	0.07248	0.03414	0.03848	0.02654
0.767	0.0586	0.0442	0.07074	0.05193	0.06721	0.05264	0.03135	0.03281	0.03731	0.03309
0.814	0.07212	0.053	0.05648	0.05897	0.0666	0.0438	0.04929	0.03865	0.04975	0.04269
0.860	0.06513	0.047	0.06237	0.05629	0.04147	0.01514	0.04786	0.02445	0.01847	0
0.907	0.0609	0.05747	0.04726	0.06514	0.05103	0.04748	0.14371	0.04107	0.03202	0
0.954	0.03498	0.05014	0.05363	0.05303	-0.2141	0	0.02802	0.02166	0	0

Table A 15. Turbulent kinetic energy in the H15T configuration.

Radial	Normalized k values at respective axial distance (x)					k/V_{tip}^2				
r/x---->	**0.277**	**0.351**	**0.426**	**0.501**	**0.576**	**0.651**	**0.712**	**0.787**	**0.862**	**0.937**
0.069	0.01056	0.04874	0.02032	0.01892	0.01591	0.05538	0.00455	0.00429	0.03213	0.00341
0.115	0.04054	0.07389	0.06071	0.02148	0.06154	0.07807	0.12269	0.04487	0.12318	0.01866
0.162	0.16509	0.14602	0.01441	0.07237	0.10624	0.05081	0.00743	0.07466	0.06463	0.02506
0.208	0.1141	0.102	0.06865	0.0808	0.06615	0.07525	0.05367	0.00967	0.0249	0.03716
0.255	0.14816	0.06388	0.0341	0.06737	0.04112	0.06536	0.03826	0.05318	0.02729	0.04727
0.302	0.081	0.05656	0.01065	0.04854	0.10537	0.05167	0.03045	0.0363	0.01905	0.02894
0.348	0.06066	0.08071	0.01216	0.07116	0.09599	0.05189	0.05167	0.0349	0.01799	0.03278
0.395	0.04156	0.04772	0.00986	0.06887	0.06873	0.02878	0.05725	0.02821	0.02363	0.01221
0.441	0.06496	0.12024	0.06206	0.10101	0.08426	0.04979	0.02213	0.01811	0.01952	0.02553
0.488	0.06709	0.09351	0.03415	0.06838	0.03384	0.05104	0.01904	0.03618	0.01047	0.04754
0.534	0.07736	0.02281	0.07132	0.07181	0.03026	0.06445	0.0414	0.03137	0.0242	0.02632
0.581	0.06486	0.02	0.12435	0.0685	0.02342	0.05297	0.03028	0.05809	0.01948	0.01635
0.627	0.04412	0.03848	0.10786	0.03551	0.04163	0.04139	0.02638	0.07804	0.0122	0.01078
0.674	0.07378	0.02139	0.03998	0.01948	0.02745	0.04644	0.03524	0.07623	0.03115	0.01384
0.721	0.14372	0.04331	0.06713	0.02961	0.04916	0.05428	0.02501	0.08878	0.03781	0.01441
0.767	0.03427	0.03205	0.01844	0.04458	0.04406	0.04646	0.04762	0.07916	0.03036	0.01789
0.814	0.04066	0.0302	0.04001	0.01466	0.03328	0.02659	0.02854	0.05784	0.01521	0.031
0.860	0.01888	0.04172	0.02709	0.02039	0.01914	0.11001	0.0125	0.07198	0.05271	0.00842
0.907	0.0157	0.0172	0.01827	0.01984	0.01163	0.01973	0.19382	0.05019	0.01355	0.00559
0.954	0.01367	0.00506	0.01171	0.03639	0.03097	0.01587	0.02619	0.04199	0.14218	0.00759

Tangential velocity component

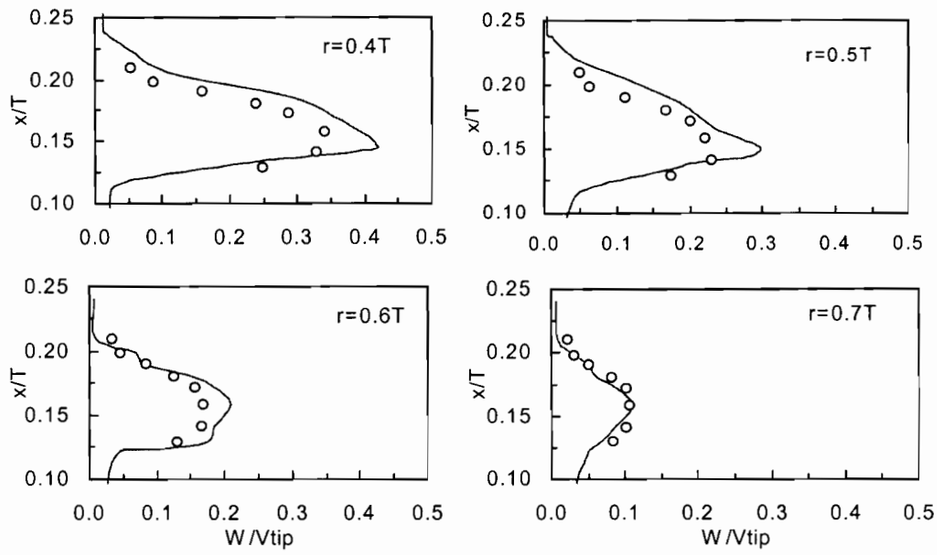

Figure A2. Velocity profile for the tangential velocity: (o) LDV, — CFD

Radial velocity component

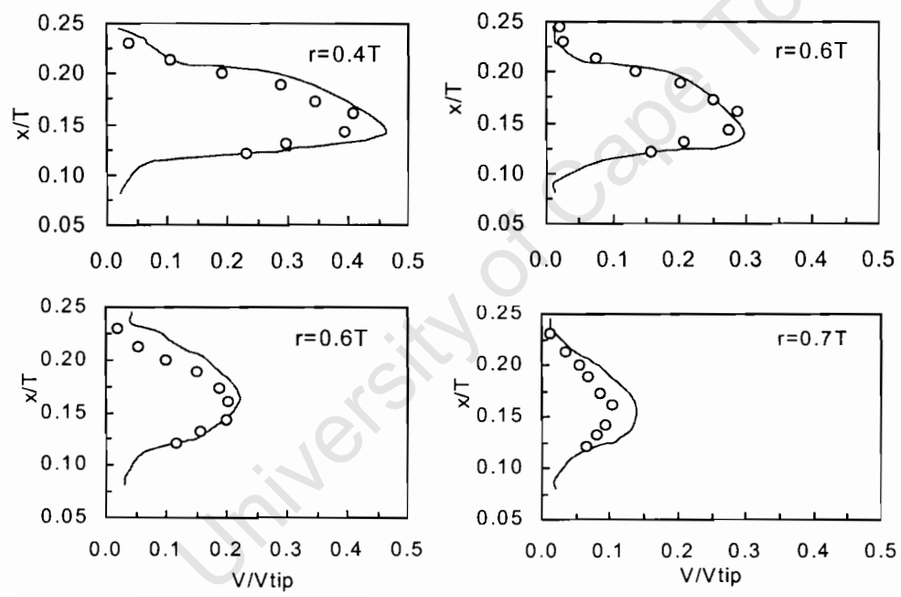

Figure A3. Velocity profile for the radial velocity: (o) LDV, — CFD

Turbulent kinetic energy and kinetic energy dissipation rate

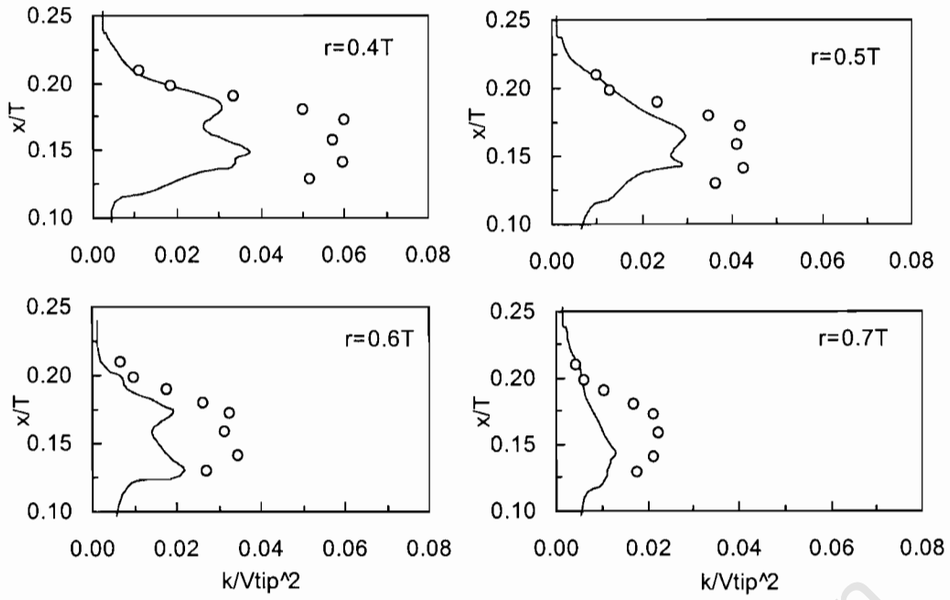

Figure A4. Turbulent kinetic energy profile: (o) LDV, — CFD

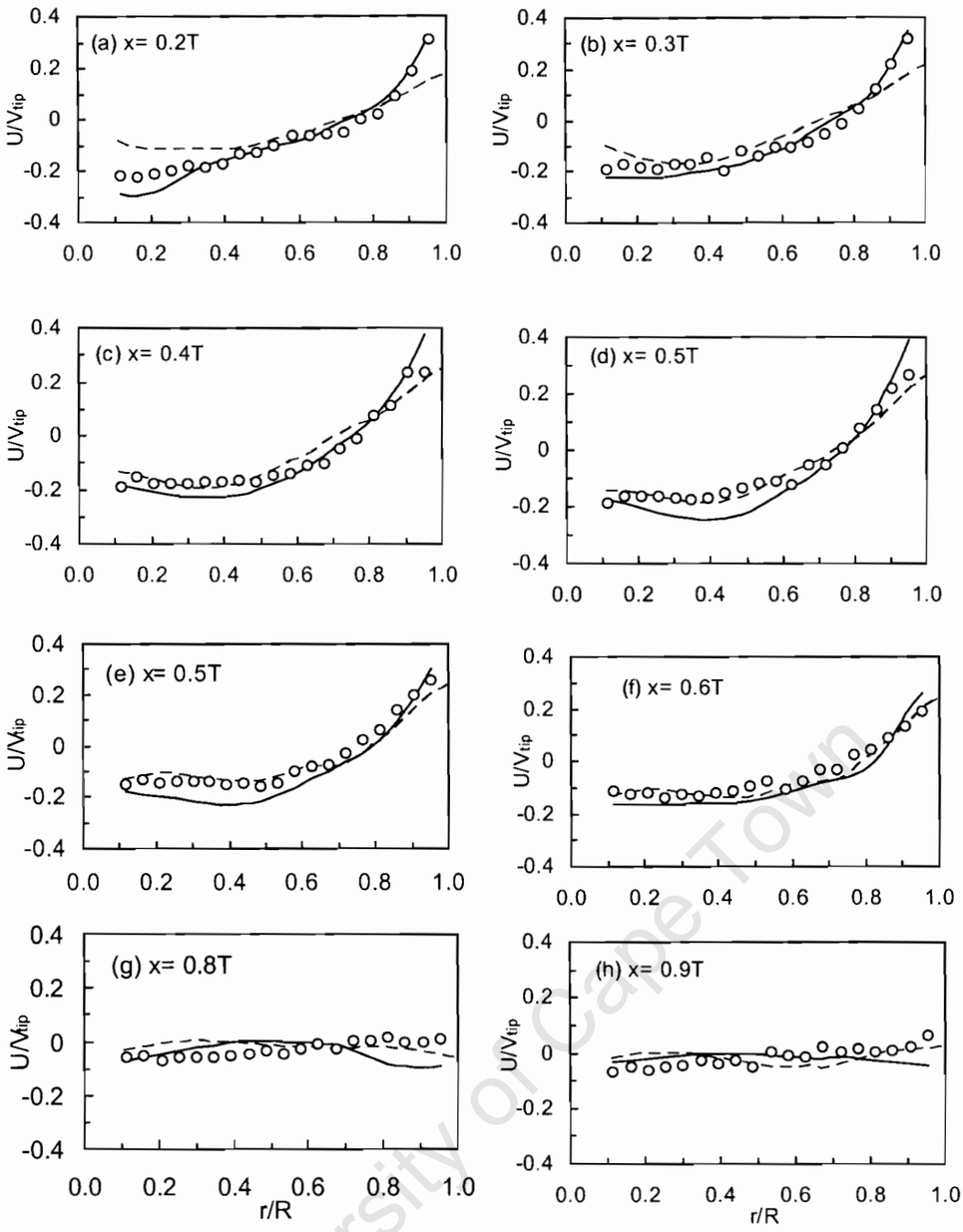

Figure A5. Axial velocity profile variation with turbulence models:

(o) Experiments —*k*-e, - - SST

Appendix II

Solid-liquid system

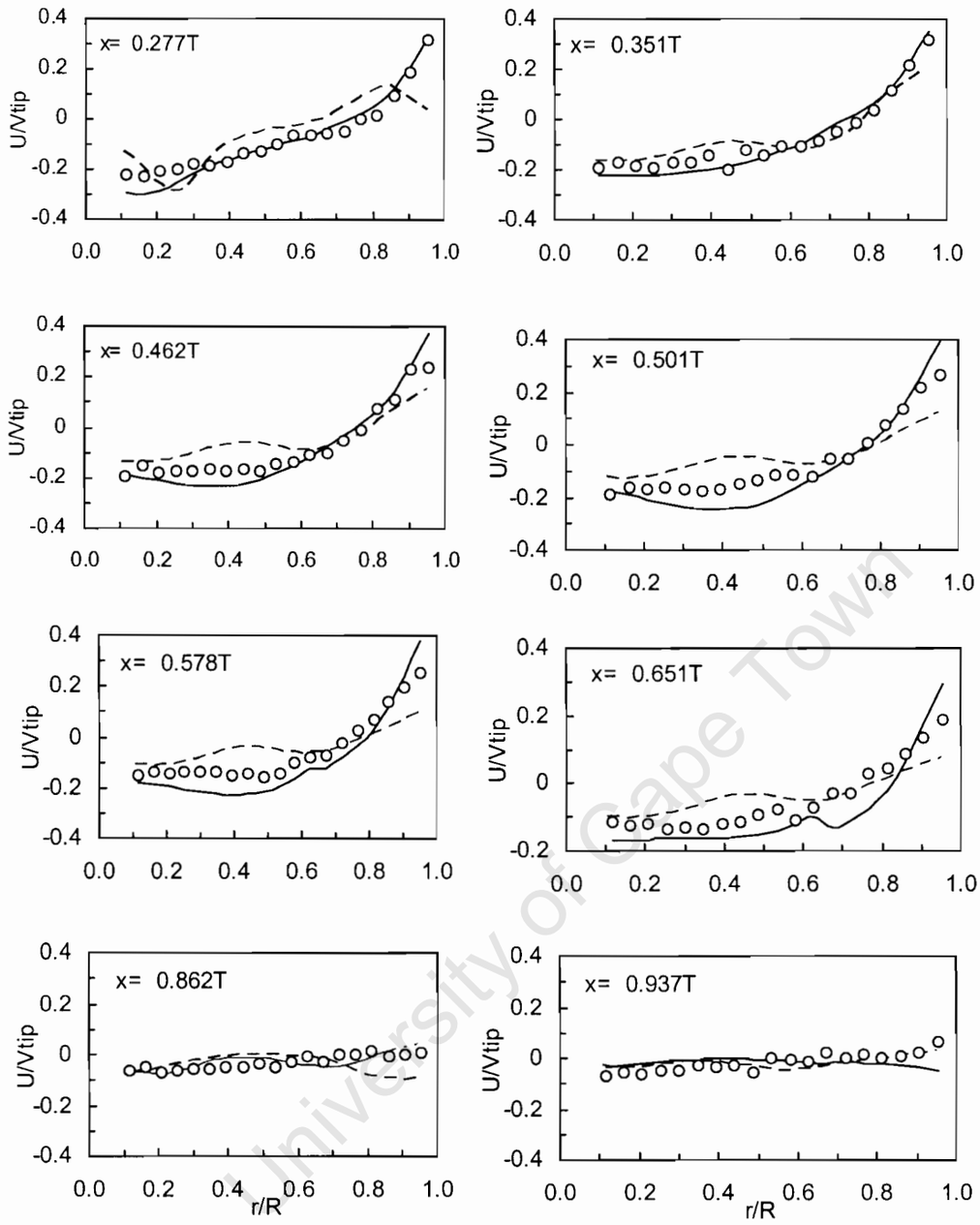

Figure A6. Effect of solids on the velocity field: (o) Experiments, ——No solids,

- - - - 2.3 kg, Nickel 150-1000 μm

Table A 16. Particle properties and flow dependent parameters

d_p, micron	d_{50}, micron	U_t-SN,cm/s	CD-SN	Re-SN	U_t-St,cm/s	U_t-exp, cm/s	Re_p-Exp	CD-Exp
53-75	64	1.53	27.99	0.980	1.957	3.686	2.36	12.9
75-106	89	2.76	12.23	2.518	3.785	5.014	4.46	7.63
106-150	128	4.63	6.105	5.935	7.830	6.080	7.78	4.98
150-300	230	9.70	2.411	22.72	25.280	9.850	22.7	2.41
300-425	363	16.20	1.414	58.79	62.969	14.500	52.6	1.50
425-600	514	22.70	1.019	116.4	126.25	19.000	97.7	1.10
600-1000	784	32.00	0.748	240.0	293.73	34.650	272	0.71

Table A 17. Particle flow properties, power and dimensionless numbers.

d_p, μm	Njs, rps	N_{90}, rpm	Ar	P,watt	ε,m^2s^{-3}	λx10-6	d_p/λ	Fr	St x 10^3
75	435		41	16	0.42	36	2.1	0.67	2.5
100	461	180	98	18	0.50	34	2.9	0.75	4.8
200	542	230	781	30	0.81	31	6.5	1.04	23
300	596	347	2636	40	1.09	28	10.6	1.26	56
400	608	353	6249	42	1.15	28	14.3	1.31	101
500	636	360	12205	49	1.31	27	18.5	1.43	165
750	694	430	41193	62	1.68	25	29.4	1.68	403
1000	730	461	97642	74	1.99	24	41.0	1.89	758

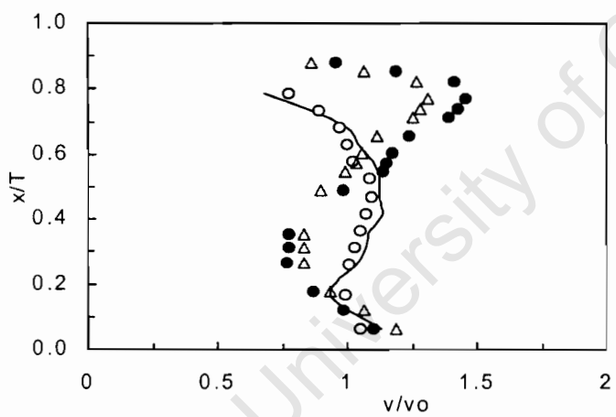

Figure A7. Axial solids concentration profile with 1.3%Ni230 using sampling method: (o) OAT, ——CFD, (•) Sampling at 22 mm from the wall, Δ mean of radial points.

Sample routine

```
        I~~~~~~~~~~~~~~~~~~~~~~~~~~~~~~~~~~~~~~~~~~~~~~~~~~~~~~~~~~~~~~~~~~~~ I
        I This program computes the terminal settling velocity and drag coefficient   I
        I according to the Schiller Naumann drag model.                               I
        I Written by Ochieng Aoyi, 22 November 2003                                   I
        I~~~~~~~~~~~~~~~~~~~~~~~~~~~~~~~~~~~~~~~~~~~~~~~~~~~~~~~~~~~~~~~~~~~~~I

        PROGRAM SETTLING VELOCITY
        INTEGER I
        PRINT *,'  UT                    DIF'
        PRINT *,'-------------------------'
        UTO = 0.1
        DP  = 513E-6
!       PRINT *,'PLEASE TYPE IN THE PARTICLE DIAMETER IN M'
!       READ *, DP
!       PRINT *, 'PLEASE TYPE IN THE UT INITIAL GUESS'
!       READ *, UTO
        EPS=0.00001
        DO 1 I=1,100
        PRINT *,'BEGINING UTO IS =', UTO
        UT = UTO+0.0001
        RE = UT*DP/1.0E-6
        VAR = 0.15*RE**0.687
        CD = (24/RE)*(1.0+VAR)
        UT1 = (4*DP/CD)*(9.81*7803/3000)
        UT = UT1**0.5
        DIF = UTO-UT
        PRINT *, I,UT, DIF
        IF(ABS(DIF). LT. EPS)THEN
        GOTO 2
        ELSE
        UTO=UT+0.00001
        ENDIF
1       CONTINUE
2       PRINT *,' '
        PRINT *,'TERMINAL VELOCITY IS ', UT
        PRINT *, ' '
        PRINT *,'FOR NICKEL PARTICLE OF DIAMETER =', DP
        PRINT *,' '
        PRINT *,'REYNOLD NUMBER IS RE= ', RE
        PRINT *,' '
        PRINT *,'DRAG COEFFICIET, CD= ', CD
        WRITE(*,34) I,UT,DP,RE,CD
34      FORMAT(1X,I,2X,1X,'UT =',F8.4,3X,'DP =',F8.6/,1X,'RE =',
   &    F8.4,3X,'CD =',F8.4/)
        END
```